Durham University

Durham E-Theses

Stellar populations of local cluster early-type galaxies

Rawle, Timothy David

How to cite:

Rawle, Timothy David (2009) *Stellar populations of local cluster early-type galaxies*, Durham theses, Durham University. Available at Durham E-Theses Online: http://etheses.dur.ac.uk/2123/

Use policy

The full-text may be used and/or reproduced, and given to third parties in any format or medium, without prior permission or charge, for personal research or study, educational, or not-for-profit purposes provided that:

- a full bibliographic reference is made to the original source
- a link is made to the metadata record in Durham E-Theses
- the full-text is not changed in any way

The full-text must not be sold in any format or medium without the formal permission of the copyright holders.

Please consult the full Durham E-Theses policy for further details.

Academic Support Office, Durham University, University Office, Old Elvet, Durham DH1 3HP
e-mail: e-theses.admin@dur.ac.uk Tel: +44 0191 334 6107
http://etheses.dur.ac.uk

Stellar Populations of Local Cluster Early-Type Galaxies

Timothy David Rawle

The copyright of this thesis rests with the author or the university to which it was submitted. No quotation from it, or information derived from it may be published without the prior written consent of the author or university, and any information derived from it should be acknowledged.

A Thesis presented for the degree of
Doctor of Philosophy

29 OCT 2009

Extragalactic Astronomy
Department of Physics
University of Durham
United Kingdom

September 2009

Dedicated to

my Family

Stellar Populations of Local Cluster Early-Type Galaxies

Timothy David Rawle

Submitted for the degree of Doctor of Philosophy
September 2009

Abstract

This thesis investigates local cluster early-type galaxies, combining new spectroscopy with multi-wavelength imaging. We probe the stellar content of elliptical and lenticular galaxies, exploring the interconnection between age, chemical composition and dynamical substructure.

We analyse the ultraviolet–infrared colour–magnitude relation, using new *GALEX* imaging of quiescent red-sequence galaxies in local clusters, and confirm that the intrinsic scatter is an order of magnitude larger than for the analogous optical relation. We compare the UV–IR colours to spectroscopic stellar populations parameters, and find a strong correlation with metallicity (albeit still with a large scatter), and only a marginal trend with age. We argue that the UV upturn is not significant in this sample, and demonstrate that the intrinsic scatter could be attributed to simple frosting by either a young *or* low metallicity subpopulation.

We present a comprehensive study of the internal gradients in age, metallicity and α-element abundance for 25 cluster early-type galaxies, using data from the VLT VIMOS integral field unit. We find negative metallicity gradients, with a large intrinsic scatter for galaxies with $\sigma \gtrsim 130$ km s^{-1}, which we speculate could be the lower limit for a formation history dominated by major mergers. Stellar population gradients are primarily related to the central metallicity: early-type galaxies with super-solar centres have steep negative metallicity gradients and positive age gradients; those with solar metallicity centres have negligible [Z/H] gradients and negative age gradients. B–R colour gradients predicted from the spectroscopic age and metallicity generally agree well with those measured directly from photometry. There is a strong observed anti-correlation between the gradients in age and metallicity. While a part of this trend can be attributed to correlated measurement errors, we demonstrate that there is an underlying intrinsic

relation.

We present new GMOS long-slit observations of seven edge-on lenticular galaxies in the Coma cluster, probing to several disc scale lengths in each. We strongly confirm that these S0s are significantly offset in luminosity from the spiral Tully-Fisher relation, and show that the size of this offset is correlated with projected local density. However, there appears to be no difference in the mean offset between S0 samples from various global environments (i.e. group and cluster). We derive the radial trends in the stellar populations, and find generally regular profiles consistent with those observed in the VIMOS sample. Significant deviations from the general radial trends coincide with structural and kinematic boundaries. We find that the age of the disc component is correlated with the offset from the Tully-Fisher relation, and agrees well with simple models of abrupt star formation truncation in a spiral disc. We show that S0 discs tend to be older and more metal poor than the central regions, supporting the theory of bulge growth alongside disc quenching, during S0 formation.

Declaration

The work in this thesis is based on research carried out in the Extragalactic Astronomy Group at the Department of Physics, University of Durham, United Kingdom. No part of this thesis has been submitted elsewhere for any other degree or qualification. The work described is my own, unless referenced to the contrary in the text. Some of this work has, however, been published in the following papers (in chronological order):

Near ultraviolet-infrared colours of red sequence galaxies in local clusters. Rawle T. D., Smith Russell J., Lucey J. R., Hudson M. J., Wegner G. A., 2008, Monthly Notices of the Royal Astronomical Society, 385, 2097

Stellar population gradients in early-type cluster galaxies with VIMOS IFU. Rawle T. D., Smith Russell J., Lucey J. R., Swinbank A. M., 2008, Monthly Notices of the Royal Astronomical Society, 389, 1891

Stellar population gradients in early-type cluster galaxies. Rawle T. D., Smith Russell J., Lucey J. R., 2009, Monthly Notices of the Royal Astronomical Society, *in press*

Copyright © 2009 by Timothy David Rawle.
"The copyright of this thesis rests with the author. No quotations from it should be published without the author's prior written consent and information derived from it should be acknowledged".

Acknowledgements

I would like to begin by thanking my supervisor, John Lucey for all his invaluable guidance, ideas and encouragement. John's infectious enthusiasm helped me maintain a relaxed and content outlook even through the most hectic of pre-deadline periods. I would also like to thank Russell Smith for his ever-present assistance: this thesis owes a lot to his knowledge and insight. Many members of the department deserve my thanks for useful discussion during the ubiquitous coffee breaks, and in particular, I would like to mention Mark Swinbank for helping me through the minefield of IFU data reduction

A special thank you must go to my housemate of the past two years, Juan Gonzalez, for being a delight to live with, keeping me sane, and showing me the emotional roller-coaster of a Chilean football fan. Many people have contributed to my social life, whether it be in poker games, playing squash, climbing, or simply sampling the fine beer available in Durham. There are too many to list everyone I've raised a glass with, but I am particularly grateful for the company of Raul Angulo, Rich Bielby, Craig Booth, Kristen Coppin, Rob Crain, Greg Davies, Nikos Fanidakis, Jim Geach, Jeanette Gladstone, Andy Goulding, Stephen Hamer, John Helly, Mike Hill, Sarah Hutton, Floyd Jackson, Dan John, Bret Lehmer, Jean-Philippe Lenain, Ian McCarthy, Alex Merson, Dave Murphy, Jim Mullaney, Mark Norris, Alvaro Orsi, Owen Parry, Claire Poppett, David Radburn-Smith, Nic Ross, Malgosia Sobolewska, John Stott, Chiara Tonini, Dave Wake, Julie Wardlow, Yamila Yayura.

I would like to thank my family for their constant belief and continued support over the years it has taken to reach this point: I owe to them my love of science and inquisitive mind. Finally, special thanks go to Kate, who has been the shining light of my final year, and has put up with so much (such as a trip to Hawaii) while I gazed at distant galaxies.

Scientific acknowledgements

I was supported in this work by the STFC Studentship PPA/S/S/2006/04341.

A major component of this thesis is based on VIsible MultiObject Spectrograph (VIMOS) IFU observations from the European Organisation for Astronomical Research in the Southern Hemisphere, Chile (programs: 078.B-0539, 081.B-0539)

The data presented in the final science chapter of this thesis were obtained using GMOS on Gemini-North (program: GN-2009A-Q52). I was lucky enough to travel to Hilo, Hawaii for observer and sea-level calibration/reduction training, courtesy of the STFC and the UK Gemini Office. I would like to thank everyone at the facility for making me feel very welcome during my visit. I would especially like to mention Sascha Fritz, Jesse Ball, Tom Geballe, Paul Hirst and Drew Serio for guiding me through seven nights at the summit of Mauna Kea.

I would also like to thank Chris Haines, Adriana Gargiulo, Paola Merluzzi and the SOS team for providing Shapley Supercluster B- and R-band imaging and photometry.

Parts of this thesis are based on observations made with the NASA Galaxy Evolution Explorer. *GALEX* is operated for NASA by California Institute of Technology under NASA contract NAS-98034. This publication makes use of data products from the Two Micron All Sky Survey, which is a joint project of the University of Massachusetts and the Infrared Processing and Analysis Center/California Institute of Technology, funded by NASA and the National Science Foundation. This research has made use of the NASA/IPAC Extragalactic Database (NED) which is operated by the Jet Propulsion Laboratory, California Institute of Technology, under contract with the National Aeronautics and Space Administration.

Contents

List of Figures

List of Tables

When I dipt into the future far as human eye could see;
Saw the Vision of the world and all the wonder that would be.

Alfred, Lord Tennyson, (from *Locksley Hall*, 1835)

Chapter 1

Introduction

The first decade of the 21st Century has seen a quantum leap forward in extragalactic observational astronomy. Wide-field ground-based photometric surveys (e.g. 2MASS, SDSS) have been joined by multi-wavelength imaging from spaceborne observatories, from X-ray (*ROSAT*), ultraviolet (*GALEX*; Martin et al. 2005), through optical and infrared bands (Hubble, Spitzer), and into the microwave regime (*WMAP*; Spergel et al. 2007). Spectroscopic surveys which cover hundreds of thousands of galaxies (e.g. 2dF Galaxy Redshift Survey, Colless et al. 2001; 6dF Galaxy Survey, Jones et al. 2004; SDSS DR7, Abazajian et al. 2009) have facilitated the investigation of general galaxy characteristics on an unprecedented scale. New analysis techniques, encompassing everything from sophisticated spectral modelling (e.g. Maraston 2005; Schiavon 2007) and fitting (e.g. Heavens, Jimenez, & Lahav 2000; Proctor et al. 2004), to harnessing the manpower of the general public (Galaxy Zoo; Lintott et al. 2008), have helped to tame these vast samples.

Small area, targeted, deep field observations (e.g. Chandra; Hubble; *SCUBA*, Holland et al. 1999) have viewed the distant past, glimpsing proto-galaxies and identifying their nurseries (e.g. Lehmer et al., 2009), while exploration of the local universe probes structure and composition of nearby galaxies with increasing resolution. As deep imaging extends our knowledge of low-luminosity galaxies and internal structure, high signal-to-noise spectroscopy, coupled to a new generation of stellar population models, offers a detailed window into the chemical evolution of local galaxies.

Studies are no longer confined to a particular bandpass, but tackle the key questions through multi-wavelength observations from a variety of instruments.

In particular, the synergy between imaging and spectroscopy is crucial to further our understanding of how galaxies form and evolve.

1.1. Galaxies in the Universe

The first recorded observation of galaxies outside our Milky Way was by Persian astronomer Al-Safi, who, in the 10th Century, described Andromeda and the Large Magellanic Cloud as "small clouds". Almost 800 years later, Immanuel Kant coined the term "Island Universe" for these nebulae; the idea that they were remote collections of stars had been speculated upon a few years earlier by County Durham polymath Thomas Wright, but was by no means the accepted theory.

Kant's poetic moniker was gradually dropped, as "Universe" adopted its modern connotation. In the 1920s, Edwin Hubble convincingly placed several spiral nebulae beyond the Milky Way, calculating their distance using Cepheid variables. Distant objects were finally disassociated from local nebulae, and the investigation into these "galaxies" (from the Greek for "Milky" as in the Milky Circle – kyklos galaktikos) could begin in earnest.

1.1.1 Galaxy formation and the cosmological context

In the last few decades there have been two prevailing theories of galaxy formation. In monolithic collapse, a large galaxy forms as a single entity at early epochs, while in hierarchical formation, small components gradually merge together to build large galaxies.

Initially, the predominant theory was monolithic, dissipative collapse (Eggen, Lynden-Bell, & Sandage, 1962; Larson, 1974a; Carlberg, 1984). Through this mechanism, an overdense region of the primordial universe collapses as it cools, forming a single galaxy from the constituent baryons. This model gives a plausible explanation for the formation of a spiral galaxy: the central gas collapses very rapidly to form the spheroidal bulge, while gas in the outer regions collapses more slowly, tending to distribute into the plane of rotation and form a disc structure. The observation of significant numbers of fully-formed massive galaxies at $z > 1$ (Drory et al., 2005) seemed to support this mechanism and, naively, appeared inconsistent with scenarios that build galaxies gradually. However, in monolithic collapse the star formation in a galaxy would be mostly complete within $\sim$1 Gyr. On this time-scale, type Ia supernovae would be unable to contribute large quantities of heavy elements to the interstellar medium before the cessation of star formation,

predicting lower metallicities than observed (e.g. Worthey, Dorman, & Jones, 1996; Proctor & Sansom, 2002).

Hierarchical merging is supported by the cosmological paradigm of cold dark matter (CDM). From an initial power spectrum of (post-inflation) density fluctuations, and implementation of basic physical principles such as gravitation and the conservation of energy and angular momentum, numerical cosmological simulations trace the build-up of dark matter halos (e.g. Efstathiou et al. 1988; Navarro, Frenk, & White 1996; Jenkins et al. 2001). As originally postulated by White & Rees (1978), galaxies form when gas condenses at the centre of these halos (also White & Frenk, 1991). However, although *ab initio* N-body simulations can specify the distribution and evolution of the dark matter, a numerical treatment of galaxy formation is difficult, due to both computational constraints and a lack of understanding for some physical processes (e.g. feedback). Instead, the evolution of baryonic components is modelled by simple, physically-motivated prescriptions implemented via a semi-analytic approach (Baugh, 2006). Recently, direct hydrodynamics has proved viable, although processes such as star formation still need modelling as 'sub-grid' physics (e.g. Springel & Hernquist, 2003).

In recent years the ΛCDM (concordance) model has become the standard cosmological paradigm for the formation of large-scale structure, as it can simultaneously account for many observable phenomena. For instance, the power spectrum of the observed galaxy clustering in large-scale redshift surveys such as 2dF-GRS (Colless et al., 2001) are accurately replicated by ΛCDM models (e.g. Cole et al., 2005). Even downsizing, the apparently anti-hierarchical behaviour in which massive galaxies complete most of their star formation earlier than small galaxies, can be reproduced in hierarchical ΛCDM (Cole et al., 2000), as feedback, due to active galactic nuclei, quenches star formation more efficiently in massive halos (Bower et al., 2006).

The ΛCDM galaxy models do not match the observed universe in every respect. Firstly, dark matter halo profiles are too steep to be consistent with the rotation curves of low-luminosity galaxies, where local mass is dark matter dominated (the cusp-core problem; e.g. McGaugh & de Blok 1998). A separate issue arises from the number of subhalos within the virial radius of a massive halo. The predicted number of satellite halos in a Milky-Way sized halo is an order of magnitude larger than visible satellite galaxies around our Milky Way (Klypin et al., 1999). However, this mismatch may be caused by unobserved 'dark satellites'. A common criticism of simulations is their reliance on

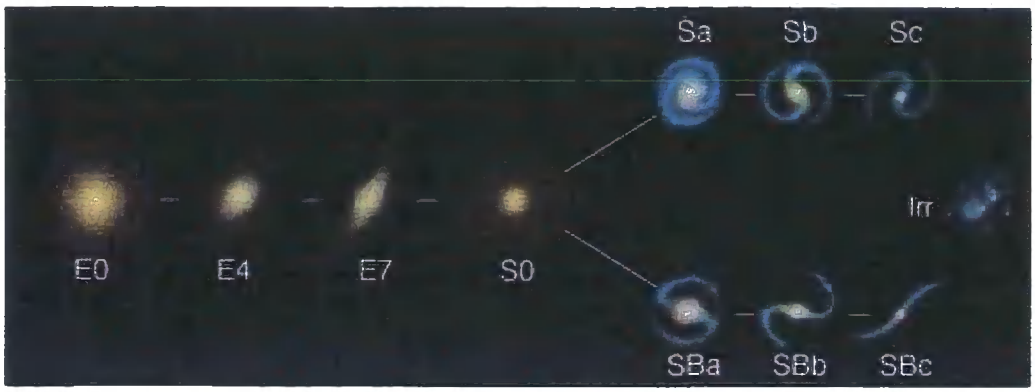

Figure 1.1: Morphological classification of galaxies by Hubble's 'tuning fork' diagram. Source: http://physics.uoregon.edu/

matching observations by varying unphysical free parameters. For instance, Baugh et al. (2005) reproduced the sub-millimeter galaxy number counts, but only by invoking a controversial top-heavy initial-mass function. To advance further, simulations need to become truly physically motivated, rather than merely incorporating *ad hoc* prescriptions based on physics.

1.1.2 Morphological classification

In the famous 'tuning fork' diagram, Edwin Hubble (1927) classified galaxies into three broad groups: ellipticals, spirals and barred spirals. The elliptical galaxies were further demarcated, by their ellipticity, and both spiral categories were sub-divided by the prominence of bulges and tightness of spiral arms (see Figure 1.1). In the centre of the scheme sit the lenticular galaxies, having both bulge and disc components, but no spiral arms. Although Hubble named the elliptical/lenticular galaxies 'early-type' and the spirals 'late-type', he did not intend the diagram to convey an evolutionary timeline[1].

de Vaucouleurs (1959) developed a more elaborate classification scheme which subdivided spiral galaxies further. However, although the immediate visual differences are easy to identify in local galaxies, or between, for instance, a well resolved E0 and face-on spiral, classification beyond early- or late-type is difficult for most galaxies. Furthermore, visual classification is extremely time consuming for modern imaging surveys which con-

[1] Baldry (2008) speculated that Hubble wished to convey a sequence of visual complexity, and borrowed these terms from stellar classification where the evolutionary connotation had disappeared several years earlier.

tain many millions of galaxies.

An intriguing method to tackle this problem is to harness the ability for a large and untrained crowd to select, on average, the correct morphology. In Galaxy Zoo, Lintott et al. (2008) invited the public to help classify millions of galaxies in SDSS imaging, ensuring high-quality results with huge repetition and tough rejection criteria. Other groups have relied on computer-power to categorise galaxies, although differentiating between the Hubble classes is CPU intensive. Morphological categorisation can also be obtained via the surface brightness profile. While disc-like structures, such as the dominating component of late-type galaxies and S0s, have an exponential profile (Freeman, 1970), elliptical galaxies and bulges tend towards an $r^{1/4}$ de Vaucouleurs (1948) profile[2]. Sérsic (1963) profiles have a generalised $r^{1/n}$ form, where n=1 is the exponential profile and n=4 is the de Vaucouleurs $r^{1/4}$. A galaxy fit best by an n=1 profile is therefore less concentrated in the centre, and more likely to be a spiral, and conversely, a higher Sérsic index (n) indicates a spheroidal structure (e.g. Bell et al., 2003; Mandelbaum et al., 2006). Algorithms such as GALFIT (Peng et al., 2002) and BUDDA (de Souza et al., 2004) generate a two-dimensional fit to the surface brightness, including multiple Sérsic components, and hence automate the process of differentiating between spirals, ellipticals and S0s. An alternate method, used with limited success, obtains morphology from the concentration, asymmetry, and smoothness of the surface brightness distribution (e.g. Blakeslee et al., 2006).

Distinguishing spiral and elliptical galaxies is important, as such disparate structures must originate via different mechanisms. Additionally, the optical colour of spiral and elliptical galaxies is clearly different, with blue galaxies very reliably classifiable as spiral galaxies (de Vaucouleurs 1977; Bamford et al. 2009). As young stars are bluer than old stars, this observation indicates that star formation continues in most spiral galaxies, while ellipticals are generally quiescent. (Colours are discussed in greater detail in Section 1.2.2.)

[2]This observational classification differs from simulations, where discs are identified directly from kinematics as rotationally supported structures, and spheroids are pressure supported, lacking coherent rotation.

1.1.3 Environment and the role of clusters

A clue to the formation of elliptical and spiral galaxies comes from the relation between galaxy population and environment. Commented upon by both Shapley (1926) and Hubble (1936), this morphology–density relation (Dressler, 1980b) indicates that the fraction of elliptical (and S0) galaxies is larger in higher density regions, while the fraction of spirals increases as density decreases (Figure 1.2).

Smith et al. (2005) investigated the morphology–density relation at z = 1, and found that it has evolved, such that the fraction of early-type galaxies decreases with redshift in high density environments, but remains relatively stable at lower densities. This is the morphology analogue of the Butcher–Oemler effect (Butcher & Oemler, 1978), which described how the fraction of red galaxies in rich clusters decreases with redshift. Observations of intermediate redshift clusters (z = 0.3 – 0.4) confirmed the evolution in colour fractions (e.g. Couch et al., 1994; Ellingson et al., 2001).

The colour–density relation (driven by stellar mass and star-formation history) is the more fundamental relation (Kauffmann et al., 2004); morphology does not strongly depend on environment at a fixed colour, whereas colour is a strong function of environment even at fixed Sérsic index (e.g. Bamford et al., 2009). Together, these studies suggest that the mechanisms that transform one type of galaxy to another are similar in all environments, but more commonly occur in the rich cluster environment (Tran et al., 2005).

1.2. Galaxy scaling relations

Exploration of the general trends in galaxies requires a homogeneous sample, with the identification and removal of selection bias paramount. Rich galaxy clusters have proven indispensable for these studies, yielding many galaxies at the same distance and within a relatively small field, where early-type cluster members can be selected by colour. Local environment (i.e number density of nearby galaxies) appears to have more influence on observable parameters than the large scale density field (global environment; Kauffmann et al. 2004; Blanton 2006). Clusters offer an opportunity to study the effect over a wide dynamic range of local densities by sampling galaxies from the core to the outer regions (e.g. Lucey et al., 1991; Guzman et al., 1992). Finally, the evolution with redshift can be examined by comparing the bulk trends within different clusters.

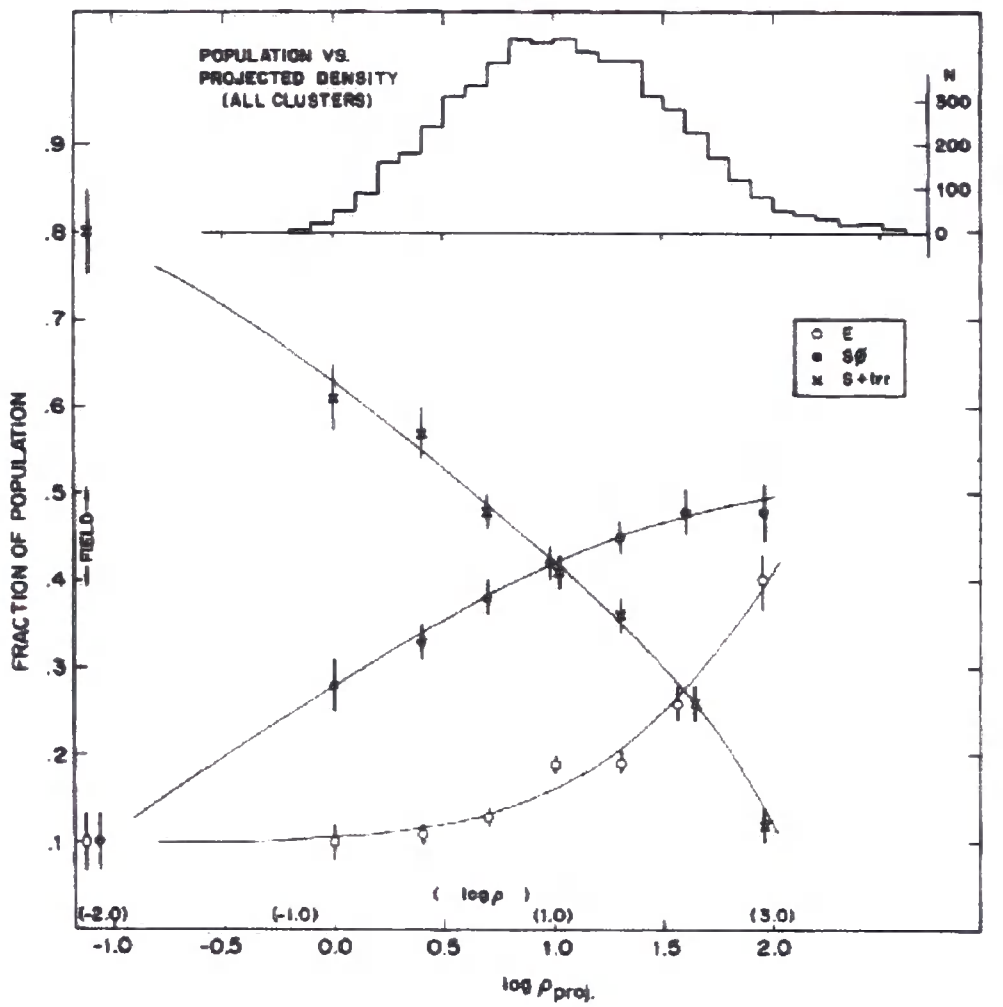

Figure 1.2: The morphology–density relation from Dressler 1980b (figure 4) showing that the early-type galaxy fraction (ellipticals: open circles; S0s: filled circles) increases with the projected local density ($\rho_{\rm proj}$). The spirals fraction (crosses) shows a corresponding decrease, and the symbols to the far left indicate the continued variation of the fractions into the field population.

1.2.1 Kinematic relations

Kinematics is the investigation of stellar motion within a galaxy, often characterised by the mean rotational velocity and velocity dispersion, σ (the rms spread of the random stellar velocities). In the composite stellar light of a galaxy with unresolved individual stars, the velocity dispersion can be measured from the width of spectral features, as the small differences in velocity shift the individual stellar spectra relative to each other. For a virialized system, σ is directly related to the depth of the potential well, and hence the total galaxy mass.

The Faber–Jackson relation (FJR; Faber & Jackson, 1976) is an empirically derived power-law for early-type galaxies, which links luminosity to central velocity dispersion, such that bright galaxies have higher dispersions: $L \propto \sigma^{\gamma}$, where $\gamma \sim 4$. For fainter early-type galaxies, Matković & Guzmán (2005) found that the relation is significantly shallower, with $\gamma \sim 2$. In general, this relation can be used to determine the absolute magnitude of an early-type galaxy directly from the velocity dispersion, and hence, by comparing to the apparent magnitude, leads to an estimate of the distance. The analogue for spiral galaxies of the FJR is the Tully-Fisher relation (TFR; Tully & Fisher, 1977). The TFR relates luminosity to the maximum circular rotational velocity, as spiral discs are rotationally supported, unlike the pressure-supported ellipticals, and can also be used to estimate distances. Recent studies have computed a TFR of $L \propto V_c^{\gamma}$, where $\gamma \sim 3.0 - 3.7$ (Tully & Pierce, 2000; Courteau et al., 2007).

Both the FJR and TFR relate luminous (baryonic) mass to the total dynamical (baryonic + dark matter) mass (via velocity). The TFR does not exhibit significant evolution to at least $z \sim 1$ (e.g. Vogt et al., 1997; Swinbank et al., 2006), as shown in Figure 1.3. The lack of evolution is predicted by hierarchical simulations (Cole et al., 2000), as the growth rate for baryons is regulated by the rate of accretion of dark matter, so total and luminous masses track one another. In contrast, in monolithic collapse, stellar mass grows within a pre-existing dark matter halo, so the luminous-to-total mass ratio should increase with time.

The intrinsic scatter in the FJR can be reduced by introducing a surface brightness term. This more precise scaling relation is usually presented in the form that relates velocity dispersion to the effective surface brightness and effective radius (Djorgovski & Davis, 1987; Dressler et al., 1987). In this parameter space, early-type galaxies are confined to a single plane, as shown in the projection in Figure 1.4. Known as the Fundamental Plane,

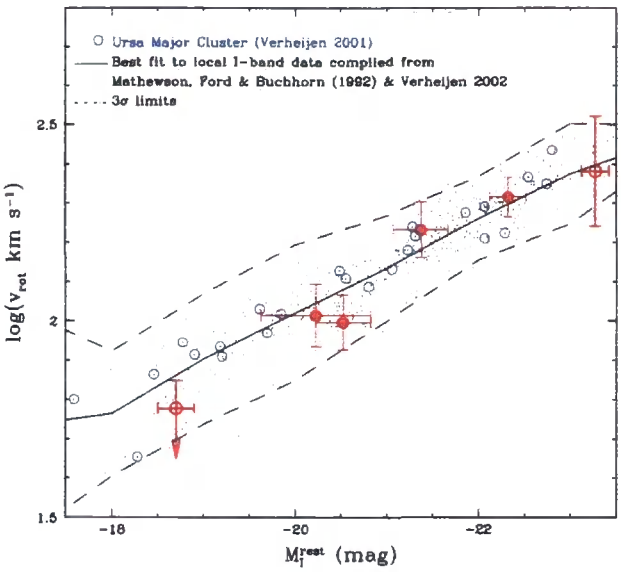

Figure 1.3: The I-band Tully-Fisher relation for spiral galaxies at $z \sim 1$ from Swinbank et al. (2006, red symbols) compared to local studies (small dots: 1355 local spiral galaxies from Mathewson et al. 1992; open circles: 24 Ursa Major cluster spirals from Verheijen 2001). There is no significant evolution with redshift. (Adapted from Swinbank et al., figure 8.)

the relation is consistent with a model in which the stars of elliptical galaxies are formed in a single, high-redshift burst (e.g. Bernardi et al., 2006). An interesting aspect of the Fundamental Plane is the tilt with respect to a naive prediction based on the virial theorem. This deviation arises from structural non-homology and the systematic variation of stellar properties with luminosity or mass (e.g. Bolton et al., 2007; Allanson et al., 2009).

1.2.2 Colour–magnitude diagrams and the red sequence

Luminosity and velocity dispersion effectively trace the stellar and total mass (respectively) in an elliptical galaxy. Besides the formation constraint imposed by the Fundamental Plane, other observed quantities can be used to investigate the evolution of galaxies.

Local galaxies can be categorised into two distinct types using an optical colour–magnitude relation: a red sequence of quiescent galaxies (Visvanathan & Sandage, 1977; Bower, Lucey, & Ellis, 1992), and a 'blue cloud' of star-forming galaxies. The left panel of Figure 1.5 presents the colour–magnitude relation for 55 000 galaxies in SDSS (Hogg et al., 2004), and clearly shows the two components, with a best fit line through the red

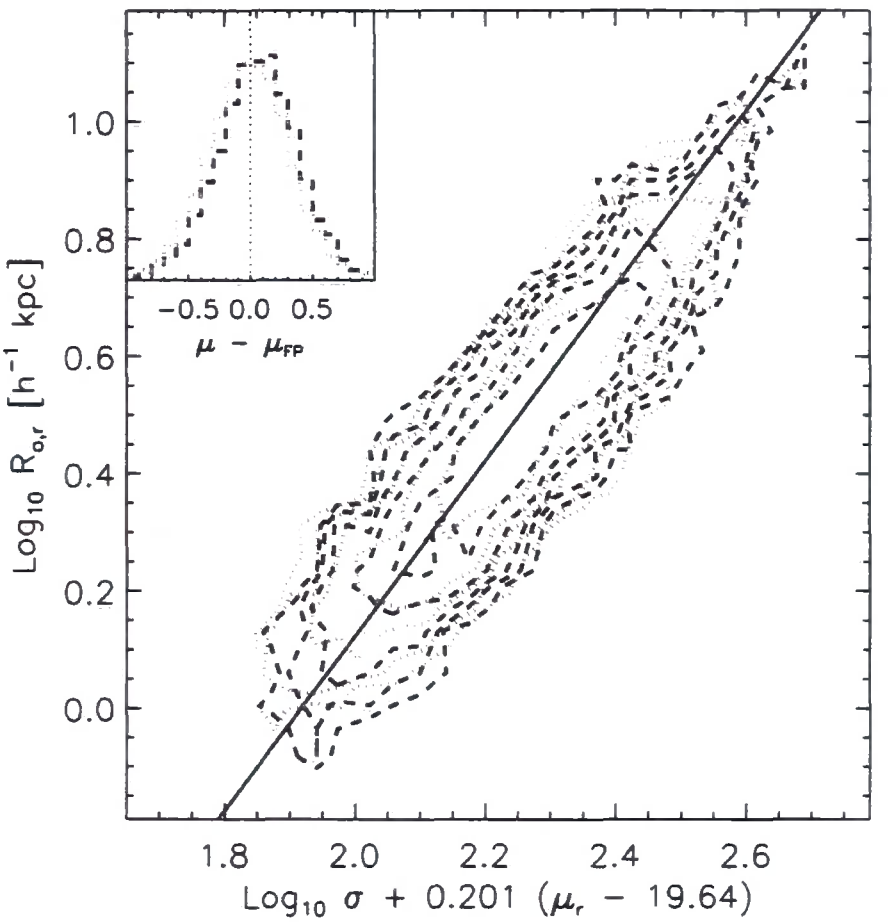

Figure 1.4: The r-band Fundamental Plane for ~40 000 early-type galaxies from SDSS (Bernardi et al., 2006, figure 3). The plane relates the effective radius R to the velocity dispersion σ and surface brightness μ. The dashed and dotted lines indicate subsamples from over- and under-dense environments respectively.

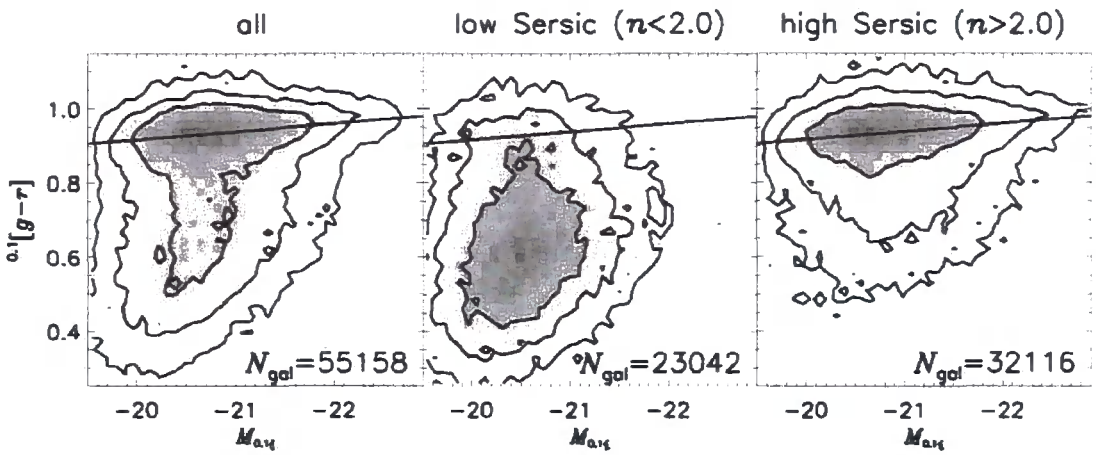

Figure 1.5: The g–r colour–magnitude diagram for ~55 000 SDSS galaxies (adapted from Hogg et al. 2004, figure 1). The left panel presents all galaxies in the sample, while the centre and right panels display sub-samples based on the Sérsic index (approximately isolating late- and early-type respectively). The red sequence (indicated by the linear fit) is dominated by early type galaxies.

sequence. The central and right panels show that low and high Sérsic subsamples mostly separate the blue and red galaxies (respectively). However, the high Sérsic subsample does contains a diminished 'blue cloud' (early-types with residual star formation), while there are also a minority of red spirals. As is expected from the morphology–density relation, the red sequence is more dominant in high density environments (Hogg et al., 2004; Bamford et al., 2009).

Interestingly the number density of bright ($\sim L^*$) galaxies on the red sequence has increased twofold since $z \sim 1$ (e.g. Bell et al., 2004; Brown et al., 2007), and faint galaxies have increased in number by a similar amount since z ~ 0.5 (e.g. Stott et al., 2009). Two mechanisms, both of which sit comfortably within the hierarchical merging model, are responsible for the increase (e.g. Faber et al. 2007; see Figure 1.6). First, galaxies of any mass join the red sequence once star formation ceases, either through quenching due to a major merger, or via truncation resulting from cluster in-fall. Secondly, once on the red sequence, a galaxy can increase in mass by accreting via gas-poor (early-type–early-type) merging, which increases the mass (luminosity) while only weakly affecting the colour.

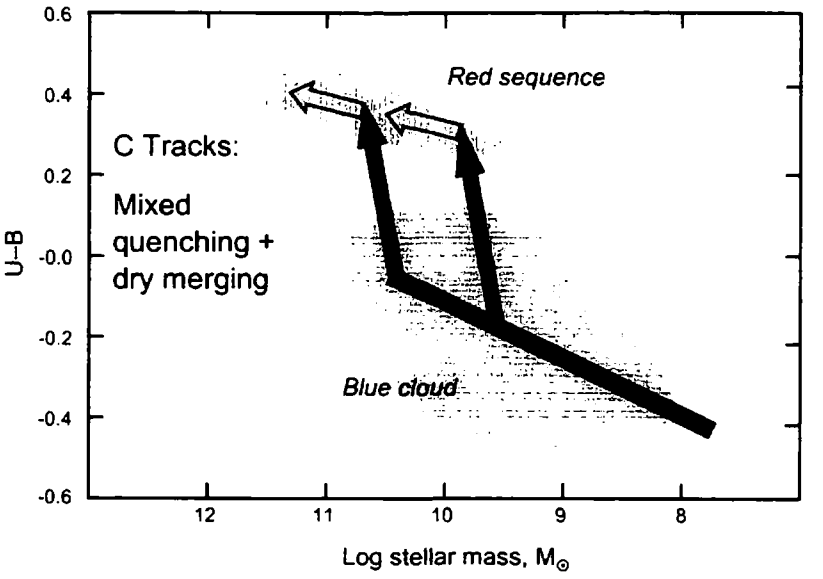

Figure 1.6: Cartoon tracks from Faber et al. (2007, figure 10), showing the dual-mechanism build up of the red sequence. Solid arrows represents quenching of late-type galaxies in the blue cloud at two epochs. Open arrows indicate gas-poor accretion (dry mergers) which moves galaxies along the red sequence.

1.3. Synergy between photometry and spectroscopy

Photometry and spectroscopy are complementary techniques. The strength of imaging is in integration over a wide band-pass, which enables exploration of low surface brightnesses (and high redshifts) without prohibitively long exposure times. In contrast, spectroscopy, while mostly unable to compete in terms of depth or spatial coverage, can investigate the composition of objects by analysing the atomic and molecular line features not isolated by broadband filters.

Often, imaging is used to locate interesting objects or define a particular subsample of galaxies, which are then followed-up by spectroscopic observations. However, the demarcation between these specialisms is not clear-cut, with narrow-band imaging allowing the coarse measurement and identification of particularly strong spectral features (for instance, the Lyman-α surveys targeting specific redshifts, e.g. Rhoads et al. 2000), and integral field units permitting spectroscopic observations with two-dimensional spatial resolution (e.g. TIGER panoramic spectrograph, Bacon et al., 1995).

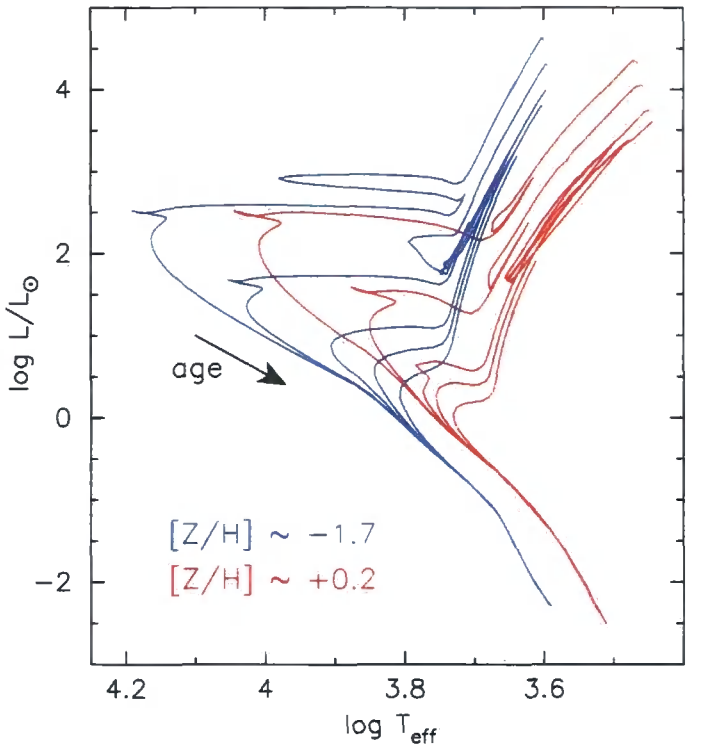

Figure 1.7: Theoretical isochrones from Girardi et al. (2000) on the Hertzsprung-Russell diagram. Two compositions are presented ([Z/H] ≈ –1.7, +0.2), and the branches show stellar ages = 0.25, 1.00, 3.98, 7.94, 15.8 Gyr. The effective temperature closely tracks colour (high temperature = blue optical colour).

1.3.1 Stellar properties in broadband colours

Photometry from multiple band-passes can help isolate the light from different populations of stars. For instance, the light from young stellar populations is dominated by the bright, hot and therefore blue stars at the massive end of the main sequence. As the system evolves, these stars are the first to become red giants (see Figure 1.7), so after ~2 Gyr the population appears considerably redder in rest-frame optical colours. Ultraviolet bands highlight one extreme of this behaviour, with enhanced luminosities in a stellar population for ~100 Myr after a starburst giving an excellent tracer of very recent star formation (Leitherer et al., 1999). One caveat to this is the hot, old, blue horizontal-branch stars that also exhibit high UV fluxes (Maraston & Thomas, 2000). Infrared luminosity traces total stellar mass better than optical bands, as the mass-to-light ratio varies by a much smaller factor across a wide range of star formation histories. However, excess light in the mid-infrared bands may also indicate recent and ongoing star formation, as UV light from young stars is re-radiated at longer wavelengths by dust.

This simple picture is complicated by the dependence of the integrated colour on the chemical composition (O'Connell, 1976). Metallicity (expressed as [Z/H]) quantifies the logarithmic abundance ratio of elements heavier than Helium to the abundance of Hydrogen, compared to the solar value[3]. Increasing metallicity tends to redden the stellar colour, independent of age (indicated in Figure 1.7). Worthey (1994) found that the effects of age and metallicity are effectively indistinguishable in optical and near-infrared broadband colours, with the degeneracy following the empirical relation Δage / ΔZ $\sim$ 3/2 (known as the Worthey 3/2 rule). In other words, broadband photometry cannot differentiate between one stellar population and a second with half the age, but three times the metallicity. Even in nearby galaxy studies with precise optical/near-infrared colours from multiple bands (e.g. $ugrizJHK$), the age and metallicity can only be determined to δ[Fe/H] $\approx$ 0.18 and δlog(age) $\approx$ 0.25 (Carter et al., 2009).

1.3.2 Spectroscopic stellar populations

The age–metallicity degeneracy in integrated light initiated a concerted effort to find spectral features that isolate the effect of either age or metallicity (e.g. Worthey et al., 1994; Rose, 1994). Spectral indices measure the strength of a feature by quantifying the total flux within a pre-defined wavelength window and above the local continuum level (as defined by two sidebands). Some indices are dominated by a single absorption line (e.g. Ca4227), but most are blends including significant contributions from several elements: Fe4668 not only traces iron, but has strong contributions from C_2, Ti, Cr, and Mg (and is often renamed C4668; Tripicco & Bell 1995).

Unfortunately, the majority of spectral indices have an age–metallicity degeneracy similar to the 3/2 rule. Despite its mongrel nature, Fe4668 is the best single tracer of the mean metallicity, with a 4 – 5 times stronger response to a decade change in [Z/H] than to age (Smith et al., 2007). The Balmer hydrogen lines were identified as the best tracers of age, with the Hβ index almost 3 times more responsive to age; Jones & Worthey (1995) demonstrated the near orthogonal nature of the age–metallicity grid in Fe4668–Hβ parameter space. Recent studies have used the responses of multiple line indices to derive the stellar population with the best fitting spectrum (e.g. Proctor et al., 2004; Trager et al., 2008; Smith et al., 2009a). This method enables the age and metallicity to be

[3] i.e. $[Z/H] = \log[(Z/H)_{gal} / (Z/H)_{\odot}]$

determined much more precisely than from broadband colours. However, to achieve a precision of ~10 per cent in log(age), a signal-to-noise ratio of at least 30 Å^{-1} is required.

Analysis of the best fitting stellar population, as derived from spectral line indices, assumes by default a single population of stars with the same age and chemical composition. Most galaxies are composed of multiple, super-imposed stellar populations so it is important to understand the origin of each parameter. The age (known as the single stellar population equivalent age) is a Balmer-line-weighted mean. As short-lived massive stars are much brighter than those in old populations, Serra & Trager (2007) calculated that there is a strong bias towards the age of the younger population. Additionally, the mass-fraction and age of the younger component are degenerate: an increase in the age of the younger population can result in the same observed age, as long as the mass-fraction is increased accordingly. In contrast to the age, Serra & Trager found that for a single-age population with two metallicity components, the single stellar population equivalent [Z/H] closely follows the optical band luminosity-weighted metallicity.

Abundance ratios greater than the solar value for sodium and heavy magnesium isotopes was predicted for very metal-rich stars (see Arnett, 1973). Peterson (1976) suggested that this elemental overabundance could explain the very strong observed sodium D lines measured for elliptical galaxies. Recent models, such as Thomas, Maraston, & Bender (2003) and Schiavon (2007), self-consistently incorporate variable abundances, although the exact prescription is model dependent. Studies using these synthetic stellar population (e.g. Thomas et al., 2005; Clemens et al., 2006; Sánchez-Blázquez et al., 2007) include α-element over-abundance [α/Fe] as a third parameter (along with age and total metallicity).

1.3.3 Age–mass–metallicity relation

For cluster early-type galaxies, Jørgensen (1999) found that central age and metallicity were anti-correlated, even after accounting for the Worthey 3/2 degeneracy. There are also correlations between central velocity dispersion and both age and metallicity (see also Trager et al., 2000b; Nelan et al., 2005), such that more massive galaxies tend to be both older and more metal rich (both of which cause a redder colour). In analysing these trends, Trager et al. (2000a) demonstrated that galaxies lie on the 'Z-plane': increasing σ raises the zero-point of the the age–metallicity trend, but the slope remains constant (two projections of this plane are shown in Figure 1.8).

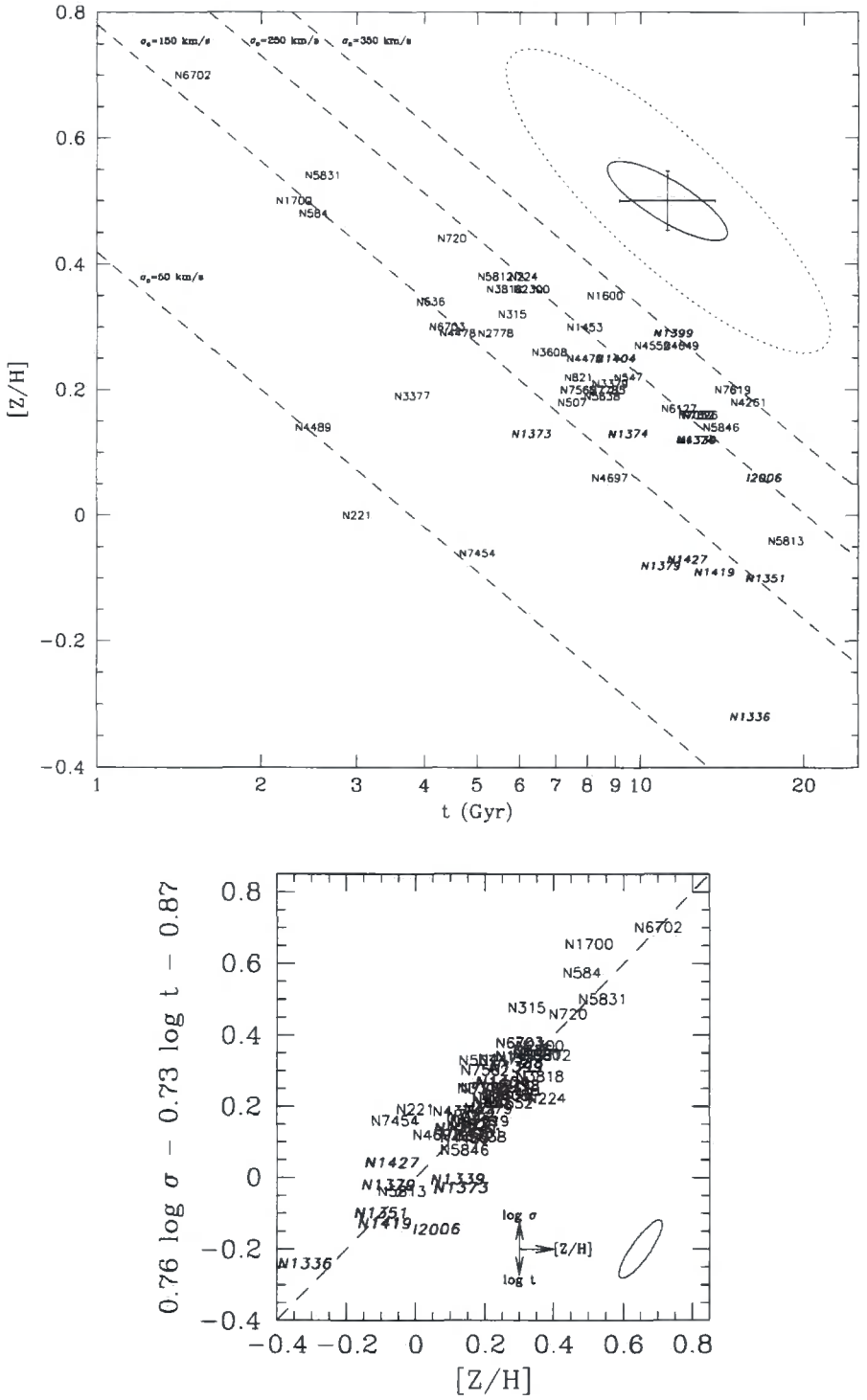

Figure 1.8: The age–mass–metallicity relation ('Z'-plane) from Trager et al. (2000a), figures 3 and 4. Upper panel: The age–metallicity plane indicating the trend with increasing velocity dispersion (dashed lines). Note that the error ellipse (top-right corner) is orientated in the direction of the correlation, due to the similarity between the slope and the age–metallicity degeneracy. Lower panel: Edge-on projection of the 'Z'=plane, indicating the tightness of the age–mass–metallicity relation.

1.3.4 Internal gradients

Radial trends in the observed parameters of a galaxy are an excellent probe of structural evolution and variations in chemical composition. The monolithic collapse and hierarchical formation theories predict very different gradients: dissipative collapse would tend to establish strong radial trends in metallicity (Larson, 1974a; Carlberg, 1984), while mergers would generally work to erase them (White, 1980). Tracing the gradients in early-type galaxies enables discrimination between these processes.

Internal gradients have traditionally been the domain of imaging, as it requires good spatial resolution compared to the galaxy size, and more importantly, good signal-to-noise in the outer regions. Optical and infrared colours are generally observed to become steadily bluer with radius (e.g. Franx, Illingworth, & Heckman 1989; Tamura et al. 2000), which has often been interpreted as a metallicity gradient. However, pure monolithic collapse predicts significantly ($\sim$2 –3 times) stronger gradients than observed (e.g. Tamura & Ohta, 2004). Further support for the merging hypothesis comes from the evolution of colour gradients with redshift. La Barbera et al. (2005) observed that mean colour gradients were stronger for more distant clusters, as would be expected if the galaxies underwent a series of mergers over time (Kobayashi, 2004).

Interpretation of colour gradients suffers from the same age–metallicity degeneracy as discussed above. Spectroscopic studies have yet to obtain the high signal-to-noise, spatial resolution or sample sizes required for detailed high redshift work. Observations of the local universe have been successful in tracing kinematic substructure (e.g. the identification of a dichotomy between 'fast' and 'slow' rotating cores in early-types; Emsellem et al., 2004) and line index gradients (e.g. Gorgas, Efstathiou, & Aragon Salamanca 1990; Mehlert et al. 2003; Sánchez-Blázquez et al. 2007). In a study of 12 local isolated galaxies, Reda et al. (2007) found that metallicity gradients were marginal stronger than previous studies had calculated for cluster galaxies of a similar mass. This result supported the conclusion that merging (which dilutes gradients) is more prevalent in the proto-cluster environments. However, up to now, few studies have derived stellar population gradients from multiple line indices, for more than a handful of cluster galaxies.

1.4. Outline of thesis

This thesis reports new results on the stellar populations of local cluster early-type galaxies. Using both multi-band imaging and spectroscopy, we employ the 'archaeological' method (the early-type galaxy fossil record) to explore galaxy stellar formation and evolution.

The thesis is structured as follows.

- Chapter 2 presents a study of the near-ultraviolet–infrared colours of cluster galaxies on the optical red-sequence. For galaxies in the Shapley Supercluster core, the origin of particularly blue NUV–IR colours is explored by comparison to stellar populations derived from absorption line features.

- Chapter 3 presents data from VLT VIMOS integral field unit observations of early-type galaxies in two local clusters: Abell 3389 and the Shapley Supercluster core. We describe the data reduction techniques in detail. Analysis concentrates on measuring the radial trends in absorption line features, in order to compute gradients in age, metallicity and α-element enhancement.

- Chapter 4 explores the stellar population gradients derived in Chapter 3. By comparison to previous studies of radial trends, we investigate possible trends in the parameters, and discuss their implication for our understanding of galaxy evolution.

- Chapter 5 presents new deep GMOS long-slit observations for a sample of seven lenticular galaxies in the Coma cluster. Analysing the stellar populations of both the bulge and disc components, we attempt to discriminate between various proposed mechanisms of formation.

- Chapter 6 draws together the studies presented in this thesis, concentrating on the physical implications. We also present ideas for future work.

Throughout this thesis, we adopt the standard cosmological parameters $(\Omega_{\rm M},\Omega_{\Lambda},h)$ = (0.3,0.7,0.7). For reference, at the redshift of the Shapley Supercluster (z = 0.048), 1 arcsec corresponds to 0.941 kpc. For Abell 3389 (z = 0.027), 1 arcsec is 0.543 kpc, and for the Coma Cluster (z = 0.023), 1 arcsec is to 0.464 kpc.

Chapter 2

NUV–IR colours of red-sequence galaxies

This chapter presents results from a study of *GALEX* near-ultraviolet (NUV) and 2MASS J-band photometry for red-sequence galaxies in local clusters. We produce the NUV–J colour–magnitude relation, and explore the origin of blue NUV–J colours in quiescent galaxies by comparing to spectroscopic age and metallicity. This work was presented in Rawle et al. (2008a).

2.1. Introduction

The optical colour–magnitude relation (CMR) shows that brighter early-type galaxies are also redder (Sandage, 1972; Visvanathan & Sandage, 1977), and is traditionally regarded as arising from the mass–metallicity sequence (cf. Dressler 1984, Kodama & Arimoto 1997). Gas loss, caused by supernova wind, occurs later in more massive galaxies. Therefore, in a less massive galaxy, a smaller fraction of gas is processed before being expelled (Mathews & Baker, 1971), resulting in a lower average metallicity (Larson, 1974b). Bower et al. (1992) found a very small intrinsic scatter in the U–V CMR ($\sim$0.05 mag) and, due to the sensitivity of the U-band to the presence of young stars, interpreted this as a small age dispersion. Age and metallicity are observed to have the same effect on broad-band optical colours, whereas spectral absorption line indices (e.g. Lick/IDS indices; Worthey et al. 1994) can be used to break the degeneracy (Worthey, 1994). Kuntschner & Davies (1998) claimed that the CMR is driven by metallicity variations with luminosity, although Nelan et al. (2005) found evidence for a strong age–mass relation in addition to

this metallicity–mass trend (see also Caldwell et al. 2003, Thomas et al. 2005).

The ultraviolet–optical CMR for non-star-forming galaxies has an intrinsic scatter an order of magnitude larger than its optical counterpart; ~0.5 mag compared to 0.05 mag (e.g. Yi et al. 2005). Hot young stellar populations dominate the ultraviolet (UV) flux for ~100 Myr after an episode of star formation (ten times longer than Hα emission after star formation; Leitherer et al. 1999). The large intrinsic scatter in the UV CMR is therefore often interpreted as differing quantities of very recent, albeit low level, star formation (Ferreras & Silk, 2000).

In intermediate age populations (~1 – 3 Gyr), the near-UV (NUV; 2000 – 3000 Å) flux is dominated by hot stars on the main sequence turn-off (e.g. O'Connell, 1999). The sensitivity of the turn-off to the epoch of formation emphasises the importance of the UV bands for age determination (Dorman et al., 2003).

Old (~10 Gyr) metal-poor populations have a significant UV flux contribution from very hot ($T_{\rm eff} \sim$ 10000K) blue horizontal branch (BHB) stars (Maraston & Thomas, 2000; Lee et al., 2002). However these tend to reside in globular clusters or galactic haloes (where [Fe/H] < -1), where they are useful age indicators (Kaviraj et al., 2007a), rather than in relatively metal-rich elliptical galaxies.

The UV picture is further complicated by the presence of the ultraviolet upturn (or UV excess, UVX) phenomenon. First observed by Code (1969), this unanticipated upturn dominates the far-UV (FUV; < 2000 Å) in UVX galaxies. In contrast, the NUV can be decomposed into two separate components: the blue end of the main sequence/subgiant branch, and the UVX contribution (Dorman, 1997). Burstein et al. (1988) found that the UVX can sometimes be appreciable at wavelengths as long as 2700 Å: for example, in NGC 4649 ~75 per cent of the NUV flux can be attributed to the UVX component. However, the UVX cannot be explained by the BHB population, as the temperature required to fit the upturn would be $T_{\rm eff} \gtrsim$ 20000K, whereas BHBs are usually no hotter than $T_{\rm eff}$ ~ 12000K (O'Connell, 1999).

Burstein et al. further reported that FUV flux (assumed to trace the UVX) is strongly correlated with the Mg_2 line strength (~metallicity) and also with the velocity dispersion, which is a proxy for galaxy mass. However, more recent studies (e.g. Rich et al. 2005) have weakened the case for a strong UVX vs metallicity relation. From analysis of internal colour gradients, O'Connell et al. (1992) concluded that the FUV flux in most early-types originates from old stellar components. Drawing on these results, the source

of the UVX is tentatively identified as hot, low mass, helium burning stars, such as extreme horizontal branch (EHB) or 'failed' AGB (AGB-manqué) stars and their progeny (see Yi et al. 1997, or the review O'Connell 1999).

The *Galaxy Evolution Explorer* (*GALEX*; launched in 2003; Martin et al. 2005, Morrissey et al. 2007) is revolutionising UV astronomy, with imaging in two bands: near-ultraviolet (NUV; $\lambda_{eff} = 2310$ Å) and far-ultraviolet (FUV; $\lambda_{eff} = 1530$ Å). Using analysis of both NUV–V and FUV–V vs B–V relations, Donas et al. (2007) suggest that the FUV–NUV colour reflects an extension of the colour–metallicity relation into the UV, as well as deducing that ~10 per cent of ellipticals have residual star formation. Using the NUV–r colour, Kaviraj et al. (2007b) also find non-negligible young stellar populations in morphologically selected early-type galaxies. Salim et al. (2007) investigated star formation rates (SFRs) from both broadband photometry (dominated by the UV) and spectroscopic indices (predominantly using Hα). They found that some galaxies with no Hα emission show signs of star formation in the UV bands and attributed this to post-starburst galaxies.

Here, we build upon these previous studies by exploring the relationship between the NUV–J colour and spectroscopic stellar population indicators for a sample of quiescent, red-sequence galaxies in nearby clusters. This chapter is organised as follows. Section 2.2 describes the two red-sequence samples, and introduces the criteria used to remove galaxies with line emission. A large intrinsic scatter is found in the NUV–J colours of these quiescent cluster galaxies (Section 2.3). Metallicity is shown to be strongly correlated with the NUV–J colour, although there remains a large intrinsic scatter. Section 2.4 discusses possible explanations for this scatter, showing that morphological abnormalities, aperture bias and the UV upturn do not contribute significantly. Simple 'frosting' models, with a low mass fraction of younger stars (or alternatively a low mass fraction population of low metallicity, blue horizontal branch stars), are investigated and can account for the scatter. The uncertainties in the NUV K-correction are also discussed. Conclusions are given in Section 2.5.

2.2. Data

We use two complementary samples of red-sequence galaxies in local clusters: the first is explicitly red-sequence selected by optical (B–R) colour, and is a large sample, con-

taining ~10 times the number of galaxies; the second has the advantage of higher quality spectroscopy, and uses an emission line cut (Section 2.2.3) to ensure a red-sequence sample. Smith et al. (2007) (figure 1) demonstrates that Hα selection efficiently removes all galaxies bluer than the red sequence and is more restrictive than a cut on colour.

2.2.1 Galaxy samples

NFPS sample

The NOAO Fundamental Plane Survey (NFPS; Smith et al. 2004, Nelan et al. 2005) is a study of X-ray selected clusters distributed over the whole sky and at redshifts between $0.015 < z < 0.072$. More than 4500 galaxies lying within 1 Mpc of the centre of each cluster, and within 0.2 mag of the cluster red sequence on the B–R CMR (see Smith et al. 2004 Figure 3), were observed spectroscopically. Of these, 3514 have redshift, velocity dispersion and spectral line strength measurements (from 2 arcsec diameter fibres).

Shapley Supercluster Core (SSC) sample

The second sample of galaxies concentrates on the core of the Shapley Supercluster (SSC; Abell clusters A3556, A3558, A3562 at $z \approx 0.049$). This sample consists of 541 galaxies selected from NFPS imaging but to a deeper limit ($R < 18$; Smith et al. 2007). Follow-up spectroscopy for these targets were obtained using 2 arcsec diameter fibres, equating to 2 kpc at the distance of Shapley. A set of three non-redundant line indices were fit to the models of Thomas et al. (2003, 2004) in order to estimate age, metallicity (Z/H) and α-abundance (α/Fe) for each galaxy. The primary tracer of age in this scheme is HγF; for metallicity Fe5015 is used; Mgb5177 is the α-abundance indicator. This method is described in detail in Smith et al. (2009a).

2.2.2 *GALEX* and 2MASS data

Galaxy Evolution Explorer (*GALEX*) near-ultraviolet (NUV) band images are available for 26 (from a total of 93) NFPS clusters. Due to a detector fault, only some clusters have associated far-ultraviolet (FUV) band images. Most of the images are from a guest investigator snapshot programme (*GALEX* GI1_004; PI: Smith) targeting a subset of NFPS clusters with low galactic extinction and a large number of galaxy spectra from Smith et al. (2004). In addition, a small number of images of comparable depth from the GR2 GI

Table 2.1: GALEX NUV images. cz ($\mathrm{km\,s^{-1}}$) is cluster redshift in the local CMB rest frame. A single exposure is used unless column six indicates the number of coadded images. Total exposure time for coadded images is given for NUV and (where the image is available) FUV.

GALEX image	Centre RA (J2000)	Centre Dec (J2000)	Cluster(s)	cz_{CMB} ($\mathrm{km\,s^{-1}}$)	Images coadded	t_{exp} (secs) NUV	FUV
GI1_004001_A2734	00 11 21.6	–28 51 00	A2734	18249	3	3535	
GI1_067001_UGC0568_0003	00 55 08.9	–01 02 47	A0119	12958		1556	3024
MISDR1_16976_0422	01 14 29.3	+15 01 46	A0160A	12794		1444	1444
GI1_004002_A0262_0001	01 52 45.6	+36 08 58	A0262	4464		1698	1698
NGA_NGC1058	02 43 26.6	+36 25 39	A0376	14371		1265	1265
GI1_004003_A3104_0001	03 14 21.6	–45 25 12	A3104	21560		1588	1588
GI1_004027_A3158_0001	03 42 57.6	–53 37 48	A3158	17542		1026	887
GI1_004004_A3266	04 31 24.0	–61 26 24	A3266	17713	2	1441	1441
GI1_004005_A0548	05 46 40.0	–25 37 21	A0548A/B	12439	4	3155	
GI1_004006_A3376	06 01 43.2	–39 59 24	A3376	14016	2	2176	2176
GI1_004007_A3389_0002	06 21 57.7	–64 57 35	A3389	8075		976	
MISDR1_24335_0270	10 13 07.7	–00 23 25	A0957	13849		1703	1703
GI1_004025_A3528_0001	12 53 57.6	–29 13 48	A3528A/B	16764		1697	

Table 2.1 continued...

GALEX image	Centre RA (J2000)	Centre Dec (J2000)	Cluster(s)	$cz_{\rm CMB}$ ($\rm km\,s^{-1}$)	Images coadded	$t_{\rm exp}$ (secs) *NUV*	*FUV*
GI1_004008_A1644_0002	12 57 12.0	−17 24 36	A1644	14478		1163	
GI1_009003_HPJ1321m31_0001	13 21 05.8	−31 32 20	A3556	14660		1615	
GI1_004010_A3556	13 25 26.1	−31 36 07	A3556, A3558	14660	2	1805	
GI1_004011_A3558_0001	13 27 57.6	−31 30 00	A3558	14660		1676	
MISDR1_33707_0586	14 42 46.3	+03 39 11	MKW8	8449		1698	1698
GI1_004016_A1991_0001	14 54 31.1	+18 38 23	A1991	17741		967	
GI1_004026_A2063_0001	15 23 36.0	+08 36 34	A2063	10444		1512	
NGA_NGC6166	16 28 39.9	+39 33 24	A2199	8872		1437	1437
GI1_004020_A3716	20 51 57.5	−52 46 48	A3716	13141	2	3179	1689
GI1_004021_A2399_0004	21 57 19.1	−07 47 59	A2399	17046		1322	
GI1_004022_A2589	23 23 57.6	+16 46 47	A2589	12001	3	4252	
GI1_004023_A4059_0003	23 56 59.9	−34 45 35	A4059	14660		635	

archive, medium imaging survey (MIS) and near galaxy survey (NGS) have been used. Table 2.1 lists all the images analysed along with their centre position and stacked exposure time. *GALEX* images have a 1.25° diameter, but only the central 1.2° field has been analysed due to the poor image quality at the edges. *GALEX* images have a plate scale of 1.5 arcsec pixel^{-1} and a PSF FWHM of ~5 arcsec.

Alongside the *GALEX* images, infrared tiles from the J-band ($\lambda_{eff} = 1.25\mu$m) of the Two Micron All Sky Survey (2MASS; Skrutskie et al. 2006) have been analysed. Measurements are taken directly from the tiles, rather than adopting photometry from the 2MASS extended source catalogue (XSC; Jarrett et al., 2000), as some of the target objects are unresolved. Additionally, photometry in all bands should be measured from images with an equal PSF. Consequently, the 2MASS J-band tiles (PSF FWHM ~3 arcsec) were convolved with a Gaussian filter FWHM = 3.35 arcsec (quadratic difference: $\sqrt{4.5^2 - 3^2}$) before analysis. For reference, 2MASS tiles have a plate scale of 1 arcsec pixel^{-1}.

SExtractor (Bertin & Arnouts, 1996) was employed in dual image mode to detect all objects in the J-band. Photometry was measured for all sample targets in both bands using a range of matched apertures: a Kron-type aperture (SExtractor's MAG_AUTO) and seven apertures 3–34.5 arcsec in diameter (MAG_APER). Throughout this work, elliptical Kron apertures are used for total J-band luminosity. The radius of the Kron aperture is twice the intensity-weighted first-moment radius (approximately equal to the half-light radius), which incorporates more than 91 per cent of the light for all galaxies at z < 0.1 (Kron, 1980). For the NUV–J colours, matched apertures are important, so we use 12 arcsec diameter circles. For objects included in the XSC, the J-band photometry measured here is in good agreement with 2MASS (~0.16 mag RMS; see Figure 2.1).

Targets with SExtractor apertures flagged as truncated, or with a deblending error, have been removed from the sample, and only confirmed cluster members with redshift and $\log\sigma$ measurements reported in the Smith et al. (2004) or Smith et al. (2007) datasets (NFPS and SSC respectively) are used in the analysis. Table 2.2 lists the number of galaxies in the samples at this stage, and after subsequent restrictions.

All colours and magnitudes are measured in the AB system ($J_{\rm AB} = J_{\rm Vega} + 0.91$; Blanton et al. 2005), and have been corrected for galactic extinction using the reddening maps of Schlegel et al. (1998); A_{FUV}=8.29×$E(B$–$V)$, A_{NUV}=8.87×$E(B$–$V)$, A_J=0.902×$E(B$–$V)$ (Cardelli et al. 1989; Schlegel et al.).

Estimates of the K-correction in the UV bands are currently derived empirically from

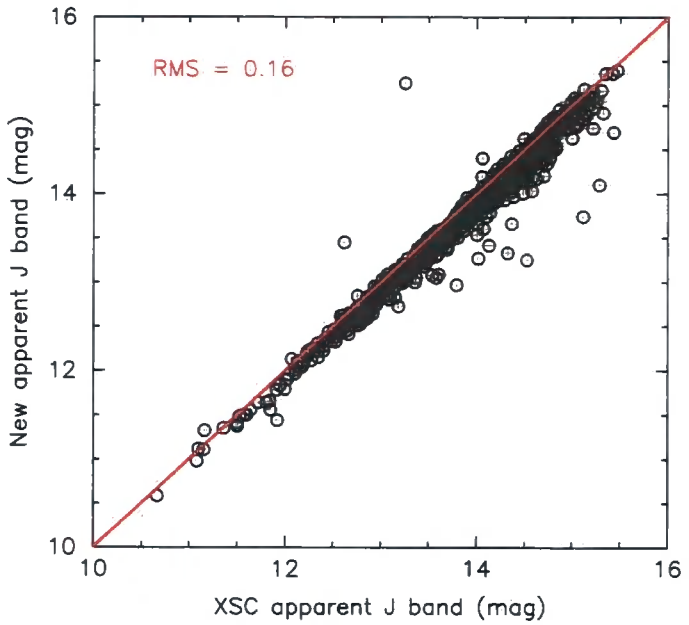

Figure 2.1: Comparison between the 2MASS J-band Kron aperture photometry measured in this study and the $J_{\rm EXT}$ photometry in the 2MASS Extended Source Catalogue (XSC; Jarrett et al., 2000). The measurements generally agree well. New photometry is required as not all targets are included in the XSC.

Table 2.2: Size of the galaxy samples, following the adopted selection criteria.

	NFPS	SSC
Original sample	4527	541
...with usable NUV and J photometry	1493	307
...with cz and log σ data	990	267
...after emission line cut	920	156
.....after optical apparent magnitude cut[1]	544	101
.....with stellar population parameters[2]	–	87
.....with FUV and HγF data[3]	222	–

NOTE – see [1](Section 2.3.1), [2](Section 2.3.2) or [3](Section 2.4.2)

poorly constrained spectra, and therefore subject to large uncertainties. Kaviraj et al. (2007b, figure 22) estimate that the $NUV-i$ correction would be ~0.1 mag throughout the range in redshift considered here. K-correction are not applied in this study. This issue is addressed further in Section 2.4.4.

2.2.3 Emission-line cuts

In order to construct a sample of emission-free red-sequence galaxies, a restriction is made on emission line strengths. Mindful of the effect of nebular emission 'fill in' for the age-sensitive Balmer lines (Hβ, Hγ and Hδ), the preferred cut is on the Hα line. Unfortunately, Hα was not measured for most NFPS galaxies, so the selection criteria of the original NFPS reduction has been adopted (Nelan et al., 2005). Specifically, this involves a cut on the Hβ emission equivalent width, EW(Hβ) > 0.6 Å, supplemented by a cut on OIII λ5007, EW(OIII λ5007) > 0.8 Å. The cut on the SSC sample, which has Hα measurements, follows the prescription of Smith et al. (2007), which uses EW(Hα) > 0.5 Å (approximately equivalent to EW(Hβ) > 0.2 Å). Applying the additional OIII cut would not remove any further galaxies. These cuts ensure red-sequence subsamples free of galaxies with a sizeable star formation component or an optically strong active galactic nucleus. The data and photometry for the resulting subsamples are reported in Tables 2.3 and 2.4 (for the full tables, see the electronic version of Rawle et al. 2008a).

2.3. Results

2.3.1 $NUV-J$ colour relations

Figure 2.2 shows the $NUV-J$ colour–(apparent) magnitude diagram for the NFPS and SSC samples. Shown in cyan are the galaxies removed by the emission cut from Section 2.2.3. Prior to the emission cut, SSC has a larger colour range than NFPS. This is because NFPS was explicitly selected on $B-R$ colour while SSC only on total R-band apparent magnitude. The Hα cut efficiently removes the very blue objects.

All target galaxies were within the 2MASS J-band detection limit, but the NUV-band has a 5σ detection limit of 22.5–23.5 mag, depending on the coadded image exposure time. Figure 2.2 (upper panel) shows that for the NFPS, these limits result in a bias against faint red galaxies. Assuming the brightest NUV detection limit, a sample cut is applied

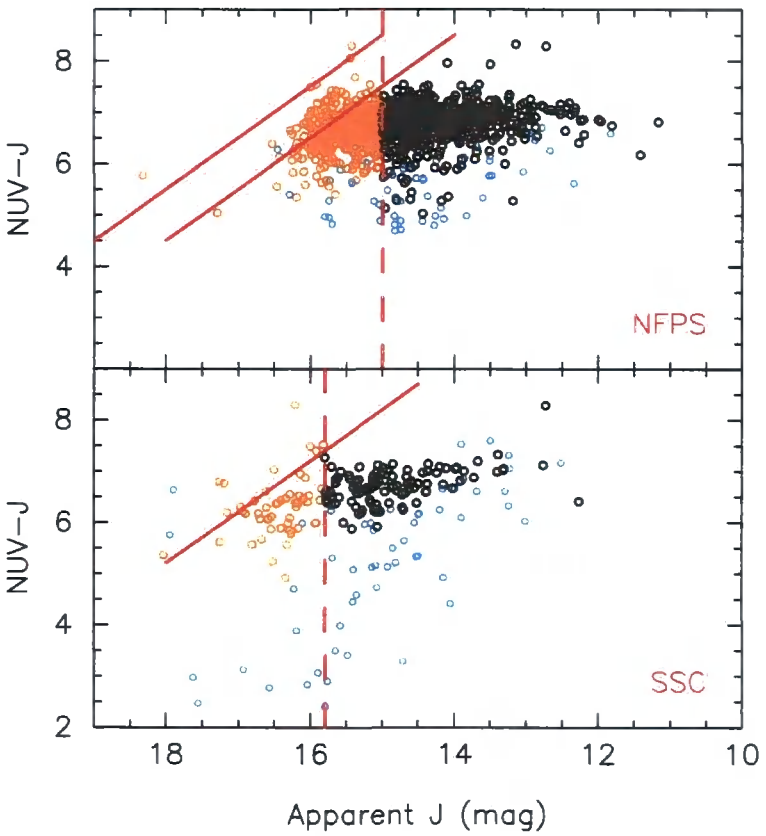

Figure 2.2: Colour–magnitude diagram for the samples (NFPS upper panel; SSC lower panel). Cyan points are those removed by emission line criteria detailed in Section 2.2.3. The larger tail of cyan points for SSC results from the lack of an explicit colour cut on the original sample. Solid lines are *GALEX* detection limits and dashed lines are the applied J-band apparent magnitude cuts. Orange points are excluded by this cut; black points remain in the sample. Median error bars are $\sim$0.05 mag in J-band and $\sim$0.1 mag in the colour.

Table 2.3: Data for galaxies in the NFPS sample. Galaxy position is encoded in the ID. $cz_{\rm CMB}$ ($\rm km\,s^{-1}$) is the mean cluster redshift in the CMB frame. $cz_{\rm hel}$ ($\rm km\,s^{-1}$) is galaxy redshift in the heliocentric frame. Magnitudes (Kron-type apertures) and colours (12 arcsec diameter apertures) are in the AB system and have been galactic extinction corrected, but not K-corrected.

Galaxy ID	cluster $cz_{\rm CMB}$	galaxy $cz_{\rm hel}$	apparent J	$NUV-J$	$FUV-J$
NFPJ043305.0–612235	17714	16144	15.750 ± 0.071	6.732 ± 0.142	7.205 ± 0.250
NFPJ043306.7–612614	17714	17702	14.898 ± 0.047	7.091 ± 0.102	7.497 ± 0.184
NFPJ043307.6–611338	17714	16356	14.659 ± 0.042	6.979 ± 0.095	7.659 ± 0.195
NFPJ054415.7–255429	12939	10674	14.693 ± 0.045	6.886 ± 0.077	-
NFPJ054431.6–255550	12939	13247	14.783 ± 0.047	6.767 ± 0.086	-

Full content of this table is available in the electronic version of Rawle et al. (2008a)

to the J-band apparent magnitude at 15.0 mag. For the SSC sample, all of the targets appear on just two NUV images with similar exposure times, and a (5σ) detection limit of 23.2 mag. Although in practice only two SSC targets have a non-positive flux in the NUV-band (compared to $\sim$8 per cent in NFPS), for consistency, SSC has been treated in a similar manner, with a cut applied at 15.8 mag. These cuts are shown as dashed lines in Figure 2.2 and ensure a complete sampling of the colour range over the selected luminosity interval.

The colour–(absolute) magnitude diagrams for the low-emission galaxies are presented in Figure 2.3. There is a correlation between the luminosity and colour, in which brighter galaxies tend to be redder. However, there is a large scatter, with rms dispersions of 0.37 and 0.30 mag for NFPS and SSC samples respectively. The smaller scatter within the SSC sample is probably due to the slightly more restrictive Balmer emission line criteria (see Section 2.2.3). The scatter in each sample does not increase by more than $\sim$10 per cent unless the cut criteria are relaxed beyond an equivalent width of 1 Å. Only 5 per cent of the scatter can be accounted for by photometric measurement error. As intrinsic scatter dominates, all correlations in this study are computed without error weighting.

Table 2.5 summarises the CMRs for the two samples. For comparison, the CMRs measured in three previous studies (Yi et al. 2005, Boselli et al. 2005, Haines et al. 2008) are also shown. Different sample selections were used for each of these studies. Yi et al.

Table 2.4: Data for galaxies in the SSC sample. As in Table 2.3. Supercluster mean $cz_{\rm CMB}$ = 14660 km s^{-1} for all galaxies. Stellar population parameters, as presented in Smith et al. (2009a), given where available (age in Gyr).

Galaxy ID	$cz_{\rm hel}$	apparent J	$NUV-J$	log(age/Gyr)	[Z/H]	[α/Fe]
NFPJ132418.2–314229	13948	14.197 ± 0.035	7.088 ± 0.085	0.94 ± 0.03	0.27 ± 0.02	0.24 ± 0.02
NFPJ132423.0–313631	14642	14.847 ± 0.048	6.706 ± 0.103	0.89 ± 0.05	0.11 ± 0.03	0.15 ± 0.02
NFPJ132425.9–314117	13888	14.380 ± 0.038	6.604 ± 0.079	–	–	–
NFPJ132426.5–315153	14922	14.676 ± 0.043	6.575 ± 0.081	0.95 ± 0.04	0.23 ± 0.03	0.24 ± 0.02
2MASXJ13250387–3132449	14266	14.792 ± 0.049	6.626 ± 0.109	–	–	–

Full content of this table is available in the electronic version of Rawle et al. (2008a)

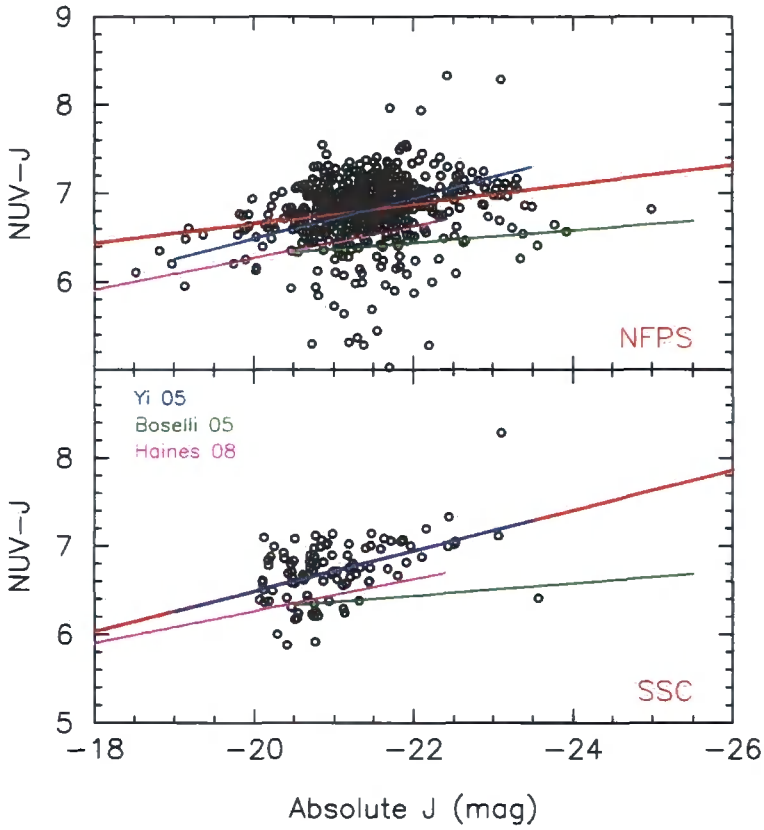

Figure 2.3: NUV–J colour–absolute magnitude diagram for both samples, with best fits in red. Relations from previous studies, Yi et al. (2005)=blue, Boselli et al. (2005)=green, Haines et al. (2008)=magenta, are shown with the line length indicating their J-band luminosity range. Median error bars are ~0.05 mag in J-band and ~0.1 mag in NUV–J.

use a 'UV-weak' early-type galaxy sample, selected from SDSS by concentration index and luminosity profiles, and then by the flux ratios F(NUV)/F(r) and F(FUV)/F(r) both being less than 0.07. The sample covers a J-band luminosity range comparable to our work. Boselli et al. use a volume-limited sample of galaxies in the Virgo cluster, with a subsample defined as elliptical by visual classification. Haines et al. use a volume limited sample of local galaxies from SDSS, with the subsample (labelled 'passive red-sequence galaxies') restricted by the emission line criteria $EW(\mathrm{H}\alpha) > 2$ Å.

Despite these selection differences, our derived relations are in good agreement with the previous studies. The scatter is consistent (~0.3 – 0.5 mag) given the different sample definitions, and considerably large in comparison to that of the optical CMR (~0.05 mag; Bower et al. 1992).

Velocity dispersion provides an alternative mass proxy to luminosity, and, for optical colours, the σ correlation appears more fundamental (Bernardi et al., 2005). Figure 2.4

Table 2.5: NUV–J CMR parameters

	original		transformed		rms
	x	y	a	b	dispersion
NFPS	J	NUV–J	–0.11	4.45	0.37
SSC	J	NUV–J	–0.23	1.93	0.30
Y05[1]	r	NUV–r	–0.23	1.88	0.58
B05[2]	H	NUV–H	–0.07	4.89	0.47
H07[3]	r	NUV–r	–0.18	2.66	0.37

NOTES – Original x and y parameters are given for reference. a and b are for relations in the form NUV–$J = aJ + b$, assuming the following colours: $(J–H)_{\rm AB}$=0.2, $R_{\rm AB}$=r–0.21, $(J–R)_{\rm AB}$=–0.8. [1]from Yi et al. (2005). [2]from Boselli et al. (2005). [3]from Haines et al. (2008).

presents the samples in terms of their NUV–J colour and $\log\sigma$. There is a clear correlation, with slopes of 0.73 ± 0.11 and 0.65 ± 0.17 for NFPS and SSC respectively, but the rms scatter (0.36 and 0.32 mags) is indistinguishable from that of the CMR.

Figure 2.5 shows the fraction of 'blue' galaxies as a function of $\log\sigma$ for the two samples. Blue galaxies are defined by NUV–$J < 6.4$ mag, as used in Schawinski et al. (2006) who study SDSS galaxies probing to much lower density environments than our samples. Their blue galaxy fractions are plotted in Figure 2.5 and show a markedly higher fraction for a given velocity dispersion. For example, NFPS and SSC have a blue fraction of ~40 per cent only at the lowest sigma ($\log\sigma < 1.8$), while the Schawinski et al. sample reaches this blue fraction at $\log\sigma = 2.2$. At face value, this result suggests a large difference between field and cluster galaxy populations. However, the differences in sample selection have to be considered (Schawinski et al. use a sample selected on morphology), which is beyond the scope of this study.

2.3.2 Stellar population parameters in the Shapley sample

The physical origin of the large intrinsic scatter found in the NUV–J colour, can be investigated by examining the relationship between colour and the stellar population parameters: age, total metallicity, α-element over-abundance. These values were derived from the AAΩ central spectroscopy (Smith et al., 2009a), introduced in Section 2.2.1.

In the following analysis, the derived limit on J-band apparent magnitude (Section

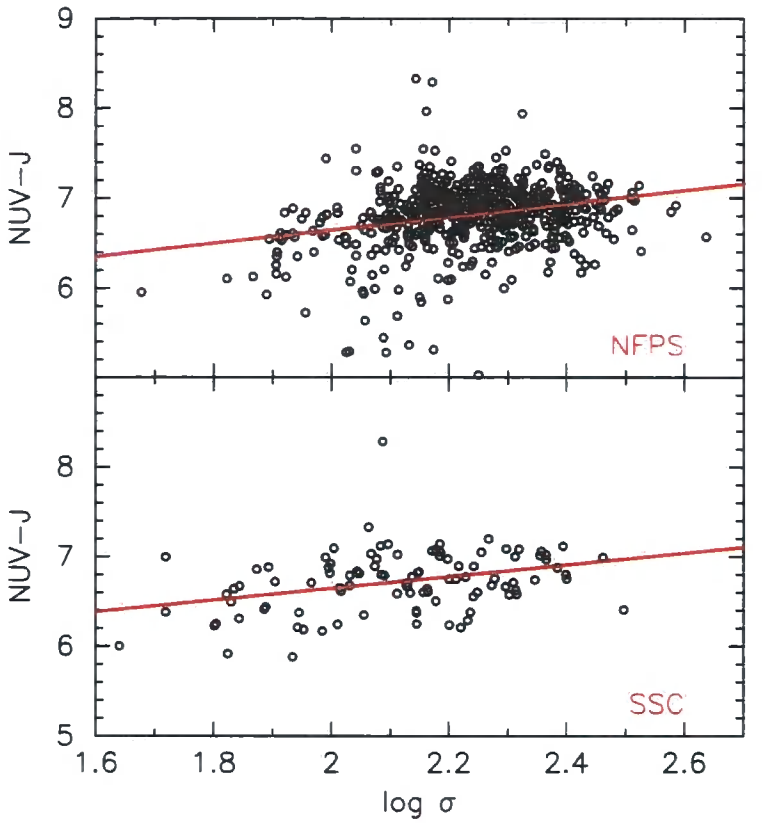

Figure 2.4: NUV–J vs $\log\sigma$ for NFPS (upper panel) and SSC (lower panel). Median error bars are ~0.02 and ~0.01 for $\log\sigma$ in the two samples respectively and ~0.1 in the colour.

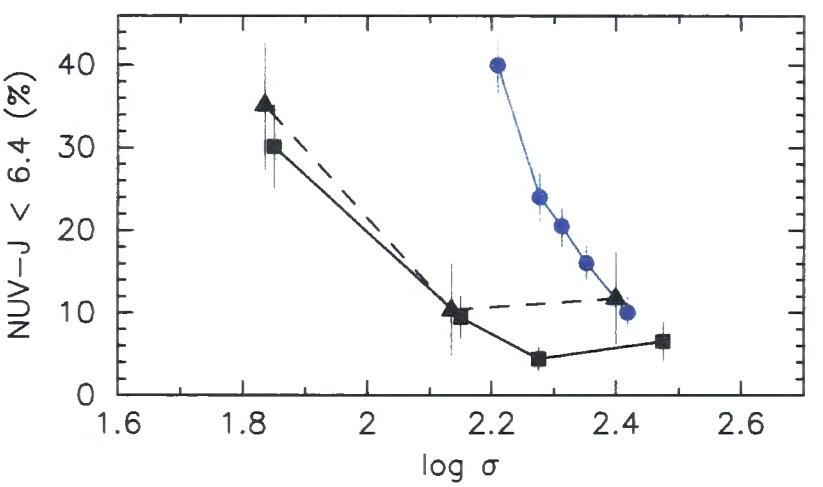

Figure 2.5: Fraction of galaxies with NUV–J < 6.4 as a function of $\log\sigma$. NFPS: squares/solid line; SSC: triangles/dashed line. Estimates from Figure 1 of Schawinski et al. (2006) are given for comparison (blue circles/line) and show a much steeper increase in the number of blue galaxies with decreasing σ.

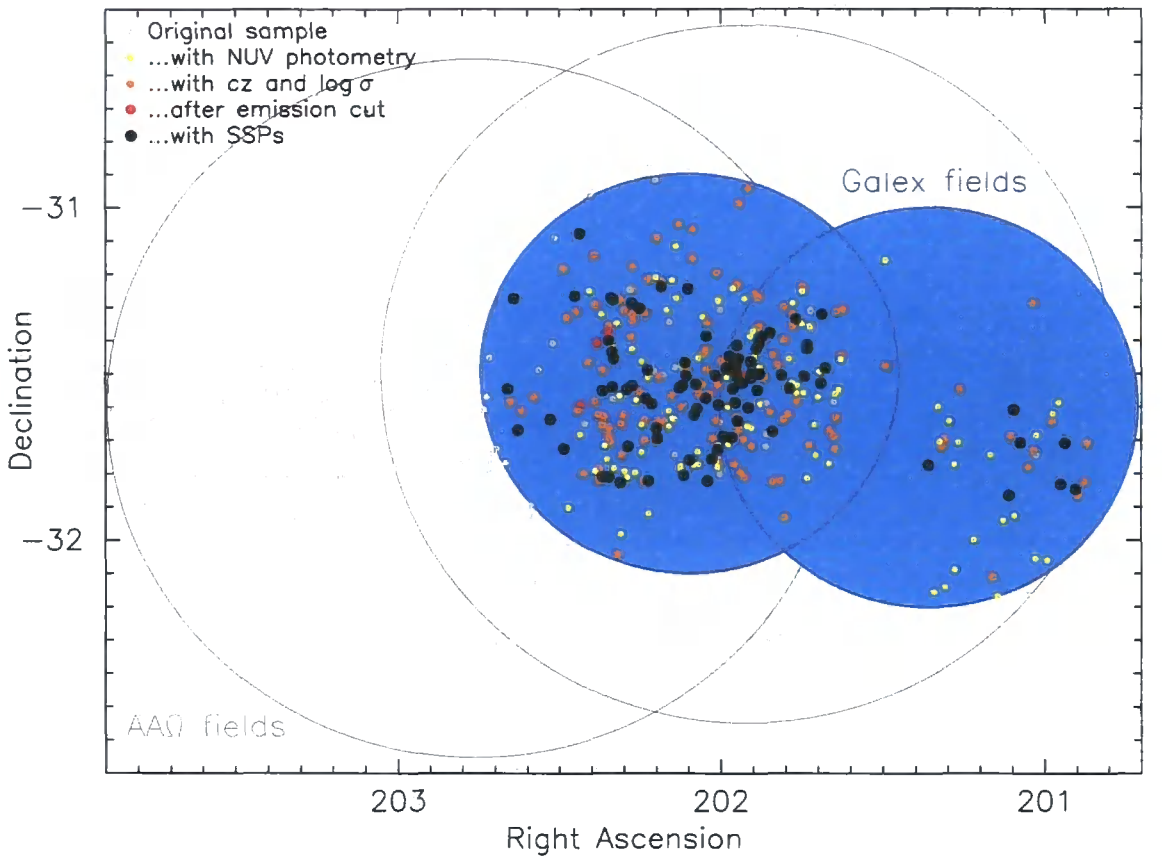

Figure 2.6: Map of the Shapley Supercluster Core, showing the original SSC sample (grey points) and the final set of galaxies (black) after the selection criteria (as presented in Table 2.2; intermediate samples are shown in yellow, orange and red). The *GALEX* and AAΩ observation fields of view are indicated by blue and dark grey ellipses respectively.

2.3.1) is not applied, leaving a greater number of galaxies. (It should be noted that the subsequent conclusions are robust against the use of the J-band cut.) The emission line selection criteria *are* retained, and the sample is further restricted by the overlap of the photometric and spectroscopic datasets (see Figure 2.6 and Table 2.2).

NUV–J vs log(age) is shown in Figure 2.7 (main panel). Galaxies with nebular emission have been removed via the emission line criteria. Therefore, if the UV sources also contribute to the optical flux and have strong Balmer lines, the NUV–J and age for the remaining objects would be correlated. We find only a marginal correlation between age and NUV–J, with a slope of 0.46 ± 0.25 and an intrinsic scatter (after accounting for the measurement error) of 0.33 mag. It is also apparent that more luminous, and by inference larger, red-sequence galaxies (J-band luminosity is shown in Figs. 2.7 – 2.9 by the symbol size) are not solely confined to the redder NUV–J colours, although they do tend to be

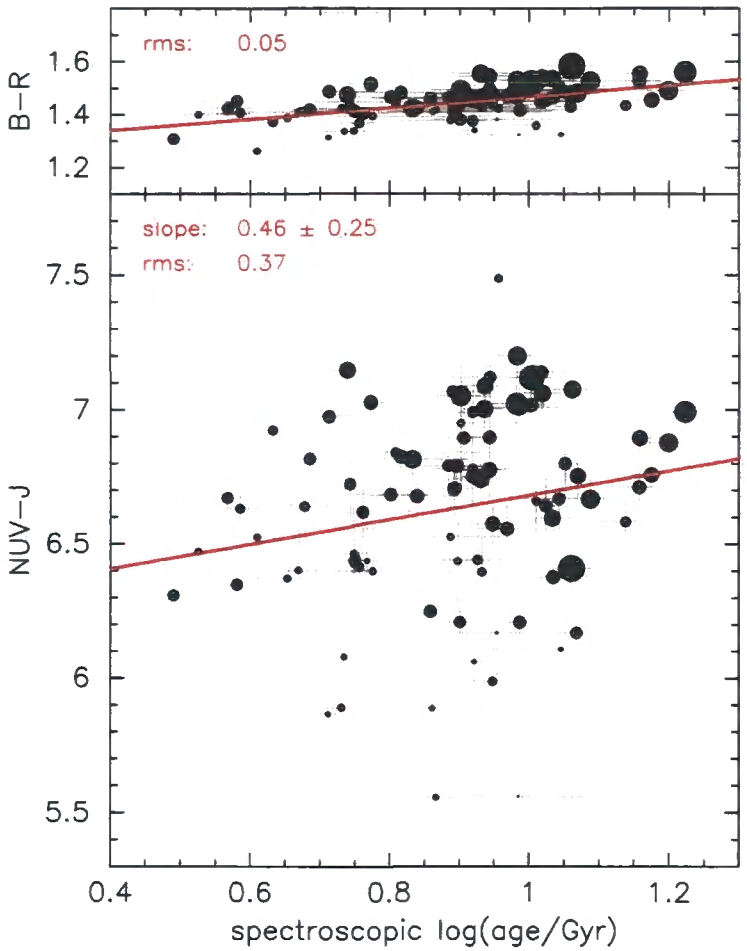

Figure 2.7: NUV–J (main panel) and B–R (upper panel; from Mercurio et al.) colours vs log(age) for the SSC sample. Symbol size represents J-band luminosity; larger=brighter.

the oldest.

Figure 2.7 (upper panel) shows the relation between age and B–R colour for the same sample of galaxies. There is a strong correlation, with a slope of 0.21 ± 0.04 and an rms dispersion of 0.05 mag. This figure confirms that the NUV scatter is not due to contamination by optically blue galaxies.

The analogous NUV–J correlation with the metallicity is given in Figure 2.8 (main panel). There is a strong trend between [Z/H] and NUV–J, with a slope of 1.27 ± 0.23 and an rms dispersion of 0.32 mag (~90 per cent of which is intrinsic scatter). The lack of galaxies to the top left is not the result of a selection effect. Of the two target galaxies undetected in the NUV-band (see Section 2.3.1), only one has a low metallicity. Assuming the non-detection is due to a redder-than-average colour, this would add a single galaxy to the upper left of the plot, but would not significantly affect the fit. In general, the most

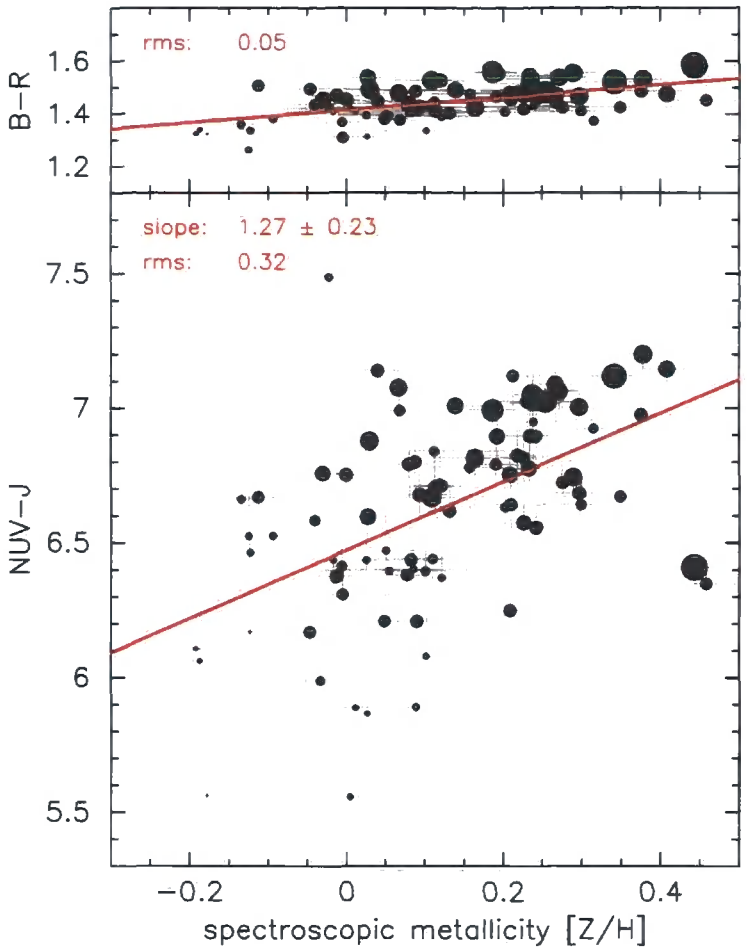

Figure 2.8: NUV–J (main panel) and B–R (upper panel) colours vs metallicity [Z/H]. Symbol size represents J-band luminosity; larger=brighter.

luminous galaxies form a ridgeline at redder colours, although there are significant bright outliers to this trend (the most obvious being the bright, blue, metal-rich galaxy on the right; NFPJ132729.7–312325). Lower metallicity galaxies tend to be bluer and less luminous. This supports Rampazzo et al. (2007), who use simulations to predict a correlation of NUV–IR colour with metallicity, but little dependence on age in populations greater than 2 – 3 Gyr after a star formation episode. However, the slope of the observed metallicity trend is 2 – 3 times weaker than that derived from theoretical spectra by Dorman et al. (2003).

Model evolutionary tracks find that stellar evolution depends on α-element overabundance (Salasnich et al., 2000), with the resulting increase in opacity affecting stellar lifetimes by $\sim$5 per cent (up to 10 per cent for Fe- or O-enhancement) compared to solar-scaled abundance (Dotter et al., 2007). However, there is no discernible relation between

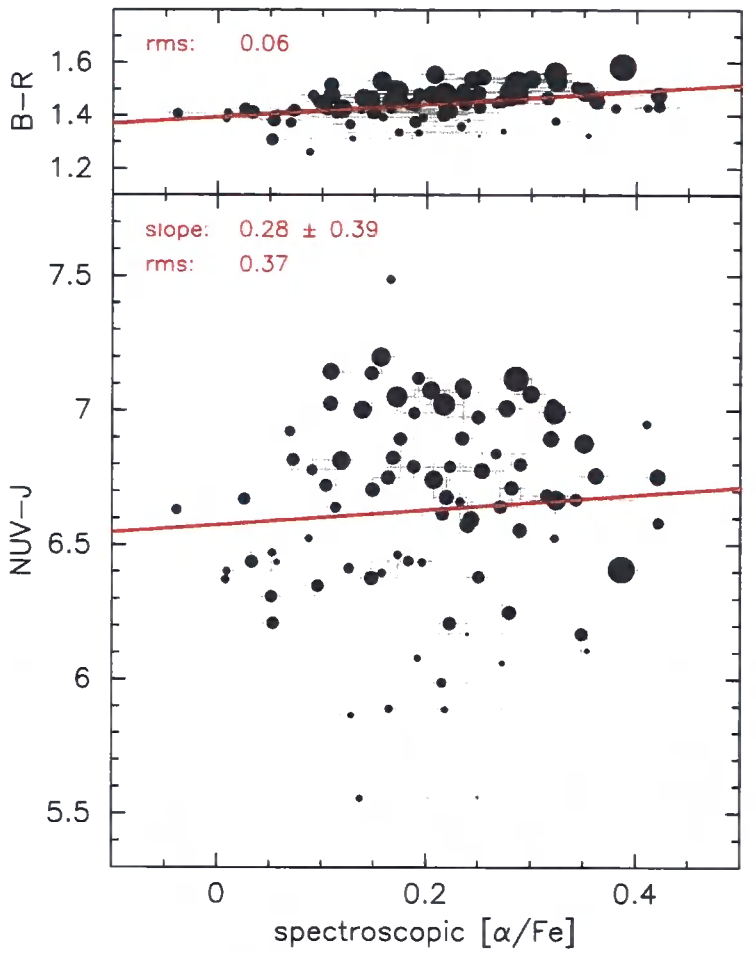

Figure 2.9: NUV–J (main panel) and B–R (upper panel) colours vs α-abundance [α/Fe]. Symbol size represents J-band luminosity; larger=brighter.

the NUV–J colour and the α-abundance in this sample of red-sequence galaxies (rms scatter of 0.37 mag; main panel, Figure 2.9).

The main panel in Figure 2.10 shows the residuals from the NUV vs metallicity relation (Figure 2.8) against log(age). Although the residuals are more strongly correlated with age ($\sim 3\,\sigma$) than the colours themselves are, the rms dispersion is only reduced to 0.3 mag ($\sim$0.25 mag intrinsic scatter). This is in contrast to the case of the B–R colour where the majority of the scatter can be attributed to age and metallicity (upper panel Figure 2.10, and also see Smith et al. 2009a).

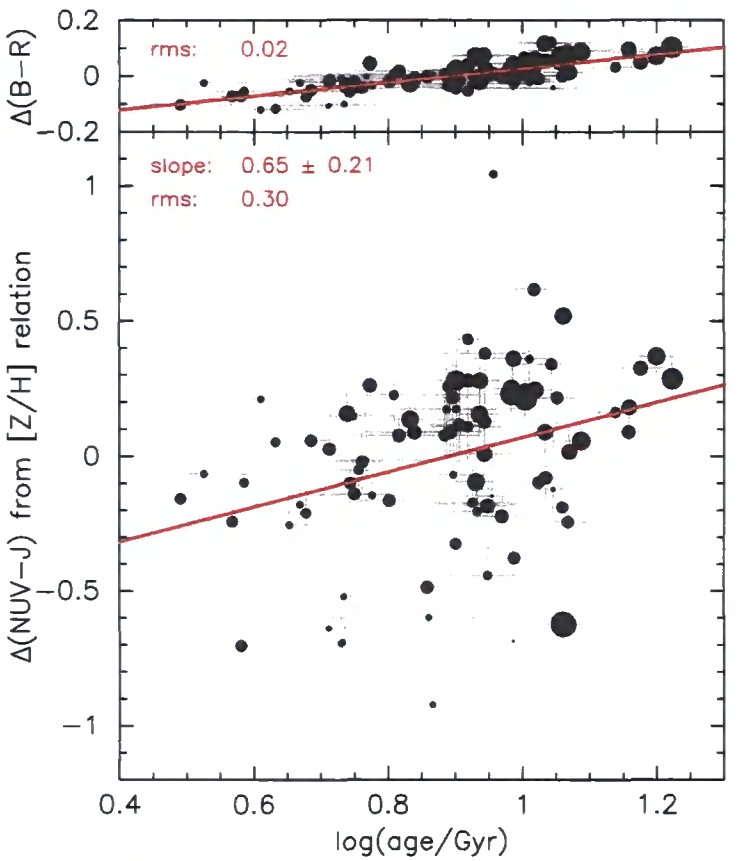

Figure 2.10: NUV–J (main panel) and B–R (upper panel) residuals from the [Z/H] relations (Figure 2.8) vs log(age). Symbol size represents J-band luminosity; larger=brighter.

2.4. Discussion

This section explores possible causes of the large intrinsic scatter observed in the NUV–J colour. Potential factors investigated are aperture bias, the UV upturn phenomenon and 'frosting' by young or metal poor subpopulations. Finally, the uncertainty in the NUV-band K-correction is commented upon.

2.4.1 Aperture bias/morphology

The spectroscopy used to estimate the stellar parameters is derived from 2 arcsec diameter fibres, whilst the NUV–J colours are from 12 arcsec diameter aperture photometry. Eliminating aperture bias completely would require matched apertures for the photometry and spectroscopy, but unfortunately the PSF of the 2MASS and *GALEX* images is too large for reliable 2 arcsec aperture photometry.

Broadband colours and spectroscopic measurements (e.g. Tamura & Ohta 2004, Sánchez-Blázquez et al. 2007) show that on average, early-type galaxies have flat radial profiles in age, and regular metallicity gradients (decreasing [Z/H] with radius). The aperture effect therefore flattens the NUV–J vs Z/H relation, as larger, redder galaxies will tend to exhibit higher metallicities within the fibre. However, the effect is small, with only $\sim$0.1 dex change in metallicity over a 1 dex difference in aperture radius. (Chapters 3 – 5 investigate the stellar population gradients in early-type cluster galaxies.)

By inspecting the galaxies in high resolution images, we can ascertain whether there are morphological peculiarities, or neighbouring objects, while could contribute to an enhanced large radius NUV flux. Figure 2.11 shows colour plotted against the age and metallicity (as in Figs. 2.7 – 2.8), highlighting the few galaxies that have high resolution *HST*-ACS images available. Fortunately, one of these objects is the most obvious outlier in the whole sample (NFPJ132729.7–312325); it is the reddest in B–R, but has an unusually blue NUV–J colour for such a metal-rich, luminous galaxy. In the *HST*-ACS image (Figure 2.12), the galaxy appears to be a large elliptical with no abnormalities. There are also no obvious contaminating objects that could be responsible for an anomalous blue colour.

On close examination, the other targets with *HST*-ACS images also appear to be 'normal' ellipticals of various sizes, with no obvious peculiarities or large radius NUV contributors. We conclude that a large scatter in NUV–J colour is present even in objects

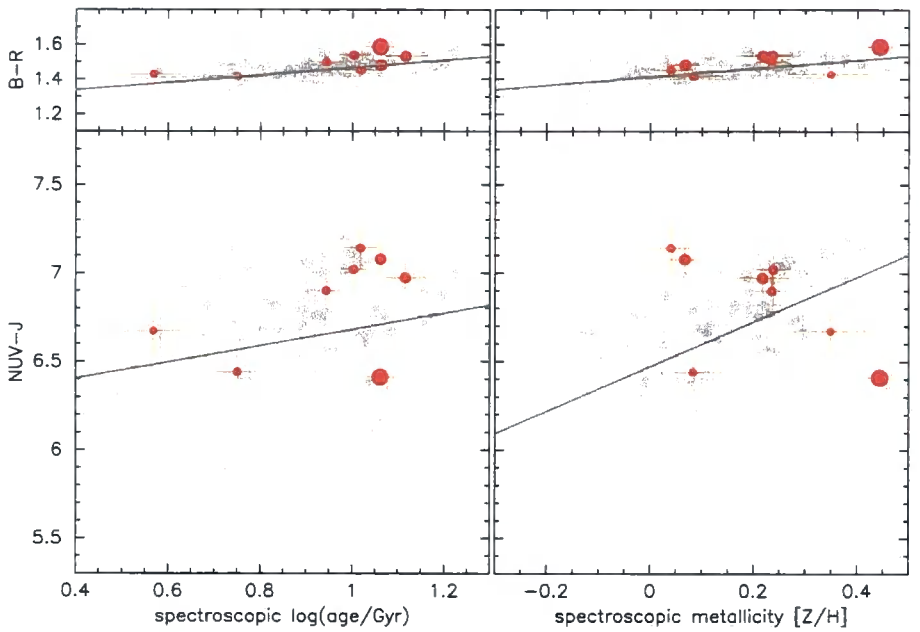

Figure 2.11: Colour versus stellar parameters, highlighting eight galaxies (red) with available *HST*-ACS images. Symbol size reflects J-band luminosity (larger=brighter). In all cases, ACS confirms early-type morphology, uncontaminated by neighbours.

with confirmed regular early-type morphologies and no contaminants. Additionally, a scatter of $\sim$0.3 – 0.35 mag is still obtained when smaller matched apertures (4.5 arcsec diameter) are used for the colour, despite the probability of a contaminating neighbour being reduced by $\sim$85 per cent.

2.4.2 UV upturn

Another possible explanation for the scatter in NUV–J colour is NUV contamination by the UV upturn (UVX). The Thomas et al. (2003) models, employed here to derive stellar populations parameters, include low-metallicity blue horizontal branch sub-populations and thermal-pulsing asymptotic giant branch stars, but do not include the low mass, metal-rich, helium burning stars with small envelopes currently thought to be the most likely candidate for the UV upturn (O'Connell, 1999). The UV upturn is one of the most heterogeneous photometric properties of old stellar populations in early-type galaxies, with a spread of up to $\sim$4 magnitudes in the FUV (O'Connell, 1999), so certainly seems a plausible explanation for the scatter.

The hot UVX component appears in the spectra as a smooth continuum with an absence of emission and absorption lines. Hence, the FUV flux from a galaxy can be used

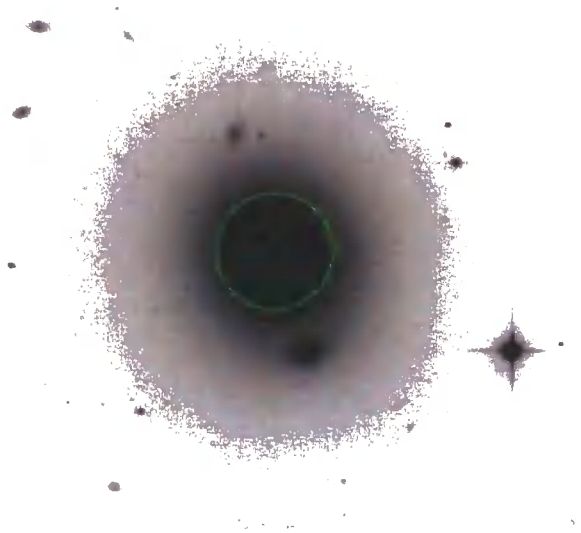

Figure 2.12: *HST*-ACS image of the outlier NFPJ132729.7–312325, with a 12 arcsec diameter aperture marked.

to estimate the extent of the contribution in the NUV-band (Burstein et al., 1988). Unfortunately, none of the SSC galaxies have available FUV photometry, so in order to estimate the extent of the UVX contribution, the corrections are calculated for all objects in the NFPS sample that have the necessary FUV data. However, stellar population ages have not been derived for individual NFPS galaxies, so instead we compare the corrected NUV–J colours to the traditional 'age-tracing' Balmer line HγF. This line does not trace age cleanly, being affected to a small degree by the metallicity.

HγF against NUV–J for the NFPS sample is shown in Figure 2.13. Given the relative strengths of the colour vs. age and [Z/H] relations (Figures 2.7 and 2.8), the correlation seen here is most likely a reflection of the metallicity, rather than age, dependence of HγF. For comparison, the observations have been overlaid by age/metallicity grids constructed from the models of Maraston (2005, M05; upper panel) and Bruzual & Charlot (2003, BC03; lower panel). Both grids lie redward of the observed data, most likely due to neither model including EHB stars, although the BC03 grid provides the better description of the data. Previous studies (e.g. Salim et al. 2007) have noted that while the BC03 models do not explicitly include EHB stars, the UV light from old stellar populations (primarily post-AGB stars) reproduce several of the correlations found in observational data, including the relation between FUV–NUV and B–V colours (see Donas et al., 2007, particularly figure 5).

Dorman et al. (2003) introduced corrections to their NUV–V colours by considering

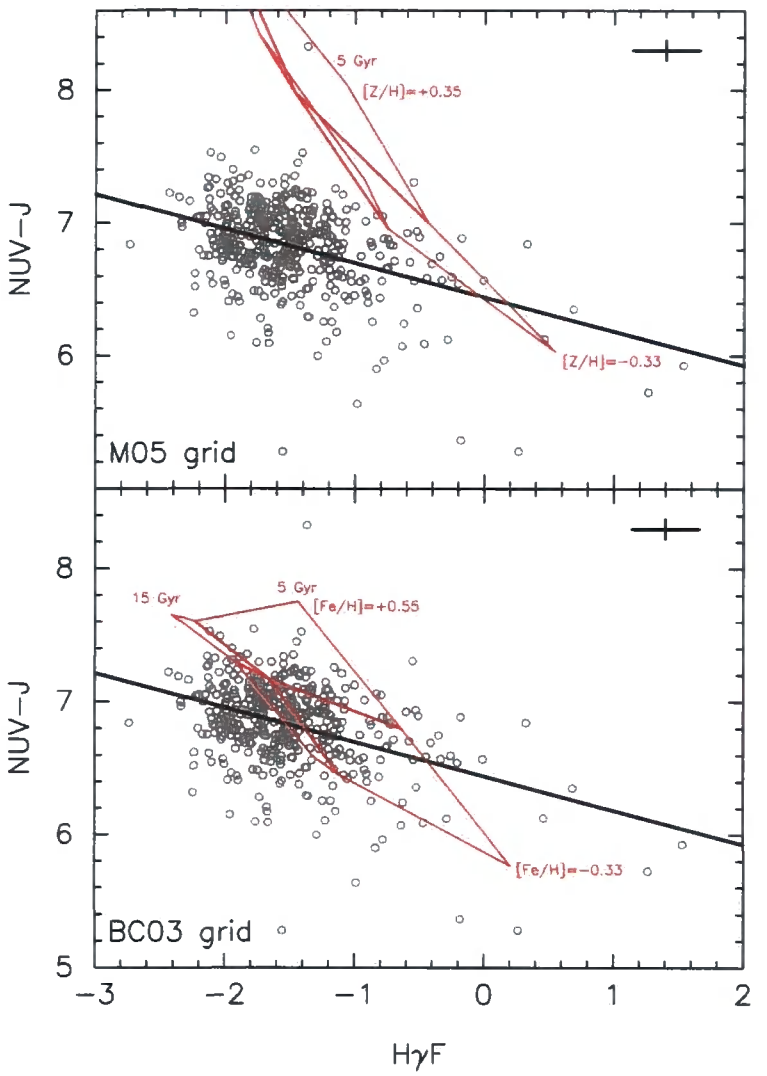

Figure 2.13: $NUV-J$ (without K-correction) against HγF Balmer index for NFPS galaxies. Upper panel: M05 grid (age={5,12,15 Gyr}, [Z/H]={–0.33,0.00,+0.35}). Lower panel: BC03 grid (age={5,12,15 Gyr}, [Fe/H]={–0.33,+0.09,+0.55}). (5,–0.33) is the bluest (age,[Z/H]) grid point. Median error bars are shown top right.

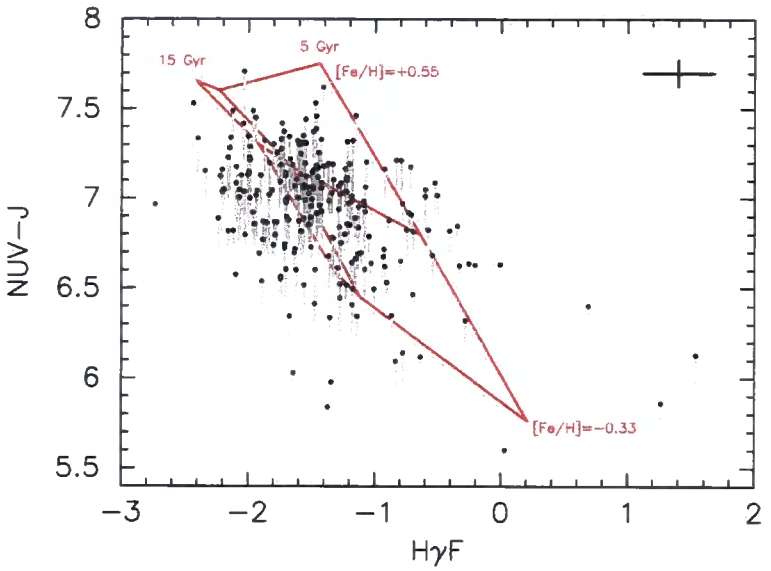

Figure 2.14: NUV–J (without K-correction) against HγF Balmer index for galaxies with available FUV data. Points indicate the UVX corrected colour, with the 'tail' showing the correction vector. BC03 grid as in Figure 2.13 (lower panel). Median error bars are shown top right.

the relative contributions of the hot and cool (i.e. non-UVX) components at FUV, NUV and V. They assumed a negligible contribution of the cool component to the FUV flux, but allowed hot stars to contribute at V. Here, analogous corrections for the NUV–J colours are used, which are simpler because it is safe to assume no UVX contribution at J. The corrected colours are given by

$$(NUV - J)_{\rm corr} = -2.5 \times log[10^{-0.4(NUV-J)_{\rm obs}} - \alpha \times 10^{-0.4(FUV-J)_{\rm obs}}] \qquad (2.1)$$

where $\alpha \approx 0.3$ is the ratio of NUV to FUV flux for the hot component (appropriate for a $T_{\rm eff} = 24000$ K star, see Dorman et al.).

The resulting corrections are shown as vertical lines in Figure 2.14 (where the points indicate the value of the corrected colour). The corrections move the colours redward as expected, but are only of the order of ~0.2 magnitudes, and do not reduce the scatter in the NUV–J (0.29 mag before corrections, 0.30 mag after). Obviously there are no extreme UVX galaxies with large hot component contributions to the NUV flux in this sample, and as such the UVX phenomenon is unlikely to responsible for the scatter in NUV–J for NFPS. We speculate that the UVX effects in the SSC sample are smaller because, on average, the galaxies have lower luminosities.

2.4.3 Stellar population 'frosting'

The simple models can be generalised by constructing composite stellar populations. A common invocation of this is residual star formation in the form of 'frosting' old galaxies with a small mass fraction of young stars (Trager et al., 2000a), which manifests itself in the observables as a bluer colour and a younger age than the base population. Frosting should not affect the spectroscopic metallicity or α-abundance significantly as these are primarily driven by the larger, older population (Serra & Trager, 2007).

Figure 2.15 shows the extent to which frosting can account for the scatter, after the effect of metallicity has been removed using the correlation of Figure 2.8. Simple stellar population (SSP) tracks from both the M05 and BC03 models are shown. The slope of the BC03 track fits the observed red envelope well, whereas M05 predicts a much steeper variation with age. Allowing for the systematic effects of aperture bias and the UV upturn ($\sim$0.3 mag bluer in observed NUV–J), $\sim$30 per cent of the galaxies cannot be accounted for by the SSP model.

Vectors of the frosting effect on NUV–J colour and spectroscopic age have been calculated using the BC03 models. Frosting of a 15 Gyr base population by a 1.5 Gyr population with a mass fraction μ=0.03, and by a 0.7 Gyr population of μ=0.01 are shown. The M05 models result in marginally steeper frosting vectors, as would be expected given the steeper SSP track. The vectors show that frosting, even at a modest level of 1 – 2 per cent for a $\sim$1 Gyr population, could account for a sizeable portion of the scatter in the NUV–J colour. A young population of this size would not be apparent in the B–R colours.

The spectroscopic age is sensitive to frosting via the increased hot-star contribution to the Balmer lines, and for a given change to the spectroscopic age, the UV colours are affected more strongly by frosting than by lowering the age of a single-burst population. This supports the assertion that UV colours are partly dependent on low-level recent star formation (Ferreras & Silk 2000, Kaviraj et al. 2007b, Salim et al. 2007). However, there are spectroscopically old galaxies with blue colours ($\sim$10 per cent of the sample) which cannot be accounted for by the frosting scenario described above. Additionally, Rose CaII index results (Smith et al., 2009a) appear not to support the presence of young stellar populations ($\lesssim$ 1.5 Gyr) in the majority of red-sequence galaxies.

For most of this study, we have neglected the blue horizontal branch (BHB) as cluster red-sequence galaxies have [Z/H] $\sim$0. However, it is possible that a low metallicity population with a BHB morphology may be present in some galaxies (Maraston & Thomas,

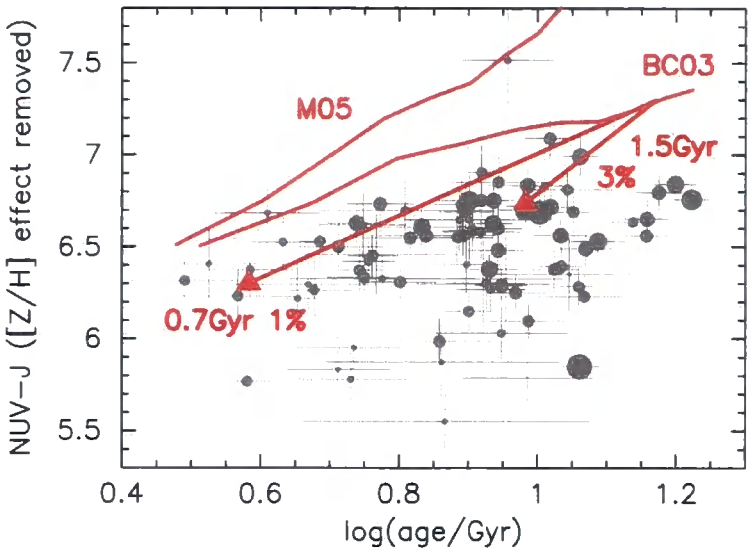

Figure 2.15: Simple stellar population tracks from the M05 and BC03 models shown in the context of the NUV–J colour (correcting to [Z/H]=0 using the correlation from Figure 2.8) vs log(age). Vectors indicate two BC03 frosting scenarios with minor populations of $\{\mu$,age$\}$ = {0.03,1.5Gyr} and {0.01,0.7Gyr}.

2000). Therefore, an alternative 'frosting' scenario consists of a low mass fraction, old, low metallicity, BHB stellar population embedded in a [Z/H]=0 galaxy. Estimates from the M05 models show that 'frosting' by a 4–5 per cent mass fraction population with [Z/H]=–1.35 could give an NUV–J colour ~1 mag bluer, while changing the B–R by only ~0.03 mag. The effect of the low-metallicity frosting on the derived spectroscopic age is likely similar to the effect of frosting by a young component, since both cases are driven by increased A-star contribution to the Balmer lines.

2.4.4 NUV K-corrections

K-corrections for the UV bands are poorly constrained, as the spectral shape of galaxies at wavelengths shorter than ~3000 Å is not well known. Previous studies of the UV CMR largely ignore the K-correction, or in the case of Yi et al. (2005, who estimate corrections of $0.1 - 0.2$ mag for $z = 0 - 0.25$) apply corrections based on the luminosity distance without considering the spectral shape of galaxies.

Kaviraj et al. (2007b) compute NUV K-corrections for best fit model SEDs derived from SDSS and *GALEX* photometry. Corrections of ~0.1 mag were found for redshifts z < 0.1. However, corrections for their model of a 9 Gyr old simple stellar population are much larger ($0.4 - 1.0$ mag for $0.04 < z < 0.11$).

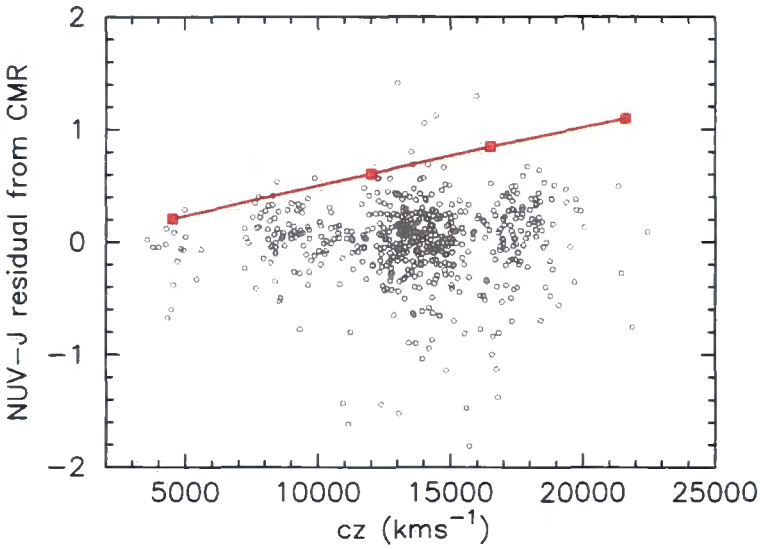

Figure 2.16: CMR residuals for the NFPS sample (Figure 2.3; upper panel) vs heliocentric galaxy redshift. The red squares and solid line show the predicted trend if the K-corrections from the M05 models were necessary, but not applied.

As an illustration, K-corrections are calculated from the Maraston models at various redshifts ($0.015 < z < 0.072$), both for simple populations and galaxies in the 'frosting' scenario described in Section 2.4.3. K-corrections of 0.2 – 1.2 mag are obtained, depending on the metallicity and age (increasing either increases the correction), and on the mass fraction of the young stellar component. The corrections are dominated by the 2640 Å spectral break (cf Eisenstein et al. 2003), which is redshifted completely out of the NUV-band by $z \approx 0.07$. In Eisenstein et al., who study the average spectra of 726 luminous, red, SDSS galaxies at $0.47 < z < 0.55$, the break appears less prominent than in the M05 spectra (a ~50 per cent drop in flux as opposed to ~80 per cent).

Figure 2.16 shows the regression line residuals from the colour–magnitude diagram for the NFPS sample (Figure 2.3; upper panel) plotted against the galaxy redshift in the heliocentric frame. The solid line shows the expected trend if the M05 K-corrections were necessary, but not applied. This implies the uncorrected residuals should have a steep correlation with redshift, which is not observed. A flatter K-correction is preferred by the data, as in Kaviraj et al. (2007b). Along with the Eisenstein et al. spectrum described above, this result highlights the uncertainty in the UV K-corrections (as well as the problems of stellar population models in the UV).

2.5. Conclusions

Using *GALEX* UV and 2MASS J-band photometry, the relationship between UV–IR colours and spectroscopically derived stellar population parameters (age, total metallicity and α-element over-abundance) have been investigated for red-sequence galaxies in local clusters.

Galaxies were selected using a strict emission criteria to avoid contamination from galaxies with very recent star formation. The NUV colour–magnitude relation (CMR) was analysed for two samples of quiescent galaxies (920 in NFPS; 156 in SSC), and rms dispersions were calculated: 0.37 and 0.30 mag (intrinsic scatter of 0.36 and 0.29 mag) respectively. This is similar to previously reported values of $\sim$0.5 mag and is an order of magnitude larger than the scatter in the optical CMR ($\sim$0.05 mag).

The NUV–J colour was compared to the spectroscopic stellar population parameters for 87 galaxies in the SSC sample and the following was found:

- There is a significant NUV–J vs metallicity trend, with a slope of 1.27 ± 0.23 and an rms dispersion of 0.32 mag.
- There is only a weak NUV–J vs age trend after the metallicity effect has been removed, and no correlation with α-abundance.
- There is a large intrinsic scatter ($\sim$0.25 mag) in the NUV–J colour at fixed age and metallicity which cannot be easily accounted for with simple stellar populations.

The unexpected blue colours of at least some objects, including an influential outlier, cannot be attributed to large radius contamination from other objects, and aperture bias cannot account for the large scatter. Corrections for the UV upturn (UVX) phenomenon are relatively small ($\sim$0.2 mag) and are similar galaxy-to-galaxy, so do not reduce the intrinsic scatter.

We conclude that the large NUV–J intrinsic scatter could be attributed to galaxy 'frosting' by small (< 5 per cent) populations of either young stars or a low metallicity blue horizontal branch.

Chapter 3

Observing radial trends in early-type galaxies with VIMOS IFU

We present a study of the internal stellar population gradients in early-type cluster galaxies, using data from the VLT VIMOS integral field unit. This chapter describes the procedure to reduce the raw observations, measure absorption line gradients to the effective radius, and ultimately, derive the radial trends in age, metallicity and α-element abundance. This work was presented in Rawle et al. (2008b) and Rawle et al. (2009). Discussion of the results, and physical interpretation of the gradients, is deferred to Chapter 4.

3.1. Introduction

For almost five decades, observations have identified systematic radial trends in the stellar properties of galaxies (de Vaucouleurs, 1961). These internal gradients are a valuable probe into the star formation histories and chemical evolution of galaxies. Traditionally, the focus has lain upon radial trends in (mostly optical) broadband colours (e.g. Franx, Illingworth, & Heckman 1989; Peletier et al. 1990; Tamura et al. 2000; Michard 2005).

Early-type galaxies typically become steadily bluer towards their outer regions. These colour gradients have often been interpreted as variations in metallicity. Tamura & Ohta (2003) estimated that $\nabla B{-}R \sim -0.1$ corresponds to ∇[Z/H] ~ -0.3[1]. The relative shal-

[1]All gradients are quoted per decade radius, with ∇X the shorthand for the change in X per decade

lowness of these estimated metallicity gradients rule out the simplest models of classic monolithic collapse (Larson, 1974a; Carlberg, 1984). Within the framework of hierarchical ΛCDM models (e.g. Cole et al., 2000; De Lucia et al., 2006; Bower et al., 2006), competing processes influence the gradients. For instance, variations in the merger gas content and feedback prescriptions can be investigated (Kawata & Gibson, 2003; Kobayashi, 2004), with mergers generally tending to dilute or erase metallicity gradients (e.g. White, 1980). However, gas dissipation could trigger star formation at the core, creating a positive age gradient whilst also strengthening the negative metallicity gradient (Barnes & Hernquist, 1991; Mihos & Hernquist, 1994).

The well-known degeneracy between age and metallicity in broadband optical colours has hindered attempts to distinguish their respective contribution to the gradients (as described in Chapter 1). Using optical and infrared colours to estimate metallicity and age gradients, Tamura & Ohta (2004) found that including the age effect weakens the mean ∇[Z/H] to -0.16 ± 0.09, while predicting small age gradients. Wu et al. (2005) used optical/IR colour gradients of 36 nearby early-types to derive a mean metallicity gradient of -0.25 ± 0.03 and a shallow mean $\nabla\log(\text{age}) = 0.02 \pm 0.04$, but with a substantial dispersion in age gradients of 0.25.

Spectroscopic data can be used to discriminate between the age and metallicity effects (Rose, 1985; Worthey, 1994). To date, most spectroscopic studies of the radial trends in early-type galaxies have used a single slit along the major axis (e.g. Gorgas, Efstathiou, & Aragon Salamanca 1990; Mehlert et al. 2003; Sánchez-Blázquez et al. 2007; Reda et al. 2007), occasionally supplemented by a perpendicular slit along the minor axis (e.g. the S0 study in Norris, Sharples, & Kuntschner 2006). Long-slit spectrographs have good optical throughput, but the majority of the light from the galaxy goes undetected, and the major axis is assumed to be representative of the whole.

An integral field unit (IFU) couples the diagnostic power of spectroscopic observations, to the spatial sampling enjoyed in imaging. The SAURON project, introduced in Bacon et al. (2001) and de Zeeuw et al. (2002), observed 72 nearby galaxies ($cz < 3000$ km s^{-1}). The excellent spatial coverage of the instrument permitted two-dimensional dynamical/kinematic mapping of the targets. However, the trade-off for the spatial resolution is a limited spectral range covering only three useful line absorption indices (Hβ,

radius

Fe5015, Mgb5177), hindering the detailed analysis of stellar populations.

In the current study, we use the Very Large Telescope (VLT) VIsible MultiObject Spectrograph (VIMOS) IFU to observe 31 early-type galaxies in two local clusters: Abell 3389 (z = 0.027) and the Shapley Supercluster core (z = 0.048). This chapter concentrates on the reduction process, spectroscopic analysis and derivation of the stellar population gradients. Section 3.2 describes the samples and observational technique, while initial data reduction is detailed in Section 3.3. As a sanity check, Section 3.4 compares central spectroscopy derived from VIMOS to data from aperture spectrographs. In Section 3.5 we present the measured absorption line gradients and derive the radial trends in the stellar populations. Chapter 4 will present galaxy-to-galaxy trends and discuss a tentative physical interpretation of the results.

3.2. VIMOS observations

3.2.1 The samples

The two IFU data sets were observed in separate semesters: ESO VLT programmes 078.B-0539 and 081.B-0348 (PI for both: J Lucey). The first study targeted galaxies in the nearby cluster Abell 3389, while the second sample of galaxies all lie within the Shapley Supercluster core.

For consistent galaxy-to-galaxy comparisons, the PSF-corrected effective radius (r_e) is a useful scale-length. We calculated r_e from 2MASS J-band imaging, which is available for all galaxies in both samples. Due to the relatively small size of the galaxies with respect to the 2MASS PSF (FWHM $\sim$ 3 arcsec), the apparent half-light radii required a correction. For this, we adopted the difference between the half-light radii of Sersic model fits (using GALFIT; Peng et al. 2002) before and after PSF convolution. The smallest object in the A3389 sample (D61), has an apparent half-light radius of 2.9 arcsec, which was corrected to 2.1 arcsec. The uncertainty in this correction, derived from the scatter in corrections for similar sized galaxies, is $\pm$0.1 arcsec. The PSF correction is significantly smaller for larger galaxies, and we estimate that the listed effective radii have an uncertainty of better than 10 per cent.

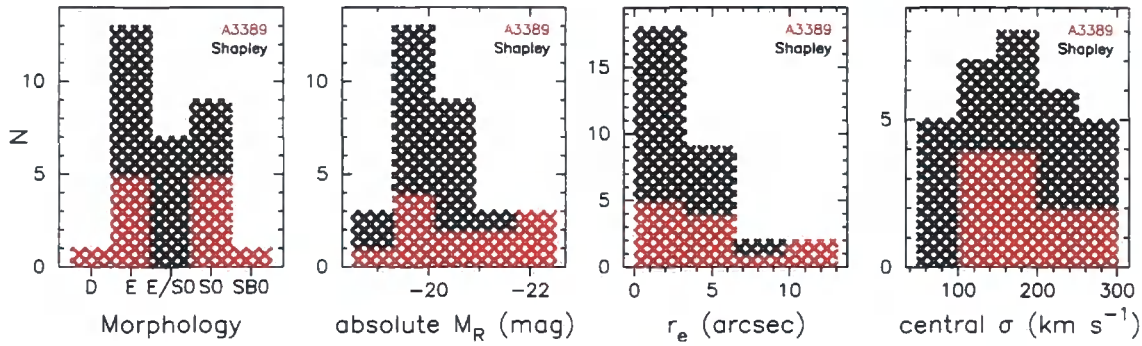

Figure 3.1: Histograms presenting the distribution of (left-to-right) morphology, R-band absolute magnitude, effective radius and central velocity dispersion for the sample galaxies (red=A3389; black=Shapley).

Abell 3389

The first sample contains 12 early-type galaxies in the nearby cluster Abell 3389 (<cz> $\approx$ 8100 km s^{-1}). This study was originally designed as a feasibility assessment of the methodology and as such, the target cluster was selected based on its low-demand RA ($\sim 6^h$). Each galaxy is a confirmed cluster member and is morphologically classified as an early-type by Dressler (1980a, D80). Central spectroscopy was previously measured for ten of the twelve target galaxies as part of the NOAO Fundamental Plane Survey (NFPS; Smith et al. 2004, Nelan et al. 2005).

The sample spans a range of three magnitudes in luminosity ($R \sim 12 - 15$ mag), and the galaxies have effective radii of 2.1 – 12.5 arcsec (1.1 – 6.7 kpc). Thumbnails of the A3389 galaxies are presented in Figure 3.2, and various parameters are listed in Table 3.1.

Shapley Supercluster

The second sample consists of 19 early-type galaxies located in the three main constituent clusters (Abell 3556, Abell 3558, Abell 3562) of the Shapley Supercluster core (<cz> $\approx$ 14660 km s^{-1}). Shapley is the richest supercluster in the nearby universe (Raychaudhury, 1989), and there is a wealth of ancillary data for each galaxy. Photometric coverage includes ESO 2.2m B- and R-band (Shapley Optical Survey; SOS; Mercurio et al. 2006), GALEX ultraviolet (Rawle et al., 2008a) and UKIRT WFCAM near-infrared (PI: Smith) imaging. Inclusion in the high-S/N multi-object spectroscopic survey of Smith et al. (2007) was a prerequisite for selection, and thirteen of the targets also have central spectra from the NOAO Fundamental Plane Survey (Smith et al., 2004). Figure 3.3 presents

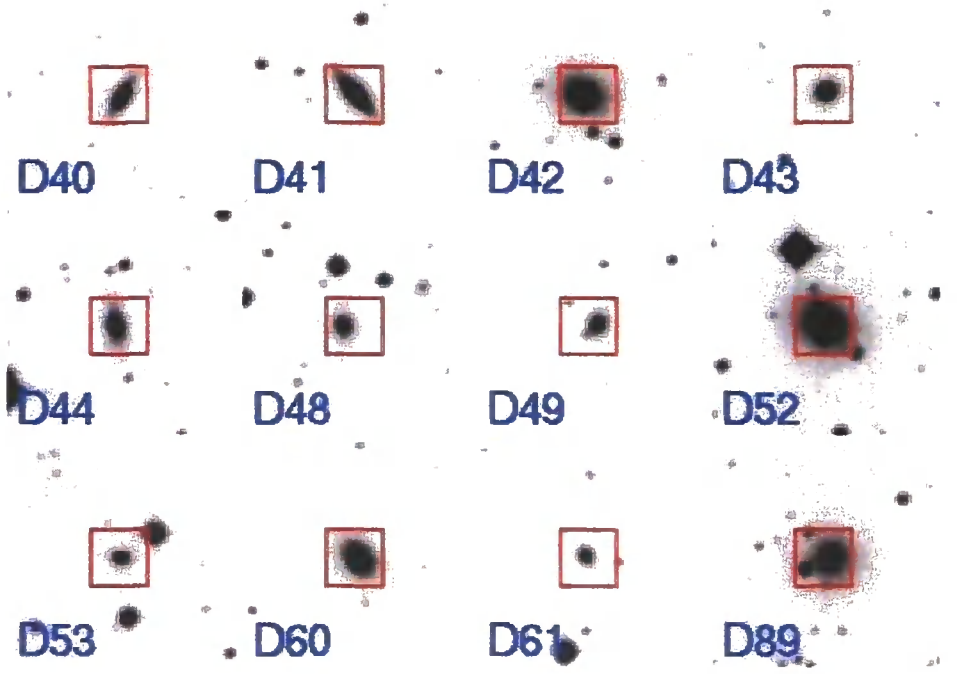

Figure 3.2: Thumbnail images from the Digitized Sky Survey, showing a 100 arcsec square field around the A3389 sample galaxies. The red boxes correspond to the 27×27 arcsec VIMOS field of view, underlining how well matched our chosen galaxies are to the instrument.

Table 3.1: Parameters for the Abell 3389 galaxies. ID and morphology from Dressler (1980a, D80). Positions, J- and K-band magnitudes, and PSF-corrected effective radius (r_e) from 2MASS images. R-band magnitude from NED. Central S/N and central velocity dispersion (σ km s^{-1}; as measured in Section 3.3.3) from an $r_e/3$ aperture. The final column indicates whether the derivation of gradients proved possible (see Section 3.5.1). The co-added VIMOS exposure time, T_{tot}, is 1730 s for all objects.

ID	NGC	RA	Dec	m_R	m_J	m_K	r_e	Morph.	S/N	σ	grads?
(D80)	#	(J2000)	(J2000)	mag	mag	mag	arcsec	(D80)	Å^{-1}	(km s^{-1})	
D40		06:21:59.7	–64:59:19	14.2	12.18	11.16	4.2	S0	22.6	178.8 ± 6.1	Y
D41	2233	06:21:40.1	–65:02:00	13.5	11.47	10.47	4.6	S0	65.1	184.6 ± 2.4	Y
D42	2230	06:21:27.5	–64:59:34	12.6	10.62	9.66	10.5	E	72.2	253.9 ± 3.1	Y
D43		06:21:13.9	–65:00:58	14.6	12.59	11.58	3.1	S0	29.8	149.8 ± 4.4	Y
D44		06:20:54.4	–65:01:08	14.0	12.08	11.13	3.8	S0	35.3	221.5 ± 4.5	Y
D48		06:23:49.0	–64:57:15	14.8	12.81	11.94	2.9	E	34.8	144.6 ± 2.3	Y
D49		06:23:07.4	–64:55:50	14.7	12.65	11.64	2.3	E	31.4	180.9 ± 3.9	Y
D52	2235	06:22:22.1	–64:56:03	12.4	10.42	9.35	12.3	D	71.3	252.1 ± 2.4	Y
D53		06:22:04.8	–64:57:36	15.1	13.14	12.18	2.8	E	20.9	113.5 ± 4.4	
D60		06:22:19.8	–64:14:04	13.5	11.52	10.58	4.5	E	73.4	194.0 ± 1.9	Y
D61		06:21:58.3	–64:53:44	15.3	13.27	12.37	2.1	S0	24.3	146.6 ± 6.7	Y
D89	2228	06:21:15.6	–64:27:32	12.8	10.81	9.79	9.3	SB0	60.0	247.7 ± 2.8	Y

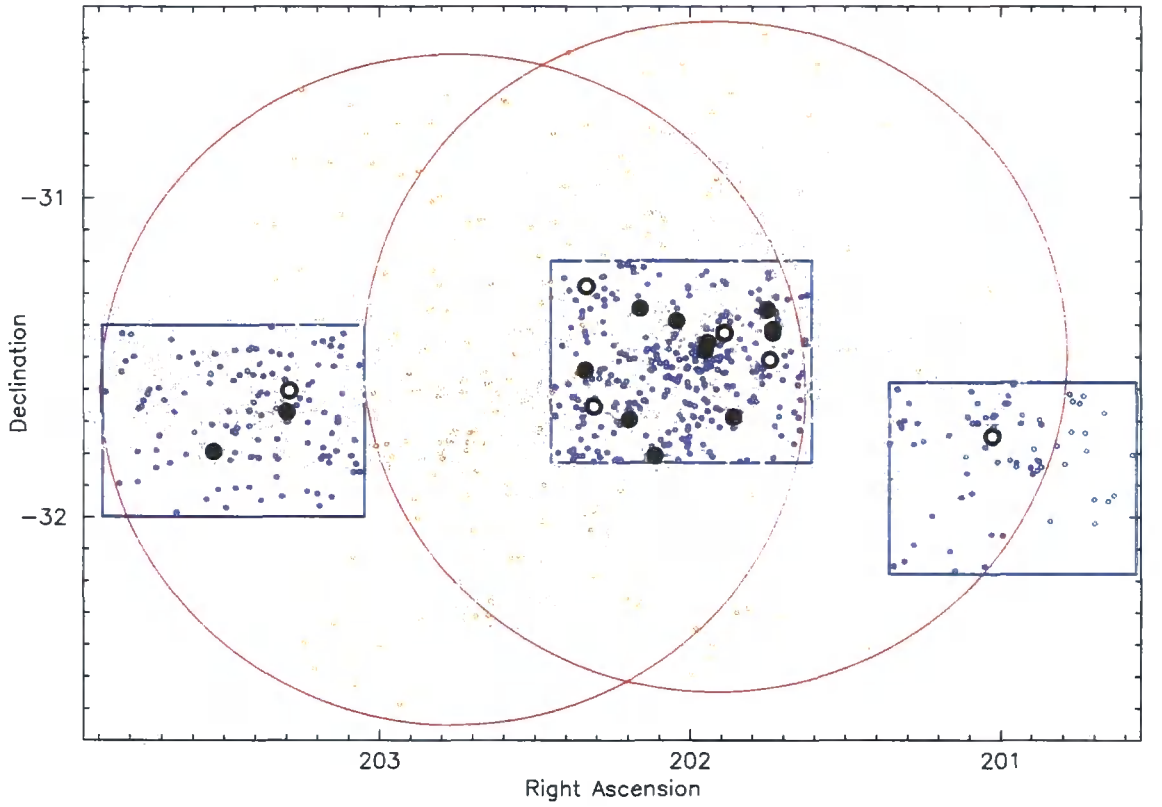

Figure 3.3: Map of the Shapley Supercluster core, highlighting the VIMOS sample (large black circles: filled have spectra from AAΩ and NFPS, open are in AAΩ only). Further galaxies are coloured as follows: orange open circles = AAΩ observations only; blue open circles = NFPS only; purple filled circles = AAΩ and NFPS spectra. Other SOS galaxies are shown in grey. Study fields are indicated: grey = SOS footprint, red = AAΩ fields, blue = NFPS regions. The NFPS fields target the centre of the three clusters: A3556, A3558, A3562.

the position of the VIMOS galaxies in the Shapley Supercluster core, and indicates the overlap with the previous studies.

The sample galaxies are all confirmed supercluster members and were visually classified as early-type (elliptical or S0) in the SOS B- and R-band imaging. The targets were selected to probe a range of masses and age/metallicity combinations (as derived from previous central spectroscopy), and span three magnitudes in luminosity ($R \sim 14 - 17$ mag). The galaxies have effective radii of 2.1 – 11.1 arcsec (2.0 – 10.5 kpc), measured from the 2MASS J-band images as previously described. Figure 3.4 presents a thumbnail image for each galaxy, and Table 3.2 lists various parameters.

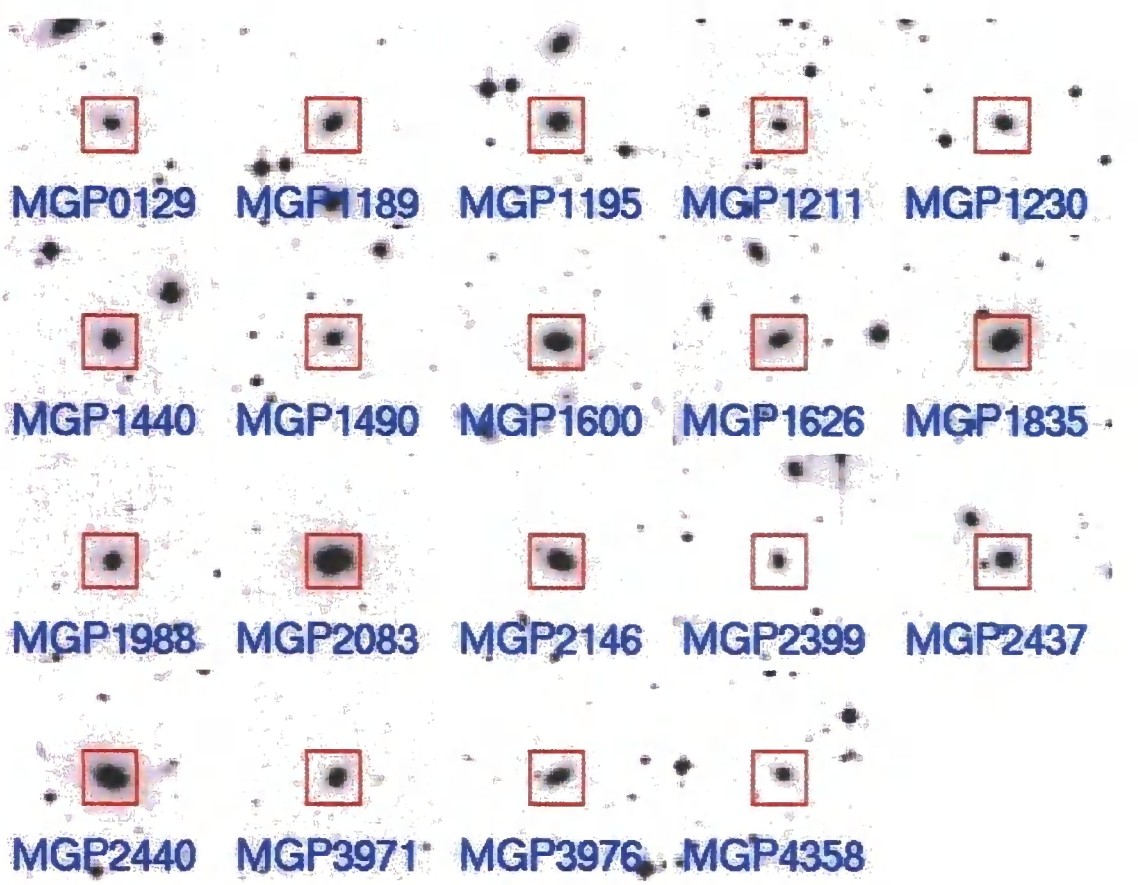

Figure 3.4: Thumbnail images of the Shapley Supercluster core galaxies. Presented as in Figure 3.2

Table 3.2: Observed parameters for the Shapley Supercluster core galaxies. ID from Metcalfe et al. (1994, MGP). Positions, central optical photometry (5 arcsec radius apertures) and morphology from SOS B- and R-band imaging (Mercurio et al., 2006). J- and K-band (total) photometry and PSF-corrected effective radius (r_e) from 2MASS images. T_{tot} is the co-added VIMOS exposure time. Central S/N Å^{-1} (averaged over the range 4700–5000 Å) and central velocity dispersion (σ km s^{-1}; as measured in Section 3.3), both from an $r_e/3$ aperture. The final column indicates whether the derivation of gradients proved possible (see Section 3.5.1).

ID (MGP)	RA (J2000)	Dec (J2000)	m_R mag	B–R mag	m_J mag	m_K mag	r_e arcsec	Morph.	T_{tot} (s)	S/N Å^{-1}	σ (km s^{-1})	grads?
MGP0129	13:24:06.8	–31:44:49	16.42	1.37	14.62	13.74	1.96	E/S0	6132	14.1	100.8 ± 4.8	
MGP1189	13:26:55.9	–31:24:47	15.46	1.47	13.50	12.52	1.66	E/S0	4088	44.4	270.1 ± 4.9	Y
MGP1195	13:26:56.0	–31:25:27	15.76	1.42	13.65	12.40	3.25	S0	2044	22.3	117.8 ± 3.5	Y
MGP1211	13:26:58.3	–31:30:30	16.83	1.39	15.19	14.08	1.14	E	4088	11.7	95.2 ± 4.8	
MGP1230	13:27:00.3	–31:21:05	16.16	1.30	14.41	13.84	2.07	E/S0	4088	19.7	57.8 ± 4.2	Y
MGP1440	13:27:27.0	–31:41:07	15.92	1.43	13.97	13.21	2.34	E	6132	25.9	186.5 ± 7.2	Y
MGP1490	13:27:33.5	–31:25:26	16.40	1.41	14.24	13.89	3.65	E	8176	14.5	76.5 ± 5.0	Y
MGP1600	13:27:46.6	–31:27:15	15.02	1.49	12.96	11.91	2.23	S0	2044	43.5	289.0 ± 5.6	Y
MGP1626	13:27:48.5	–31:28:46	15.35	1.55	13.33	12.23	1.66	S0	2044	36.8	242.8 ± 4.1	Y
MGP1835	13:28:10.5	–31:23:10	15.19	1.53	12.93	12.05	3.68	E	2044	44.3	203.0 ± 4.0	Y

Table 3.2 continued...

ID (MGP)	RA (J2000)	Dec (J2000)	m_R mag	$B-R$ mag	m_J mag	$m_{K'}$ mag	r_e arcsec	Morph.	T_{tot} (s)	S/N $Å^{-1}$	σ (km s^{-1})	grads?
MGP1988	13:28:27.6	–31:48:18	15.76	1.54	13.69	12.78	2.48	E/S0	2044	26.9	168.7 ± 4.2	Y
MGP2083	13:28:38.7	–31:20:49	14.76	1.65	11.86	10.99	9.62	E	4088	47.8	268.0 ± 3.3	Y
MGP2146	13:28:47.2	–31:41:35	15.69	1.42	13.36	12.49	4.61	S0	4088	21.6	116.8 ± 6.2	
MGP2399	13:29:14.5	–31:39:11	16.52	1.39	14.70	13.64	2.33	E	6132	11.8	81.4 ± 8.3	
MGP2437	13:29:20.1	–31:16:39	15.74	1.54	13.84	12.82	1.87	E	2044	29.2	179.5 ± 4.5	Y
MGP2440	13:29:20.7	–31:32:25	14.99	1.48	12.38	11.37	6.34	E	4088	50.1	230.7 ± 4.5	Y
MGP3971	13:33:09.5	–31:36:12	15.77	1.51	13.84	12.73	1.93	E/S0	2044	21.0	180.1 ± 5.5	Y
MGP3976	13:33:11.7	–31:40:09	15.26	1.52	13.15	12.23	2.52	E/S0	2044	27.5	247.2 ± 6.7	Y
MGP4358	13:34:08.1	–31:47:34	16.86	1.46	15.11	14.23	2.20	E/S0	6132	9.0	65.1 ± 7.9	

3.2.2 Line emission

If present, nebular emission fills in the Balmer absorption lines, causing an overestimation of the galaxy age. We inspected central spectroscopy from previous surveys to quantify the effect of possible contamination from line emission. Smith et al. (2007) established that Hα emission is the most reliable indicator of contaminating Hβ nebular emission.

Unfortunately, the available central spectra for A3389 do not cover the Hα line, so instead we search for other emission lines. The only target to display line emission is D52 with EW[O III λ5007] = 0.55 Å. D52 is a bright galaxy with a 'D'-type morphology, so the emission is most likely LINER-like rather than due to star formation. The emission line ratio [OIII]/Hβ is greater than 3 for LINER-like objects and Hγ/H$\beta \sim 0.6$, as inferred from nebular emission spectra. Therefore, in the worst-case Abell 3389 galaxy, emission decreases the Hβ and HγF absorption indices by no more than 0.2 and 0.1 Å respectively. Using the Thomas et al. (2003, 2004) stellar population model grids, we find that this causes an over-prediction in the ages of < 10 per cent (< 1 Gyr for D52).

For the Shapley galaxies, central Hα emission measurements are available from AAΩ spectroscopy (Smith et al., 2007). Eleven of these galaxies have no trace of Hα emission. Of the other eight, only three have EW(Hα) $\approx$ 0.3 – 0.5 Å (MGP0129 MGP2083, MGP3976), and none have EW(Hα) $>$ 0.5 Å. Smith et al. (2009b) calculate that EW(Hα) = 0.5 Å corresponds to a maximum Hβ contamination of 0.1 Å(an over-prediction of < 5 per cent).

At this low level, estimation of the Balmer emission would be unreliable, especially from the [O III] line. Therefore, we have not attempted to correct for line emission in any galaxy.

3.2.3 Observing with the VIsible MultiObject Spectrograph

This study uses observations from the VIsible MultiObject Spectrograph (VIMOS; LeFevre et al. 2003) on the ESO VLT unit telescope Melipal at Paranal. VIMOS was operated in the Integral Field Unit (IFU) mode with the high resolution, blue grism. Table 3.3 details the instrument configuration. In this mode, an array of 1600 fibres (giving 40 $\times$ 40 spatial pixels) feed the spectra onto four individual detectors, each identifiable with a 20 $\times$ 20 quadrant.

Observations for this study were made during dark time, with an average seeing (FWHM) of 0.7 arcsec for A3389 and 0.85 arcsec for Shapley. The A3389 galaxies were

Table 3.3: VIMOS instrument configuration.

Mode	IFU
Grism	HR blue
Field of view	27×27 arcsec
	(40×40 spaxels)
Spatial sampling	0.67×0.67 arcsec/fibre
Wavelength range	4150 – 6200 Å
Spectral resolution	2.1 Å FWHM
	($\sigma \sim 50$ km s^{-1})
Dispersion	0.51 Å/pixel

observed in October and November 2006, while the Shapley sample was observed in April–July 2008. ESO VLT observations are organised into self-contained one hour observing blocks, consisting of acquisition imaging, on-source exposures, offset sky frames (if required) and any necessary calibration. As noted below, observations differed slightly between the two samples.

A 1 hour observing block was devoted to each galaxy in the A3389 sample, with a total on-source time of 1730 s, split into three exposures of $\sim$ 577 s. The exposures followed a dither pattern to avoid loss of coverage due to bad pixels. An offset sky frame with an exposure time of 120 s was obtained for each galaxy. The observations required a minimum signal-to-noise ratio (S/N) of $\sim$ 18 Å^{-1} at 5000 Å, for a 1 arcsec wide annulus at the effective radius (r_e).

The Shapley Supercluster is almost twice as distant as Abell 3389, so the on-source time had to be maximised as much as possible. To minimise readout noise but allow for some repetition, each hour observing block consisted of two 1022 s spatially offset exposures. Efficiency was further enhanced by not observing separate offset sky frames. The Shapley galaxies have smaller angular sizes than in A3389, so the sky background can be calculated from pixels at the detector extremities. We aimed for the same minimum S/N $\sim$ 18 Å^{-1} at 5000 Å for a 1 arcsec wide annulus at r_e. To achieve this S/N for the five faintest objects (R $<$ 16.0), the observing block was executed twice. A potential issue with instrument fringing led to the repetition of several planned observations. Data quality was not in fact impacted, so all of the blocks have been included, increasing the

co-added exposure time for some galaxies (detailed in Table 3.2).

3.3. Data reduction

3.3.1 Initial reduction procedure

The raw frames were first treated for cosmic rays using the IRAF routine LACOSMIC (van Dokkum, 2001). Conversion to a useful science datacube (spatial–spatial–wavelength axes) requires knowledge of how to disentangle the mapping between the detector pixels and the pseudo-slits/fibres in the IFU head. The process is simplified using the ESO common pipeline (ESOREX), which efficiently handles the transformation for each quadrant, given a science frame, nightly calibration observations (a bias frame, flat field and arc lamp exposure), and the ancillary VIMOS technical files (line catalogue, fibre identification table and bad pixel maps). ESOREX ensures that each wavelength slice is correctly arrayed in the spatial dimensions, although the quadrants are at this stage not joined together.

For each of the quadrants, a master sky background spectrum was generated. In the A3389 observations, this was calculated from the median of the corresponding quadrant in the offset sky exposure. For the Shapley observations, which included no offset sky, the sky spectrum was computed from the median over all the spatial pixels in the outer region of the quadrant (rejecting bad pixels). In both cases, the sky spectrum was subtracted from each spatial element, pixel-by-pixel, after normalising to the total flux in the [OI] λ5577 Å sky line.

After sky subtraction, the quadrants were stitched together, before using the IRAF routine IMCOMBINE to produce a single median-combined datacube from all the exposures. Finally a relative flux calibrated was performed, with reference to the response curve calculated from a spectroscopic standard star (in this case Hiltner 600).

3.3.2 Spatial binning of the data

The intention of this study is to characterise the general radial trends in the stellar populations of early-type galaxies, similar to those measured using the conventional long-slit technique. With the VIMOS IFU data, it is also tempting to generate full spatial maps, such as those seen in the SAURON kinematic studies, e.g. Emsellem et al. (2004).

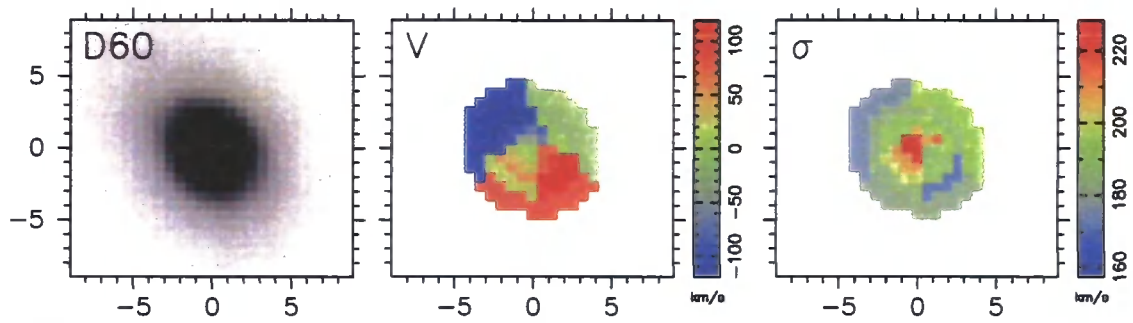

Figure 3.5: VIMOS wavelength-collapsed luminosity (left panel), radial velocity (V; central panel) and velocity dispersion (σ; right panel) maps for D60. Panel dimensions are in arcsec, and both kinematic quantities are in km s^{-1}, with the scale shown to the right of each panel. Figure 3.6 presents kinematic maps for further galaxies.

Full spatial maps

The underlying requirement of any such binning configuration is that the spectrum from each element must exceed a target S/N. The SAURON project observed galaxies an order of magnitude closer than our VIMOS galaxies, resulting in a high S/N even for relatively small bins at r_e. The SAURON team used a sophisticated Voronoi tessellation algorithm (Cappellari & Copin, 2003) which optimised the bin size and pixel allocation in order to maximise the spatial sampling, while maintaining a constant S/N per bin. Kinematic maps were generated for the SAURON sample from both stellar absorption lines (Emsellem et al., 2004) and ionised gas spectral features (Sarzi et al., 2006). The galaxies fall into two clear categories, segregated by the presence of large scale rotation ('fast rotators') or not (Emsellem et al., 2007). The authors proposed that the slowest of the 'slow rotators' are the evolutionary end-point, in which dissipationless merging dominates and most angular momentum has been expelled.

In an attempt at full spatial mapping, it is astute to begin with the galaxy that has the highest total S/N within r_e: D60 from the A3389 sample. Even the observation for this galaxy has too low a S/N to implement adaptive Voronoi binning. Instead, binning was achieved through a simple trial and improvement method, in which bin boundaries were based on segments of elliptical annuli. The S/N per bin was not restricted to a constant value, ranging from S/N $\sim 35-40$ Å^{-1} in the centre, to S/N $\sim 16-20$ Å^{-1} at r_e. For D60, twenty-three separate data bins were created.

Spatial maps were generated for the rotational velocity, V, and velocity dispersion,

σ (Figure 3.5; see Section 3.3.3 for more details on the kinematic fitting procedure). Although the spatial sampling is coarse, the maps do highlight the regular variation of the kinematic parameters. The central panel of Figure 3.5 shows that D60 has major axis stellar rotation of $\sim$110 km s^{-1} (in SAURON-parlance, D60 is a 'fast rotator'). The right panel demonstrates that the velocity dispersion in D60 is symmetric, peaking at $\sim$230 km s^{-1}.

Using the same binning technique, kinematic maps were created for five other galaxies with a high total S/N: D41, D42, D52, D89 and MGP2440 (Figure 3.6). The galaxies generally exhibit major axis rotational velocities of $\sim$50–130 km s^{-1}, with D42 (a comparatively edge-on S0 galaxy) having the strongest rotation. The exception is D89 (the SB0 galaxy), which does not have a coherent rotational structure. It is beyond the scope of this study to ascertain whether D89 is a true 'slow rotator', or whether the lack of observed rotation is due to a large central bar. As expected, the velocity dispersion maps generally show a symmetric negative gradient.

These VIMOS observations do not have sufficient S/N to generate full two-dimensional mapping of the spectral features. The total S/N within r_e for the other VIMOS galaxies does not even allow kinematic mapping. For galaxies at $cz = 8000 - 15000$ km s^{-1}, VIMOS observations with only a few hours on-source, are generally unsuited to SAURON-esque spatial mapping.

Radial binning

With the S/N per unit area too low for two-dimensional mapping of the spectral features, we use a series of annuli to compress the information down to one spatial dimension (ellipticity-corrected radius).

For each galaxy, the ellipticity and position angle of an ellipse fit to the wavelength-collapsed image, formed the basis of the annuli used as radial bins. The annuli were arranged out to r_e for each galaxy individually. Each annulus was required to have a S/N > 18 Å^{-1} and a width greater than 0.7 arcsec; in practice most galaxies have few annuli with $\Delta r < 1$ arcsec. The central bin was an exception with a semi-major axis of 0.5 arcsec if the minimum S/N was exceeded. The galaxies were assigned between three and seven radial bins, depending on the effective radius and surface brightness.

As an illustration, the adopted bins for three galaxies are shown in Figure 3.7. (The bins for all galaxies in the sample are displayed in Appendix B). Spectra from the adopted bins of MGP2440 (central panel, Figure 3.7) are shown in Figure 3.8. For each galaxy,

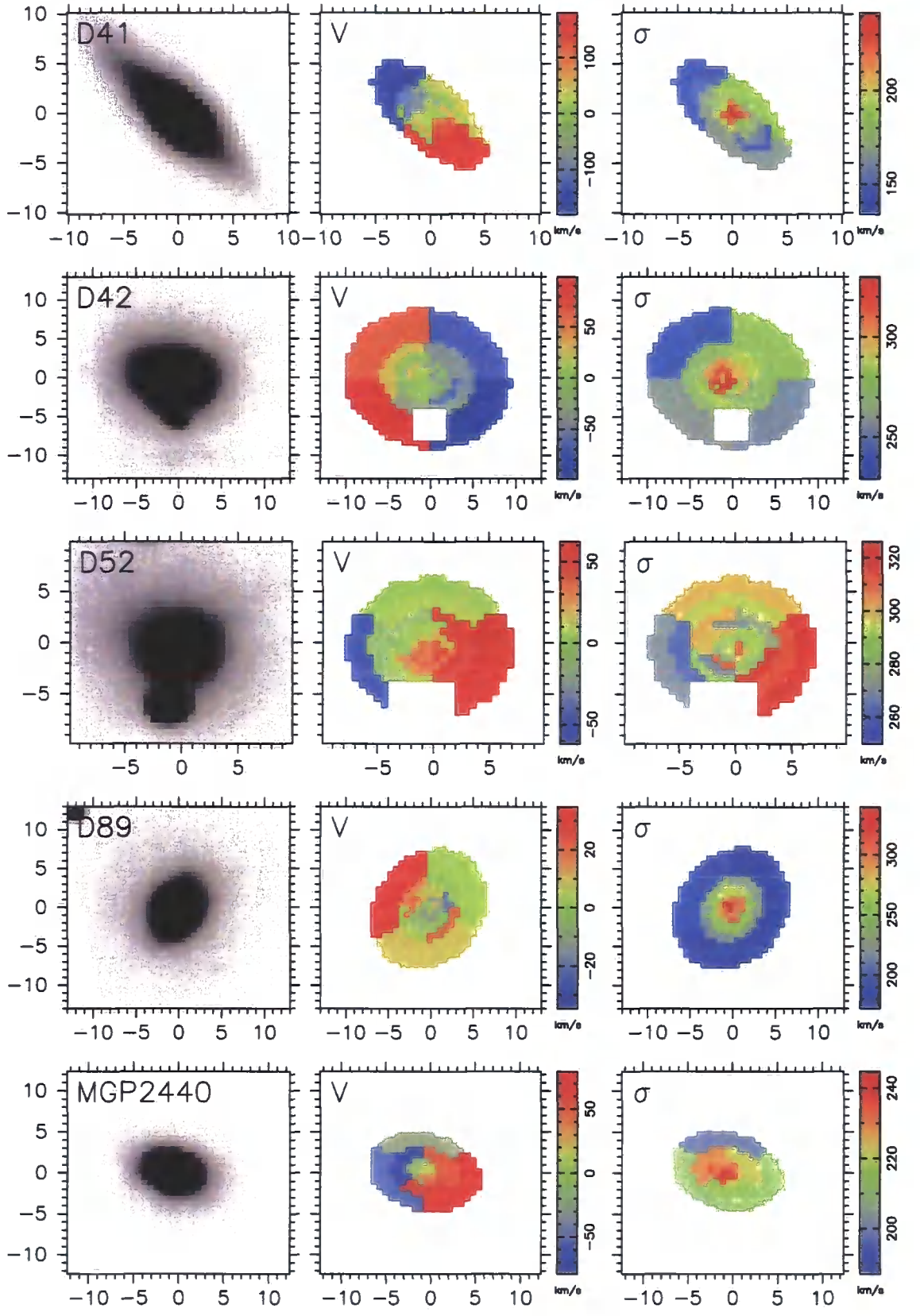

Figure 3.6: Kinematic maps for (top-to-bottom) D41, D42, D52, D89 and MGP2440. Layout of each row as in Figure 3.5.

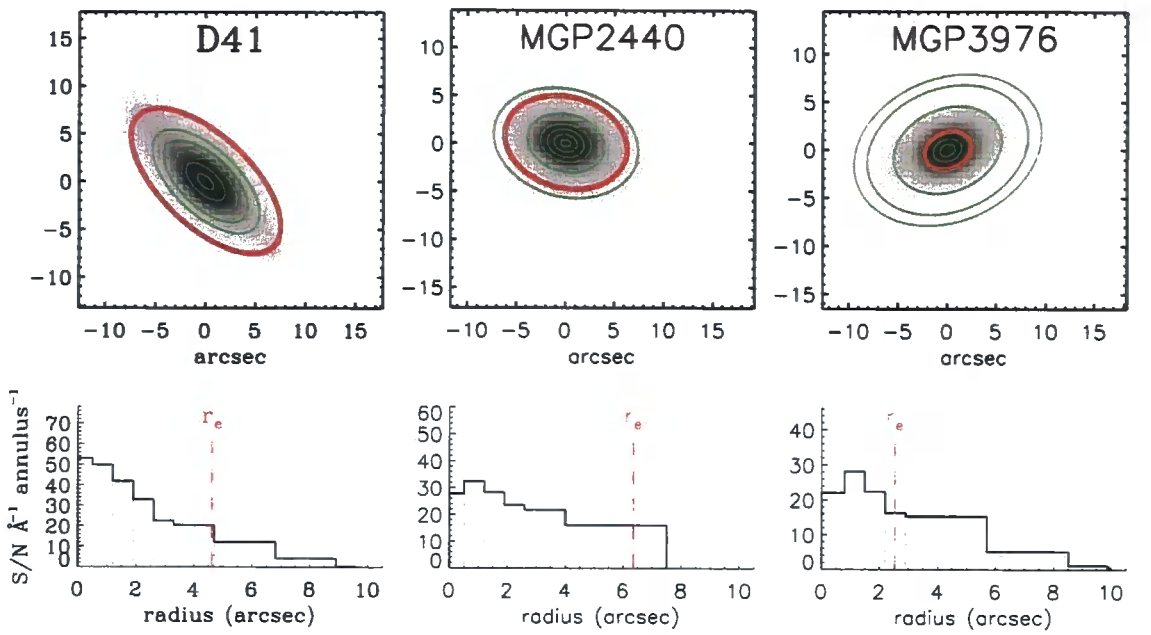

Figure 3.7: Adopted radial bins for three example galaxies: (left-to-right) D41, MGP2440, MGP3976. Upper panels show the wavelength-collapsed images from VIMOS, overlaid by the bin boundaries (green) and the effective radius (r_e; red). Lower panels show the S/N Å^{-1} (averaged over the region 4700 – 5000 Å) within each annulus out to 10 arcsec; r_e is indicated.

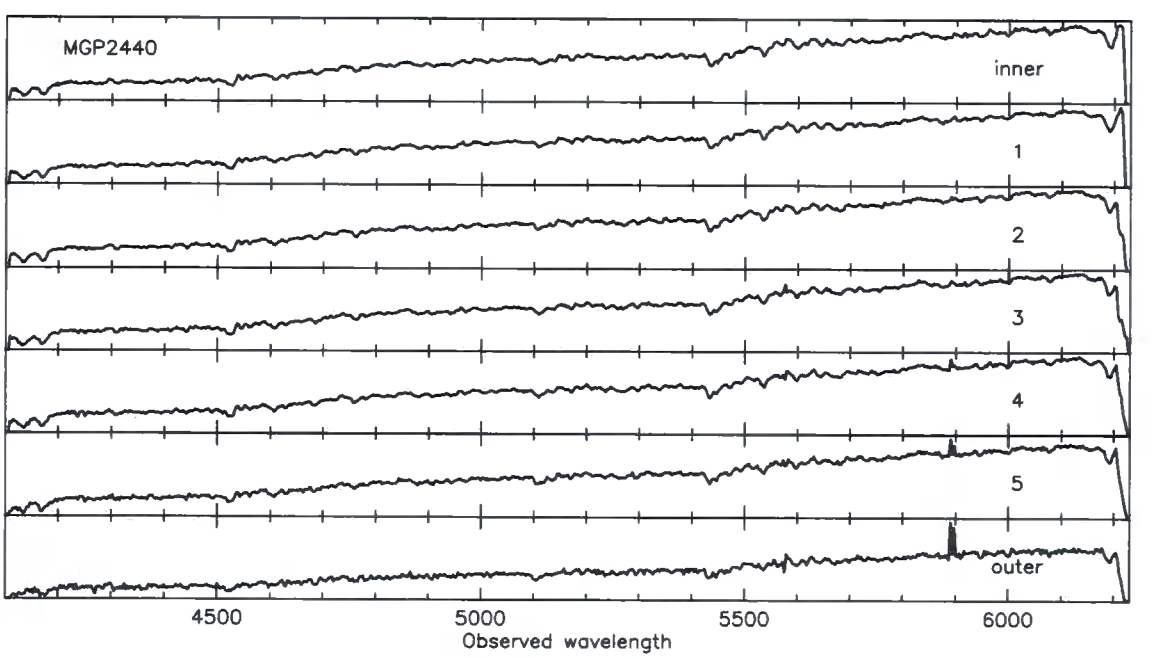

Figure 3.8: Spectra extracted from the adopted radial bins of MGP2440. Inner bin is in the uppermost panel.

spectra were also extracted from within two circular apertures, with radii of 1 arcsec (for direct comparison to central spectroscopy; Section 3.4.3) and $r_e/3$ (for physically consistent central parameters; Section 4).

3.3.3 Velocity dispersion measurements

Stellar kinematics (V,σ) were measured using the Penalized Pixel-Fitting (PPXF) routine of Cappellari & Emsellem (2004). PPXF extracts kinematics by fitting to a large set of weighted stellar templates, virtually eliminating template mismatch. The non-linear least-squares direct pixel fitting computation is broken into several iterations which find the best-fitting linear combination of the stellar templates. The derived residual spectrum from each iteration forms a penalisation term in the non-linear optimisation.

The Vazdekis (1999) evolutionary stellar population templates were used, covering a similar wavelength range to VIMOS (~4900 – 5500 Å was used for fitting) and having a higher spectral resolution (FWHM = 1.8 Å) than the VIMOS HR blue grism. Kinematic uncertainties were calculated using 51 Monte Carlo realisations of the input spectrum, obtained through the addition of Poisson noise. The 1σ intervals were taken from the 8th and 42nd values after sorting numerically.

3.3.4 Absorption line strengths

We used INDEXF[2] to measure twenty-three atomic and molecular Lick indices (Worthey et al., 1994) from de-redshifted, flux-calibrated spectra at the VIMOS instrument resolution ($\sigma \sim 50$ km s^{-1}). For measuring the gradients, model comparisons are performed in a relative sense, so we do not calibrate to the Lick instrumental response. Uncertainties were propagated by INDEXF (as described in Cardiel et al. 1998) from error spectra estimated from the variance plane.

The line indices require a correction to account for velocity-broadening and the instrumental resolution. Rather than use a multi-stage additive/multiplicative correction technique (e.g. Davies et al., 1993; Kuntschner, 2000), we adopted the single-stage linear correction method introduced in Smith, Lucey, & Hudson (2007). Indices measured from a range of stellar population templates, smoothed to the Lick resolution, are compared to those measured from the same templates smoothed to the instrument resolution and fur-

[2]http://www.ucm.es/info/Astrof/software/indexf/

ther degraded to mimic various levels of velocity broadening. For each index, at a given velocity dispersion, this comparison gives a near linear relation between the measured and corrected index. This technique is preferable, as it removes the need to artificially broaden the observed galaxy spectra prior to index measurement, thereby preserving the non-uniform noise properties.

3.3.5 Stellar population derivations

We transform the absorption line strengths into simple stellar populations via the models of Thomas, Maraston, & Bender (2003) and Thomas, Maraston, & Korn (2004), hereafter TMBK. These models characterise the stellar population in terms of age, total metallicity [Z/H] and α-element over-abundance [α/Fe] assuming a single, instantaneous starburst followed by passive evolution. The [α/Fe] was calculated for a fixed total metallicity by counteracting an increased abundance of the enhanced group (the α elements O, Ne, Mg, Si, S, Ar, Ca and Ti together with N and Na) with a decrease in the abundance of Fe and Cr.

The simplest visualisation of the transformation, uses pairs of indices to form grids in projections of the age–metallicity–α-abundance space. Figure 3.9 displays the age–[Z/H] grid on a plot of HγF–Fe4383 index measurements, with the grid in each panel representing a different [α/Fe] value. The orientation of the grid shows that Fe4383 is a good discriminator of metallicity, while HγF has a strong response to age. The analogous plot for Mgb5177–Fe4383 space is shown in Figure 3.10, where the [Z/H]–[α/Fe] is plotted (age varies from panel to panel). Mgb5177 is a strong indicator for α-abundance. It is clear from these grids that the various line indices have different responses to underlying physical parameters. Inverting several of these grids simultaneously harnesses the complementary power of each to effectively discriminate between the galaxy characteristics.

In this study, stellar population parameters were derived using a grid inversion technique similar to that of Proctor et al. (2004) and Smith et al. (2009a). This involves a non-linear χ^2 minimisation over a large set of indices, using a cubic-spline interpolation in age–[Z/H]–[α/Fe] to ensure continuity between cells. For points lying beyond the model grids, the parameters are estimated by linear extrapolation. This occurred in $\sim$5 per cent of cases (from a total of $\sim$320). Half of those were due to weak Balmer lines (giving ages $>$ 15 Gyr), and the remainder were from marginally sub-solar α-enhancements ($-0.1 <$ [α/Fe] < 0.0) which are not covered by the models. All metallicity derivations lay

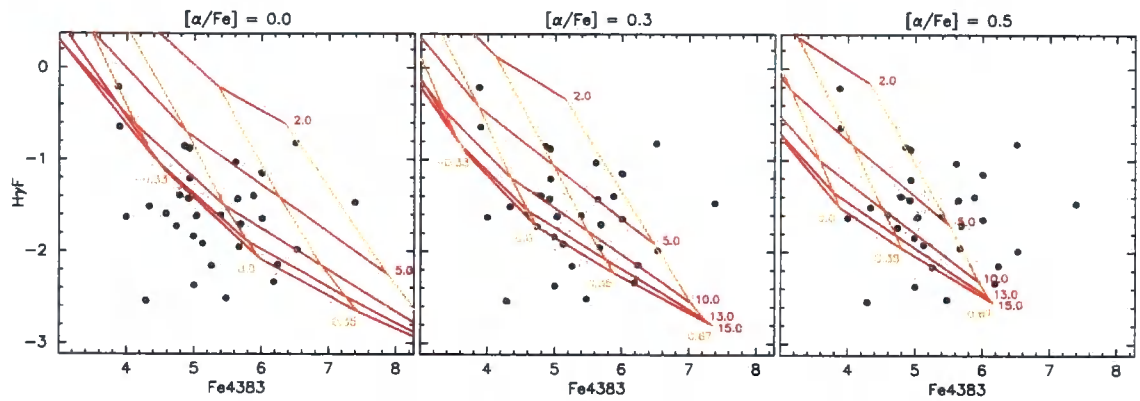

Figure 3.9: Index–index plot showing HγF versus Fe4383 for central r_e apertures (black) and all elliptical annuli (grey), overlaid by age–metallicity grids. Lines of constant age = 2, 5, 10, 13, 15 Gyr (red); lines of constant [Z/H] = –1.35, –0.33, 0.0, +0.35, +0.67 (orange). Each panel shows grids for a particular [α/Fe] = 0.0, +0.3, +0.5 (left-to-right)

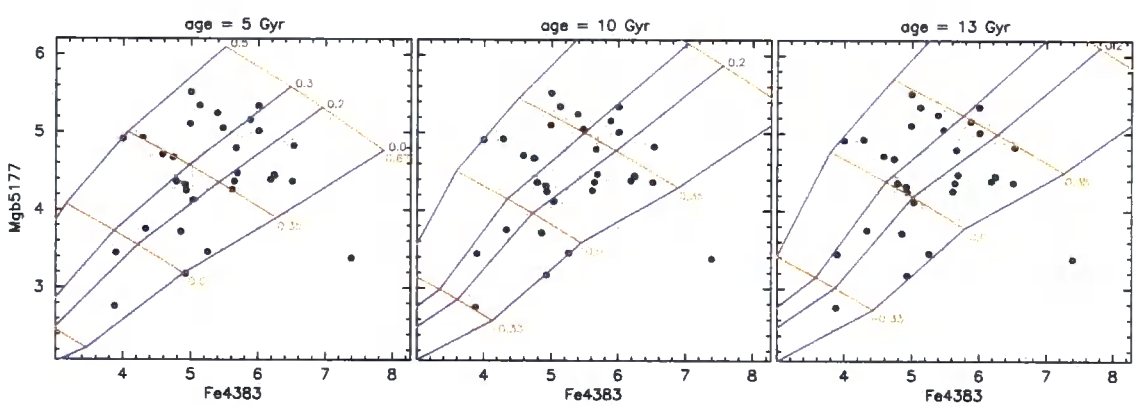

Figure 3.10: Index–index plot showing Mgb5177 versus Fe4383 for central r_e apertures (black) and all elliptical annuli (grey), overlaid by metallicity–α-abundance grids. Lines of constant [Z/H] = –1.35, –0.33, 0.0, +0.35, +0.67 (orange); lines of constant [α/Fe] = 0.0, +0.2, +0.3, +0.5 (purple). Each panel shows grids for a particular age = 5, 10, 13 Gyr (left-to-right).

Table 3.4: Average S/N Å^{-1} of each sample (A3389, Shapley) from the three studies (VIMOS 1 arcsec radius apertures, NFPS, AAΩ), calculated over the wavelength range $\Delta\lambda$.

Sample	Study	n_{gals}	$\langle$ S/N $\rangle$ Å^{-1}	$\Delta\lambda$ Å
A3389	VIMOS	12	37	4700 – 5000
	NFPS	10	60	5000 – 5500
Shapley	VIMOS	19	25	4700 – 5000
	NFPS	13	40	5000 – 5500
	AAΩ	19	100	4700 – 5000

within the grid boundaries.

As noted from the grids in Figures 3.9 and 3.10, each index has a response to all three parameters (the tilt with respect to the axes), so consequently, the errors are correlated. In order to propagate this correlation, full error ellipsoids are calculated from the χ^2 surface. (See Section 3.4.3 for further discussion on these errors.)

The VIMOS wavelength range covers twenty-three Lick indices, but not all of them are useful for the grid inversion. Several lines towards the red end of the spectrum ($\sim$ 5500 – 5600) are contaminated by sky features, so the set of those affected depends on the target redshift. Of the remaining indices, some merely duplicate the response of the same feature (e.g. HγF and HγA; Mg_2 and Mgb5177), while others disagree with the majority, degrading the fit quality (e.g. G4300). The chosen indices for each sample will be described in detail in Section 3.4.3.

3.4. IFU central spectroscopy

One attraction of IFU data is the versatility in possible approaches to the analysis. By extracting a spectrum from a circular aperture, it is trivial to mimic a single aperture spectrograph. Using the 1 arcsec radius apertures introduced in Section 3.3.1, the VIMOS data can be compared directly to results from two previous spectroscopic studies. We also use these central spectra to test the stability of the derived stellar populations. For reference, Table 3.4 lists the average S/N of each sample from the different studies.

3.4.1 Previous aperture spectroscopy

The NOAO Fundamental Plane Survey (NFPS; Smith et al., 2004) analysed 1.5–2 hour exposures from the Hydra multi-fibre spectrograph on the 4 m CTIO telescope. The spectral resolution was ~3 Å (FWHM) and the fibre diameter was 2 arcsec. NFPS spectroscopy is available for ten A3389 galaxies, while 13 of the Shapley galaxies are common to the VIMOS sample.

The second comparison is a deeper study by Smith et al. (2007), which employed 8 hour exposures with the AAΩ fibre-fed multi-object spectrograph on the 3.9 m Anglo-Australian Telescope. The spectral resolution was ~3.5 Å (FWHM) and the fibre diameter was again 2 arcsec. The 19 Shapley sample galaxies were all observed by AAΩ; Abell 3389 was not covered.

3.4.2 Comparing the central line strengths

Figure 3.11 compares the VIMOS line strength measurements (for Fe4383, Fe4668, Hβ and Mgb5177) to those from the studies introduced above. Agreement between the VIMOS and NFPS line strength values is generally very good, with a reduced χ^2 very close to 1 (after accounting for small mean offsets). The only exception is the Fe4383 line, which has a large offset between VIMOS and NFPS for the A3389 sample (reduced $\chi^2 \sim 4$), although the agreement is much better in the Shapley sample. Measurements of the Hβ lines agree well across all three instruments. Fe4668 and Mgb5177 exhibit comparatively large offsets between AAΩ and both other studies, with AAΩ tending to observe weaker lines.

For Fe4668, these is a ($> 5\sigma$) correlation between the VIMOS–AAΩ offset and the Fe4668 line strength (Figure 3.12, open black symbols/line - trend exclude the obvious outlier). The Fe4668 index is one of the most susceptible to errors in the continuum level, as it is a particularly broad feature. Exploring factors that could systematically affect the continuum level, we find no correlation between the offset and either airmass (see Figure 3.13) or position in the AAΩ multi-object spectrograph field.

Aperture 'smearing', the increase of the effective aperture size in co-added multi-object observations due to fibre placement or telescope pointing errors, may be able to explain the offset. The VIMOS data set can be used to replicate this behaviour by simply increasing the aperture size for the central measurements. The coloured symbols in Figure 3.12 displays the VIMOS line strengths for 1.2 (blue) and 1.5 (orange) arcsec aper-

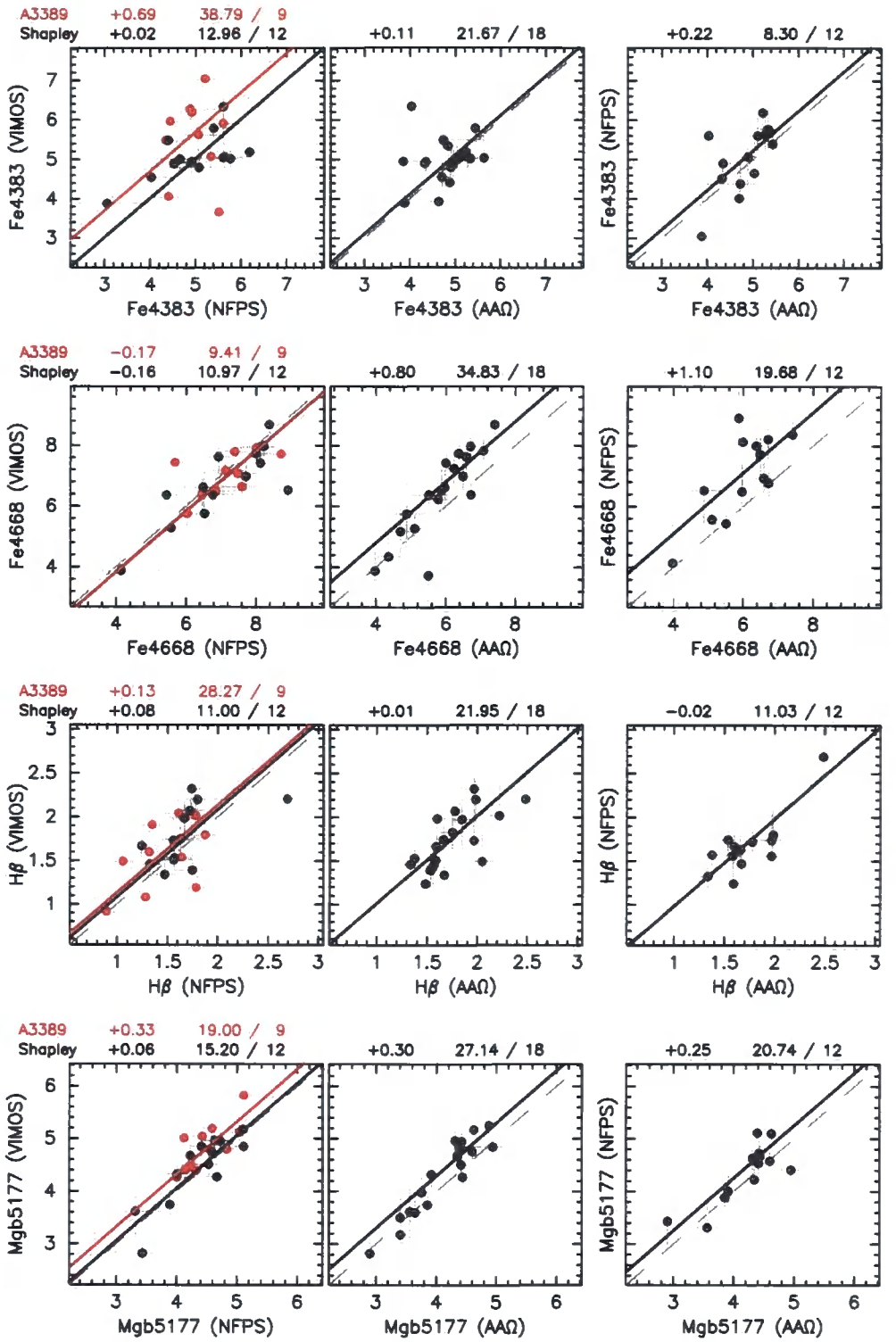

Figure 3.11: Comparison of VIMOS central spectroscopy to NFPS (left column) and AAΩ (central column). Plots of NFPS versus AAΩ index measurements for these objects are displayed in the right column. Red symbols (left column only) from A3389; black for Shapley. Dashed lines are equality; solid lines shows the median offset. The values above each panel show the median offset and the χ^2 / degrees of freedom (taking into account the offset).

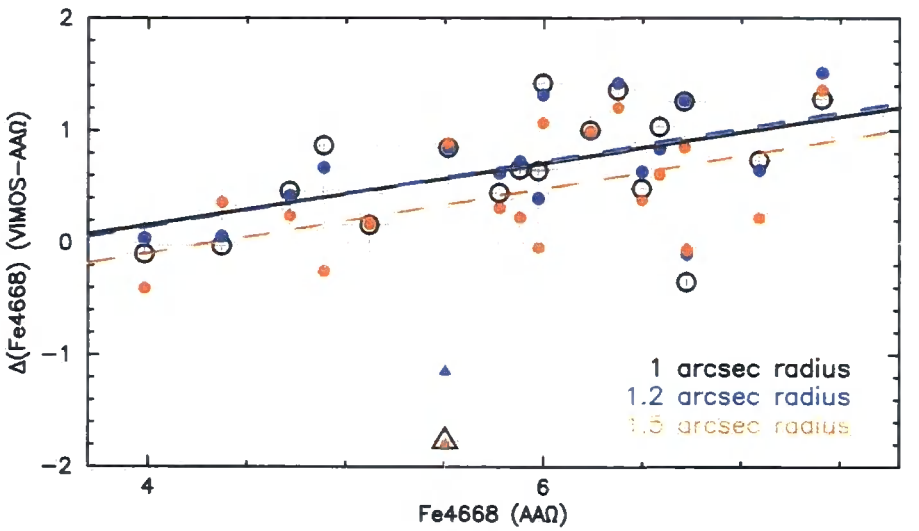

Figure 3.12: Offset between the Fe4668 line strength measured by VIMOS and AAΩ versus the equivalent width of the same line from AAΩ. Open black symbols are for the usual 1 arcsec radius apertures in VIMOS, while the closed symbols display values for 1.2 (blue) and 1.5 (orange) arcsec radius apertures. Best fits are shown, and exclude the obvious outlier MGP1211, indicated by triangles. For clarity, errors on the closed symbols are not plotted but are comparable to those on the open points.

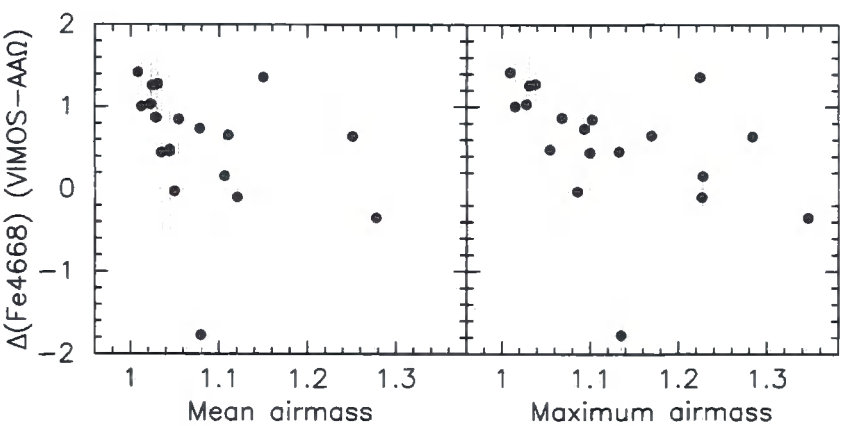

Figure 3.13: Offset between the Fe4668 line strength measured by VIMOS and AAΩ versus the mean airmass over all exposures (left panel) and the maximum airmass (right panel) of the VIMOS observations.

tures. The trend is still visible, indicating that 'smearing' is at least not the sole factor behind this effect. However, the VIMOS–AAΩ offset for several galaxies, including the outlier (MGP1211; shown by triangles), is significantly reduced by the use of an increased effective aperture, so it is likely 'aperture smearing' does affect the co-added fibre spectroscopy for some galaxies.

While the responsible factor has not been identified, the agreement between VIMOS and NFPS measurements, and the similar offsets of these from AAΩ, suggests that the problem may lie with the multi-object spectra from AAΩ.

3.4.3 Calculating the IFU central stellar populations

Central age, metallicity and α-element abundance were derived using the grid inversion technique described in Section 3.3.5. The total set of twenty-three Lick indices (displayed as a function of rest wavelength in the top panel of Figure 3.14), was whittled down to eight indices for the Abell 3389 and nine for Shapley. The heterogeneity of the two sets is due to the different cluster redshifts: the observed wavelength range varies and the sky features shift into the defined bands for different indices.

Analysis of the A3389 sample used eight indices (termed 'master' set 1): two Balmer lines (HγF, Hβ), five iron lines (Fe4383, Fe4531, Fe4668, Fe5270, Fe5335) and Mgb5177. Hδ is deemed too close to the blue cut-off, while HγA is considered redundant as it mostly duplicates the response of HγF. Fe4506 is contaminated by sky lines, while inclusion of the widely-used Fe5270 and Fe5335 is preferable to Fe5015 (which may be susceptible to low level [OIII]λ5007 emission) and the redder Fe indices. The central panel of Figure 3.14 shows an example A3389 galaxy spectrum (in the observed frame) with the chosen indices indicated.

Nine indices were used in the inversion for the Shapley galaxies ('master' set 2): three Balmer lines (HδF, HγF, Hβ), five iron lines (Fe4383, Fe4531, Fe4668, Fe5015, Fe5406) and Mgb5177. At the redshift of Shapely, Fe5270, Fe5335, Fe5709 and Fe5782 are all contaminated by sky features such as [OI] λ5577, necessitating the inclusion of Fe5015 and Fe5406. However, HδF is further from the blue cut-off, enabling its inclusion. The lower panel of Figure 3.14 indicates the chosen indices on an example Shapley galaxy spectrum (in the observed frame).

Inversion of these index sets, via the method described in 3.3.5, ensures a sensible modelling, with age primarily tracked by the Balmer lines and metallicity predomi-

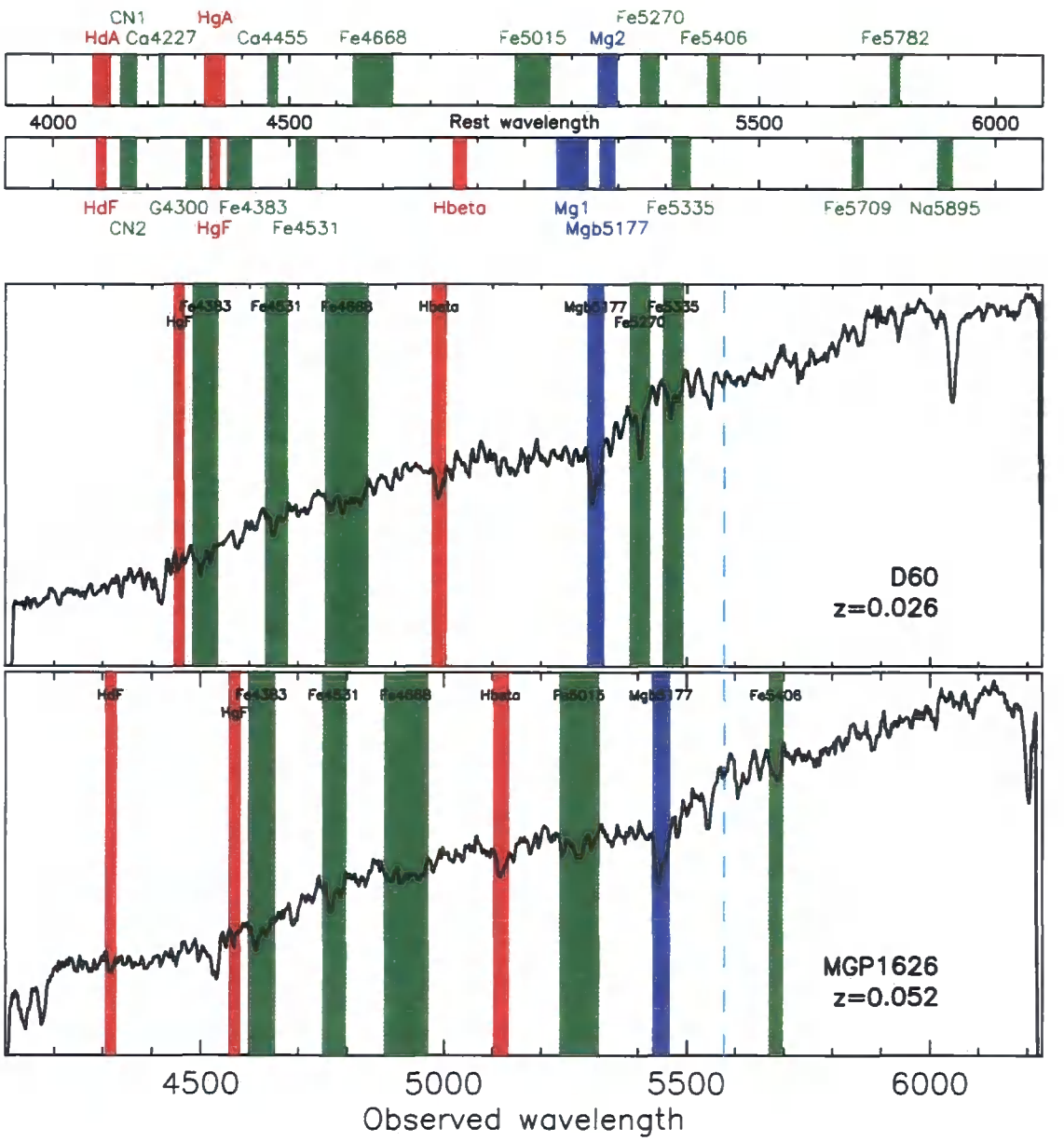

Figure 3.14: Upper panel: Lick absorption indices within the VIMOS HR blue grism wavelength range, displayed by rest wavelength (red = Balmer hydrogen lines; blue = magnesium lines; green = iron and miscellaneous lines).

Lower panels: chosen index sets for the A3389 and Shapley samples, plotted over an example spectrum (galaxy ID and redshift given), shown at the observed wavelength. Colours as above. Cyan dashed line indicates the position of the [OI] λ5577 sky line.

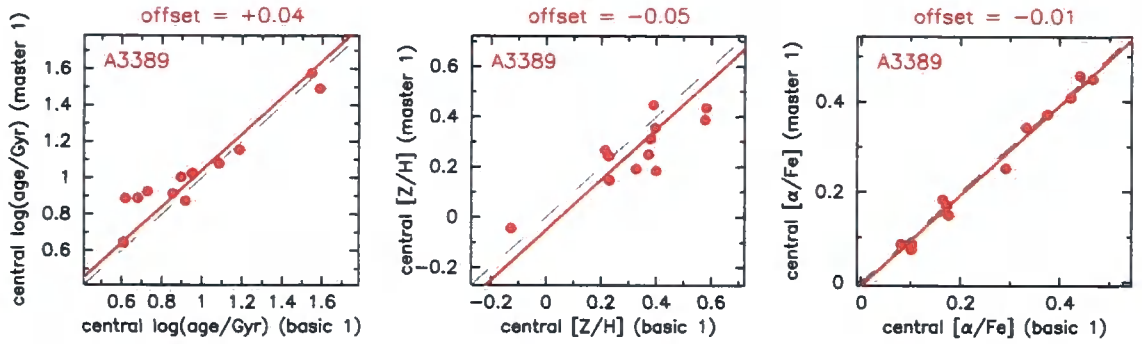

Figure 3.15: For the Abell 3389 galaxies, comparison between VIMOS spectroscopic central age (left panel), metallicity (centre panel) and α-abundance (right panel) derived using two different index sets: base 1 (HγF + Hβ + Fe4383 + Fe5270 + Fe5335 + Mgb5177; top line in Table 3.5); master 1 (basic 1 + Fe4531 + Fe4668; bold line in Table 3.5). Solid line shows the mean offset; dashed line is equality. The offset and χ^2 / degrees of freedom about the mean offset, are displayed above each panel.

nantly traced by iron lines. The only index used to indicate the α-element abundance is Mgb5177, so [α/Fe] closely resembles [Mg/Fe] (c.f. some studies also include lines such as CN_1, e.g. Nelan et al. 2005).

Stability of the stellar population estimates

To test the stability of the index grid inversion technique, we derive central stellar populations using several different sets of indices. The two VIMOS samples require different index sets due to the position of the sky features, so for the purposes of this test they

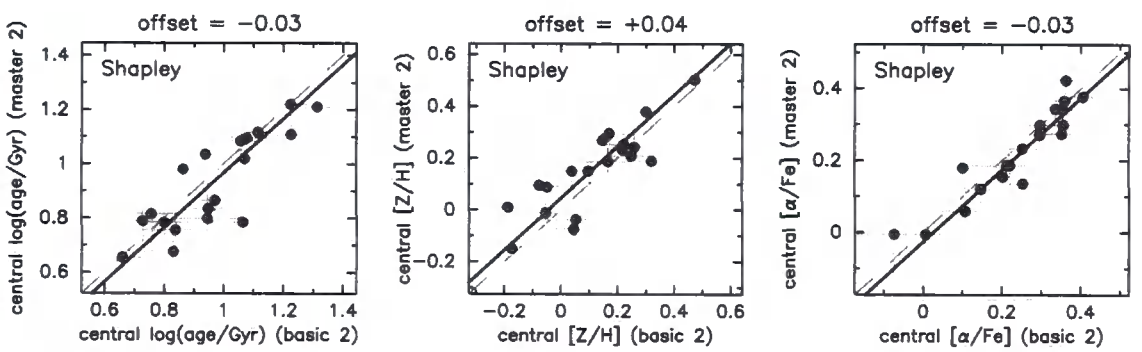

Figure 3.16: For the Shapley galaxies, comparison shown as in Figure 3.15, using two different index sets: base 2 (HγF + Hβ + Fe4383 + Fe5015 + Mgb5177; top line in Table 3.6); master 2 (basic 2 + HδF + Fe4531 + Fe4668 + Fe5406; bold line in Table 3.6).

Table 3.5: Mean values of the central age, metallicity [Z/H] and α-element abundance [α/Fe] for the A3389 sample, derived using different index sets in the model inversion.

Index set	log(age/Gyr)	[Z/H]	[α/Fe]
HγF + Hβ + Fe4383 + Fe5270 + Fe5335 + Mgb (*base 1*)	0.97 ± 0.10	0.33 ± 0.05	0.26 ± 0.04
base 1 + Fe4531	0.99 ± 0.09	0.30 ± 0.06	0.26 ± 0.04
base 1 + Fe4668	1.03 ± 0.08	0.27 ± 0.04	0.25 ± 0.04
***base 1* + Fe4531 + Fe4668** (*master 2*)	1.04 ± 0.08	0.26 ± 0.04	0.25 ± 0.04
base 1 + Fe4531 + Fe4668 + HδF	1.00 ± 0.08	0.28 ± 0.04	0.27 ± 0.04

Table 3.6: Mean values of the central age, metallicity [Z/H] and α-element abundance [α/Fe] for the Shapley sample, derived using different index sets in the model inversion. The mean central stellar population parameters derived from AAΩ observations of the same 19 galaxies are displayed in the final row for comparison.

Index set	log(age/Gyr)	[Z/H]	[α/Fe]
HγF + Hβ + Fe4383 + Fe5015 + Mgb (*base 2*)	0.97 ± 0.04	0.12 ± 0.04	0.24 ± 0.03
base 2 + Fe4531	0.97 ± 0.04	0.12 ± 0.04	0.24 ± 0.03
base 2 + Fe5406	0.94 ± 0.04	0.14 ± 0.04	0.23 ± 0.03
base 2 + Fe4668	0.95 ± 0.04	0.14 ± 0.04	0.24 ± 0.03
base 2 + HδF	0.97 ± 0.04	0.11 ± 0.04	0.24 ± 0.03
base 2 + Fe4531 + Fe5406	0.95 ± 0.04	0.14 ± 0.04	0.22 ± 0.03
base 2 + Fe4531 + Fe4668	0.95 ± 0.04	0.15 ± 0.04	0.24 ± 0.03
base 2 + Fe4668 + Fe5406	0.94 ± 0.04	0.15 ± 0.04	0.23 ± 0.03
base 2 + HδF + Fe4531 + Fe5406	0.93 ± 0.04	0.15 ± 0.04	0.22 ± 0.03
base 2 + HδF + Fe4531 + Fe4668	0.94 ± 0.04	0.14 ± 0.04	0.23 ± 0.03
base 2 + HδF + Fe4668 + Fe5406	0.93 ± 0.04	0.16 ± 0.04	0.22 ± 0.03
base 2 + Fe4531 + Fe4668 + Fe5406	0.94 ± 0.04	0.16 ± 0.04	0.22 ± 0.03
***base 2* + HδF + Fe4531 + Fe4668 + Fe5406** (*master 2*)	0.93 ± 0.04	0.16 ± 0.04	0.22 ± 0.03
AAΩ [Shapley targets] *base 2* + HδF	0.96 ± 0.04	0.10 ± 0.03	0.24 ± 0.03

have been segregated. Starting from a basic set of indices for each sample (base 1: HγF, Hβ, Fe4383, Fe5270, Fe5335, Mgb5177; base 2: HγF, Hβ, Fe4383, Fe5015, Mgb5177), various sets were created by adding combinations of the other lines in the 'master' lists. Table 3.5 shows the mean derived age, metallicity and α-abundance for the 12 galaxies in the A3389 sample, using the listed index set in the inversion. Table 3.6 presents similar information for the Shapley galaxies.

The mean stellar populations of the samples are robust with respect to the different index sets. For both samples, the mean age varies by less than 5 per cent, and the mean metallicity and α-abundance generally deviate by only 0.05 dex and 0.02 dex respectively. The mean central parameters of the same Shapley galaxies derived from AAΩ spectroscopy (final row, Table 3.6) are well matched to the VIMOS values. Individually, the derived central stellar populations of galaxies are also independent of the index set used. Figures 3.15 and 3.16 compare values computed from grid inversions using the basic and master sets, for the A3389 and Shapley samples respectively.

Comparison of central stellar populations to AAΩ

The remainder of this study uses the 'master' sets of indices (bold rows in Tables 3.5 and 3.6) to calculate the stellar population parameters. For the Shapley sample, Figure 3.17 compares the central values of age, metallicity and α-abundance derived from VIMOS to the equivalent values from the AAΩ spectroscopy. Although the mean value for each parameter is well matched between observations, the reduced χ^2 is ~ 4 for age and [α/Fe], and ~ 6 for metallicity. It appears that the formal errors propagated through the index inversion are underestimated by a factor of 2–2.5. Errors on the indices themselves are well determined, as noted in Section 3.4.2 (Figure 3.11). Consequently, in the following sections, we quote the uncertainty on stellar population parameters as derived from Monte Carlo simulations of the **index values**, rather than using the error ellipsoids from the χ^2 surface calculated during the grid inversion.

3.4.4 r_e/3 aperture central spectroscopy

The previous few sections have concentrated on spectra from 1 arcsec radius apertures, to facilitate comparison with fixed aperture spectroscopy. In the remainder of this study (including Chapter 4), we will use spectra from $r_e/3$ apertures for the central parameters. Apertures which scale with the galaxy effective radius, provide a better parametrization

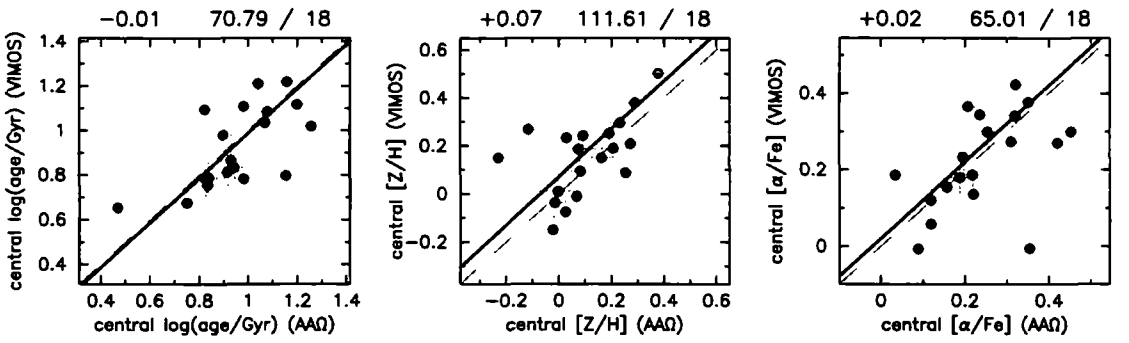

Figure 3.17: Comparison between derived stellar population parameters from VIMOS (using master index set) and AAΩ. Layout as in Figure 3.15. The distributions and mean values in each parameter are well matched between the two observations, although the errors appear slightly underestimated, particularly in [Z/H].

of the physical galaxy centre, and allow for comparisons between galaxies. For a galaxy with an r_e of 3 arcsec (roughly the mean of our sample), the two apertures are, of course, identical.

The distributions of the central stellar populations, from $r_e/3$ apertures, are presented in Figure 3.18. The distributions of central parameters in each of the two VIMOS samples are similar. Appendix A lists the central values for all galaxies.

3.5. Gradients

The internal gradients of a galaxy are calculated from all of the elliptical bins (described in Section 3.3.2) within the effective radius (r_e). Six of the galaxies (D53 from Abell 3389 and MGP0129, MGP1211, MGP2146, MGP2399, MGP4258 in Shapley) have S/N < 18 Å^{-1} at r_e, due to their lower surface brightness. These galaxies are excluded from further analysis as the quality of the spectra is insufficient to compute reliable gradients. Twenty-five galaxies remain: 11 in A3389, 14 from Shapley.

3.5.1 Line strength gradients

Line strength gradients were measured using an unweighted linear least-squares fit to all the bins within r_e, such that ∇I = ΔI / Δlog(r/r_e), where I is any absorption line index. Most previous studies of radial trends have used the log(r/r_e) convention, resulting in straight forward comparisons. A small fraction of galaxies would be better fit in linear

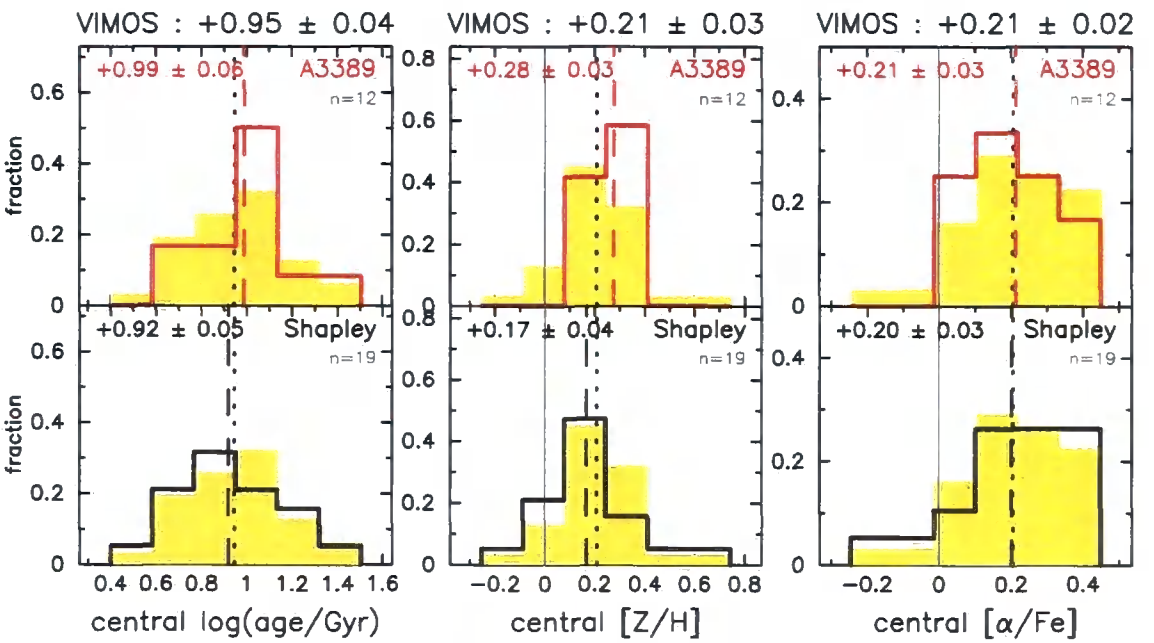

Figure 3.18: Histograms showing the fractional distribution of central values of (left-to-right) log(age/Gyr), [Z/H] and [α/Fe], for Abell 3389 (upper) and Shapley (lower). Mean gradients are marked by a dashed line, and are shown in the top–left of each panel. Background shaded histograms are for the combined VIMOS distributions, with the mean gradient represented by a dotted line, and shown above each column of panels.

radial space; a weighted fit to these in $\log(r/r_e)$ would bias the overall gradient towards the radial trend of the inner region, where the index values are better determined. The unweighted fit ensures a meaningful parametrization of the average gradient out to r_e in all galaxies. The radial position of each bin was assumed to be the centre in linear space: weighting by luminosity would not alter the radial positions significantly, and is not obviously more desirable considering the Balmer-weighted age response. For the A3389 galaxy, D60, Figure 3.19 shows the measured line strengths for individual bins, and presents the gradients. Similar plots for all galaxies are shown in Appendix B.

Generally, the metal lines show negative gradients, i.e. weaker lines at larger radii, while the Balmer lines have small positive gradients (Figure 3.20). The gradients do not exhibit simple trends with the central velocity dispersion, although the exclusion of most of the small galaxies, due to low surface brightness, results in a poor sampling of the low mass end ($\log\sigma < 2.2$). For reference, the central velocity dispersion of the six excluded galaxies are marked in Figure 3.20 by the open points above each column of panels.

3.5.2 Stellar population gradients

For each of the 25 galaxies with measured gradients, the linear fits described above were extrapolated to estimate the index values at $r = 0.1\times r_e$ and $r = r_e$. The corresponding stellar population for these two points was derived using the grid inversion technique described in Sections 3.3.5 and 3.4.3 (and the 'master' sets of indices). Finally, gradients in age, metallicity [Z/H] and α-element enhancement [α/Fe] were calculated from the difference between these inner and outer points.

An alternate method (used in my original Rawle et al. 2008b paper) computes stellar population parameters for each annulus, deriving gradients in a similar manner as for the line strengths. To test the sensitivity of the results to the choice of technique, Monte Carlo simulations were computed for the measured line strengths (based on the INDEXF errors), and stellar population gradients were derived for each galaxy using both methods. The new method proved to be more stable, relying on 2–3 times fewer model inversions and not requiring a linear fit to noisy stellar population values. The average simulated gradient for each parameter is method-independent. Errors quoted for the stellar population gradients are computed from these Monte Carlo simulations.

As a continuation of Figure 3.19, Figure 3.21 shows the stellar population gradients for D60, computed by the new method (in red) and by the alternate method (in black).

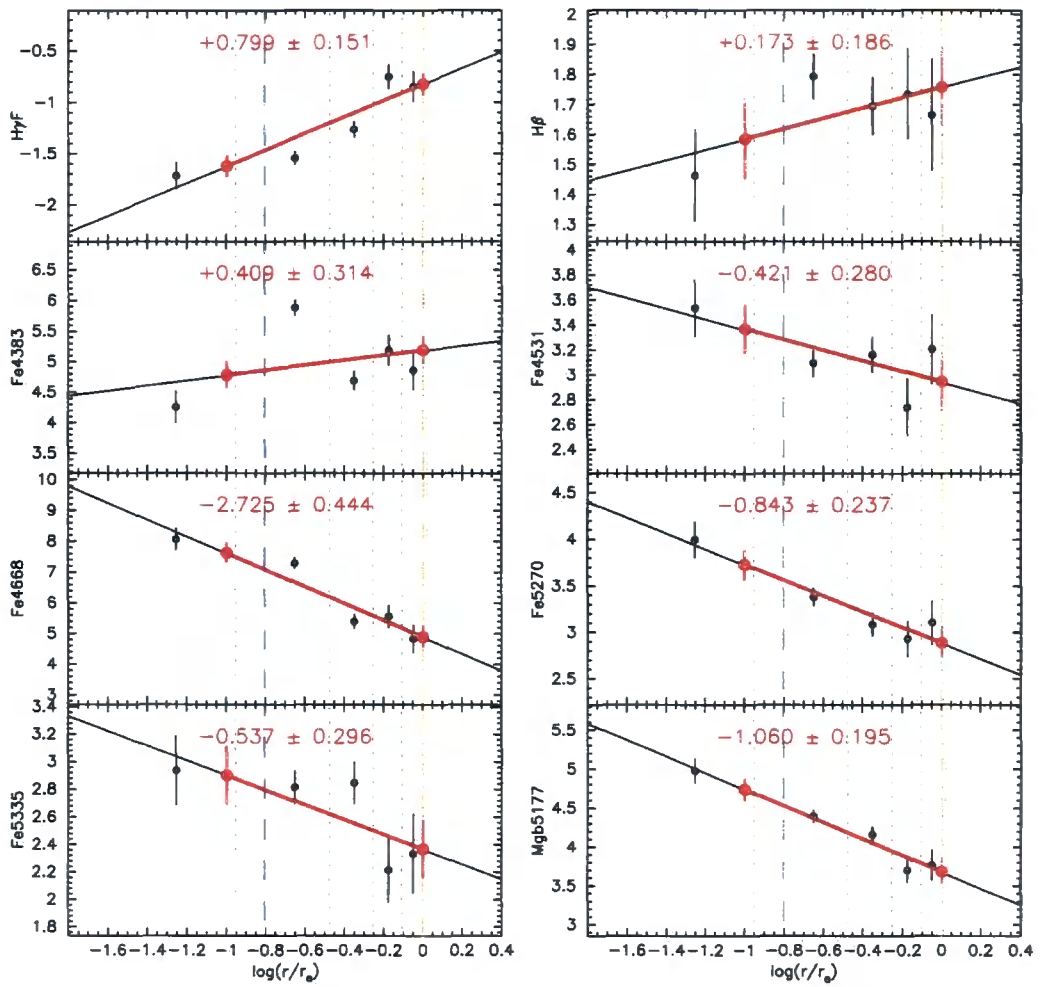

Figure 3.19: Line strength gradients for D60 (for HγF, Hβ, Fe4383, Fe4531, Fe4668, Fe5270, Fe5335, Mgb5177). Black points show index measurements for each radial bin (boundaries marked by grey dotted lines) and the black line is the unweighted linear fit to points within r_e (orange dashed line). The gradient is recorded at the top of each panel. Red points (joined by a line) show the estimated index values at $0.1 \times r_e$ and r_e, used to derive the stellar population gradient (see Section 3.5.2 and Figure 3.21). The blue dashed line shows the approximate PSF radius (= $\mathrm{PSF}_{\mathrm{FWHM}}/2.355$). Similar plots for all galaxies are shown in Appendix B.

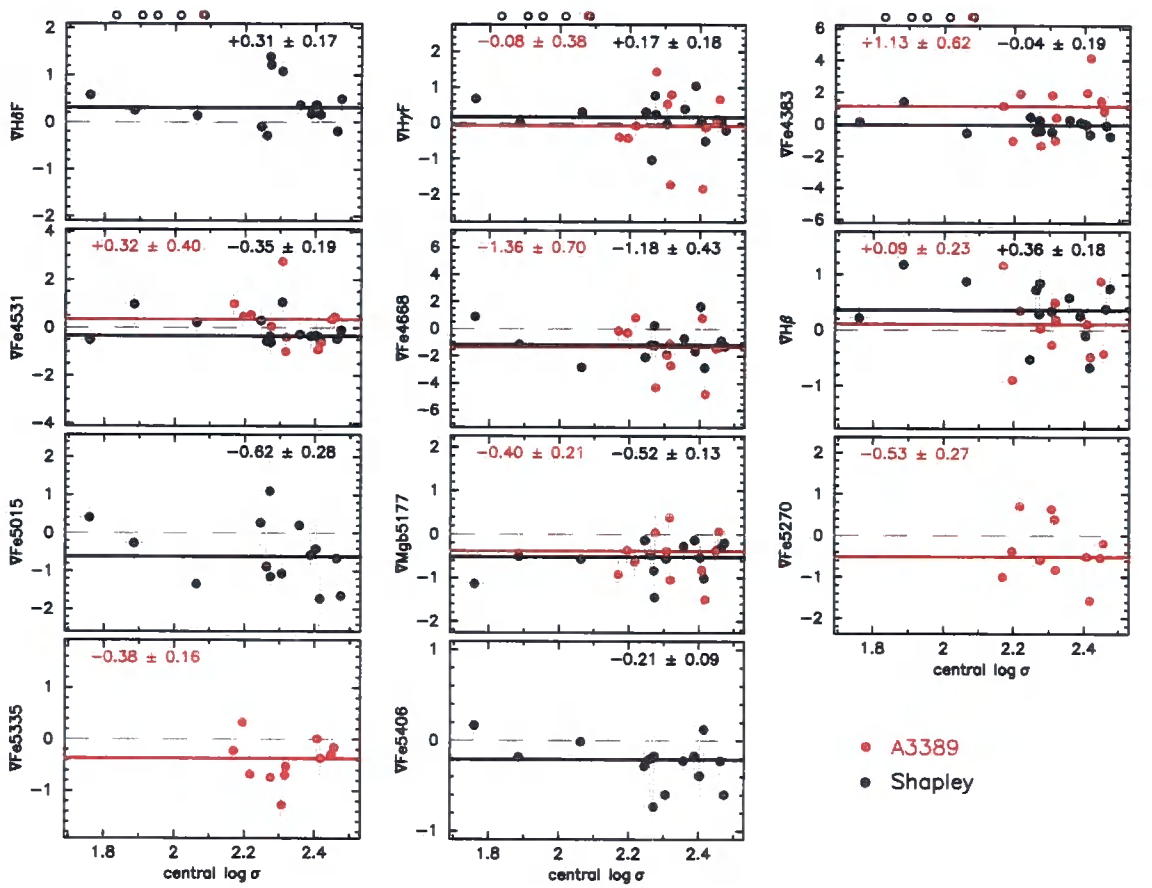

Figure 3.20: Absorption line strength gradients versus central log σ ($r_e/3$ radius aperture) for indices used in the respective 'master' sets. Red = A3389; black = Shapley. The solid lines in each colour represents the median gradients (also displayed at the top of each panel); dashed line indicates zero gradient. The central velocity dispersion of the six galaxies not analysed for gradients are indicated by open points above each column of panels.

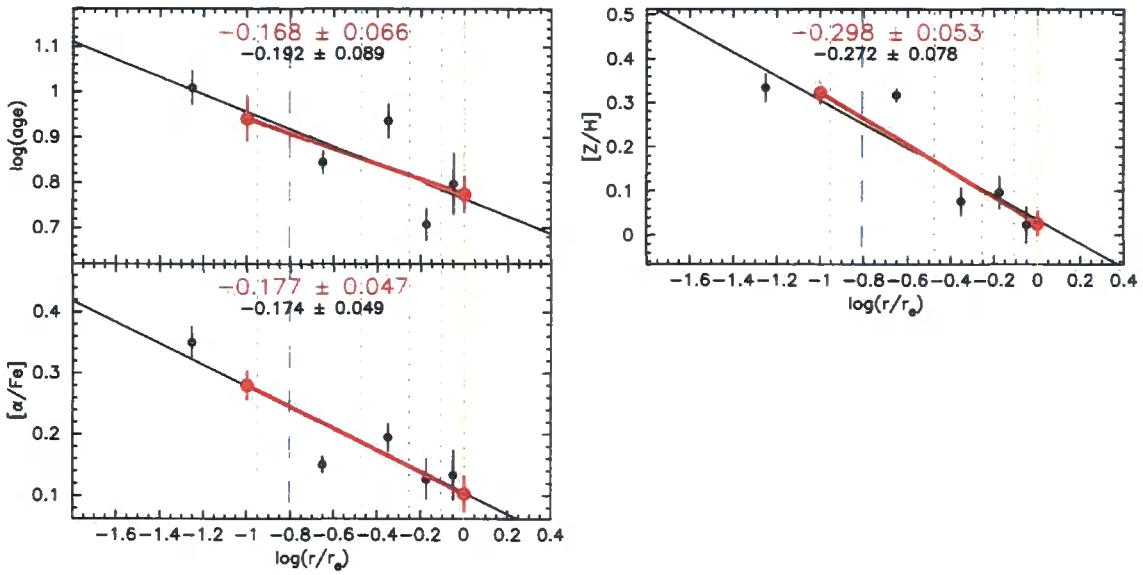

Figure 3.21: Example stellar population gradients for D60 (age, total metallicity and α-element over-abundance). The red points show the derived stellar population for the inner and outer points, and the resulting gradient is recorded at the top of each panel (in red). For comparison, the black points show the alternate method – stellar populations for each radial bin, and the black line is the unweighted linear fit within r_e (orange dashed line). This gradient is also shown at the top of each panel (in black). Blue dashed line shows the approximate seeing disc radius. Similar plots for all galaxies are shown in Appendix B.

The similarity in the computed gradients from the two method is obvious. The same plots for all galaxies are shown in Appendix B, which also tabulates the derived stellar population gradients for each galaxy.

The point spread function (PSF) of the observations, may lead to an underestimation of the gradients in the smallest galaxies, as the central light is smoothed into neighbouring bins. To quantify the effect, a two dimensional model of luminosity weighted metallicity was constructed with a simple $r^{1/4}$ profile and a known gradient. Different seeing conditions were simulated by smoothing the model using a Gaussian filter with widths in the range of the measured PSFs (mean FWHM = 0.85 arcsec; maximum FWHM = 1.2 arcsec). For each smoothed model, the 'observed' gradients were derived from radial bins similar to those used for the real data. The results are shown in Figure 3.22, in terms of the error in ∇[Z/H] for a given ratio PSF σ / r_e (FWHM = 2.355 σ). In the worst observed case, with a PSF $\sigma = 0.34 \times r_e$ (i.e. a 2.34 arcsec galaxy observed in 0.93 arcsec

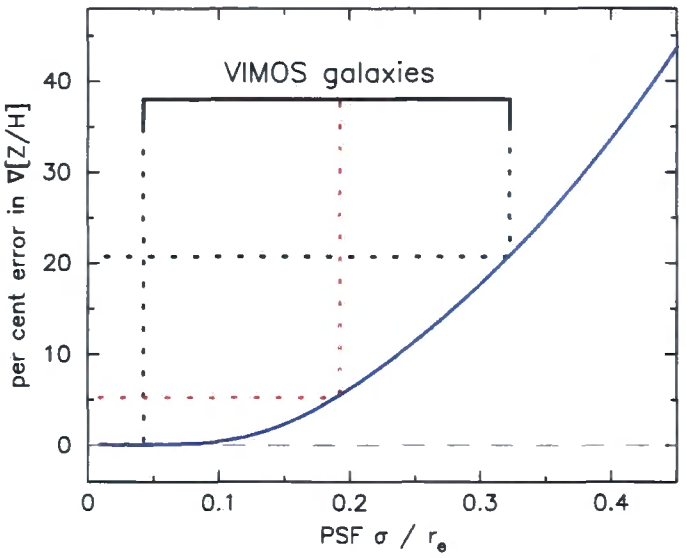

Figure 3.22: Using a simple model to estimate the change in observed luminosity-weighted metallicity gradient with increasing PSF (in terms of PSF σ as a fraction of r_e; blue line). The PSF σ / r_e range for the VIMOS observations is shown by the brace; black dotted lines indicate the extremes, red dotted line the mean. The mean fractional systematic error from the PSF effect is $\sim$ 5 per cent.

FWHM seeing; MGP1440), the measured gradient was flatter than the actual gradient by $\sim$ 20 per cent. For the majority of galaxies, the effect is estimated to be at the 5 – 10 per cent level, so no corrections have been applied.

Figure 3.23 presents the distributions of the stellar population gradients for the 25 VIMOS galaxies. On average, the galaxies exhibit negative gradients in age, [Z/H] and [α/Fe]. The mean age gradient is –0.02 $\pm$ 0.06, although 40 per cent of galaxies have an age gradient not consistent with zero ($> 2\sigma$) in both positive and negative orientations. There is a significant mean negative metallicity gradient $\langle\nabla$[Z/H]$\rangle$ = –0.13 $\pm$ 0.04, and no galaxies have a significant positive ∇[Z/H]. There is also a marginal negative mean gradient in the α-element abundance $\langle\nabla$[α/Fe]$\rangle$ = –0.10 $\pm$ 0.04. We compare these gradients to those calculated in previous works in Chapter 4.

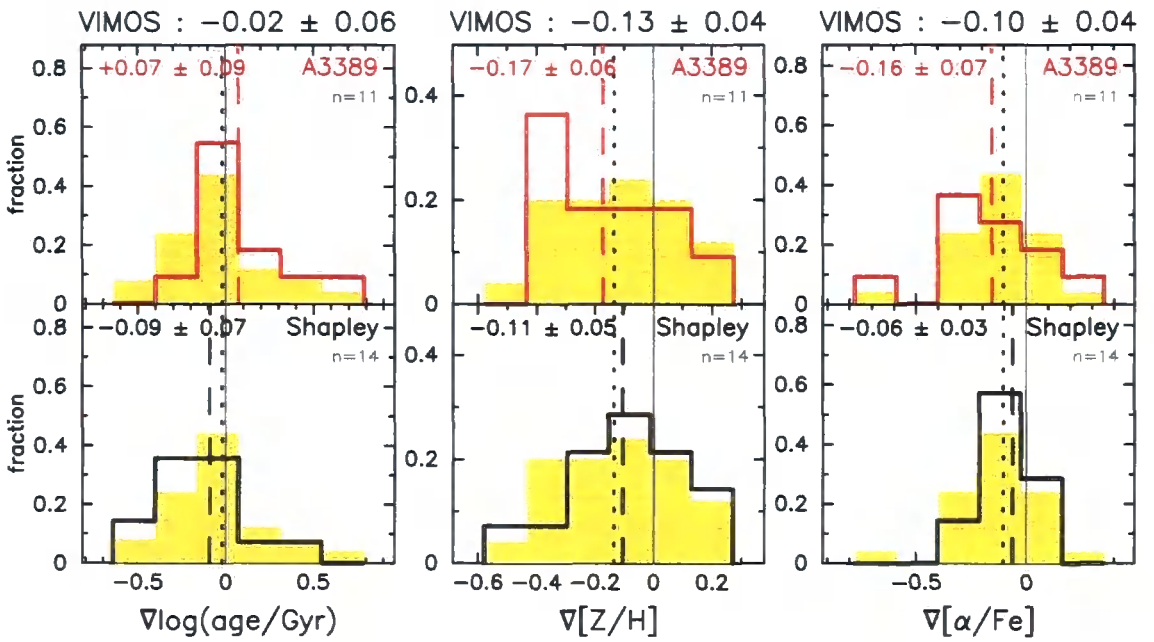

Figure 3.23: Histograms showing the fractional distribution of gradients in (left-to-right) log(age/Gyr), [Z/H] and [α/Fe], for Abell 3389 (upper) and Shapley (lower). Mean gradients are marked by a dashed line, and are shown in the top–left of each panel. Background shaded histograms are for the combined VIMOS distributions, with the mean gradient represented by a dotted line, and shown above each column of panels.

3.6. Conclusions

The internal gradients of early-type galaxies offer a valuable insight into their star formation histories and chemical evolution. Using the VLT integral field unit, VIMOS, we observed 25 galaxies in two separate local cluster environments: Abell 3389 and the Shapley Supercluster core. This chapter described the procedure for deriving individual radial trends in the stellar populations (to the effective radius) from raw observations. To summarise, data from individual spatial elements were binned in order to produce spectra from a series of elliptical annuli, effectively compressing the datacube down to a single dimension (eccentricity-corrected radius). Multiple optical absorption line indices were measured for each spectra, from which the gradients were computed. Line strength measurements were compared to stellar evolution models, via a grid inversion technique, enabling us to derive radial trends in luminosity-weighted age, total metallicity and α-element over-abundance.

We find a significant average metallicity gradient of -0.13 ± 0.04, and no galaxies with significant positive metallicity gradients. Mean negative gradients in age and α-element abundance were of marginal significance (-0.02 ± 0.06 and -0.10 ± 0.04 respectively). However, 40 per cent of galaxies do have an age gradient not consistent with zero.

In the next chapter, we explore the relationship between a galaxy's central properties and the stellar population gradients. From our results, we form a simple physical explanation of the observed gradients.

Chapter 4

Stellar population gradients in early-type cluster galaxies

This chapter presents results from a VLT VIMOS study of internal gradients in early-type galaxies. The previous chapter described the galaxy sample, observation and analysis of the integral field unit data, culminating in the derivation of stellar population gradients for 25 galaxies in two local cluster environments (Abell 3389 and the Shapley Supercluster core). Here, we explore these gradients in detail, investigate possible trends in the parameters, and discuss their implications for our understanding of galaxy evolution. This work was presented in Rawle et al. (2008b) and Rawle et al. (2009).

4.1. Introduction

The first studies into the radial variance of spectral features in galaxies, used narrow-band filters tuned to the wavelength of lines such as Mg, Na and CN (e.g. Spinrad, Smith, & Taylor, 1972; Burstein, 1979). These provided evidence for the existence of gradients in the strong absorption features, and suggested that galaxies become less metal rich with increasing radius. However, early works included only a handful of the nearest galaxies, and were limited to measuring gradients in relatively central regions.

In a ground-breaking paper, Gorgas, Efstathiou, & Aragon Salamanca (1990) studied absorption line gradients in a sizeable sample (n = 15) of early-type galaxies. Importantly, their spectroscopy was deep enough to measure gradients much further out (to approximately the half-light radius; r_e). The study identified evidence for possible relations

between the Mg_2 line strength gradient and both central velocity dispersion and central index value. The authors also concluded that typically, elliptical galaxies have roughly solar metallicity at r_e, although the scatter in line strength values suggests a wide range in star formation histories. Fisher, Franx, & Illingworth (1996) found comparable trends in the gradients of S0 galaxies, indicating an approximately similar recent formation histories, and Carter, Bridges, & Hau (1999) observed the same negative Mg_2 gradients in three brightest cluster galaxies.

In the last ten years, several studies have further investigated the radial trends in early-type galaxies. Improvements in the instrument throughput and telescope size have led to long slit observations out to, and beyond, the effective radius for a much larger sample of galaxies (e.g. Mehlert et al. 2003; Sánchez-Blázquez, Gorgas, & Cardiel 2006). Increased wavelength coverage has allowed for a detailed investigation of the stellar population gradients (e.g. 19 indices measured in Sánchez-Blázquez et al., 2007). These studies have generally confirmed the existence of metallicity gradients, and its correlation with central parameters, such as metallicity. Several studies have focussed on the relation between metallicity gradient and galaxy mass, as conflicting evidence for its existence arose (e.g. Carollo, Danziger, & Buson, 1993; Kobayashi & Arimoto, 1999; Forbes, Sánchez-Blázquez, & Proctor, 2005). Recent observations of low-mass galaxies (Spolaor et al., 2009) indicate that the correlation (stronger gradients with increasing mass) is itself dependent on galaxy mass, with the smallest galaxies showing the tightest trend.

The Spectroscopic Areal Unit for Research on Optical Nebulae (SAURON; Bacon et al. 2001) has offered a glimpse of the power of an IFU in studying internal galaxy gradients. The main study of 24 cluster early-type galaxies (de Zeeuw et al., 2002) has so far concentrating on kinematics (Sarzi et al., 2006; Emsellem et al., 2007), or qualitative analysis of line strength maps – Kuntschner et al. (2006) showed that while the spatial maps of Hβ imply that early-type galaxies typically exhibit no radial trend in age, the Fe5015 map indicates that metallicity gradients are generally negative. Weijmans et al. (2009) used multiple deep SAURON pointings of two nearby galaxies (NGC3379 and NGC821; cz = 1000, 2500 km s^{-1} respectively), to measure line strength gradients to $\sim 4\ r_e$. They found that the observed radial trends to r_e, remain constant out to at least 4 r_e.

This chapter begins by summarising the gradients derived in Chapter 3 (Section 4.2). We then concentrate, in turn, on discussing the ∇[Z/H]–log σ relation (Section 4.3), the gradient–central parameter trends (Section 4.4) and the correlation between age and metal-

licity gradients (Section 4.5). In Section 4.6, we explore the colour gradients, comparing predictions made from the spectroscopic age and metallicity to observations from imaging. Section 4.7 draws together our findings to suggests a physical implication for galaxy formation, while Section 4.8 summarises the results from this chapter.

4.2. The VIMOS results

Chapter 3 described the technique for deriving stellar population gradients from the integral field unit (IFU) datacubes. In addition to the gradients, central stellar populations were calculated within an r_e aperture. First, we explore the relationship between these central characteristics (particularly velocity dispersion, age and metallicity), and compare to the results from large spectroscopic surveys (Section 4.2.1). We then summarise the simple trends in the gradients (Section 4.2.2), and introduce two published long-slit studies (Section 4.2.3) used for comparison in subsequent sections.

4.2.1 Central characteristics

Central spectra for each of the 31 early-type galaxies observed with VIMOS were extracted from r_e apertures, as described in Section 3.4.4. Here, we compare the trends in these parameters to results from large studies of central spectroscopy. Of particular interest are the relations between the central age, metallicity and velocity dispersion (which is a tracer of the dynamic mass of the galaxy).

Correlations with velocity dispersion

For the VIMOS sample, we find that the central stellar population parameters (age, total metallicity and α-element over-abundance) are all significantly ($> 3\,\sigma$) correlated with the central velocity dispersion (Figure 4.1). To validate the VIMOS spectroscopy and analysis technique we compare the results to four large spectroscopic surveys: Nelan et al. 2005; Thomas et al. 2005; Graves et al. 2007; Smith et al. 2009a.

Nelan et al. (2005) studied X-ray selected local cluster galaxies using a fibre spectrograph, while Thomas et al. (2005) drew their sample from various sources (and instruments), including galaxies from dense local groups and clusters (Virgo, Coma) as well as low density environments. Graves et al. (2007) analysed ~22 500 passive galaxies in the redshift range $0.06 < z < 0.08$, using SDSS fibre spectroscopy. Finally, Smith et al. (2009a)

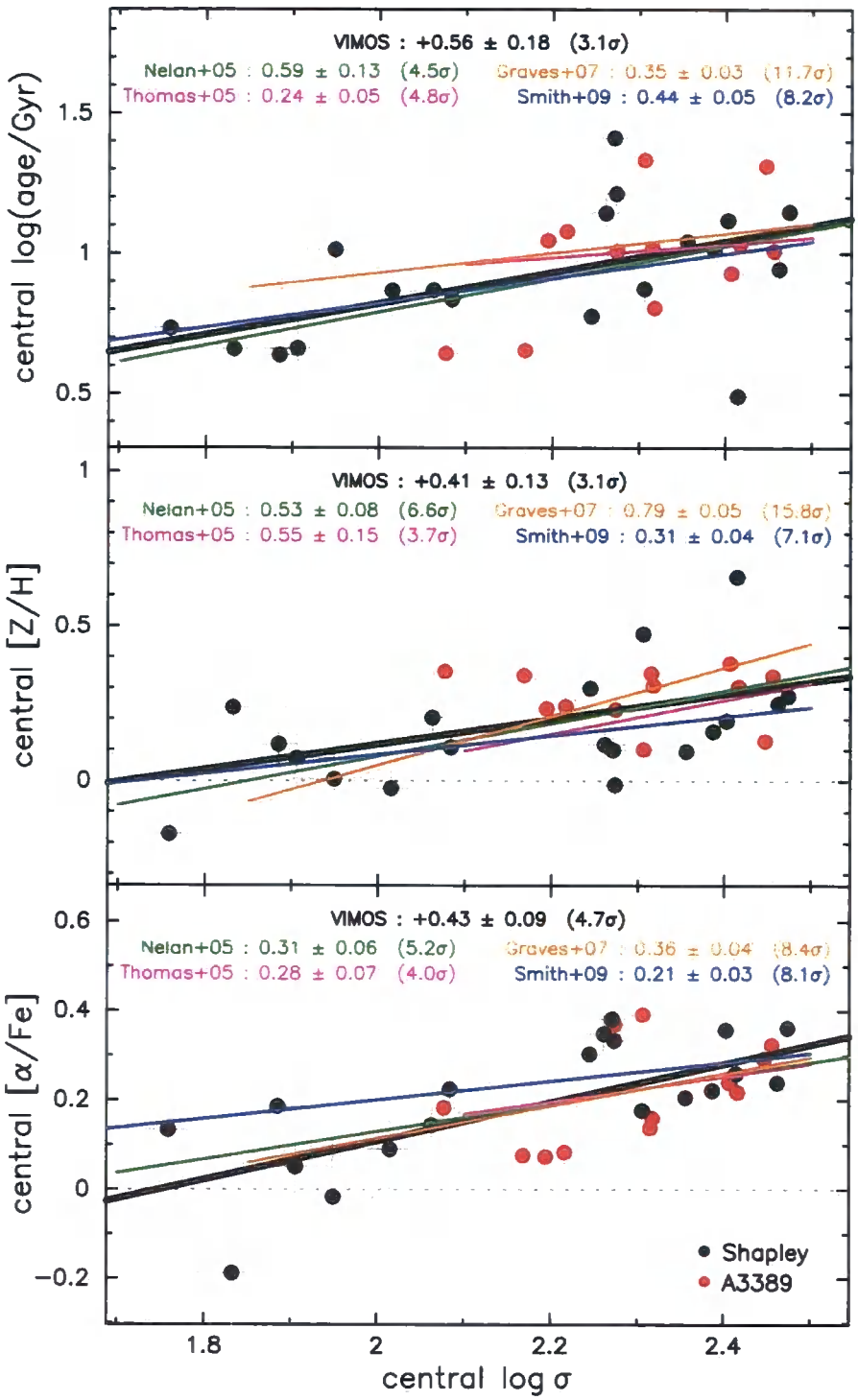

Figure 4.1: Central age (uppermost panel), metallicity (centre) and α-abundance (lowest) versus central velocity dispersion ($\log \sigma$). Panels present the VIMOS data (Shapley = black; A3389 = red) and bet fit slope (black line). The relations reported by four large spectroscopic studies are also displayed (green=Nelan et al. 2005; magenta=Thomas et al. 2005; orange=Graves et al. 2007; blue=Smith et al. 2009a), with the line length indicating the σ range in each case. The relations are very similar to the VIMOS slopes.

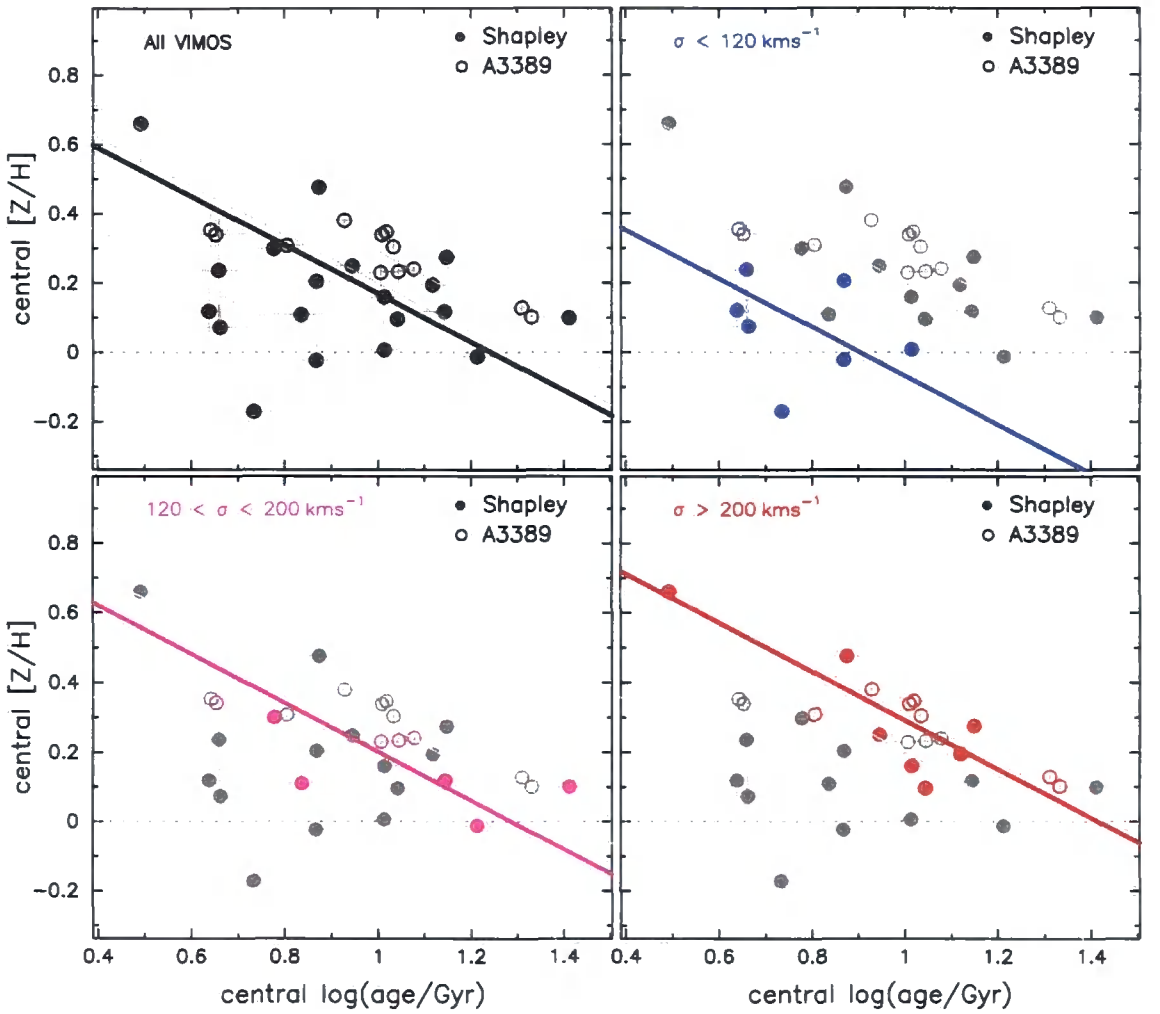

Figure 4.2: Central age versus central metallicity for the VIMOS sample. Upper left panel presents the whole VIMOS sample (A3389 = open symbols; Shapley = closed symbols). The best fit line (with fixed slope = –0.7 from Jørgensen 1999) is shown in black. Other panels highlight galaxies in coarse velocity dispersion bins, with the best fit line (with fixed slope) shown in colour (in ascending σ: blue, magenta, red). For comparison, other galaxies and best fit lines are shown in grey. The plots demonstrate the sigma dependence of the age–metallicity relation. Without fixing the slope to –0.7, the whole sample is best fit by -0.23 ± 0.13, due to the under-sampling of old, low-mass galaxies. The individual σ bins (in order of increasing σ) have slopes of –0.45, –0.34, –0.61.

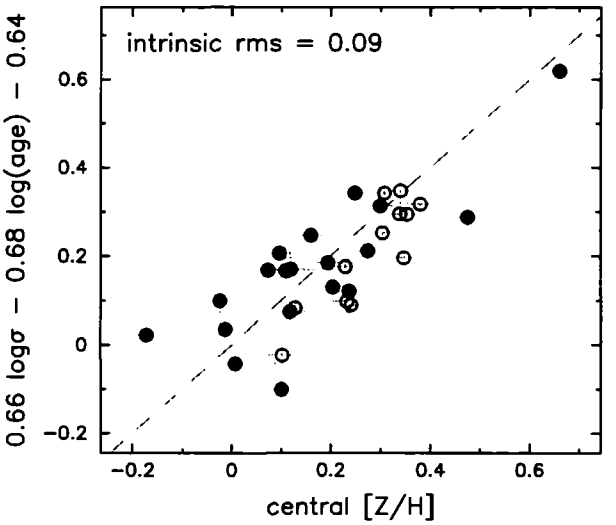

Figure 4.3: VIMOS sample in the edge-on view of the central 'Z-plane': A3389 = open symbols, Shapley = closed symbols. 'Z-plane' fit from Smith et al. (in prep.). The intrinsic rms scatter in the [Z/H] is indicated.

observed $\sim$ 200 red-sequence galaxies in the Shapley Supercluster core using the AAΩ fibre spectrograph. Graves et al. derived stellar populations via the models of Schiavon (2007), while the other three studies all used the TMBK models. Figure 4.1 shows that the central parameters derived from VIMOS are typical compared to the results from these large spectroscopic surveys.

The age–mass–metallicity plane

Central age and metallicity are mutually correlated with the velocity dispersion. The upper-left panel of Figure 4.2 displays the relation between the central age and metallicity. In the VIMOS sample, there is a marginal anti-correlation, with significant scatter (rms = 0.15). However, there is much less scatter for the A3389 galaxies alone (rms = 0.05). These galaxies cover a much smaller range in $\log\sigma$ than the Shapley sample, suggesting that the scatter in the age–metallicity relation may be dictated by velocity dispersion.

The remaining panels in Figure 4.2 split the VIMOS sample into three coarse bins based on central $\log\sigma$. Although the relation in each σ-bin has approximately the same slope[1], they shift to older ages and higher metallicities with increasing velocity dispersion. The age–metallicity relation is just one projection of the age–mass–metallicity plane

[1]Due to the small number of points in each bin, Figure 4.2 fixes the slope to the Jørgensen 1999 value of −0.7. See the figure for more details.

(or 'Z'-plane; Jørgensen 1999; Trager et al. 2000a), describing how both parameters can correlate with velocity dispersion, while being anti-correlated themselves. Although we have too few points for the bivariate fit, it is interesting to see how well the VIMOS sample matches the 'Z-plane' from a previous study. From spectroscopic observations of $\sim$ 220 cluster early-type galaxies, Smith et al. (in preparation) derived a 'Z'-plane of [Z/H] = 0.66 $\log\sigma$ – 0.68 log(age) – 0.64, with an intrinsic rms residual of 0.075 dex in [Z/H]. Figure 4.3 shows that the VIMOS data agrees well with the relation, with a marginally larger intrinsic scatter (0.09 dex in [Z/H]).

4.2.2 Trends in the gradients

As presented in Section 3.5.2, the 25 VIMOS galaxies have a significant average negative metallicity gradient of –0.13 $\pm$ 0.04, a negligible mean age gradient of –0.02 $\pm$ 0.06 and a marginal mean gradient in the α-element abundance of –0.10 $\pm$ 0.04. The distributions of these gradients are presented in the top row of Figure 4.4.

We explore the existence of trends between pairs of central parameters and gradients, using a simple linear regression. The gradient is treated as the dependent variable, as initially, our interest lies in determining how well the gradients can be predicted from knowledge of the central properties. Fits were calculated without weighting for errors as intrinsic scatter may be significant. Most pairs of parameters do not show a significant trend in the VIMOS sample. Table 4.1 lists the slope and significance for each of these combinations. For example, unlike the central parameters shown in Section 4.2.1, none of the gradients have a simple dependency on central velocity dispersion. Two significant correlations stand out: the metallicity gradient is related to the central metallicity with a slope of –0.63 $\pm$ 0.20 (significance of 3.1 σ); the age gradient is also correlated with the central metallicity (with a slope of 1.09 $\pm$ 0.28 (3.9 σ). Conversely, neither central age versus age gradient or versus metallicity gradient show a significant correlation.

The final row of Table 4.1 refers to the relation between age gradient and metallicity gradient. In this case, it is unclear which parameter is dependent on the other. Hence, the trend is calculated from the bisecting linear relation of the two simple regressions (age on metallicity; metallicity on age). A strong relation is found in the VIMOS sample, with a slope of –0.69 $\pm$ 0.10 (significance of 7.0 σ).

We explore and interpret all of these relations in more detail in subsequent sections. The upper panels of Figures 4.5 – 4.14 present many of the trends listed in Table 4.1.

Table 4.1: Summary of the relations between central parameters (within $r_e/3$ apertures) and gradients discussed in the text (see also Figures 4.5 – 4.13 as displayed in column 3). The slope, error on the slope and significance (in parenthesis) are calculated by minimising the residuals in the Y–direction. The columns display trends for A3389, Shapley, VIMOS (= A3389 + Shapley) and the comparison studies (M03 and SB07). Significant trends in the VIMOS sample ($> 3\sigma$) are presented in bold type. The final row shows the slope for the bisector of the two simple regressions between age and metallicity gradients (Figure 4.14).

X	Y	Fig.	A3389	Shapley	VIMOS	M03	SB07
$\log\sigma$	∇log(age)	4.5	+0.01 ± 0.95 (0.0)	+0.43 ± 0.34 (1.3)	+0.45 ± 0.33 (1.4)	–0.02 ± 0.26 (0.1)	–0.11 ± 0.18 (0.6)
$\log\sigma$	∇[Z/H]	4.6	–0.17 ± 0.62 (0.3)	–0.23 ± 0.25 (0.9)	–0.25 ± 0.22 (1.1)	–0.13 ± 0.24 (0.5)	+0.26 ± 0.22 (1.2)
$\log\sigma$	$\nabla[\alpha/\mathrm{Fe}]$	4.7	–0.66 ± 0.78 (0.9)	+0.42 ± 0.07 (5.6)	+0.20 ± 0.22 (0.9)	–0.06 ± 0.13 (0.5)	+0.13 ± 0.12 (1.1)
$\log\sigma$	$\nabla\log\sigma$		–0.13 ± 0.22 (0.6)	–0.08 ± 0.08 (1.0)	–0.07 ± 0.09 (0.8)	+0.04 ± 0.08 (0.5)	
log(age)	∇log(age)	4.9	–0.15 ± 0.49 (0.3)	–0.49 ± 0.28 (1.7)	–0.32 ± 0.26 (1.3)	–0.09 ± 0.11 (0.8)	–0.20 ± 0.08 (2.6)
log(age)	∇[Z/H]	4.13	+0.23 ± 0.31 (0.7)	+0.33 ± 0.20 (1.6)	+0.27 ± 0.17 (1.6)	+0.19 ± 0.10 (1.9)	+0.24 ± 0.11 (2.2)
log(age)	$\nabla[\alpha/\mathrm{Fe}]$		–0.04 ± 0.42 (0.1)	+0.22 ± 0.10 (2.1)	+0.10 ± 0.17 (0.6)	+0.03 ± 0.06 (0.5)	+0.00 ± 0.08 (0.0)
[Z/H]	**∇log(age)**	4.12	+1.45 ± 0.94 (1.5)	+0.97 ± 0.27 (3.6)	**+1.09 ± 0.28 (3.9)**	+0.22 ± 0.21 (1.0)	+0.20 ± 0.12 (1.7)
[Z/H]	**∇[Z/H]**	4.11	–0.72 ± 0.64 (1.1)	–0.60 ± 0.22 (2.8)	**–0.63 ± 0.20 (3.1)**	–0.59 ± 0.17 (3.5)	–0.21 ± 0.16 (1.3)
[Z/H]	$\nabla[\alpha/\mathrm{Fe}]$		–0.07 ± 0.90 (0.1)	+0.27 ± 0.13 (2.1)	+0.15 ± 0.23 (0.6)	–0.08 ± 0.11 (0.8)	+0.07 ± 0.10 (0.7)
$[\alpha/\mathrm{Fe}]$	∇log(age)		–0.72 ± 0.78 (0.9)	+0.20 ± 0.90 (0.2)	–0.51 ± 0.57 (0.9)	+0.09 ± 0.42 (0.2)	–0.12 ± 0.44 (0.3)
$[\alpha/\mathrm{Fe}]$	∇[Z/H]		+0.04 ± 0.53 (0.1)	+0.22 ± 0.64 (0.3)	+0.18 ± 0.39 (0.5)	–0.05 ± 0.39 (0.1)	+0.23 ± 0.57 (0.4)
$[\alpha/\mathrm{Fe}]$	$\nabla[\alpha/\mathrm{Fe}]$	4.10	+0.24 ± 0.69 (0.3)	+0.67 ± 0.29 (2.3)	+0.51 ± 0.36 (1.4)	–0.01 ± 0.21 (0.0)	–0.16 ± 0.31 (0.5)
∇log(age)	**∇[Z/H]**	4.14	–0.75 ± 0.47 (1.6)	–0.72 ± 0.08 (9.4)	**–0.69 ± 0.10 (7.0)**	–0.95 ± 0.11 (8.6)	–1.33 ± 0.37 (3.6)

4.2.3 Comparison studies

Many factors potentially contribute to the observed trends in stellar population gradients. Hence, there is a risk of reaching a misleading conclusion due to sparse sampling of a complex parameter space. To minimise this possibility, we test the validity of the trends found in Section 4.2.2 by comparing to data from two published early-type galaxy studies: Mehlert et al. (2003, hereafter M03) and Sánchez-Blázquez et al. (2007, SB07). Both were long-slit spectroscopic studies, and employed a similar analysis technique and models to the method described in Chapter 3.

Mehlert et al. (2003)

Mehlert et al. (2003) derived stellar population gradients for 32 early-type galaxies in the Coma cluster. The authors rebinned the spectra to achieve a S/N > 30 Å^{-1} per bin out to r_e, and computed the stellar population parameters using an index–pair iteration technique, with Hβ, Mgb5177 and $\langle$Fe$\rangle$ = (Fe5270+Fe5335)/2, in conjunction with the TMBK models. Their original analysis excluded the two cD galaxies (NGC4889, NGC4874) and an S0 (NGC4865), as they lie beyond the model grids, and NGC4876 due to systematically larger errors. We followed suit, using the remaining 28 galaxies in the sample.

M03 defined central values as the average along the major axis inside $0.1r_e/\sqrt{1-\epsilon}$, where ϵ is the ellipticity. Gradients were derived in a method similar to that presented in Chapter 3. The absorption line gradients were extrapolated to give the values at $0.1 \times r_e$ and r_e. The stellar population at each point was derived, from which the gradients could be calculated. The distributions for the gradients are shown in the second row of Figure 4.4.

Sánchez-Blázquez et al. (2007)

Sánchez-Blázquez et al. (2007) observed a sample of 11 local early-type galaxies in various environments (field, group, Virgo cluster), rebinning the spectra to achieve a S/N > 50 Å^{-1} out to $2r_e$. Using a χ^2 minimisation technique, with 19 Lick indices and the TMBK models, stellar population gradients were derived for all of the sample galaxies. NGC2865, a merger remnant in the field, contains an extremely young core, and has been excluded from our fits.

For central values, SB07 used an aperture size of 1.5 arcsec $\times$ $r_e/8$. Stellar population

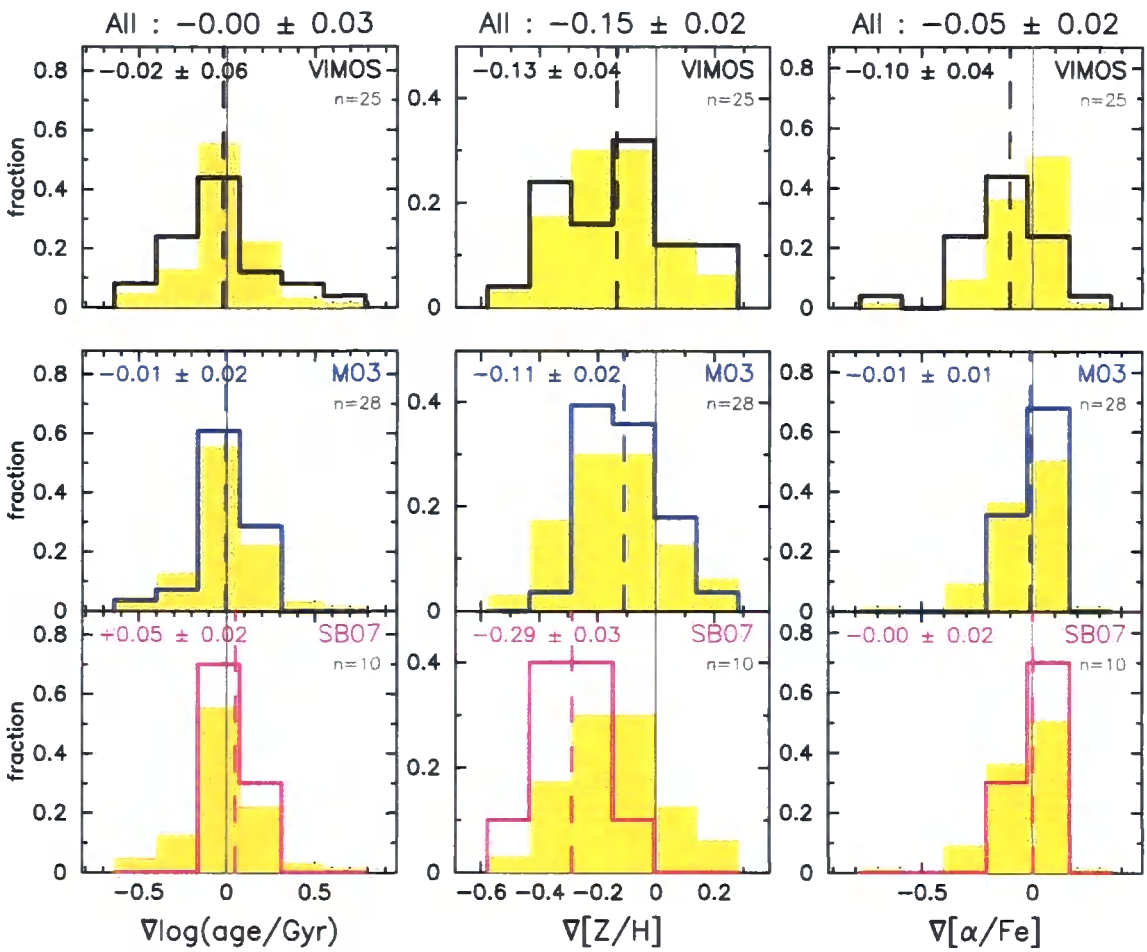

Figure 4.4: Histograms showing the fractional distribution of gradients in (left-to-right) log(age/Gyr), [Z/H] and [α/Fe], for VIMOS (upper), M03 (centre) and SB07 (lower). Mean gradients are marked by a dashed line, and are shown in the top–left of each panel. Background shaded histograms are for the combined distributions (VIMOS + M03 + SB07), with the mean gradient represented by a dotted line, and shown above each column of panels.

gradients were derived by performing a weighted best fit to the radial profile in each parameter, excluding points within the seeing disc. Stellar population parameters were derived from discrete models without interpolation, and as a result, gradients flatter than the model bin size, were quoted to be 0.000 ± 0.000. When computing the trend between parameters in later sections, we use an un-weighted fit to avoid misinterpreting intrinsic scatter. This also has the advantage of not unduly biasing towards the SB07 galaxies with 'zero' uncertainty. The final row of Figure 4.4 displays the distribution of gradients for the 10 SB07 galaxies.

Comparing the distributions of the gradients

In general, the average gradients of the two long-slit studies are similar to the VIMOS sample, and the distributions are similar. However, it is worth noting that the combined VIMOS sample has a larger mean $\nabla[\alpha/\mathrm{Fe}]$ than either of the comparison studies. Also, the mean negative metallicity gradient from SB07 is nearly twice as steep as in the other samples. Those authors derived large negative $\nabla[\mathrm{Z/H}]$ gradients for galaxies in both high and low density environments, so this difference is not due to the inclusion of non-cluster targets.

4.3. Gradients versus central $\log \sigma$

The combined VIMOS sample does not show a significant correlation between any of the stellar population gradients and the central velocity dispersion. The lack of a simple linear relationship is confirmed in the comparison studies in each case, as shown in Figures 4.5 – 4.7. The K-band luminosity is often used as a proxy for stellar mass in a galaxy (whereas velocity dispersion traces the dynamical mass). We find no significant trend for any of the gradients with the absolute magnitude (Figure 4.8).

Although there is no simple trend with the metallicity gradient (Figure 4.6), evidence has been previously reported in favour of the [Z/H] gradient depending on mass (via various observable proxies). A simple model of galaxy formation asserts that enrichment gradients depend on galactic wind efficiency, which scales with the potential and hence galaxy mass (Kobayashi, 2004). In an early study of 42 early-types, Carollo, Danziger, & Buson (1993) calculated the gradient in the Mg_2 absorption line (a simple proxy for metallicity) and discovered that it became shallower with decreasing central velocity dis-

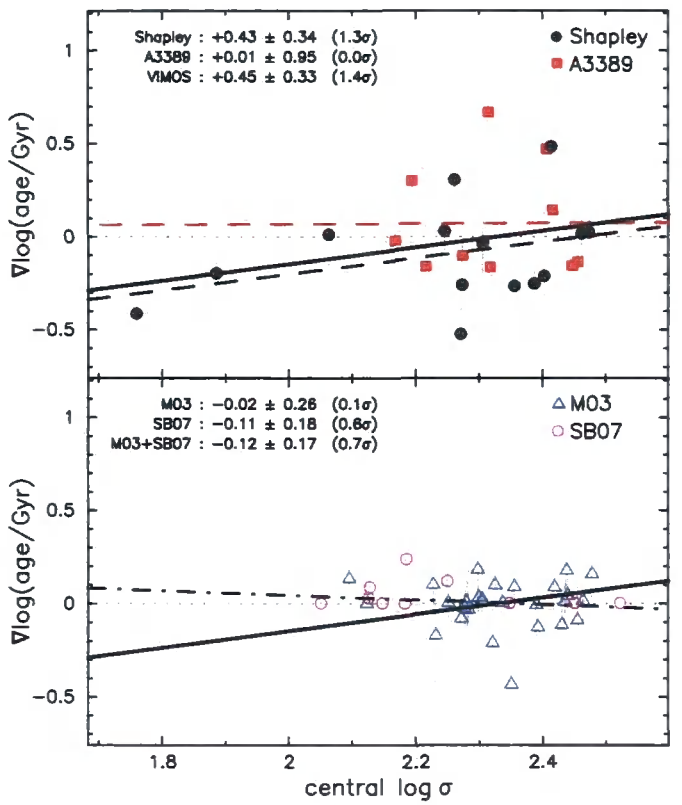

Figure 4.5: Age gradient versus central velocity dispersion ($\log \sigma$). Upper panel presents the VIMOS data (Shapley = black circles; A3389 = red squares), together with best fit lines (dashed; solid black = combined VIMOS) as described in Section 4.2.2. Lower panels show results from M03 (blue triangles) and SB07 (magenta open circles). Dash–dot line indicates the best fit to the combined comparison sample (M03 + SB07); solid line displays the combined VIMOS best fit. The slope and significance of the best fits are displayed to the top-left of the panels, and in Table 4.1.

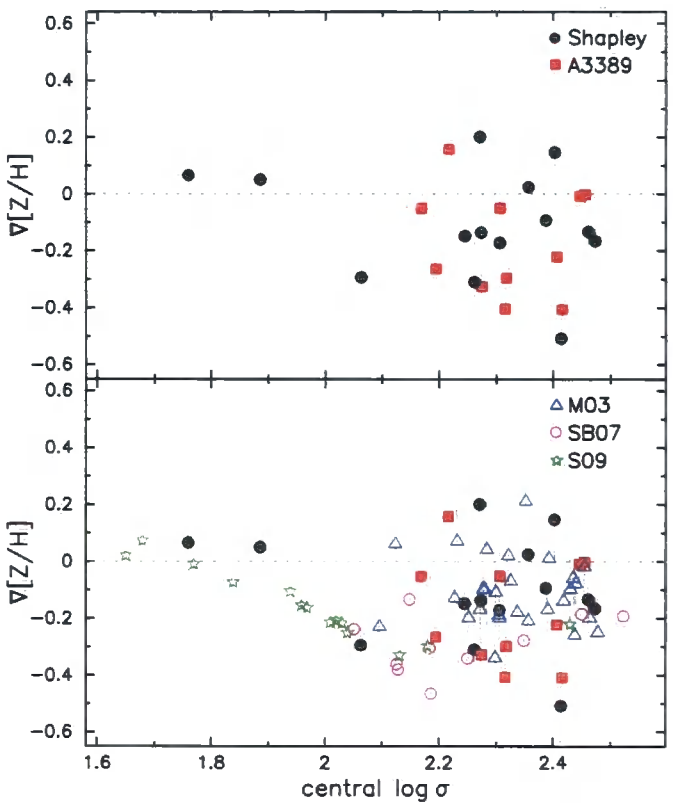

Figure 4.6: Metallicity gradient versus central velocity dispersion ($\log \sigma$). Upper panel displays the VIMOS data (Shapley = black circles; A3389 = red squares). Lower panel shows VIMOS data together with M03 (blue triangles), SB07 (magenta open circles) and Spolaor et al. (2009, S09; green stars – measured directly from their figure 1). The two low mass galaxies from Shapley are consistent with the tight relation for low mass early-types in S09.

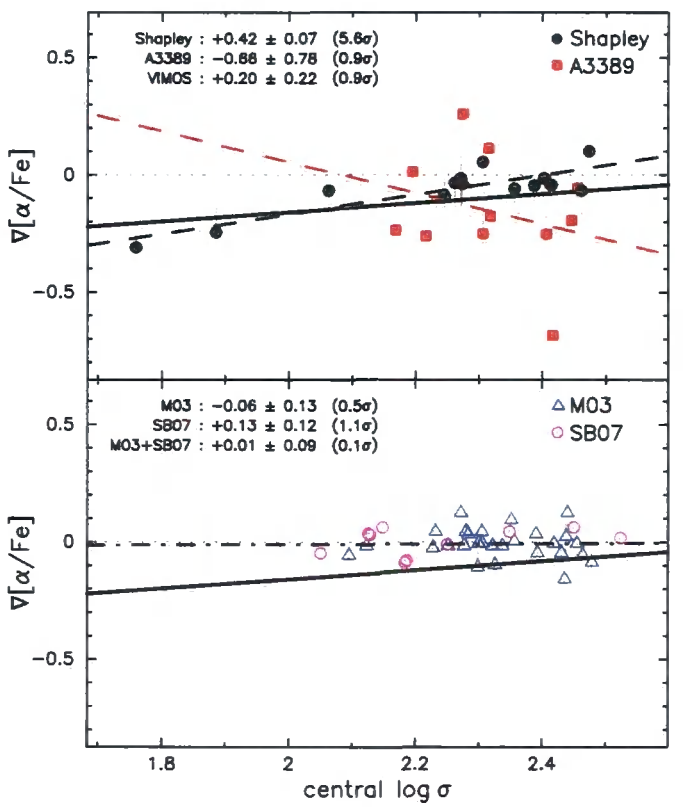

Figure 4.7: α-abundance gradient versus central velocity dispersion ($\log \sigma$). Layout as in Figure 4.5.

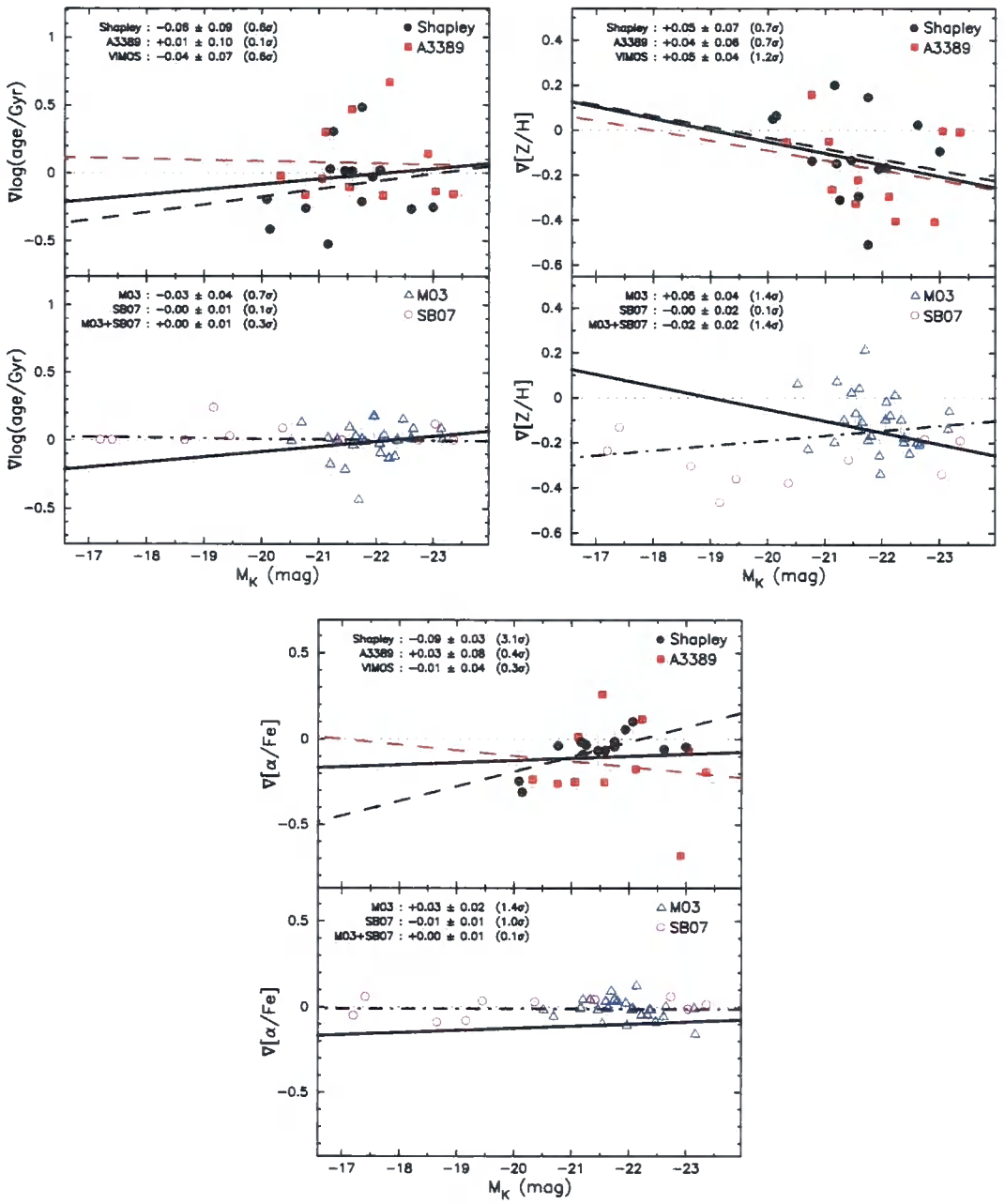

Figure 4.8: Stellar population gradients in age (upper-left), metallicity (upper-right), α-abundance (lower panel) versus the K-band luminosity. Layout of each panel, as in Figure 4.5.

persion (galaxy mass) for low-mass systems ($\log\sigma < 2.26$). High-mass galaxies, however, showed no such correlation. Kobayashi & Arimoto (1999) studied the Mg_2 gradients of 80 galaxies (above and below the Carollo et al. transition point), but were unable to find a statistically significant trend with any mass estimator (central velocity dispersion, B-band luminosity, effective radius or the dynamical mass).

In contrast, Forbes, Sánchez-Blázquez, & Proctor (2005) claimed a significant relation between metallicity gradients and galaxy mass (K-band luminosity, central velocity dispersion and dynamical mass) for a literature sample of Coma cluster galaxies (including the M03 sample). Recently, Spolaor et al. (2009) have resurrected the idea of a mass transition point after observing 14 low mass early-types in local clusters. These authors found that for low mass galaxies ($\log\sigma < 2.15$), metallicity gradients are remarkably tightly correlated with velocity dispersion, in the sense that (negative) ∇[Z/H] becomes shallower with decreasing $\log\sigma$ and positive at very low $\log\sigma$. They conclude that while some higher mass galaxies have steep negative ∇[Z/H], there is also a visible downturn and a markedly broader scatter. Physically, the transition point may mark the mass above which galaxy formation histories are dominated by late-epoch, gas-poor merging, which dilute the metallicity gradient (Hopkins et al., 2009). The magnitude of the dilution is related to the individual merger properties and the metallicity gradients of the progenitors (di Matteo et al., 2009), causing the observed inflated scatter at larger masses.

As already noted, Figure 4.6 confirms the large scatter and apparent absence of correlation for high mass galaxies. Unfortunately, the A3389, M03 and SB07 studies do not include galaxies below the Spolaor et al. mass transition point. Low mass galaxies are also under-represented in the Shapley sample, as several small galaxies have been excluded by low surface brightness at r_e. However, the remaining galaxies with $\log\sigma < 2.15$ are not inconsistent with the mass–metallicity gradient trend reported in Spolaor et al. (2009).

4.4. Gradient trends with central values

We now explore the relation between central stellar population parameters and gradients. The VIMOS sample shows no significant correlation of the age gradient with central age (Figure 4.9), or in the analogous relation for α-enhancement (Figure 4.10). The comparison studies confirm the lack of trends in these cases, as shown in the final

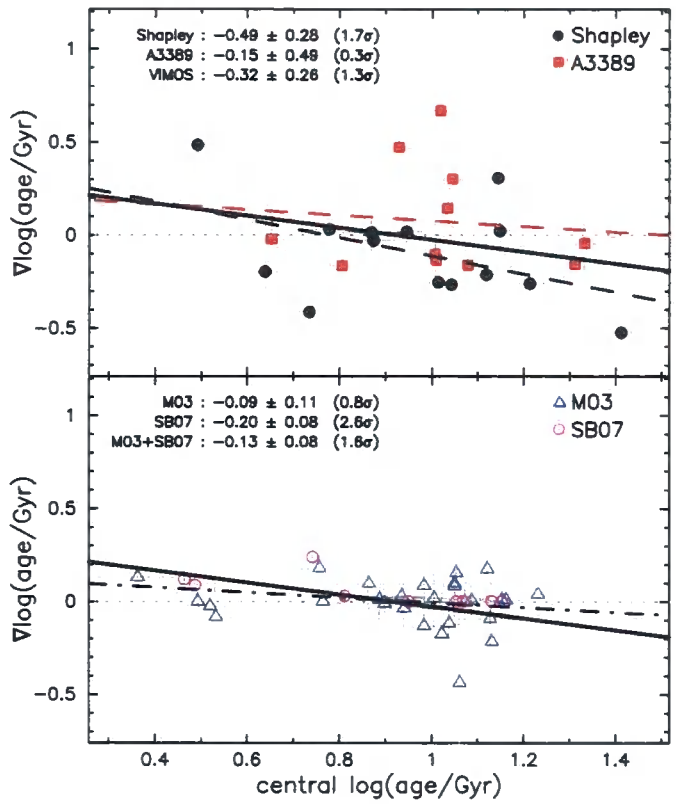

Figure 4.9: Age gradient versus the central age. Layout as in Figure 4.5.

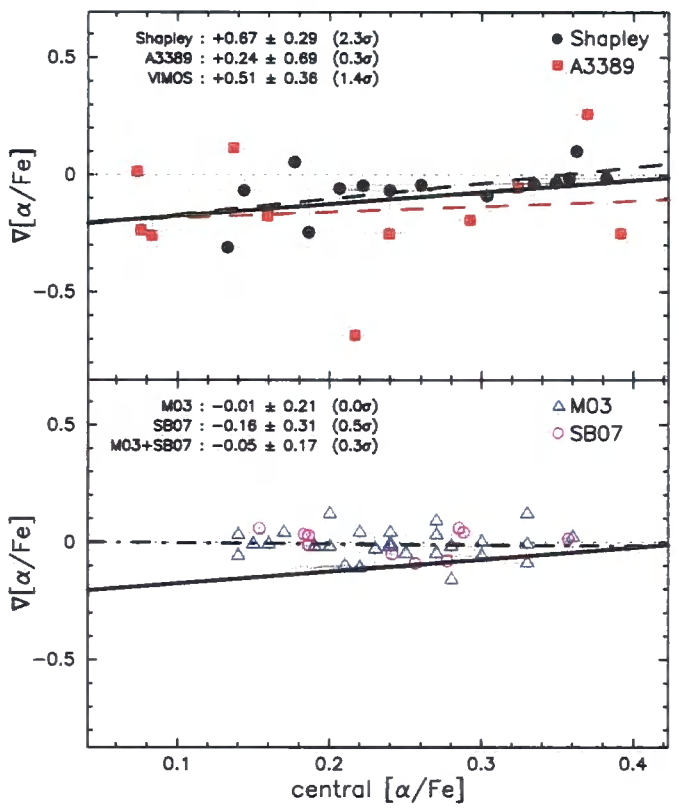

Figure 4.10: α-abundance gradient versus the central [α/Fe]. Layout as in Figure 4.5.

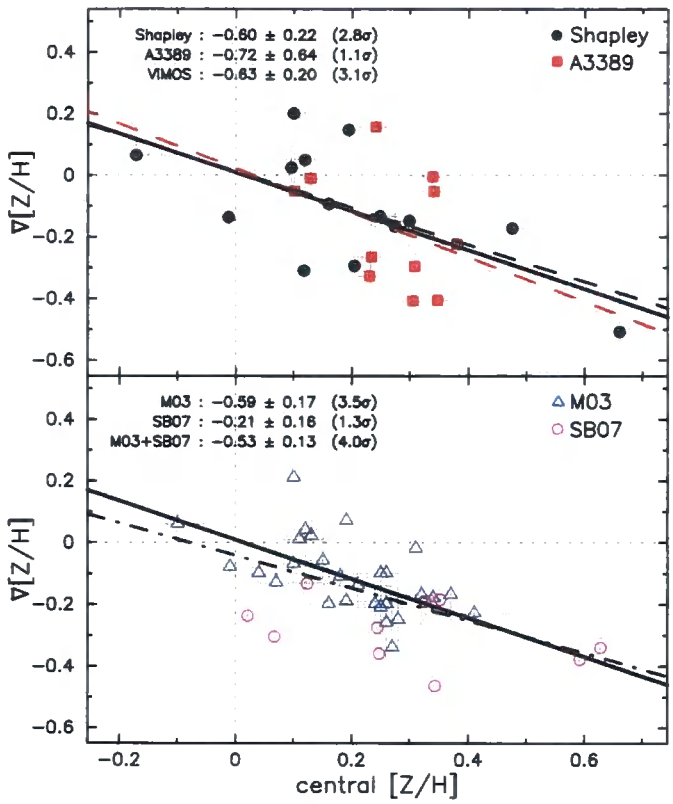

Figure 4.11: Metallicity gradient versus the central metallicity. Layout as in Figure 4.5.

two columns of Table 4.1.

In contrast, the metallicity gradient is related to the central [Z/H], with a slope of –0.63 ± 0.20 (3.1 σ significance; Figure 4.11). This relation is confirmed in M03, but is not significant in SB07. A similar relation, with a slope = –0.71 ± 0.34, was reported by Morelli et al. (2008) for the bulges of nearby spiral galaxies, which are sometimes considered akin to low-luminosity ellipticals (e.g. Thomas & Davies, 2006). The trend intercepts the origin, and the orientation of the gradients suggest that in general, galaxies tend towards solar metallicities ([Z/H] = 0) at $\sim$ 2–3 r_e. In rapid dissipative collapse, in-falling gas becomes enriched by evolved stars, and contributes to the metal-rich stars forming in the core. In recent models by Pipino et al. (2008) as much as 90 per cent of metals in central stars originated in outer regions. The onset of galactic wind depends on local escape velocity and occurs later in inner regions. As a result, star formation abates earlier in outer regions causing lower [Z/H] at r_e than the core (Arimoto & Yoshii, 1987; Matteucci, 1994). Both of these processes work to strengthen the metallicity gradient and raise the central [Z/H].

The age gradient is correlated with central metallicity in the VIMOS sample, with a

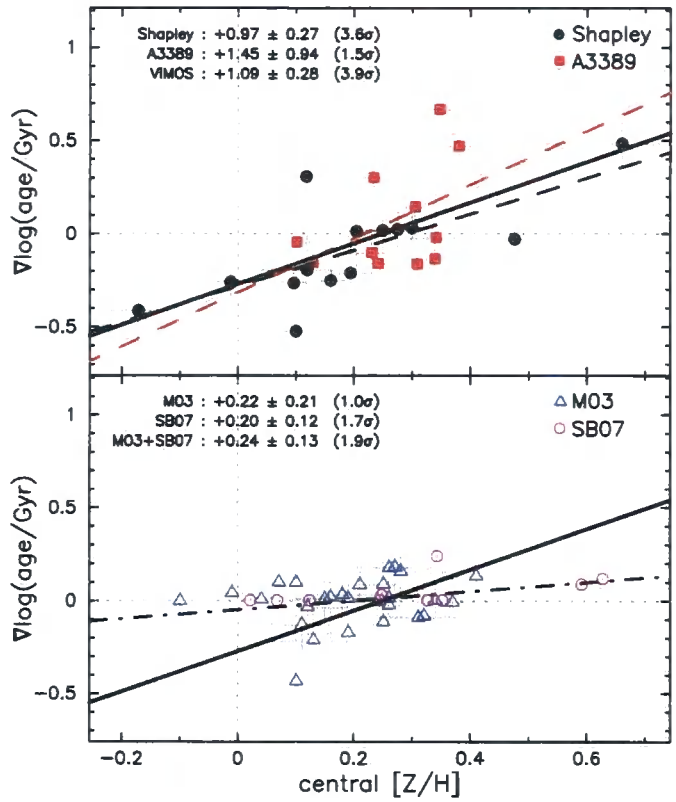

Figure 4.12: Age gradient versus central metallicity. Layout as in Figure 4.5.

slope of 1.09 ± 0.28 ($3.9\,\sigma$ significance; Figure 4.12). The relation is such that galaxies with more metal rich centres have stronger age gradients. However, the relation is not significant in either comparison study, or in the A3389 sample alone, implying that it is driven mainly by the Shapley sample. The metallicity gradient versus the central age also displays a marginal trend (Figure 4.13), in which centrally young galaxies favour stronger negative metallicity gradients, and galaxies with old cores exhibit weaker metallicity gradients.

To summarise, the metallicity gradient has a strong dependence on the central metallicity, such that metal rich cores are associated with stronger negative gradients, so all galaxies have approximately solar metallicities in their outer regions. Although further correlations between parameters are only marginal, some tentative generalisations can be noted: on average, a galaxy with a metal rich core not only has a steeper negative metallicity gradient but also $\nabla\log(\text{age}) > 0$; conversely, a galaxy with a solar (or marginally sub-solar) metallicity centre tends to have $\nabla[\text{Z/H}] \sim 0$ and a negative age gradient. These results suggest, or are possibly driven by, a mutual correlation between the age and metallicity gradients.

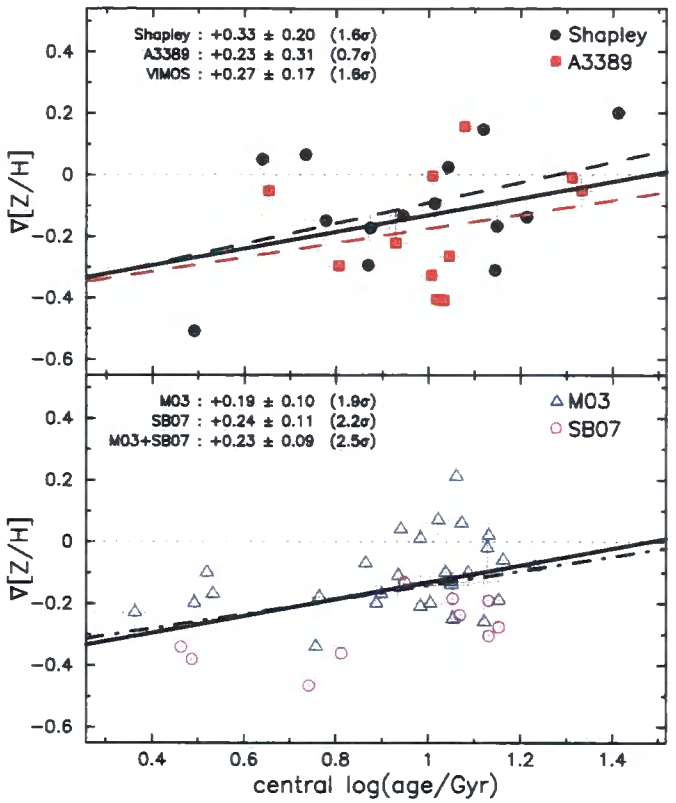

Figure 4.13: Metallicity gradient versus central age. Layout as in Figure 4.5.

4.5. Gradient–gradient relations

The gradients in age and metallicity are strongly anti-correlated in the VIMOS sample, with a slope = –0.69 ± 0.10 (see Figure 4.14, upper panel; we discuss the issue of correlated measurement errors in the next paragraph). The relation is confirmed by both comparison studies (lower panel of Figure 4.14, and the final row of Table 4.1). The trend is reminiscent of the central parameter age–metallicity relation, as presented in Section 4.2.1. However, the central relation is a two-dimensional projection of the three parameter age–mass–metallicity plane (Trager et al., 2000a), with the scatter originating from the mass dependence. This is shown by the correlation between the residuals from the age–metallicity relation, and the central velocity dispersion (left panel, Figure 4.15; also see Section 4.2.1). In contrast, the residuals from the trend in gradients has no observed dependence on the velocity dispersion (right panel, Figure 4.15).

The strong anti-correlation between ∇log(age) and ∇[Z/H] suggests that generally, a positive age gradient is coupled with a strong negative metallicity gradient, and a negative age gradient is usually associated with a weak or flat metallicity gradient. However,

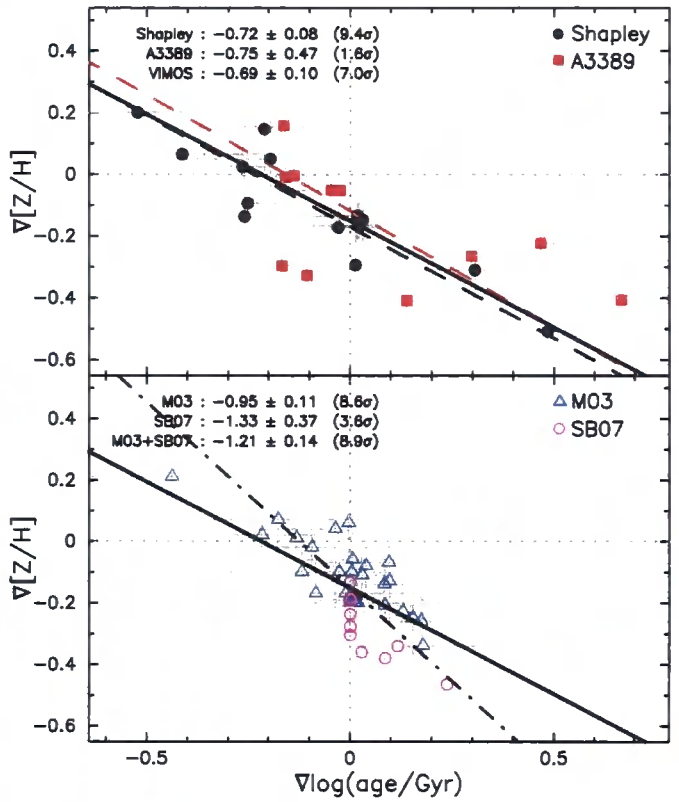

Figure 4.14: Relation between the age and metallicity gradients. Layout as in Figure 4.5.

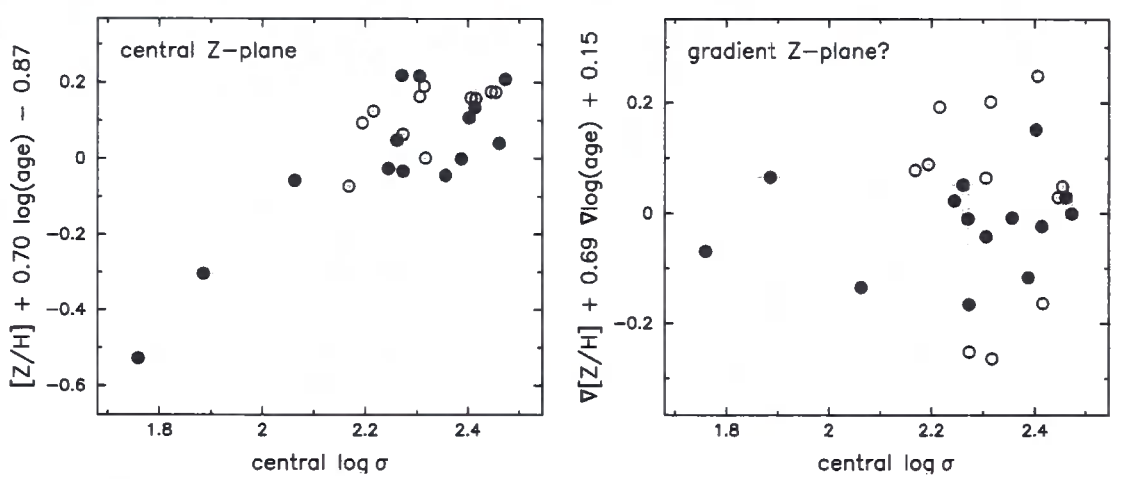

Figure 4.15: Residuals from the central age–metallicity relation (left panel; see Figure 4.2) and the ∇log(age)–∇[Z/H] trend (right panel; see Figure 4.14) versus the central velocity dispersion, for the VIMOS sample (Shapley=solid points; A3389=open points). Whereas $\log\sigma$ is highly correlated with the residuals from the central values, no such relation is present for the gradients.

the use of multiple absorption line indices to derive the age and metallicity does not entirely erase the degeneracy, with a correlation dominating the errors (discussed further in Kuntschner et al. 2001). It is prudent to calculate whether the strong trend seen in Figure 4.14 could be predominately caused by the correlated measurement errors.

The upper panel of Figure 4.16 again presents the gradients for the Shapley and A3389 samples. In this figure, the conventional one-dimension ($1\,\sigma$) error bars in each axis have been replaced by the $1\,\sigma$ error ellipses, based on the distribution of the Monte Carlo realisations. The error ellipses are clearly orientated in the direction of the correlation.

The lower panels of Figure 4.16 show the distribution of the galaxies projected onto the best-fitting line from the upper panel. We consider a null hypothesis in which the scatter around the zero value is entirely due to the correlated errors. The Shapley sample alone does not disprove this hypothesis, with an estimated probability of $q = 0.2$. However, the A3389 sample is incompatible with the null hypothesis ($q = 1 \times 10^{-7}$), i.e. that although there is a sizeable correlation of errors, there is also a real intrinsic scatter in the same direction. The combined VIMOS sample confirms this conclusion. While not contrary to the null hypothesis, the Shapley sample on its own is also not inconsistent with the presence of intrinsic scatter. To explain the age–metallicity gradient relation for the VIMOS sample without invoking intrinsic scatter, the errors in the stellar population gradients would have to be a factor of $\sim$3 larger. Such an underestimation is unlikely, as the gradient errors, derived via Monte Carlo simulations, scale approximately linearly with the well determined index uncertainties.

4.6. Colour gradients and spectroscopy

Many studies of broadband colour gradients have ignored the possibility of age gradients (e.g. Peletier et al. 1990; Tamura et al. 2000), but here we find that ∇log(age) is inconsistent with zero in 40 per cent of our sample. By measuring colour gradients in multiple bands, recent studies have attempted to include the age gradient. From SDSS and 2MASS photometry, Wu et al. (2005) derived average ∇[Z/H] = -0.25 ± 0.03 and ∇log(age) = 0.02 ± 0.04. However, the age and metallicity predictions are strongly correlated due to the usual degeneracy in broadband colours, leading to large uncertainties in the derived stellar population (Carter et al., 2009). A negative B–R colour gradient could be the result of a negative gradient in either metallicity or age. Additionally, our study

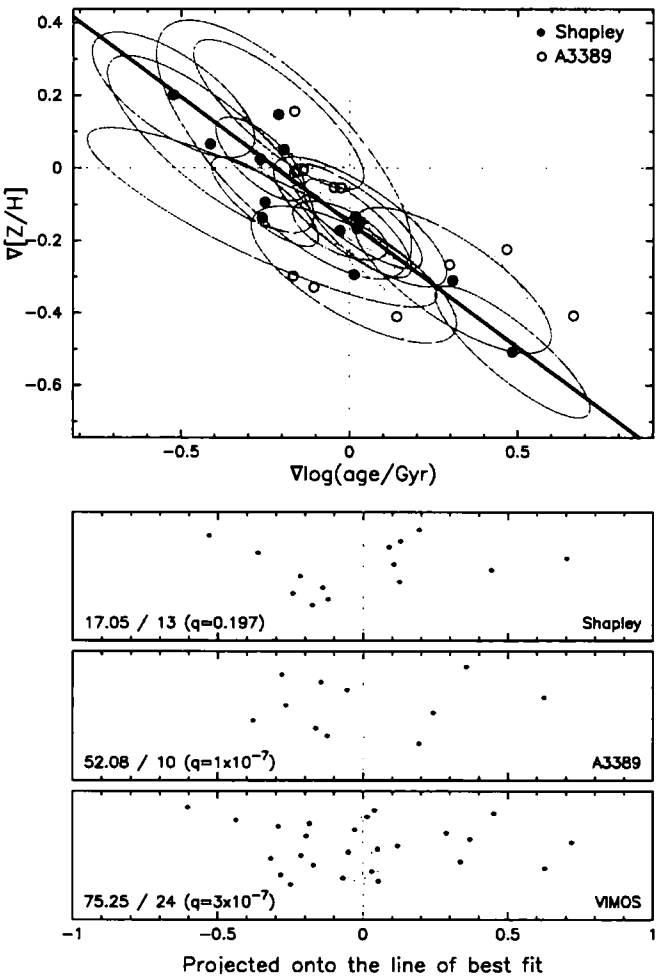

Figure 4.16: Upper panel: The age gradient–metallicity gradient relation for Shapley (solid points) and A3389 (open points), with the error estimates represented by ellipses (Shapley = dark grey; A3389 = light grey). The best fit line is shown. Lower panels: For each sample (top-to-bottom: Shapley, A3389, VIMOS = Shapley + A3389) the points are projected onto the best fit line and shown as a displacement from the median value (y-axis position is arbitrary). The one-dimensional chi-squared, degrees of freedom and q, the probability that the distribution could be entirely attributed to the effect of correlated errors, are displayed.

has found that age and metallicity gradients are intrinsically anti-correlated, affecting the colour gradient in opposite directions.

From a known stellar population and given models, the broadband colour can be predicted. In this section, we compare B–R colour gradient predictions calculated from VIMOS spectroscopic age and metallicity, to those observed in images. Optical imaging is only available for the Shapley Supercluster galaxies.

4.6.1 Colour gradients from imaging

Imaging is from the ESO Wide Field Imager (WFI) courtesy of the Shapley Optical Survey (Mercurio et al., 2006, SOS). The pixel size is 0.24 arcsec, and the average seeing was ~0.8 arcsec (FWHM) in the B-band and ~0.7 arcsec for R, corresponding well to the spatial information from VIMOS (0.68 arcsec sampling and an average seeing of 0.85 arcsec).

For consistency, the B–R gradients were computed using a method as similar as possible to the calculation of VIMOS line strength gradients. B- and R-band magnitudes were measured for the same elliptical annuli and circular central apertures ($r_e/3$ and r_e) described in Section 3.3.2. As an example, Figure 4.17 presents the gradient measurement for the galaxy MGP2440. The upper panels show the B- and R-band imaging overlaid by the adopted bin boundaries. Raw photometry in the Johnson (Vega) system was converted to absolute magnitudes using individual galaxy redshifts, and corrected for galactic extinction with the reddening maps of Schlegel, Finkbeiner, & Davis (1998)[2].

The B–R colour in each bin is presented in the lower panel of Figure 4.17. The colour gradient was computed using an unweighted linear fit to all bins within the effective radius: $\nabla B\text{–}R$ = $\Delta B\text{–}R$ / $\Delta\log(r/r_e)$. This is identical to the fitting technique used for the index gradients (Section 3.5.1). Appendix C presents the B–R photometry and colour gradient fits for all of the Shapley galaxies.

4.6.2 Predicted colours from VIMOS spectroscopy

The evolutionary stellar population synthesis models of Maraston (2005) compute spectral energy distributions for a wide range of ages and metallicities. These models are the basis of the TMBK models, which themselves implement variable α-element abundance ratios, so [α/Fe] is not an input parameter for the colour predictions. (We attempt

[2] A_B=4.315×$E(B\text{–}V)$, A_R=2.673×$E(B\text{–}V)$

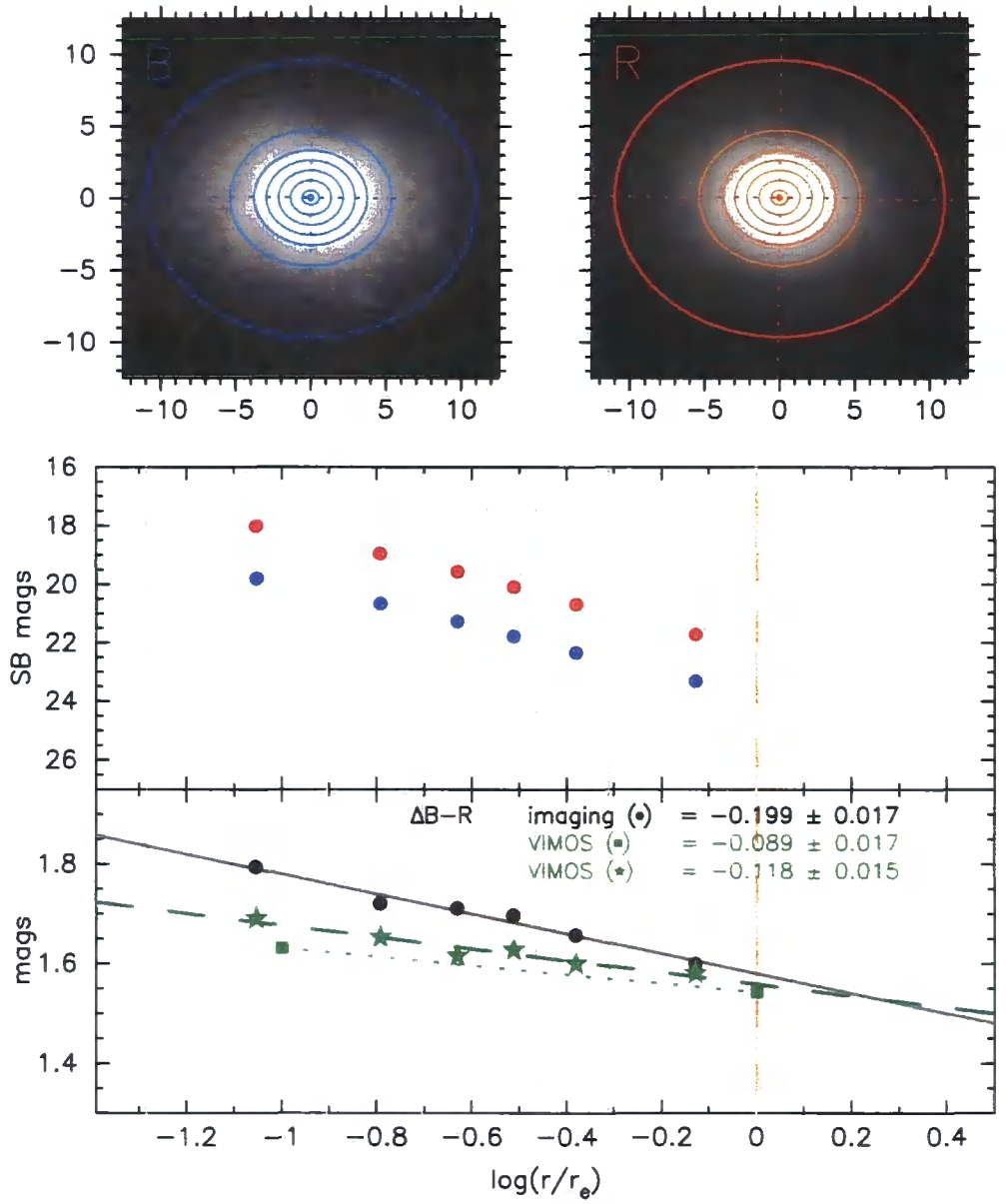

Figure 4.17: B–R photometry and colour gradient fits for MGP2440. Upper panels: display the B- and R-band imaging overlaid by the adopted bin boundaries (thin ellipses) and r_e (thicker ellipse). Central panel: the B- and R-band surface brightness from each radial bin. Lower panel: circles and solid line show the B–R gradient as measured from the imaging. Green stars/dashed line show the gradient derived from VIMOS using the first method (fitting to all bins with r_e; see Section 4.6.2) and the green squares/dotted line show the gradient derived from VIMOS using the second method (inner/outer points). Grey vertical dashes are the bin boundaries. Orange dashed line indicates r_e. Appendix C presents similar figures for all of the Shapley galaxies.

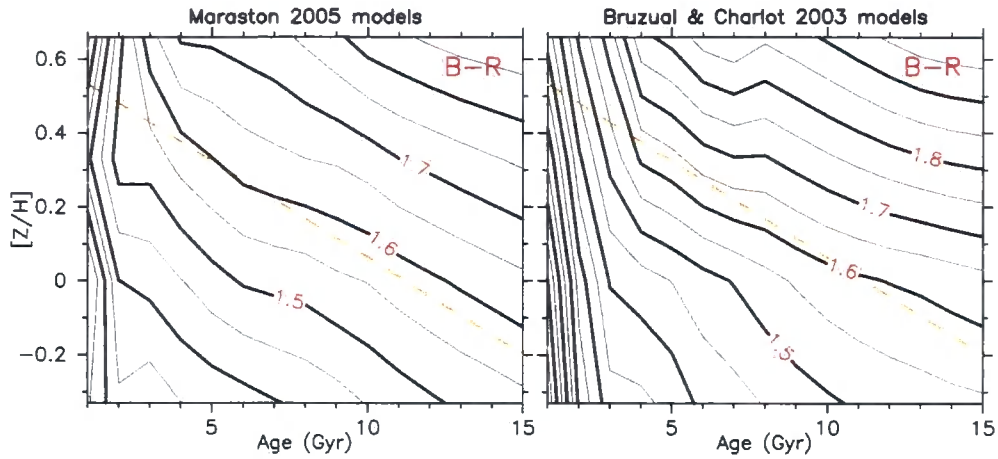

Figure 4.18: Dependence of the B–R colour on the stellar population age and metallicity in the models of Maraston 2005 (left panel) and Bruzual & Charlot 2003 (right panel). The orange dashed line indicates the slope of the Worthey 3/2 rule.

to correct the colours to account for the effect of [α/Fe] in the next section.) From the model spectra, and given a filter transmission curve, it is straightforward to calculate the broadband colour of various stellar populations.

The left panel of Figure 4.18 shows that in the Maraston models, B–R colour varies in a regular manner throughout the age–metallicity space. Generally, B–R becomes redder with increasing age or metallicity. For ages $\gtrsim$ 5 Gyr, the colour contours are generally parallel, so the colour gradient will only depend on the age and metallicity gradients, and not absolute values. For ages younger than 5 Gyr, the contours become less regular, and the absolute position in the age–metallicity plane becomes important. For comparison, the right-hand panel of Figure 4.18 presents the same plot for the models of Bruzual & Charlot (2003). The colour contours from both models are very similar, although Bruzual & Charlot tend to predict redder colours and slightly steeper colour gradients for a given change in age or metallicity (i.e. the contours are closer together). Tracing further differences between these models is beyond the scope of this study – for a more thorough exploration, see Carter et al. (2009).

In analogy to the stellar population derivation in Section 3.5.2, there are two different methods for calculating the B–R colour gradients. The first predicts a colour from the age and metallicity of each radial bin, from which we compute the gradient using an unweighted linear fit to all bins within the effective radius, as for the colour gradients from imaging. The alternate method predicts colours for the inner and outer points (at $0.1 \times r_e$ and r_e) used in the stellar population gradient derivation. As with those gradi-

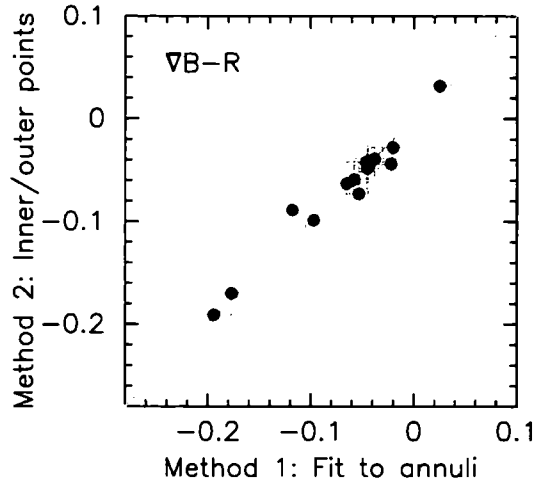

Figure 4.19: B–R predicted colour gradients using two different techniques (see text for details). The predicted gradients are generally independent of the method used.

ents, we would expect the latter method to be more robust (see Section 3.5.2), relying on fewer grid inversions. However, the former method has the advantage of more closely following the technique used to measure the colour gradients from imaging.

The lower panel of Figure 4.17 displays the B–R colour gradient predictions for both methods (in green), alongside the gradient measured from the imaging. Figure 4.19 compares the B–R colour gradients predicted by each method. The two methods predict very similar colour gradients in nearly all cases. As the results are generally method independent, in the following sections we use the results from the first, as the technique is most similar to that used for the imaging.

4.6.3 Comparing predicted colours to photometry

First, we compare the absolute B–R colours for individual VIMOS apertures and annuli (left panel, Figure 4.20). The predicted colours generally agree well with the photometry, with an overall rms dispersion of 0.068 mag. For reference, the innermost bins have been distinguished from other annuli, as they are most likely to be affected by the PSF (aperture diameter $\approx$ PSF FWHM).[3] In several cases they are very similar to the circular $r_e/3$ central apertures.

The best VIMOS predictions are for the r_e apertures (red points in Figure 4.20), which

[3]The innermost 'annuli' are the central ellipses adopted during the spatial binning described in Section 3.3.2.

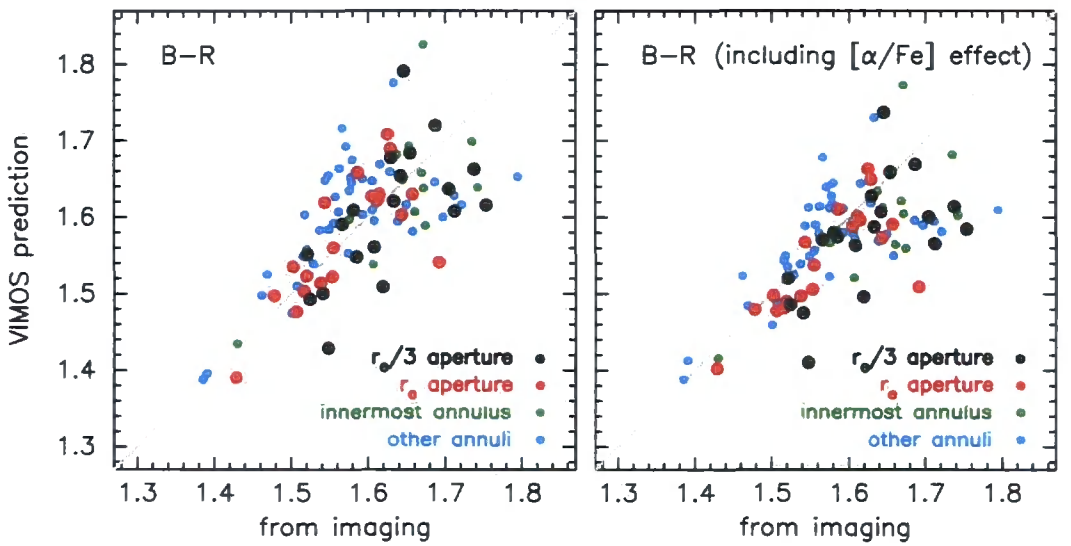

Figure 4.20: Left panel: Comparison of B–R colours from imaging with those derived from the VIMOS stellar population parameters. Each point corresponds to a matched aperture from a target: $r_e/3$ radius aperture (black), r_e radius aperture (red), innermost annulus from VIMOS radial binning scheme (green), other annuli from VIMOS radial binning scheme (blue). Equality is shown. The red (B–$R > 1.75$) predictions from VIMOS are all from MGP2437. Right panel: Similar comparison after the predicted B–R colours have been corrected using δB–R = –0.14 × $\delta[\alpha/\mathrm{Fe}]$ from Smith et al. (2009a).

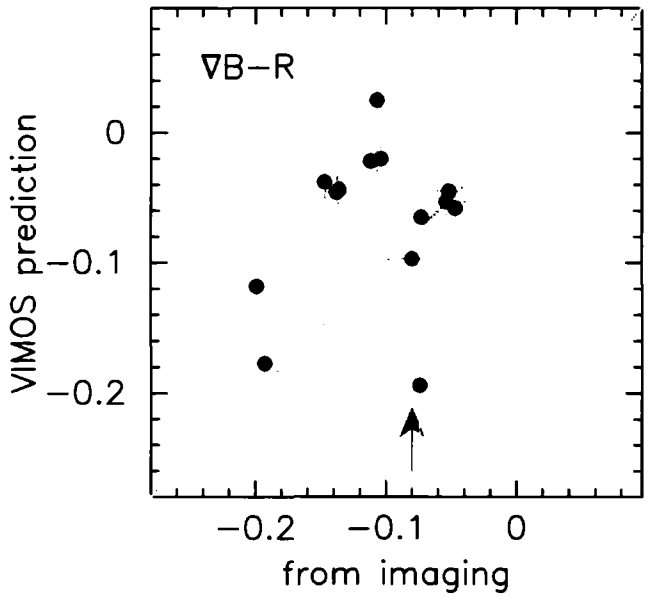

Figure 4.21: Comparison between the B–R colour gradients from imaging and VIMOS stellar population parameters. Equality is shown. The arrow displays the mean ∇B–R = –0.08 ± 0.01 mag dex^{-1} from Wu et al. (2005).

have high S/N and are not affected by seeing. The comparison has an rms dispersion = 0.056 mag, which decreased to 0.039 mag if the single outlier (MGP2083: prediction = observed – 0.16 mag) is excluded. This scatter is consistent with that found by Smith et al. (2009a), who studied ~230 galaxies in Shapley using AAΩ spectroscopy and SOS aperture colours. To account for the effect of α–abundance on the colour, that study empirically derived the relation δB–R = –0.14 × δ[α/Fe]. Using this, our scatter for the r_e apertures is reduced to 0.034 mag (right panel, Figure 4.20).

The three outlying points with very red predicted colours from VIMOS (B–R > 1.75) are all from MGP2437 (r_e/3 aperture and the two innermost annuli). The red colour prediction results from a large spectroscopic central age estimation of log(age/Gyr) = 1.412, which lies beyond the model grids. The extreme age is not observed in the larger 1 arcsec radius aperture, so the cause must be localised in the core. The anomaly appears to be due to extremely weak HδF and HγF measurements, resulting from a combination of poor S/N at the blue end of the spectrum and an unusually deep G4300 line (which lies in the blue 'continuum' sideband of HγF).

Figure 4.21 compares the predicted colour gradients to those observed. The predictions are reasonably consistent with the observations, with a reduced $\chi^2 \sim 3.4$ (rms scatter

of 0.08 mag). The sample mean is well matched to the mean ∇B–R = –0.08 ± 0.01 mag dex^{-1} from Wu et al. (2005). Accounting for $\nabla[\alpha/\mathrm{Fe}]$ in the colour gradient (using the Smith et al. formula above) has only a marginal effect, as the mean correction is < 0.01 mag.

4.7. Towards a physical explanation

Drawing together our observed trends, we propose the following tentative explanation. Galaxy mass dictates both the efficiency of gas in-fall during rapid dissipative collapse (Pipino et al., 2008), and the delayed onset of galactic winds in the core compared to outer regions (Matteucci, 1994; Kobayashi, 2004). The former process raises the central metallicity, while the latter inhibits metal enrichment at larger radii. Together, they ensure that the strength of the negative metallicity gradient correlates with central metallicity, and that both parameters generally increase with velocity dispersion. For low mass galaxies ($\sigma < 140$ km s^{-1}) these are the prevailing processes, driving the relation for $\log\sigma < 2.15$ (e.g. Carollo et al. 1993; Spolaor et al. 2009). Above this transition point, mergers play a dominant role.

Gas-rich merging may prompt a central starburst, resulting in an increased central metallicity and a more negative metallicity gradient (Kobayashi, 2004), reinforcing the strong ∇[Z/H]–central [Z/H] relation. The starburst also creates a positive age gradient (Mihos & Hernquist, 1994), which may be the origin of the ∇log(age)–central [Z/H] relation. However, the logarithmic age gradient from a central starburst is diluted over time, introducing a dependency on the epoch of the last merger, and weakening the ∇log(age) correlations. Late-epoch, gas-poor mergers tend to flatten metallicity gradients (White, 1980; Hopkins et al., 2009), with the extent of the dilution dependent on the properties of the merger (di Matteo et al., 2009). This increased scatter in ∇[Z/H] weakens all of the correlations further.

4.8. Conclusions

The internal gradients of early-type galaxies offer a valuable insight into their star formation and chemical evolution. We have used the VIMOS integral field unit to determine the gradients in spectroscopic features for 25 galaxies in local clusters (Abell 3389

and the Shapley Supercluster core). From these, we derived gradients within the effective radius for age, total metallicity and α-element over-abundance. Our principal results are summarised below.

- The average metallicity gradient is ∇[Z/H] = –0.13 ± 0.04. No galaxies have significant positive metallicity gradient.
- We find that the mean ∇log(age/Gyr) = –0.02 ± 0.06, but that 40 per cent of galaxies have age gradients inconsistent with zero ($> 2\,\sigma$).
- The mean α-element enhancement gradient is $\nabla[\alpha/\mathrm{Fe}]$ = –0.05 ± 0.02.
- Above a velocity dispersion of $\log\sigma \sim 2.1$, galaxies exhibit a large intrinsic scatter in metallicity gradient, suggesting that mergers with widely varying characteristics dominate their formation histories.
- Galaxies with metal rich cores have steep negative ∇[Z/H] and a preference for ∇log(age) > 0. Galaxies with solar (or sub-solar) metallicity centres have ∇[Z/H] ~ 0 and ∇log(age) < 0.
- There is a strong anti-correlation between the gradient of age and metallicity, with a slope of –0.69 ± 0.19. While part of this observed trend can be attributes to the correlation of measurement errors, we demonstrate that there is an underlying intrinsic relation.
- Optical colours and colour gradients derived from the VIMOS spectroscopic age and metallicity are generally consistent with values obtained directly from imaging. Comparison between the spectroscopically and photometrically derived B–R gradients has a reduced $\chi^2 \sim 3.4$.
- We have briefly discussed a physical interpretation of these results in terms of the gas-rich and gas-poor merging history of early-type galaxies.

A larger set of IFU observations, probing more of the galaxy parameter space (particularly towards lower mass), is required to explore the relationship between the gradients further. Our results have successfully demonstrated the power of the integral field unit in measuring stellar population gradients for local cluster ($z < 0.05$) early-type galaxies.

Chapter 5

Stellar populations in S0 bulges and discs

This chapter presents an analysis of new, deep Gemini GMOS long-slit observations of seven S0 galaxies in the Coma Cluster. To test the hypothesis that S0s are transformed spirals, we analyse the kinematics and compare the galaxies to the spiral Tully-Fisher relation. We investigate the radial profiles of the absorption lines in both the bulge and disc. Finally, we explore the connection between the stellar population of the two structural components, focussing particularly on the age of the disc.

5.1. Introduction

The previous two chapters investigated internal gradients for early-type galaxies, a classification including both elliptical and lenticular objects. Many other studies have taken this approach (e.g. Mehlert et al., 2003; Sánchez-Blázquez et al., 2007), as S0 galaxies observed to the half-light radius are typically dominated by the bulge, which is akin to a low-luminosity elliptical galaxy (Thomas & Davies, 2006; Moorthy & Holtzman, 2006; Morelli et al., 2008).

Although the stellar content of an S0 galaxy is broadly similar to a quiescent elliptical galaxy, the structure and kinematics are generally comparable to spiral galaxies (Bedregal et al., 2006b). Turn off the star formation in a spiral galaxy, and within approximately 1 Gyr, an S0-like object is formed. With their spheroidal bulge and flat, mostly gas-free disc, S0s have long been postulated to be a transitional stage between spiral and elliptical

galaxies (Hubble, 1927; de Vaucouleurs, 1959). Possible mechanisms for this transformation include minor mergers, slow encounters, harassment, or some combination of these (Dressler & Sandage 1983; Neistein et al. 1999). However, as S0s make up the plurality of galaxies in rich local clusters (e.g. Dressler et al., 1987; Poggianti et al., 2009), many evolutionary mechanisms have been proposed in which the star formation in a spiral has been abruptly truncated by processes specifically related to cluster in-fall. Theories include starvation (removal of hot gas reservoirs via interaction with the intracluster medium; e.g. Larson et al. 1980; McCarthy et al. 2008), tidally-induced starbursts (Christlein & Zabludoff, 2004) and ram-pressure stripping of cold gas (Abadi et al., 1999). However, if S0s are the direct descendants of objects analogous to local spirals, then for a common environment, the luminosity distribution of S0s would be systematically fainter than spirals, and the bulge-to-disc ratios would be comparable. Instead, Burstein et al. (2005) and Sandage (2005) both showed that the typical surface brightness of S0s is greater than spirals, and Dressler (1980b) found that S0s have larger bulge-to-disc ratios. These studies suggest that S0 galaxies form via minor mergers, harassment or tidally-induced central starbursts, which would increase the stellar mass (Wilman et al., 2009). Recently, a population of obscured starburst galaxies were discovered in distant clusters, which may be the progenitors of the young S0s observed in nearby clusters (Geach et al., 2009).

Poggianti et al. (2001) measured the stellar populations of 33 S0 galaxies in the nearby Coma cluster, and found that 40 per cent had undergone star formation during the last $\sim$5 Gyr. Additionally, Dressler et al. (1997) found that the fraction of S0s in rich clusters at $z\sim0.5$ is 2–3 times smaller than in their local analogues, with a corresponding increase in the spiral fraction. This evidence implies that a large proportion of S0s were transformed from spirals over the last 5 Gyr.

For spiral galaxies, the Tully–Fisher relation (TFR; Tully & Fisher, 1977) is a strong correlation between luminosity (proportional to stellar mass) and the maximum rotational velocity. Several studies have investigated this relation for local S0s (Neistein et al., 1999; Bedregal et al., 2006a; Norris, 2008), and found that they have a systematic luminosity offset compared to the spiral population (in the B-band: -1.7 ± 0.4 mag compared to the Tully & Pierce 2000 TFR). As truncation of star formation would fade the galaxy disc (by failing to replenish the population with young, luminous stars), this was advocated as evidence for disc fading, with the increased scatter in the relation interpreted as differing epochs of truncation. S0s may form a continuum with other red spirals, which are

also offset from the Tully-Fisher relation (offset $\sim$ 0.5 mag for high rotational velocity Sa galaxies; Courteau et al., 2007; Pizagno et al., 2007). In contrast, the merger hypothesis struggles to explain the TFR offset unless the progenitor population was significantly different to the present day. However, the TFR for S0s is still controversial, with some studies (e.g. Hinz, Rieke, & Caldwell, 2003; Williams, Bureau, & Cappellari, 2009) finding no discernible luminosity offset from spirals, and a large scatter in the S0s TFR. These support a variety of scenarios to form the heterogeneous set of S0s observed.

Identification of the dominant formation mechanism can be achieved through stellar population analysis, as the resulting bulge and disc age and chemical abundance is process-dependent. For example, if discs grow around passive bulges until their gas is remove by stripping, then the resultant stellar discs will be younger than the bulges. Alternatively, tidal interactions with other galaxies, or with the cluster potential, could trigger gas flow from the disc to the galaxy centre and a consequent nuclear starburst. In this case, S0s would harbour young bulges as well as younger discs. Other mechanisms involve concurrent formation of the bulge and disc, resulting in similar observed ages. The metallicity and α-element enhancement are similarly useful as discriminants.

From spectroscopic observations of 20 S0 bulges, Fisher et al. (1996) concluded that the nuclear regions of S0s are typically a few Gyr younger than the outer regions. Their sample comprised S0s residing in the 'field' and low density groups/clusters, where gas stripping could not dominate. The estimates of Coma S0 ages derived by Poggianti et al. (2001) were from only the central $\sim$1.3 kpc, i.e. dominated by light from the bulge. Recent star formation activity in the disc itself was not investigated. The Mehlert et al. (2003) study of Coma early-types, including 13 S0s, used long-slit spectroscopy to derive central stellar populations and gradients. While they confirmed the presence of some S0s with young centres, they found negligible age gradients, implying that stellar populations at different radii must have formed at a common epoch. However, Mehlert et al. observed only four S0s to large enough radii to reach the disc dominated regime. In three cases the observed age of the disc was younger than the bulge, while the remaining galaxy displayed marginal evidence for an older disc.

In a more recent study, MacArthur et al. (2004) investigated the optical and near-infrared colour gradients of 172 disc-dominated galaxies, including 12 S0s from Bell & de Jong (2000). They found that while the optical (B–R) colours for the bulge and disc were similar in each S0, the optical–near-IR colour (R–K) of the disc was significantly (0.2–0.3

mag) bluer. In contrast, the discs of spiral galaxies in the sample were ~0.25 mag bluer in both B–R and R–K. The R–K colour gradient in S0s was interpreted as a gradient in both age and metallicity (although a significant reddening by dust could not be ruled out). Finally, MacArthur et al. found that the age (and to a lesser extent metallicity) show steeper gradients in the inner regions of S0 galaxies compared to the disc.

Previous studies of the disc-dominated regions in rich cluster S0 galaxies have thus been limited in the radial extent of the observations. In this study, we analyse deep GMOS long-slit spectroscopy of seven S0 galaxies in the Coma cluster. We probe out to several disc scale lengths, to determine the stellar population profiles in both their bulge *and* disc components. We start by summarising the sample and observations (Section 5.2). Section 5.3 describes the data reduction, decomposition of the structural components and kinematic measurements. In Section 5.4, we discuss the results in terms of the Tully-Fisher relation and explore the stellar population profiles of each component in the context of the formation scenarios described above. The conclusions are summarised in Section 5.5.

5.2. The data

5.2.1 GMOS Coma cluster sample

The sample consists of seven edge-on S0 galaxies in the nearby Coma cluster (Abell 1656; $< cz_{cmb} > \approx 7200$ km s^{-1}), as listed in Table 5.1. Each galaxy is a confirmed cluster member and was morphologically classified as lenticular (S0) by Dressler (1980a, D80). Two of the targets (GMP1176 and GMP1853) were observed in the long-slit study of Mehlert et al. (2000, 2003). The original GMOS sample consisted of 12 S0s, but was not completed due to poor weather and scheduling constraints.

The galaxies were selected to cover a range in luminosity (m_r = 13.0 – 15.5) and lie on the red sequence, as shown in Figure 5.1. They are located at various cluster radii, in order to probe the effect of local environment (see Figure 5.2). However, the sample was not intended to be complete, or evenly cover a particular parameter, as the study was conceived to assess the effectiveness of the analysis technique. Each galaxy was examined in optical imaging, and visually classified as an 'optimum' edge-on S0 by confirming a break in the smooth surface brightness profile. Six of the seven galaxies appeared to have a prominent bulge and an extended disc with a g-band surface brightness $\mu_r > 22$

Table 5.1: The Coma cluster (Abell 1656) S0 galaxy sample observed with GMOS. GMP ID from Godwin, Metcalfe, & Peach (1983). Position (in decimal degrees), position angle (PA) and r- and g-band photometry from SDSS. Heliocentric velocity ($cz_{\rm hel}$ km s^{-1}) and observed maximum rotation velocity ($V_{\rm obs}$ km s^{-1}), as measured in Section 5.3.3.

GMP ID	NGC	RA	Dec	PA	m_r	g–r	$cz_{\rm hel}$	$V_{\rm obs}$
	#	(J2000)	(J2000)	(deg)	mag	mag	(km s^{-1})	(km s^{-1})
GMP1176	4931	195.7536	28.0325	77.7	13.06	0.74	5344	195.0
GMP1504		195.5897	28.2308	239.1	14.34	0.76	5569	149.4
GMP1853		195.4459	28.0950	87.2	14.09	0.80	5808	191.8
GMP2219		195.3012	27.6045	312.3	15.48	0.78	7581	111.1
GMP2584		195.1482	28.1461	169.3	14.88	0.73	5449	123.1
GMP2815	4894	195.0688	27.9675	212.3	14.90	0.71	4635	103.7
GMP5160		194.2357	28.6234	99.4	14.70	0.74	6581	136.5

mag arcsec^{-2} (see Section 5.3.2 for the final bulge/disc decomposition). An abundance of ancillary data is available for each galaxy, including deep optical imaging from the CFHT MegaCam and *GALEX* ultraviolet imaging.

5.2.2 GMOS observations

This investigation uses long-slit spectroscopy from the Gemini Multi-Object Spectrograph (GMOS; Hook et al., 2004) on the Gemini-North telescope, Mauna Kea (program: GN-2009A-Q-52; PI: J Lucey). GMOS was operated with the B1200 grating and a 2 arcsec wide slit, resulting in a spectral resolution of 5.1 Å FWHM. The full instrument configuration is summarised in Table 5.2.

For a successful exploration of the disc-dominated region of these S0 galaxies, we needed to probe to a g-band surface brightness μ_r ~23 mag arcsec^{-2}. Derivation of reliable stellar population parameters requires a signal-to-noise ratio (S/N) > 30 Å^{-1}. To achieve this, we devoted three hours of observing time to each target, with four exposures of 2380 s (9520 s in total) on-source. For each observation, the slit was centred on the S0 bulge and orientated along the disc major axis.

The galaxies were observed during dark time in March and April 2009. The seeing was < 1.0 arcsec (FWHM) for all observations, and better than 0.8 arcsec for all galax-

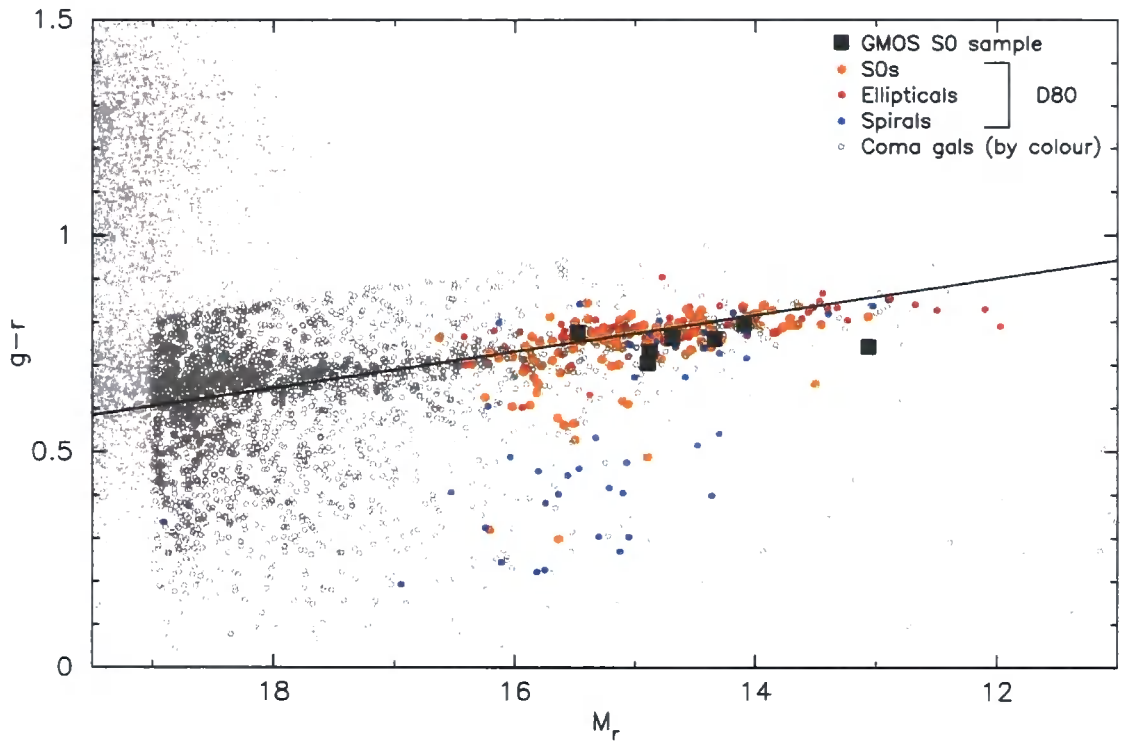

Figure 5.1: SDSS g–r colour–magnitude relation for Coma galaxies. The GMOS S0 sample are shown as black squares. Coma cluster galaxies included in the morphological catalogue of Dressler (1980a, D80) are displayed as filled circles (see key), with the red sequence indicated by a solid line. Probable Coma galaxies in SDSS (complying with the cuts $m_r < 19$ mag and g–$r < -0.04 \times m_r + 1.6$) are shown as open circles; other SDSS sources are indicated by grey dots.

Table 5.2: GMOS instrument configuration.

Mode	Long-slit
Grating	B1200
Slit width	2 arcsec
Slit length	330 arcsec
CCD binning	4×4
Wavelength range	4060 – 5522 Å
Spectral resolution	5.1 Å FWHM
	($\sigma \sim 136$ km s^{-1})
Spectral sampling	~0.95 Å pixel^{-1}
Spatial sampling	0.2908 arcsec pixel^{-1}

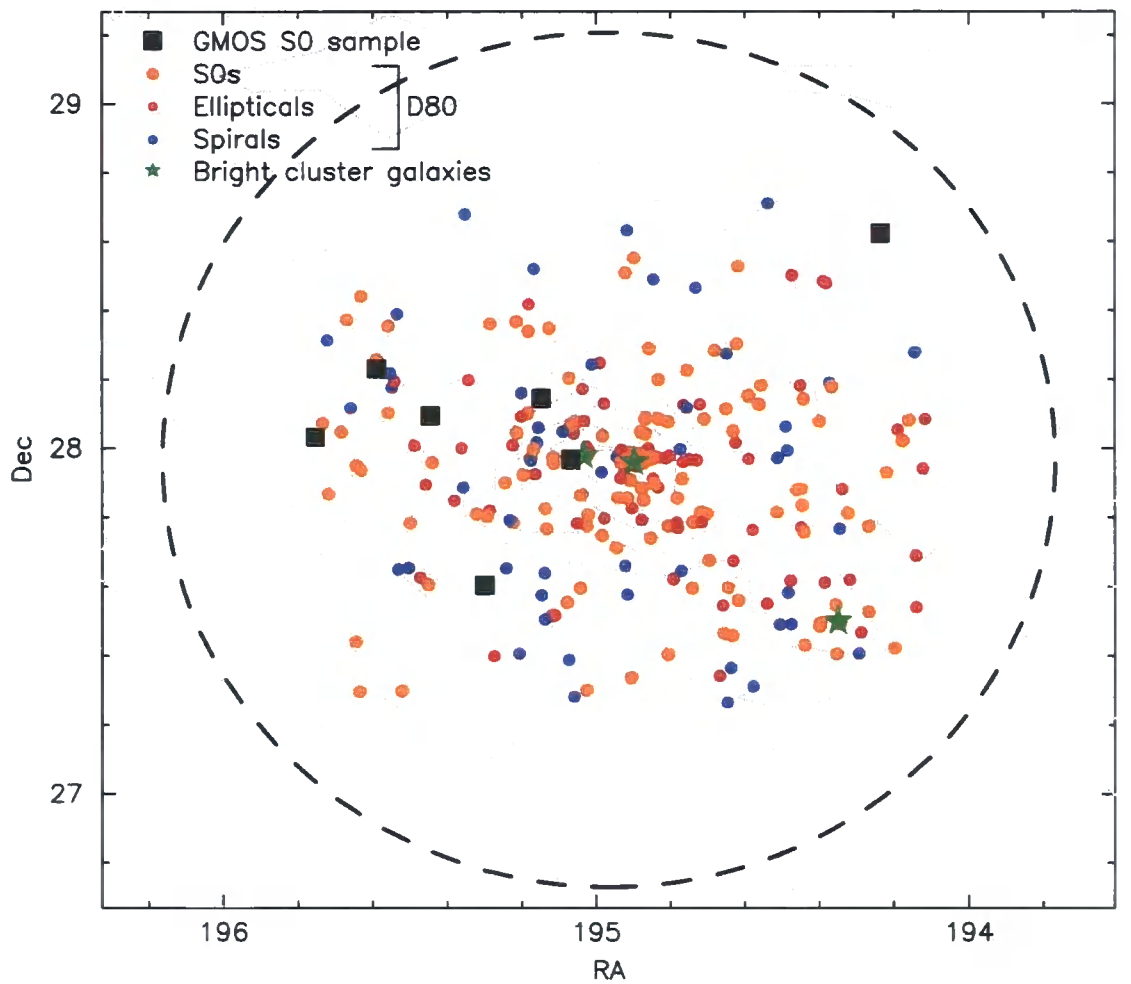

Figure 5.2: The seven GMOS S0 sample galaxies (black squares) in the Coma cluster core field (dashed line has a 2 Mpc radius, $\sim$ the cluster virial radius). Green stars indicate the three bright cluster galaxies (left-to-right) NGC4889, NGC4874 and NGC4839. Coma cluster galaxies included in the D80 catalogue are shown by filled circles (see key). Contours illustrate the projected local density of galaxies (using 0.18×0.18 deg bins), showing that our targets are distributed between the high density centre and less dense outer regions.

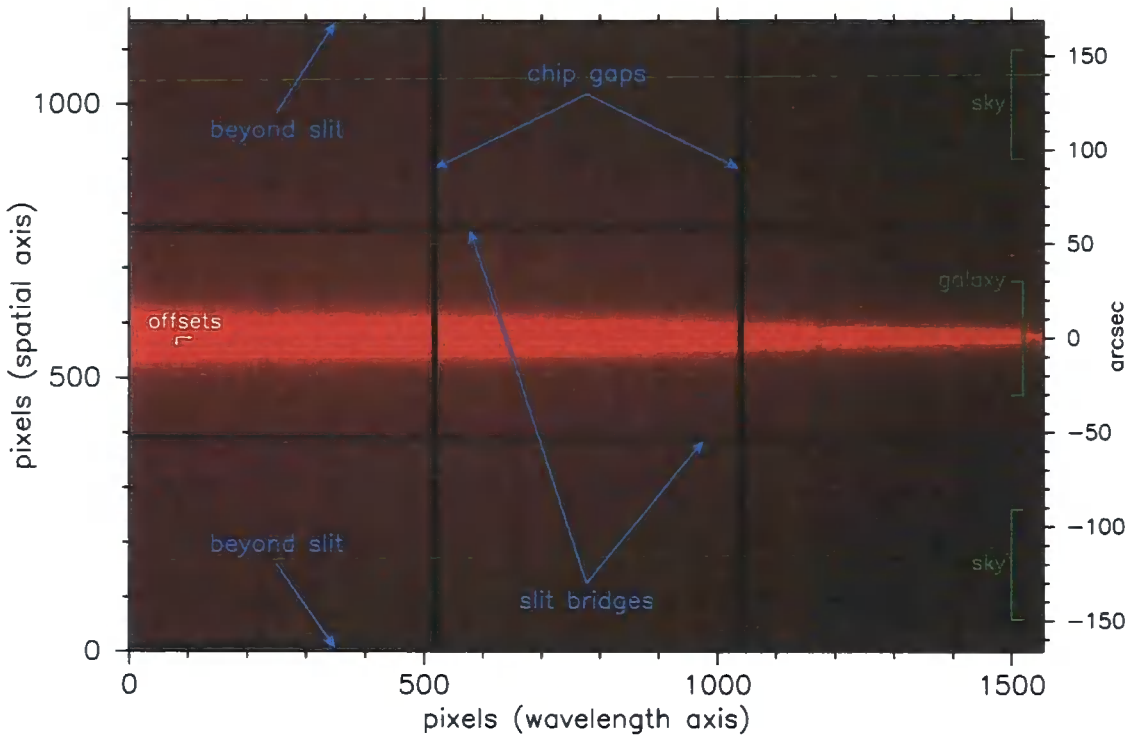

Figure 5.3: GMOS raw detector output (for an example exposure of GMP1176), highlighting the chip gaps, slit bridges and unexposed pixels at either end of the slit. The magnitude of the exposure-to-exposure offsets are indicated by the small white arrows. The maximum spatial extent of any sample galaxy is shown by the central green brace, and the regions used to calculate the sky background are also indicated. The frame is shown prior to wavelength transformation; the red end is towards the left.

ies apart from GMP1504 and GMP1853. GMP5160 was observed in particularly cloudy conditions, so the co-added frame does not quite reach the target surface brightness.

The GMOS detector consists of a three chip array, with gaps ($\sim$ 39 pixels wide) perpendicular to the wavelength axis. Additionally, the slit shape is stabilised by two bridges, which divide the slit into three equal segments of $\sim$110 arcsec, and results in 20 unexposed pixels perpendicular to the spatial axis. To avoid discontinuities due to these gaps and bridges, each set of four exposures contained a spatial and wavelength offset. The wavelength offset was 30 Å, with the central wavelengths for each target individually tailored according to redshift, to avoid losing signal in important spectral features. The spatial offset was less important as the observable extent of each target ($\sim$10 – 30 arcsec) sits well within the central third of each chip (therefore unaffected by the bridges). However, to reduce the impact of dead pixels, we introduced a 5 arcsec offset along the slit

(~17 pixels). Figure 5.3 presents an example raw GMOS frame, indicating the detector features and the offsets in each axis.

We chose the slow readout and low gain modes, to minimise readout noise (~3.3 counts rms). Sky background is expected to be the largest noise contribution when investigating low surface-brightness features, so maximising the on-source exposure time was crucial. Separate sky exposures were deemed unnecessary, as the spatial extremes of the slit have no contamination from the target galaxy.

5.3. Data reduction

5.3.1 Initial reduction

The initial data reduction used the standard Gemini GMOS IRAF routines. Given bias and flat field frames, an arc lamp exposure and GMOS_B1200 grating calibration file, the routines successfully removed cosmic rays, normalised and mosaiced together data from the three chips, and produced wavelength-calibrated science exposures. Each exposure was rebinned to 1 Å pixels and restricted to the wavelength range 4000 - 5500 Å, to facilitate the final combination. The average sky background for each wavelength slice was calculated from a linear fit to 400 spatial pixels at the extremes of the detector array (see Figure 5.3). Flux calibration was achieved with reference to the response curve calculated from observations of the spectroscopic standard star Hiltner 600. The final combined frame was computed from the pixel-to-pixel mean, with outliers rejected by 3σ clipping about the median.

Variance frames were calculated from the quadrature sum of the Poisson noise in the raw detector counts and the read noise, and propagated through the same mosaic and flux calibration routines. We have assumed that the noise associated with bias and flat field frames is negligible.

GMOS scattered light

Visual inspection of the raw detector frames showed that the unexposed pixels in the slit bridges and beyond the slit ends do not have zero counts. The cause of this phenomenon is scattered light in the instrument, most likely due to the classically ruled grating (see Norris et al., 2006), which is not accounted for in the standard reduction

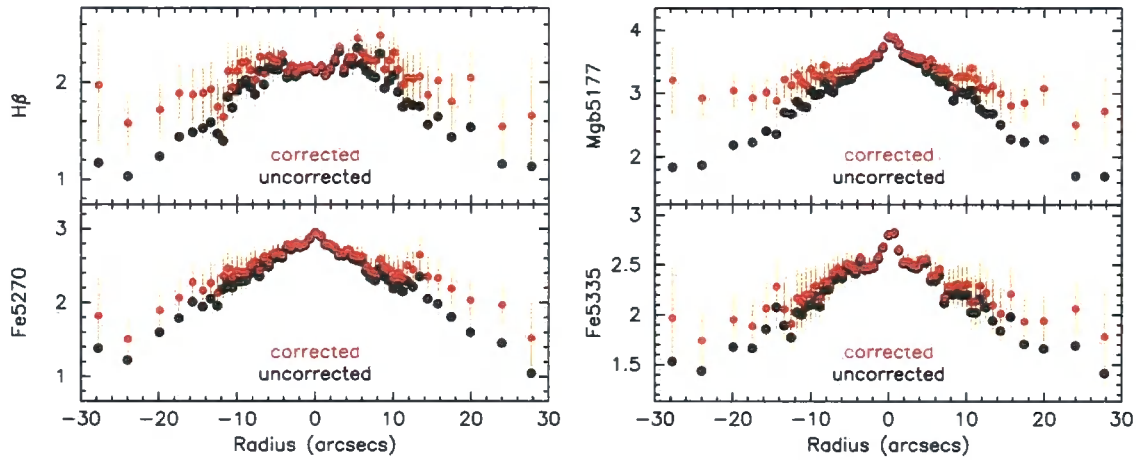

Figure 5.4: The effect of scattered light on the radial trends of absorption line strengths (Hβ, Mgb5177, Fe5270, Fe5335) measured for GMP1176. Scattered light adds a constant offset to the continuum level, which decreases the line measurements in outer regions to a larger extent than in the centre, strengthening the observed gradients.

routines. The scattered light appears as a featureless constant offset which artificially enhances the continuum level, thus decreasing the measured absorption line strengths. The effect is increasingly significant as the galaxy surface brightness decreases ($\sim$50 percent of the measured flux in the outer regions of the galaxy), so scattered light tends to spuriously strengthen index gradients. For an example galaxy (GMP1176), Figure 5.4 shows the radial trend in four absorption indices (see Section 5.4.2 for the measurement technique), before and after accounting for the scattered light. The scattered light significantly inflates the line strength gradients by weakening the indices at large radii, and the correction is obviously important for this study.

To quantify the scattered light in each raw exposure, the flux was measured in the unexposed regions (slit bridges and ends). For each wavelength pixel, we interpolated between these regions (using two linear fits) to calculate the scattered light frame. Figure 5.5 shows the interpolated scattered light along the spatial axis, for an arbitrary wavelength slice. The correction removes the inflated wings of the integrated surface brightness profile. During the reduction described above, the scattered light frame is subtracted from the raw image before wavelength calibration.

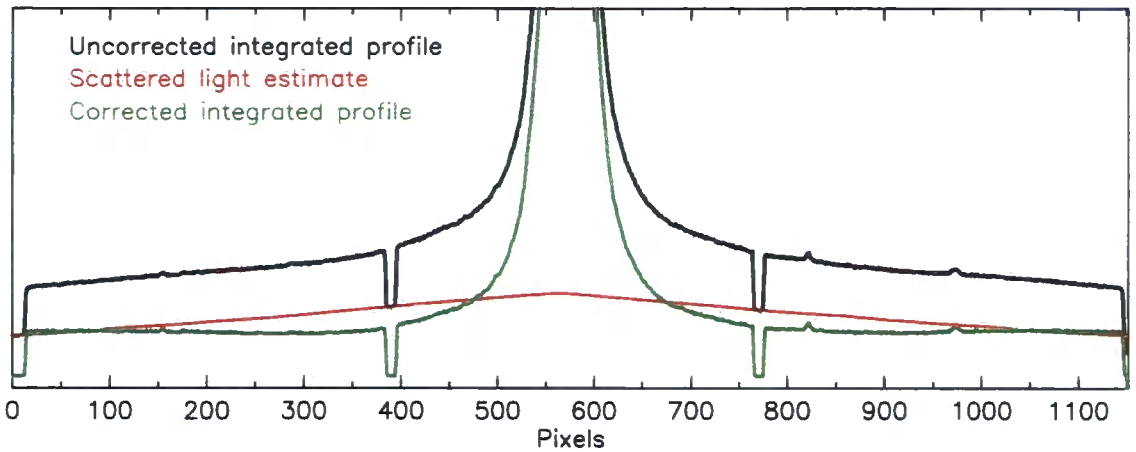

Figure 5.5: The integrated brightness profiles of the uncorrected (black) and corrected (green) frames for GMP1176. The red line shows the scattered light correction profile, as interpolated from the unexposed slit bridges and ends.

5.3.2 Bulge and disc decomposition

Parametrization of the bulge and disc components of each S0 target was accomplished using deep g-band imaging from MegaCam (pixel scale = 0.187 arcsec pixel^{-1}). The decomposition employed the GALFIT algorithm (Peng et al., 2002), which fits multiple analytic components to the two-dimensional light distribution of a galaxy. GALFIT obtains the best fit by minimising the residuals between the real input data and an image formed from the model parameters. The point spread function (PSF) of the observation is accounted for by convolving the model data with a model PSF (estimated from a nearby star on the same CCD image) before calculating the residuals.

We fitted a two component model combining a Sérsic profile (the bulge) with an exponential profile (the disc). Each component is parametrized by a scale length, inclination and, for the bulge, the Sérsic index. The bulges were forced to a Sérsic index $n \leq 6$, and ellipticities[1] were limited to a maximum of 0.9. Table 5.3 lists the resulting two component parameters from the GALFIT decompositions. Assuming an intrinsic edge-on disc axis ratio q_0 = 0.22 (de Vaucouleurs et al., 1991), the inclination can be computed by

$$i = \arcsin\left(\sqrt{\frac{1-q_0^2}{2e-e^2}}\right) \tag{5.1}$$

The ellipticities calculated through the decomposition confirm that this sample of S0s are all edge-on (i = 75 – 90 deg).

[1] e = 1 – (semi-minor axis / semi-major axis)

Table 5.3: Bulge and disc parameters for the GALFIT decomposition. The bulge was fit by a Sérsic profile, limited to $n \leq 6$, and additionally parametrized by the effect radius r_e and ellipticity, e. The disc was fit by an exponential profile, parametrized by the exponential scale-length r_{exp} and ellipticity, e. The disc inclination angle i assumes an intrinsic axis ratio of $q_0 = 0.22$ (de Vaucouleurs et al., 1991).

GMP ID	Sérsic bulge			Exponential disc			Type
	r_e (arcsec)	Sérsic n	e	r_{exp} (arcsec)	e	i (deg)	
GMP1176	13.3	6.0	0.57	3.4	0.90	~90	(3)
GMP1504	1.4	4.4	0.21	3.9	0.71	79	(1)
GMP1853	2.2	3.0	0.36	6.8	0.81	~90	(1)
GMP2219	7.3	3.2	0.60	4.3	0.89	~90	(2)
GMP2584	2.3	4.6	0.11	5.7	0.85	~90	(1)
GMP2815	0.8	1.5	0.16	4.4	0.67	75	(1)
GMP5160	5.6	6.0	0.29	4.1	0.80	~90	(2)

Type (1) – 'classic' S0: small bulge, disc dominating at large radii

Type (2) – extended bulge, disc dominating at large radii

Type (3) – bulge dominated at all radii

The luminosity profile of each component was computed numerically by integrating along a 2 arcsec major axis slit in the best fitting model image. Figure 5.6 shows the bulge, disc and total luminosity profiles for each galaxy. Examining these best-fit two component decompositions, the relative size of the bulges in this sample vary widely, and can be separated into three distinct types. The 'classic' S0s (GMP1504, GMP1853, GMP2584, GMP2815) have bulges dominating the luminosity at small radii, and significant discs at large radii, where $r_{\rm exp} > 2 \times r_{\rm e}$ (see Table 5.3). The second class show extended bulges with $r_{\rm e} \gtrsim r_{\rm exp}$ (GMP2219, GMP5160), although the discs still dominate the surface brightness profile at large radii. The final type, exemplified only by GMP1176, has a large bulge and a small embedded disc ($r_{\rm e} \gg r_{\rm exp}$) which only contributes a small fraction of the light at any given radii. Two of the most bulge-dominated galaxies (GMP1176 and GMP5160) have bulge Sérsic indices = 6 (the imposed upper-limit). These galaxies may be better fit by a three-component model including a large-scale spherical halo, although that is beyond the scope of the current study. The selection criteria we employed to observe optimum 'classic' S0s was successful in 6 out of 7 cases. Apart from GMP1176, the observation limit on the g-band surface brightness ($\sim$23 mag arcsec^{-2}) enables us to probe into the disc dominated regime.

5.3.3 Spatial binning and kinematics

The required S/N in each spectrum (S/N $>$ 30 Å^{-1} for absorption line analysis) was acheived by binning the data along the slit, using a simple adaptive algorithm. The analysis requires spatial sampling of both the bulge and disc components, so the bin widths are as small as possible, while still meeting the target S/N. In practice, the innermost bins have many times the required S/N, whilst the outer bins only marginally surpass the target (the outermost bin in some galaxies may not always exceed the S/N; see Figure 5.7). The bins were symmetrical about the galaxy centre, so each pair at an equal radii could be summed together, decreasing the necessary bin width. Before combining the bins at equal radii, both spectra were de-redshifted to account for the differential effect of the rotational velocity.

Absorption line kinematic analysis does not require such a high S/N as the line strengths, so we measured the mean velocity and velocity dispersion (V, σ) of each bin before combining the two sides (S/N $>$ 21 Å^{-1}). We used the PPXF algorithm for the kinematic analysis, which is described in Section 3.3.3. The two central panels of Figure

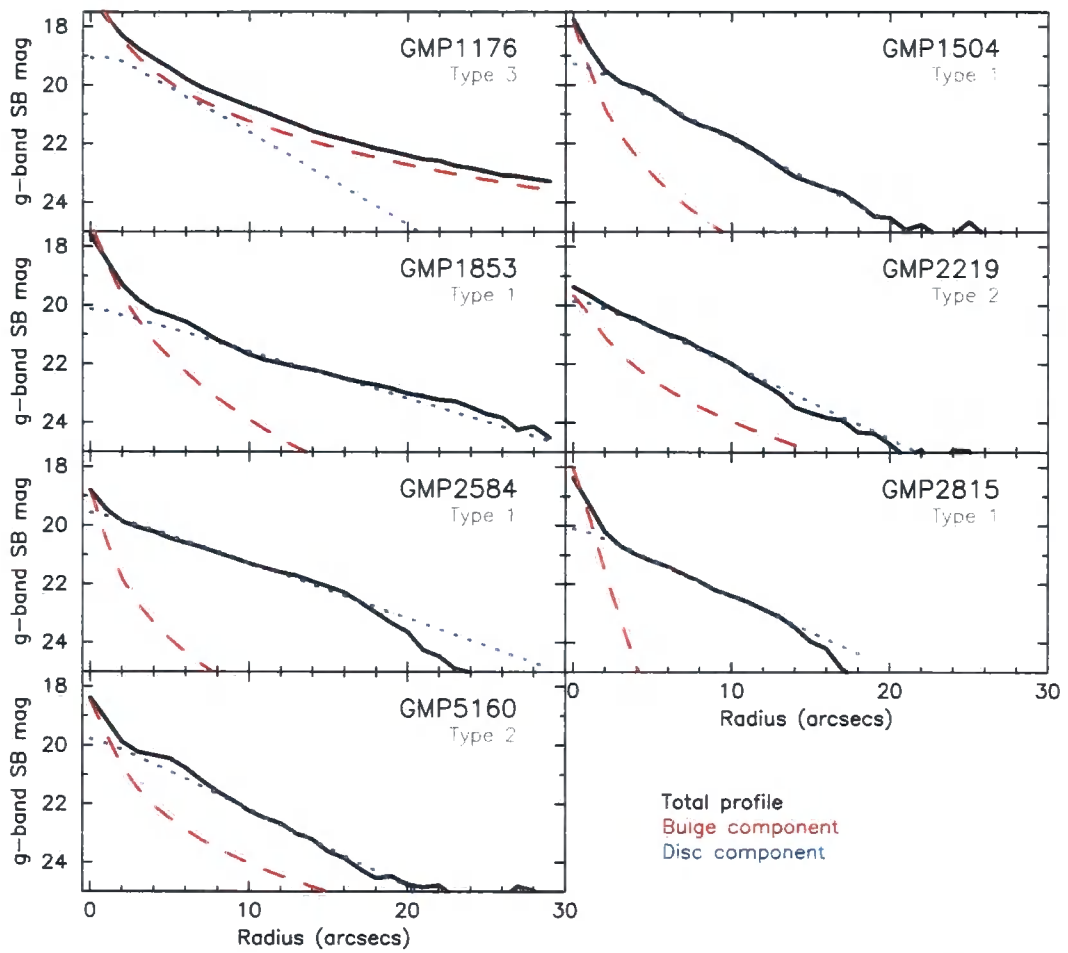

Figure 5.6: The observed g-band surface brightness profile for each galaxy (black line). The profiles for the model bulge (red dashes) and disc (blue dots) components, as derived using GALFIT, are superimposed. The dashed horizontal line indicates the approximate limit of the GMOS observations (23 mag arcsec^{-2}). The galaxy name is indicated at the top of each panel, and the structural types are described in Table 5.3.

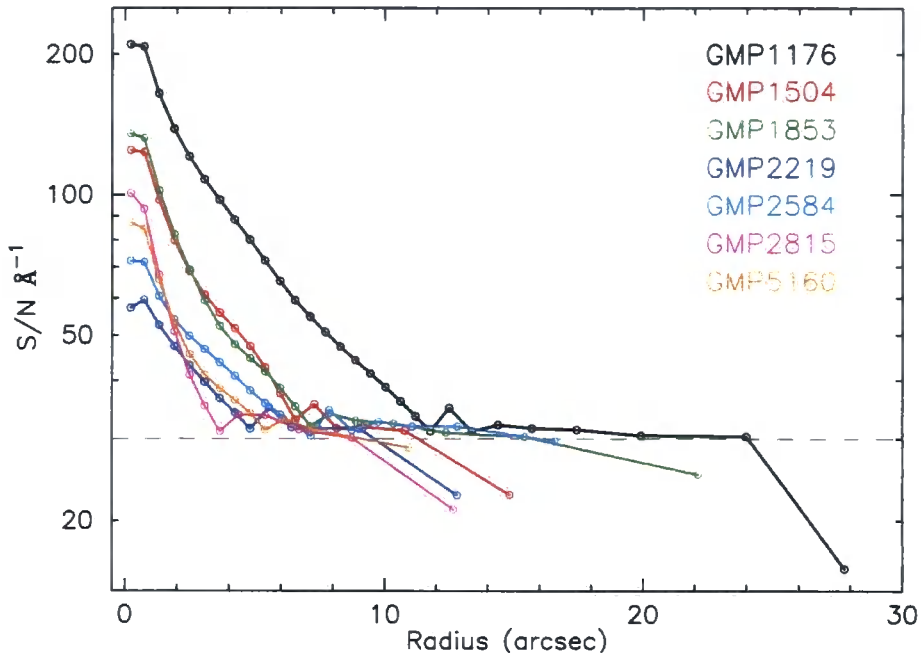

Figure 5.7: Signal-to-noise ratio in each spatial bin (both sides combined). Points indicate the bin centre, and galaxies are identified by colour. The required S/N (30 Å^{-1}) is shown by the grey dashed line.

5.8 present the observed rotational velocity and velocity dispersion of GMP1176 (the upper panel repeats the surface brightness profiles for comparison). Figure 5.9 shows the similar plots for the more typical S0 galaxy, GMP1504 (this section uses GMP1176 and GMP1504 as examples throughout), and equivalent figures for the other galaxies can be found in Appendix D. The final column of Table 5.1 lists the observed maximum rotational velocity for each galaxy.

The galaxies all show rotation, with a maximum $V_{\rm obs}$ of 100 – 200 km s^{-1}, and every GMOS observation probes beyond the turn-over point. Two of the galaxies show significant maximum velocity dispersions of ~150 km s^{-1} (GMP1176, GMP1853), while an additional two (GMP1504, GMP5160) have maximum $\sigma_{\rm obs} \sim 50$ km s^{-1} (approximately the resolution limit). The remaining three galaxies have no significant velocity dispersion, and it is interesting to note that they have the least peaky bulge surface brightness profiles (GMP2219, GMP2584 and GMP2815; Figure 5.6).

Derivation of circular velocities

In disc galaxies, the fundamental velocity parameter is the maximum circular velocity. Deriving the circular velocity from observed velocity is model-dependent, and we

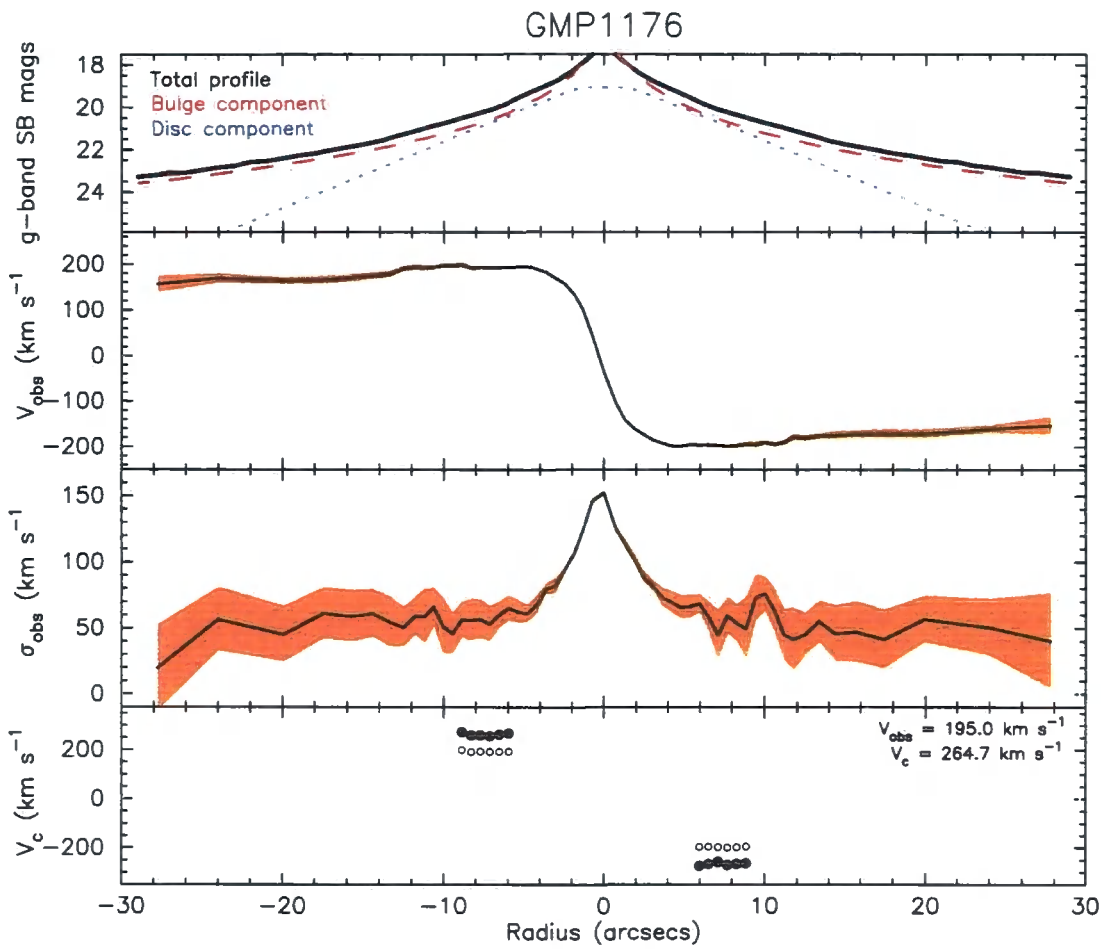

Figure 5.8: Kinematic profiles for GMP1176. Upper panel: g-band surface brightness profiles for the bulge (red dashes) and disc (blue dots) components (as in Figure 5.6). Central panels: observed rotational velocity ($V_{\rm obs}$) and velocity dispersion ($\sigma_{\rm obs}$). $1\,\sigma$ errors are indicated by orange shading. Lowest panel: open circles show observed velocities, and filled circles show the circular rotation velocity (V_c, see text for details). The maximum values of $V_{\rm obs}$ and V_c are given in the top right.

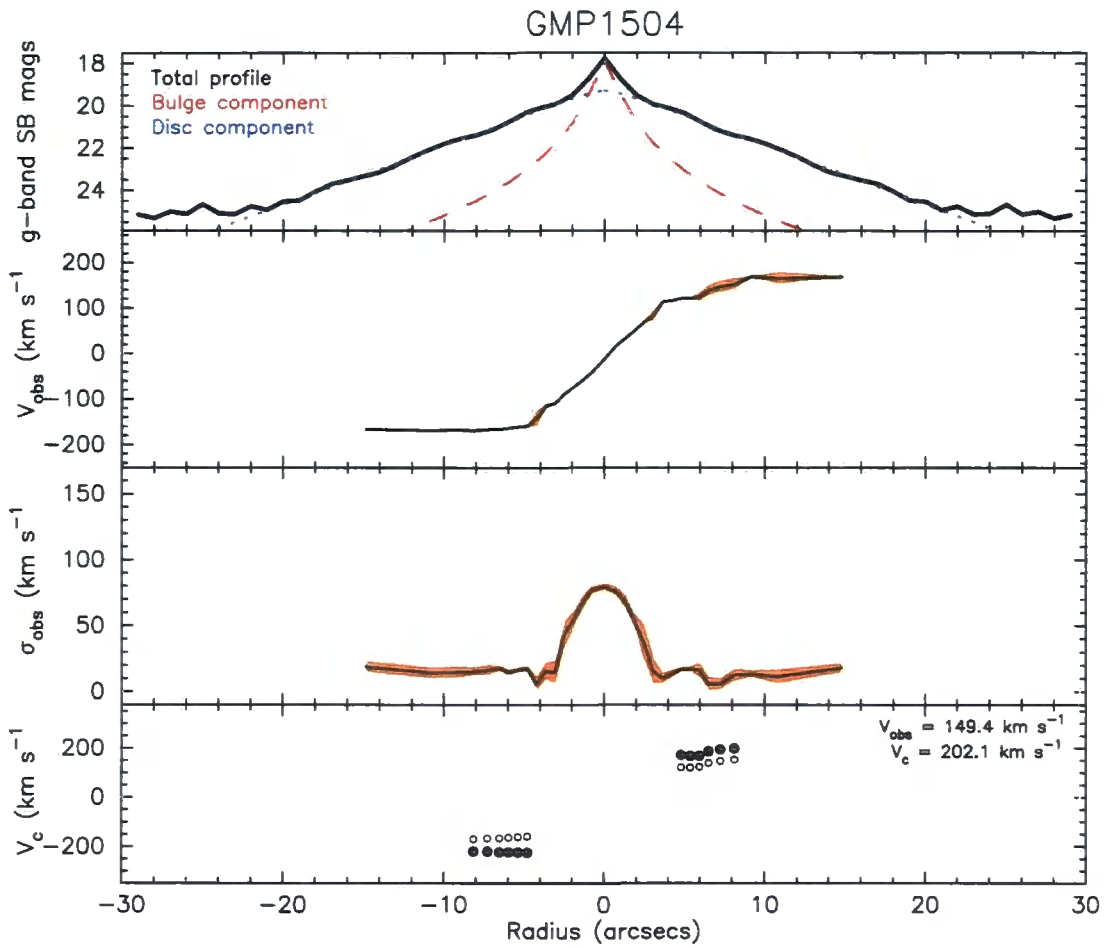

Figure 5.9: Kinematic profiles for GMP1504. Layout as in Figure 5.8. Note that for this galaxy, V_c is uncorrected for asymmetric drift; see text for details.

have used the prescription described in Neistein et al. (1999), implemented in numerous S0 studies: Hinz, Rieke, & Caldwell (2003); Bedregal, Aragón-Salamanca, & Merrifield (2006a); Norris (2008). For edge-on S0 galaxies (those with disc inclinations $i > 67$ deg), two steps are required to calculate the circular velocity at a given radius. First, we compute the kinematics in the azimuthal (ϕ) direction by accounting for line-of-sight integration through the disc. For an exponential disc with a scale height $h_s = 0.2r_{\rm exp}$, Neistein et al. computed the corrections as

$$V_\phi(r) = \frac{V_{\rm obs}(r)}{f(r/r_{\rm exp})} \tag{5.2}$$

$$\sigma_\phi(r)^2 = \sigma_{\rm obs}(r)^2 - \frac{1}{2}(V_\phi(r) - V_{\rm obs}(r))^2 \tag{5.3}$$

where

$$f(x) = \frac{exp(-x)}{-0.5772 - \ln x + x - \frac{1}{2}x^2/2! + \frac{1}{3}x^3/3! - ...} - x \tag{5.4}$$

(V_ϕ,σ_ϕ) are the corrected azimuthal values, and ($V_{\rm obs}$,$\sigma_{\rm obs}$) are the observed values. For inclinations $i > 70$ deg, the error due to assuming $i = 90$ deg is $\Delta \log V_\phi \sim 0.025$. In all but one of the Coma S0 galaxies presented here (GMP1176; see Figure 5.8, lowest panel), the observed velocity dispersion corresponding to the flat rotation curve region is less than half of the GMOS instrument resolution ($\sim$ 136 km s^{-1}), and we were unable to determine σ_ϕ.

The second stage corrects for 'asymmetric drift'. Although the net velocity of stars is zero in the vertical and radial directions, the average velocity in the azimuthal direction is not equal to the local circular velocity. The greater the random velocity for individual stars, the larger the lag between net motion and circular velocity. Neistein et al. (1999) corrected for this effect using the formula

$$V_{\rm c}(r)^2 = V_\phi(r)^2 + \sigma_\phi(r)^2 \left(2\frac{r}{r_{\rm exp}} - 1\right) \tag{5.5}$$

The maximum circular velocity is calculated by taking the mean value of all V_c data points lying on the flat portion of the rotation curve (generally $1.5 < r/r_{\rm exp} < 2.5$). For the approximations in the asymmetric drift correction to hold, all points also have to conform to the constraint $V_\phi/\sigma_\phi > 2.5$. For the galaxies with no computed σ_ϕ, we were unable to correct for asymmetric drift and, when quoting V_c for these galaxies (see Figure 5.9 and the final column of Table 5.4), we have given V_ϕ. However, as $V_{\rm c} \approx V_\phi$ if $\sigma_{\rm obs} \to 0$, this should not lead to a significant under-estimation. To test this, we used the uncorrected

$\sigma_{\rm obs}$ to account for the asymmetric drift (which over-estimates the correction). The difference between this $V_{\rm c}$ and V_{ϕ} was < 10 per cent of the uncertainty on the values, so will not have a significant effect on any conclusions.

5.4. Analysis and discussion

This study primarily investigates variation in the stellar populations of the S0 bulge and disc. However, before embarking on that aspect of the spectral analysis, we explore the Tully-Fisher relation for S0 galaxies (Section 5.4.1). In Section 5.4.2, we investigate the radial trends in the absorption line features, paying particular attention to the difference between the structural components. Section 5.4.3 extends this analysis by deriving the radial profiles in the stellar population age, metallicity and α-abundance from the absorption lines. Finally, in Section 5.4.4, we link the disc age to the Tully-Fisher relation.

5.4.1 The Tully-Fisher relation

The Tully-Fisher relation (TFR) relates the luminosity of spirals to their maximum circular velocity. S0s are thought to be spirals in which the star formation has been quenched. If this is the case, the ageing stellar population of the disc will result in a decrease in luminosity. In contrast, the galaxy mass (and hence rotational velocity) should remain constant, causing an offset between the spiral and S0 TFRs.

We consider the TFR in the B-band. For the S0 sample presented here, we have converted SDSS g- and r-band photometry to the B-band using the formulae in Table 5.4. The magnitudes are corrected for Galactic extinction using the reddening maps of Schlegel et al. (1998), and we adopt the distance modulus to Coma of 35.05 $\pm$ 0.15 mag (from NED; corrected for the flow model including the Virgo cluster and Great Attractor). No internal extinction correction was applied, as the amount of dust in S0s is thought to be small. The maximum circular velocity was calculated in Section 5.3.3. Table 5.4 lists the TFR parameters for our sample of Coma S0s.

Figure 5.10 presents the Tully-Fisher relation for these S0s. For reference, the spiral galaxy TFRs from three independent studies (Tully & Pierce, 2000; Sakai et al., 2000; Meyer et al., 2008) are indicated. We calculate the S0 TFR offset by fixing the slope to each spiral TFR in turn (slopes of –7.27, –7.97, –8.07 respectively). Assuming the difference is entirely due to luminosity, the offsets from these spiral relations are –1.35 $\pm$ 0.16, –1.11

Table 5.4: Tully-Fisher relation parameters for the Coma S0 galaxies. B-band magnitudes derived from SDSS r- and g-band photometry. A_B extinction from NED, using the reddening maps of Schlegel et al. (1998). M_B is the extinction-corrected absolute magnitude. Maximum circular velocity (V_c km s^{-1}) as calculated in Section 5.3.3.

GMP ID	m_B	A_B	M_B	V_c
	mag	mag	mag	km s^{-1}
GMP1176	14.25 ± 0.03	0.04	−20.75 ± 0.15	265 ± 20
GMP1504	15.56 ± 0.02	0.04	−19.44 ± 0.15	203 ± 7
GMP1853	15.36 ± 0.04	0.04	−19.72 ± 0.15	257 ± 29
GMP2219	16.72 ± 0.02	0.03	−18.35 ± 0.15	152 ± 15
GMP2584	16.06 ± 0.02	0.05	−19.03 ± 0.15	166 ± 24
GMP2815	16.05 ± 0.01	0.04	−19.03 ± 0.15	143 ± 17
GMP5160	15.89 ± 0.03	0.05	−19.20 ± 0.15	187 ± 28

$m_B = m_r + 1.31(g-r) + 0.22$ (Jordi et al., 2006)

$A_B = 4.32 \times E(B-V)$ (Cardelli et al., 1989)

$M_B = m_B - A_B - \mu_{\rm Coma}$

$\mu_{\rm Coma} = 35.05 \pm 0.15$ mag, adopted from NED (Virgo+GA)

Table 5.5: Luminosity offset between the spiral and S0 Tully-Fisher relations. Offset of the TFR for each S0 sample (and combinations of samples), fixed to the slope of the spiral TFRs by Tully & Pierce (2000), Sakai et al. (2000) and Meyer et al. (2008) in turn.

Sample	Location	$n_{\rm gals}$	S0 TFR offsets (mag)		
			Tully & Pierce	Sakai et al.	Meyer et al.
This study	Coma	7	−1.35 ± 0.16	−1.11 ± 0.17	−1.56 ± 0.18
Hinz et al. (2003)	Coma	11	−1.66 ± 0.15	−1.47 ± 0.15	−1.93 ± 0.17
Hinz et al. (2003)	Virgo	8	−1.70 ± 0.13	−1.43 ± 0.13	−1.88 ± 0.14
Bedregal et al. (2006a)	Fornax	7	−1.54 ± 0.19	−1.22 ± 0.18	−1.67 ± 0.19
Norris (2008)	Local	18	−1.74 ± 0.14	−1.58 ± 0.14	−2.05 ± 0.14
Neistein et al. (1999)	Local	18	−1.51 ± 0.14	−1.34 ± 0.17	−1.80 ± 0.17
This study + Hinz et al.	Coma	18	−1.54 ± 0.13	−1.33 ± 0.13	−1.79 ± 0.12
Combined sample	–	69	−1.61 ± 0.11	−1.39 ± 0.11	−1.85 ± 0.11

± 0.17, −1.56 ± 0.18 mag respectively (see first row, Table 5.5). Recalling that six of the seven S0s have $V_{\rm c}$ uncorrected for asymmetric drift (Section 5.3.3), it is worth noting that this would lead to an underestimation, meaning that the offset may be slightly larger for these galaxies. To increase the number of S0 galaxies, we combine our sample with four previous works: Neistein et al. (1999); Hinz, Rieke, & Caldwell (2003); Bedregal, Aragón-Salamanca, & Merrifield (2006a); Norris (2008). Hinz et al. compiled the TFR for 8 S0s in the Virgo cluster and 11 in Coma; there is no overlap with galaxies in our study. For the Hinz et al. S0s, we have computed the B-band luminosity from SDSS photometry, as described above. Bedregal et al. observed seven S0s in Fornax, while both Neistein et al. and Norris studied local S0s in a variety of environments, with heliocentric velocities $<$ 2000 km s^{-1} and $<$ 4000 km s^{-1} respectively.

Table 5.5 presents the TFR luminosity offset for each individual sample (and combinations therein). There is a clear offset between the spiral and S0 TFRs: −1.61 ± 0.11, −1.39 ± 0.11, −1.85 ± 0.11 mag between the whole S0 sample and Tully & Pierce, Sakai et al., Meyer et al. respectively. The maximum circular velocity relies on kinematic observations beyond the turn-over of the galaxy rotation curve. Measuring $V_{\rm c}$ from a radius inside the turn-over, would lead to an underestimated velocity parameter. Although random error on the magnitudes is small, instrument/filter zero-points, bandpass conversion and the

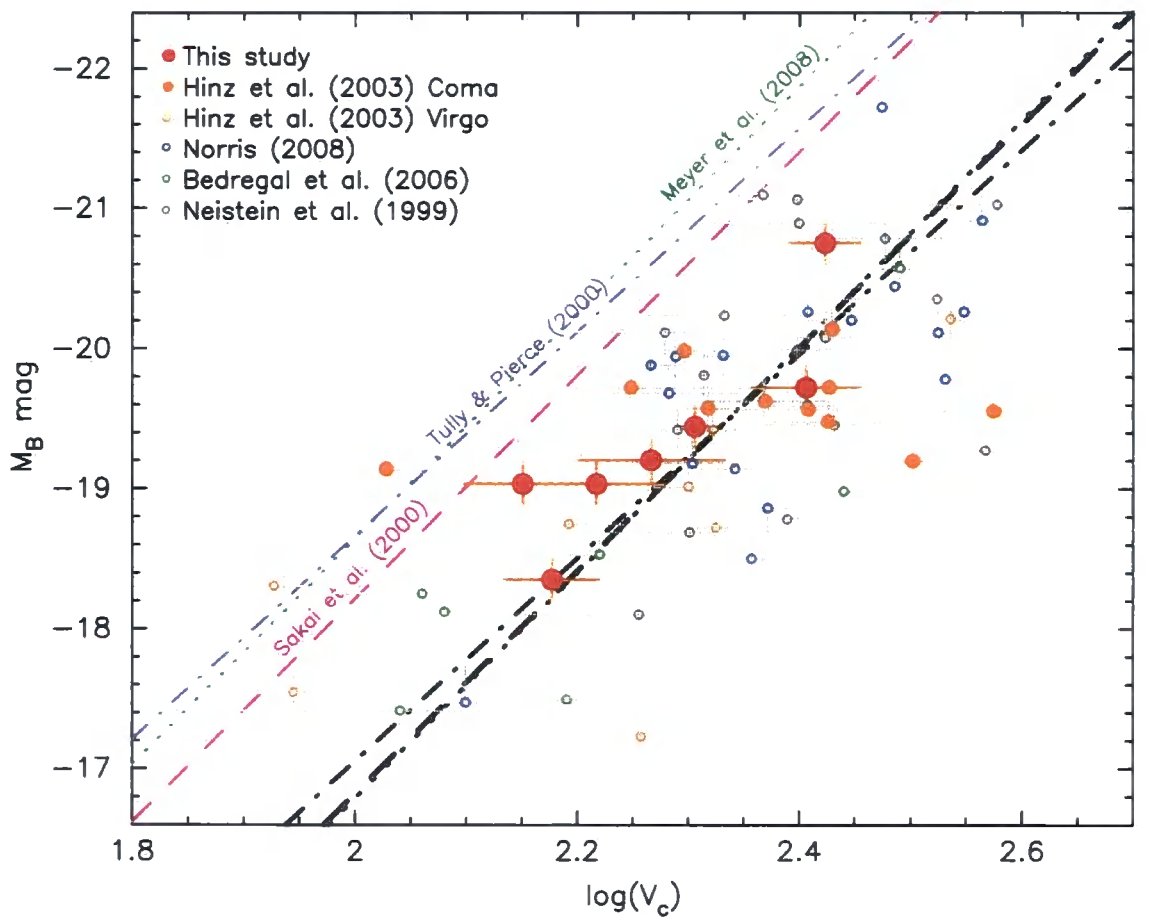

Figure 5.10: Tully-Fisher relation for the Coma S0 sample (large red points). Further S0 galaxies are shown by circles: Hinz et al. (2003) Coma and Virgo samples, Norris (2008), Bedregal et al. (2006a), Neistein et al. (1999). For comparison, the TFRs from three spiral studies are indicated by labelled lines: Tully & Pierce (2000), Sakai et al. (2000) and Meyer et al. (2008). The black dash-dot and dashed lines show the best fit to all the S0 galaxies, fixing the slope to the TFR from Tully & Pierce and Sakai et al. respectively (for simplicity, the S0 TFR corresponding to Meyer et al. has been omitted, as the slope is very similar to Sakai et al.).

apparent-to-absolute magnitude calculation could introduce systematic offsets, with the dominant source being the distance modulus. However, this uncertainty is ~0.15 mag, which could account for no more than 10 per cent of the observed offset.

The Neistein et al. and Norris (2008) studies included galaxies from a variety of densities. Bedregal et al. observed the Fornax cluster which has a low galaxy density compared to Virgo, which in turn has a lower central density than Coma. Combining the Coma cluster galaxies from this study and Hinz et al. (2003), the offset is within the errors of the full sample (final two rows, Table 5.5). None of the individual studies are significantly offset from one another, with the differences comparable to the formal errors and to the variation between spiral TFRs. This suggests that the S0 TFR offset is independent of global environment.

We examine the offset for the Coma galaxies (from this study and Hinz et al. 2003) in more detail. The upper panels of Figure 5.11 present the Coma cluster S0 TFR and the distribution of the galaxies within the Coma cluster core. The S0s are well distributed in cluster radius, giving a range of local densities within Coma, although the higher density south-west region (near NGC4839; see Figure 5.2) is unfortunately not sampled in either studies.

The lower-left panel of Figure 5.11 explores the relation between the offset and the projected cluster-centric radius of the galaxy. This plot has a prominent wedge shape: the radii are lower limits on the three-dimensional physical radius, as observations only account for distance in the sky plane, and not along the line-of-sight. The lower-right panel re-plots this data with radius in log-space. There is a significant trend (5.6σ; rms scatter of 0.71 mag), in which galaxies with larger offsets are preferentially found in the cluster centre. Again, there is a scatter towards lower radii. GMP2815 is an obvious outlier, with a very low offset for a galaxy with such a small projected radius. This galaxy also has a low $cz_{\rm hel}$ (= 4634 km s^{-1}), as shown by the right panel of Figure 5.12. This galaxy may be behind the core, moving towards us along our line of sight, meaning its true physical radius is much higher than the projected value. Excluding this point improves the correlation, with a strong significance of 9σ and an rms scatter of 0.57 mag.

The relation between radius and TFR offset could be explained by the truncation of star-formation due to cluster in-fall. In this mechanism, the disc fade is related to the time elapsed since the galaxy entered the density regime responsible for the quenching. For a galaxy passing through the core for the first time, and depending on the timescale

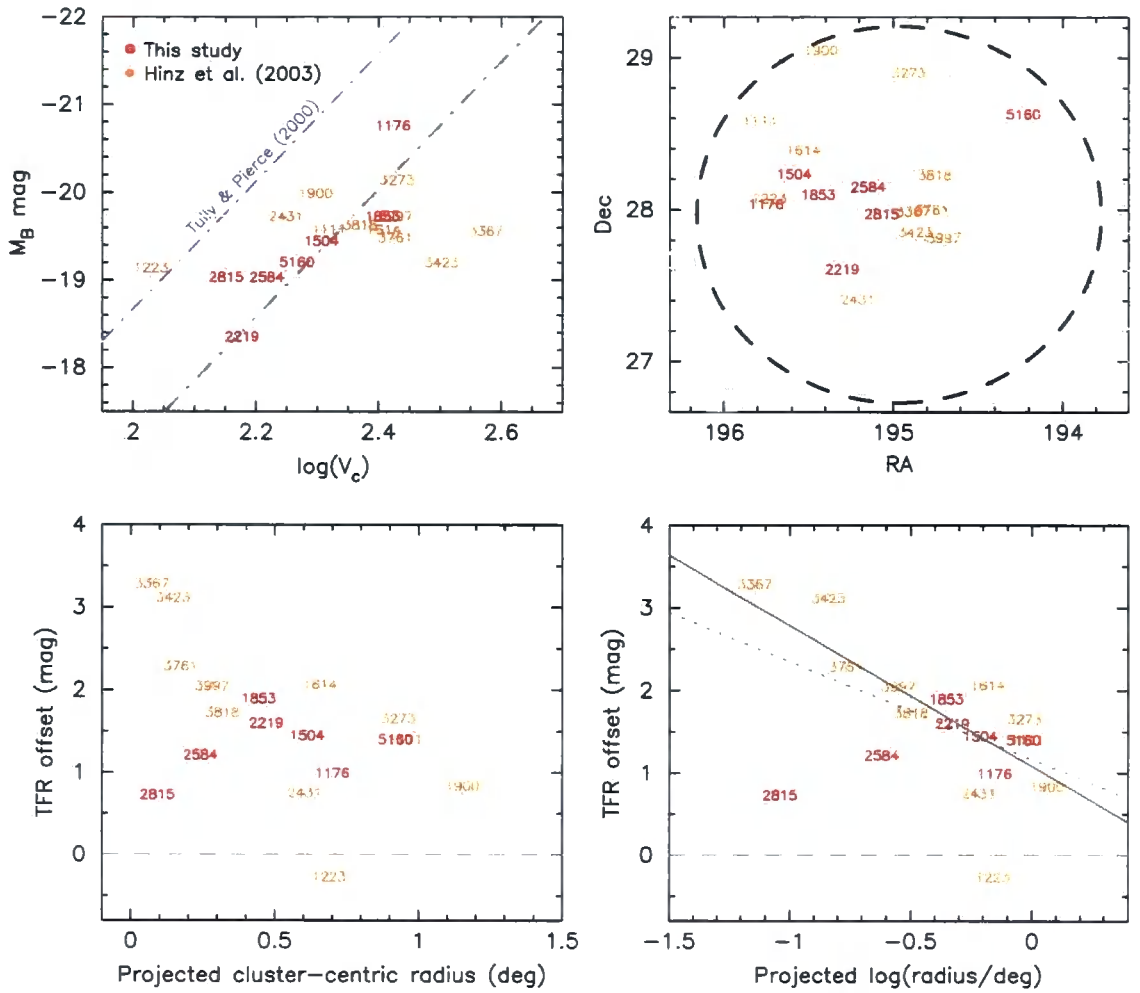

Figure 5.11: Upper-left panel: The Tully-Fisher relation for the Coma S0 galaxies in this study and in Hinz et al. (2003): red and orange GMP ID respectively. For comparison, the spiral TFR from Tully & Pierce (2000, purple dash-dots) is shown. The black dash-dot line indicates the bivariate best fit to the S0s, fixing the slope to the spiral relation. Upper-right panel: The distribution of these S0 galaxies within the Coma cluster core. The contours indicate the local galaxy density, and the dashed circle highlights a cluster-centric radius of 2 Mpc. Lower panels: the luminosity offset from the spiral TFR versus the cluster-centric radius of the galaxy, in linear (left) and logarithmic space (right). The dotted and solid dark grey lines indicate the weighted best fit including and excluding the outlier, GMP2815, respectively.

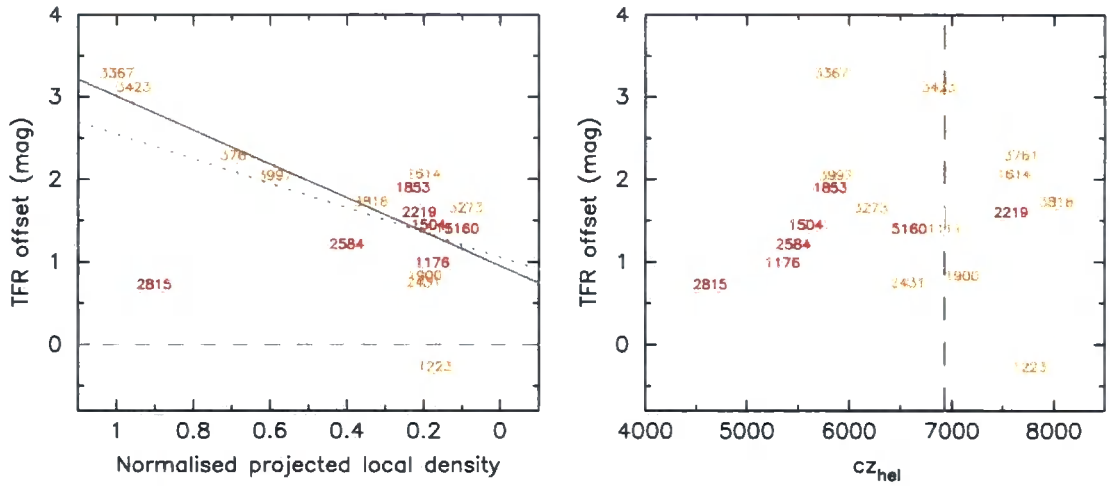

Figure 5.12: Left panel: The luminosity offset from the spiral TFR versus the normalised, projected local galaxy density (densest = 1). Labels as in Figure 5.11. The dotted and solid dark grey lines indicate the weighted best fit including and excluding the outlier GMP2815. Right panel: TFR offset versus the observed (heliocentric) velocity ($cz_{\rm hel}$) of the galaxies. The vertical dashed line indicates the mean $cz_{\rm hel}$ of the Coma cluster ($cz_{\rm hel}$ = 6925 km s^{-1}). GMP2815 has a low $cz_{\rm hel}$ suggesting that the galaxy is moving towards us through the cluster core.

of the delayed reaction, this may correlate with the cluster-centric radius. Carter et al. (2002) observed a general metallicity gradient in Coma, indicating that the cluster is not well mixed: galaxies formed in the outer regions spend most of their time there. It is not obvious whether radius, or local environment is a more fundamental driver of disc fading (assuming the galaxies are on their first pass through the core). We generate a map of projected density by counting the number of galaxies in a spatial grid (0.18 × 0.18 deg bins) for the SDSS colour–magnitude selected cluster sample (displayed as dark grey circles in Figure 5.1; the contours in Figures 5.2 and 5.11). Projected local density is calculated by interpolating the map to the galaxy position. Figure 5.13 highlights the strong relation between projected cluster-centric radius and local density in the Coma cluster core, and indicates the effect of the higher density south-west region. The correlation between the TFR offset and projected local density is stronger than with radius (Figure 5.12, left panel), with a significance of $>10\sigma$ and an rms scatter of 0.53 mag (excluding GMP2815 as before).

Unfortunately, there is no way around the the projection effect. However, the significance of the trend in Figure 5.12 suggests a connection between projected local density

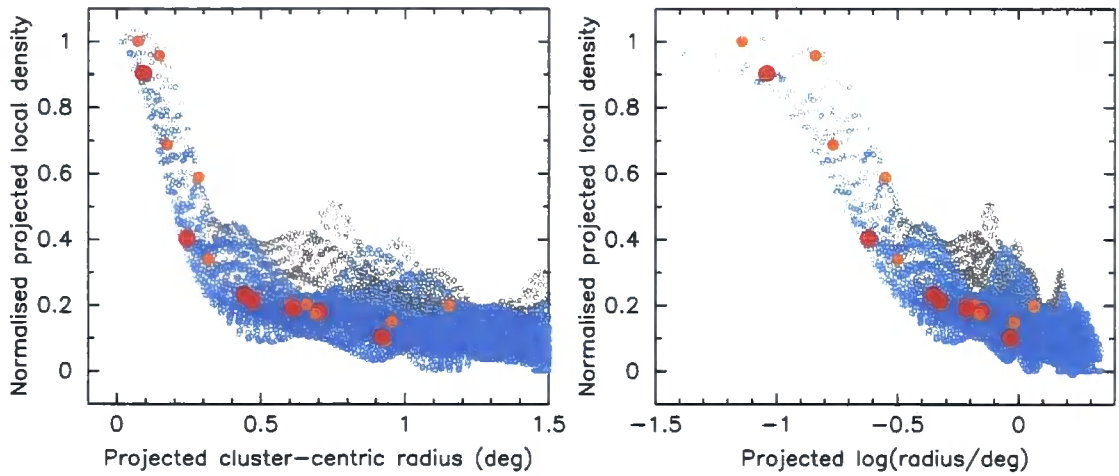

Figure 5.13: Normalised, projected local galaxy density versus the projected cluster-centric radius in linear (left) and logarithmic space (right). Coma S0 galaxies in this study and in Hinz et al. (2003) shown in red and orange respectively. Additional symbols indicate the local density and radius at 10 000 gridded test positions throughout Coma: blue for the majority and grey highlighting the higher density south-west region. Generally, radius and local density are highly correlated.

and the spiral–S0 TFR luminosity offset. Reconciling this result with the lack of a significant offset between studies of different global environments, calls for multiple mechanisms and a heterogeneous population of S0s. In lower density regions, the formation of S0s must be unconnected to cluster in-fall, while in clusters, this process is important and is imprinted in the strong trends. We return to the TFR offsets in Section 5.4.3.

5.4.2 Absorption line profiles

Absorption line strengths were measured for each radial bin, combining the spectra from the two sides of the galaxy together (see Section 5.3.3). We employed INDEXF to measure eight selected Lick indices (highlighted in Figure 5.14), from the de-redshifted spectra, and at the GMOS instrument resolution ($\sigma \sim 136$ km s^{-1}). Using the method described in Chapter 3, we corrected the line indices to account for velocity-broadening and the instrumental resolution, but have not calibrated to the Lick instrumental response. Uncertainties were propagated by INDEXF from the error spectrum.

Figures 5.15 and 5.16 present the line strength profiles for GMP1176 and GMP1504 respectively. As noted in Section 5.3.2, GMP1176 is an atypical S0 galaxy, with a small disc component and a dominant bulge at all radii. For this galaxy, HδF and Hβ do not

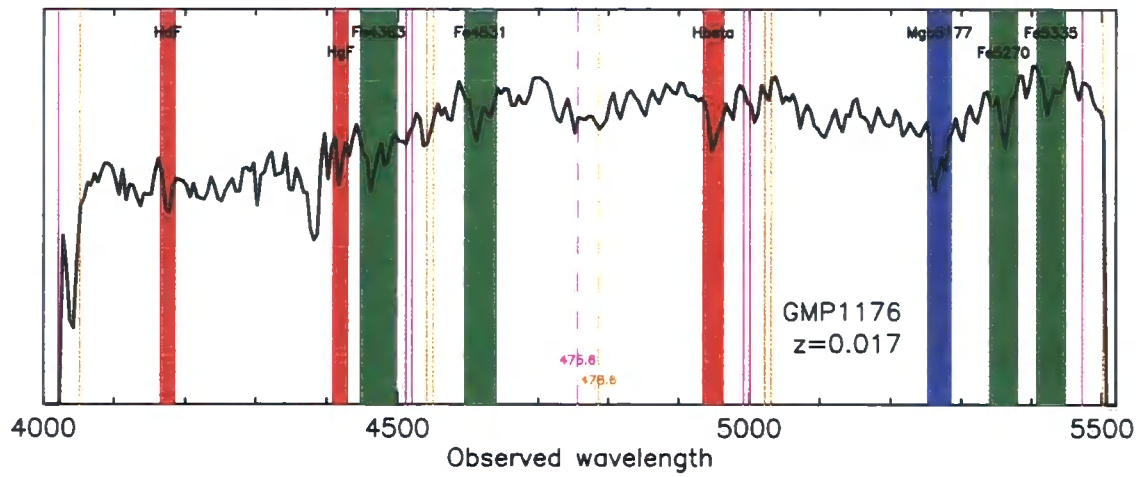

Figure 5.14: The eight chosen Lick absorption line indices (red = Balmer hydrogen lines; blue = magnesium lines; green = iron and miscellaneous lines) plotted over an example spectrum at the Coma cluster redshift, shown at the observed wavelength. The orange and magenta lines indicate the approximate position of the chip gaps for the two spectral offsets.

have a significant trend with radius, but there is a positive gradient in the inner regions for HγF. The metal lines all show general negative gradients out to the observation limit ($\sim 2\ r_e$). GMP1504 is a 'classic' S0 (Section 5.3.2). In this galaxy, the Balmer lines have little visible gradient (excluding the outer bin, which has a S/N ~ 20 Å^{-1}), Mgb5177 has a marginal negative gradient, and the iron lines generally show negative radial trends. However, in the innermost regions ($r < 1$–2 arcsec), Fe4383, Fe5270 and Fe5335 all have a steep negative gradients, outside which the index becomes abruptly stronger again, before continuing the general downward trend. By comparison to the structural profiles (upper panels), this 'U' shape in the radial trends is seen to coincide with the onset of the disc dominated regime.

The absorption line radial trends for each of the other galaxies are shown in Appendix D. On average, the metal lines decrease in strength with radius, while the Balmer line profiles remain relatively flat. However, there are large deviations from these trends (e.g. abrupt positive gradients in GMP5160), which generally coincide with variations in the relative strength of the structural components, such as the transition between bulge and disc dominated regions.

GMP1176 and GMP1853 were also studied by Mehlert et al. (2000), who observed

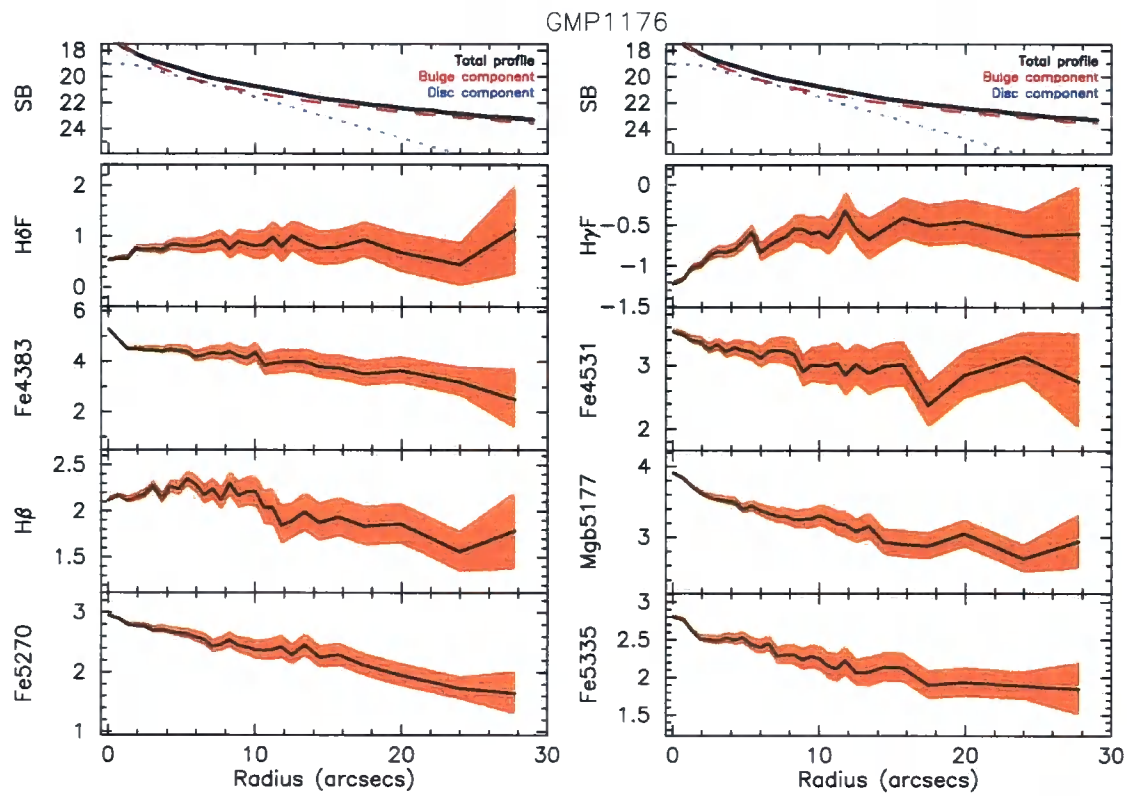

Figure 5.15: Absorption line strength profiles for GMP1176. Upper panels: g-band surface brightness profile for the bulge (red dashes) and disc (blue dots) components, repeated for each column to facilitate radial comparison between structural and spectral features. Main panels: observed line strength profiles for the indices highlighted in Figure 5.14. Orange shaded indicate 1σ uncertainties.

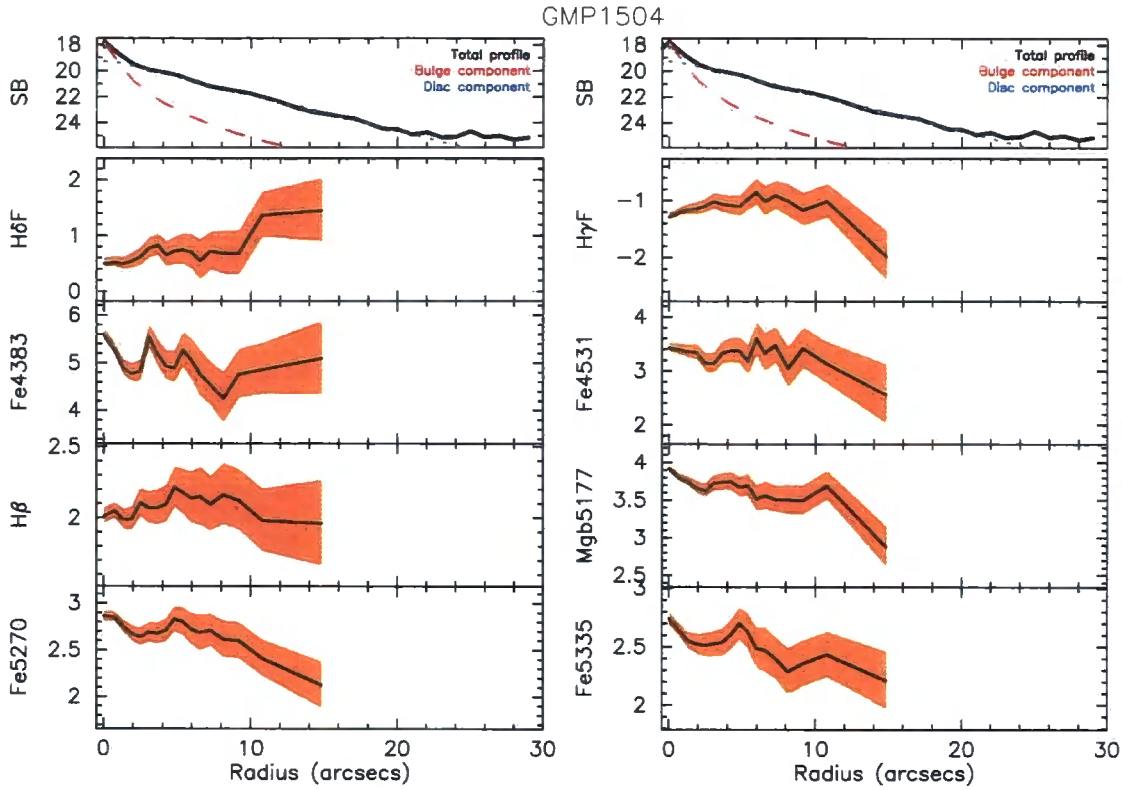

Figure 5.16: Absorption line strength profiles for GMP1504. Layout as in Figure 5.15.

GMP1176 for 9000 s on a 3.5 m telescope[2], with a 3.6 arcsec wide slit and 2 arcsec seeing (FWHM). GMP1853 was observed for 10800 s on a 2.4 m telescope[3], with a 1.7 arcsec wide slit and average seeing of 1.6 arcsec (FWHM). Figure 5.17 over-plots the GMOS absorption lines presented in this study, with those from Mehlert et al., for the indices Hβ, Mgb5177, $\langle$Fe$\rangle$ = (Fe5270 + Fe5335)/2 and [MgFe] = $\sqrt{\text{Mgb}\langle\text{Fe}\rangle}$. The line index profiles are very similar given the different instruments and observing conditions. The upturn in line strengths at large radii in the Mehlert et al. observations is most likely due to an over-subtracted sky or scattered light issue. Continuation of the regular radial trend (for example, in [MgFe] for GMP1176) gives us confidence in the GMOS measurements, as other studies have found that gradients continue at large radii (e.g. Proctor et al., 2009; Weijmans et al., 2009).

Figure 5.18 presents the line strength gradients for two index–index plots: Hβ–Fe5335 and Mgb5177–Fe5335. To facilitate physical interpretation of the lines, each index–index plot is overlain by stellar population grids (Thomas et al., 2003, 2004). The panels high-

[2]German–Spanish Astronomical Centre, Calar Alto.
[3]Michigan–Datrmouth–M.I.T observatory, Kitt Peak.

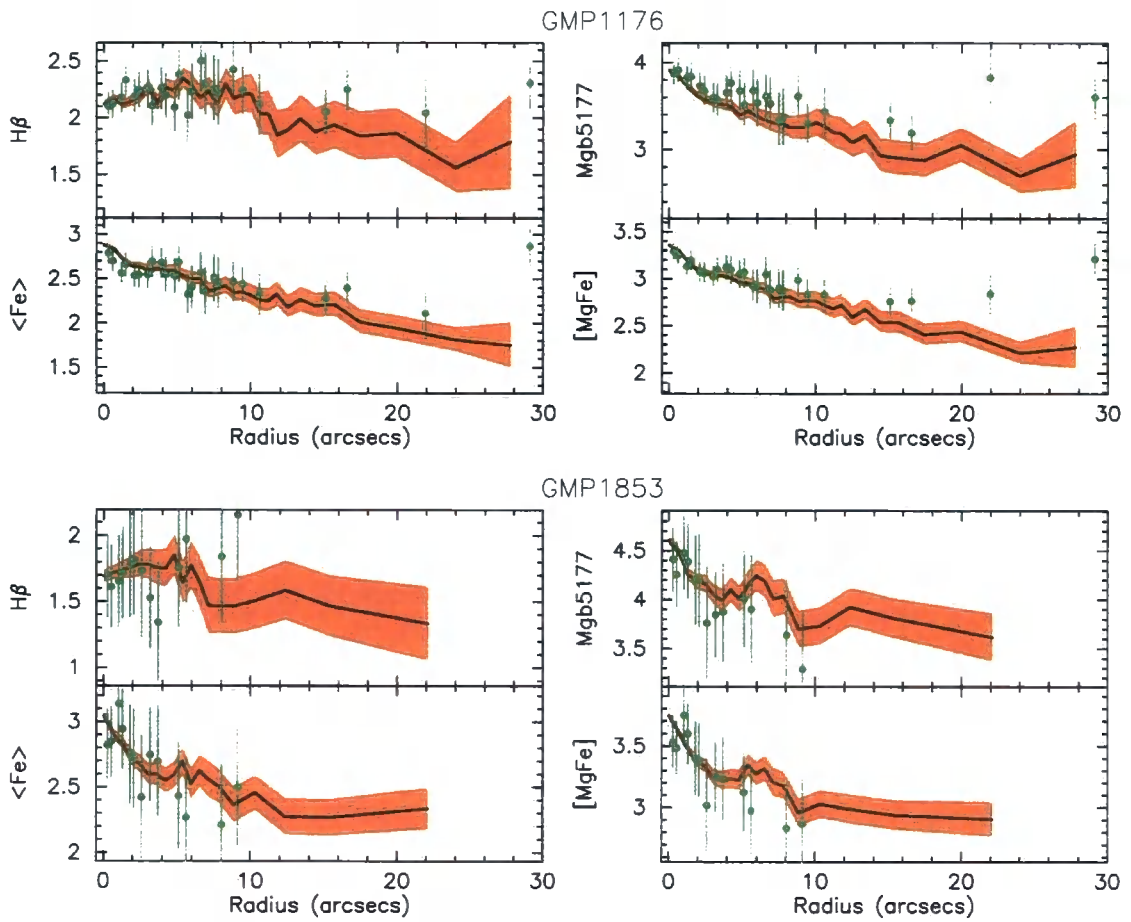

Figure 5.17: For GMP1176 (upper panel) and GMP1853 (lower panel), GMOS line strength gradients for the indices Hβ, Mgb5177, $\langle$Fe$\rangle$ and [MgFe], shown by black line (1 σ errors indicated by orange). Index measurements for the same galaxies from Mehlert et al. (2000) over-plotted in green. The agreement is generally very good.

light the general gradients in the bulges (red) and discs (blue), as identified from the surface brightness profiles (Section 5.3.2). As presented in Figure 5.8, the bulge in GMP1176 dominates at both small and large radii. The two components show distinct behaviour, with the turning points in the index profiles coinciding with the structural boundaries. The bulges tend to show little radial trend with age or α-abundance, whereas the discs have a greater internal variation. Apart from GMP5160, where the Fe5335 line strength increases in the outer regions, the metallicity gradients are generally negative in all components. Additionally, this crude measure of stellar properties indicates that discs are generally older than the bulges. We investigate the radial trends in stellar population parameters further in the next section.

5.4.3 Stellar populations profiles in bulges and discs

For each radial bin, we derived the stellar population parameters (age, metallicity and α-abundance) via a multi-index grid inversion technique. The method is described in detail in Section 3.3.5, and in this study, we inverted the grids of eight Lick indices highlighted in Figure 3.14 (HδF, HγF, Fe4383, Fe4531, Hβ, Mgb5177, Fe5270, Fe5335). Stellar population errors were calculated by repeated Monte Carlo simulations of the index values.

In Figures 5.19 and 5.20, we present the radial trends in the stellar populations for GMP1176 and GMP1504 respectively (c.f. index trends shown in Figures 5.15 and 5.16). GMP1176 shows a regular gradient in all three stellar population parameters, out to the largest observable radius ($\sim$25 arcsec). The age and [α/Fe] gradients are positive (becoming older and more enhanced towards the outside), and the metallicity decreases with radius, and is quite metal-poor at large radii. The generally smooth profile is indicative of the dominant bulge component at all radii. At $\sim$2–5 arcsec, all of the quantities appear marginally flatter, corresponding to the radii at which the small disc component is most significant. The extent of the profile, which is observed to approximately twice the effective radius (bulge r_e = 13.3 arcsec), suggest that gradients continue regularly beyond the r_e observations of most studies (e.g. Mehlert et al. 2003, Chapter 4 of this Thesis). [Z/H] does not tend to solar in the outer regions (see Section 4.4), but is increasingly metal poor, as observed out to $\sim$4 r_e in two nearby elliptical galaxies (NGC3379 and NGC821) by Weijmans et al. (2009).

GMP1504 shows very little radial trend in age and [α/Fe] (to the outermost bin). The metallicity gradient is generally negative, although the 'U' shape at small radii, noted in

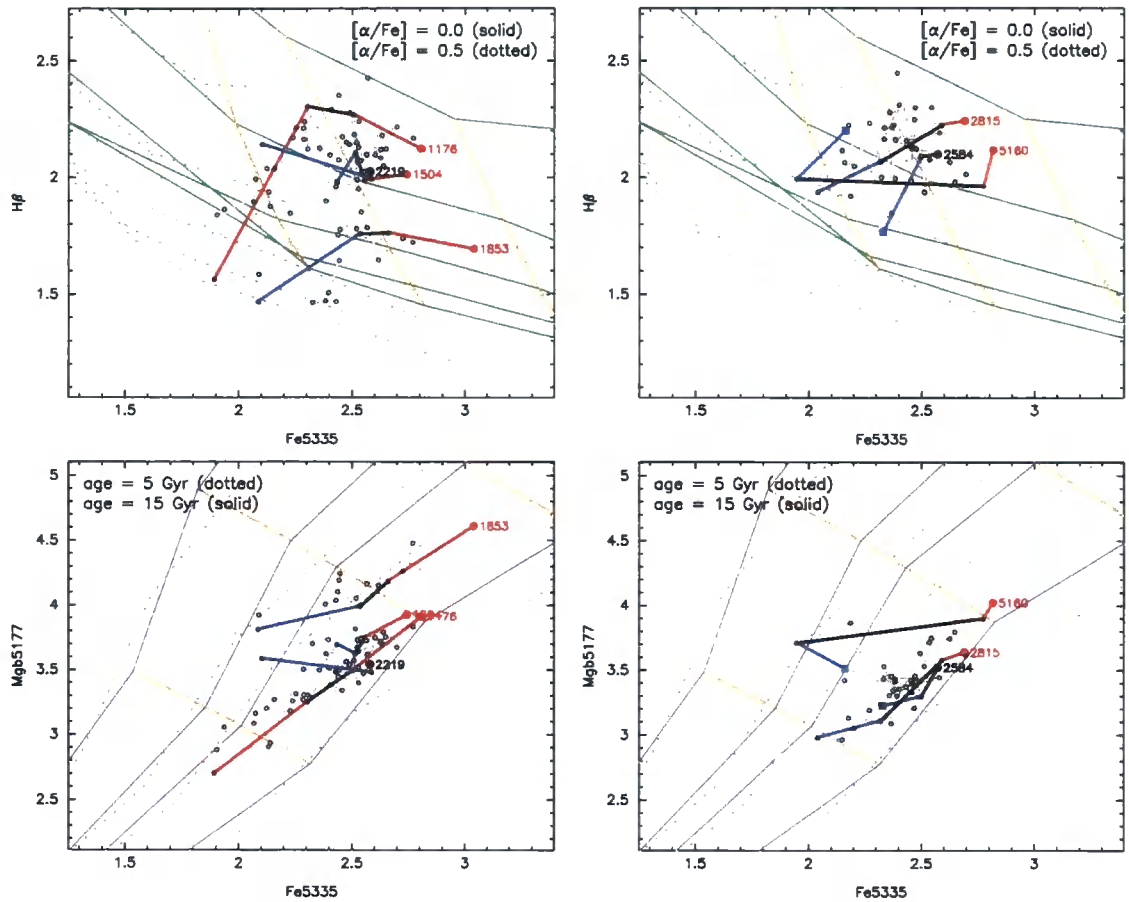

Figure 5.18: Index–index plots showing the radial trends in the absorption line. The sample is divided in two for clarity (left: GMP1176, GMP1504, GMP1853, GMP2219; right: GMP2584, GMP2815, GMP5160). Each galaxy is represented by thick red/blue/black lines, showing the overall gradient in the bulge, disc and transition regions respectively. The innermost bin of each galaxy is shown by a filled circle, the outermost by a filled square. In cases where the outer bin did not reach the required S/N (30 Å^{-1}), it has been excluded from the general gradients. The open grey points show index measurements for individual bins, linked by a thin, grey line.

Upper panels: Hβ–Fe5335, backed by age–metallicity grids (from Thomas et al. 2004). Lines of constant age (green; top-down) = 2, 5, 10, 13, 15 Gyr; lines of constant [Z/H] (orange; left-to-right) = –1.35, –0.33, 0.0, +0.35, +0.67. [α/Fe] = 0.0, 0.5 indicated by solid/dotted grid lines respectively. Lower panels: Mgb5177–Fe5335, overlying metallicity–α-abundance grids. Lines of constant [Z/H] (orange; bottom-up) = –1.35, –0.33, 0.0, +0.35, +0.67; lines of constant [α/Fe] (purple; right-to-left) = 0.0, +0.2, +0.3, +0.5. Age = 5, 15 Gyr indicated by dotted/solid lines respectively.

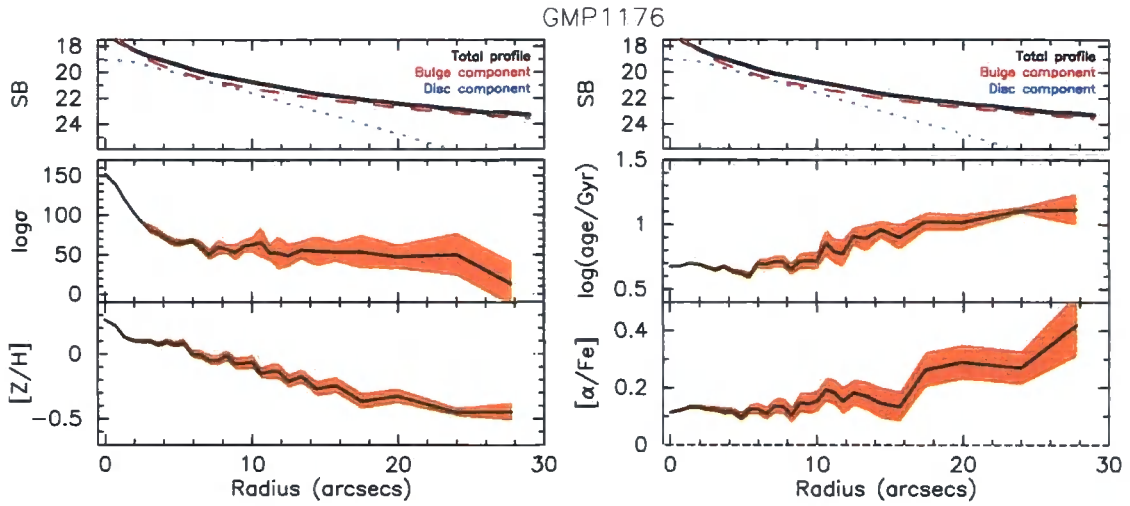

Figure 5.19: Stellar population profiles for GMP1176. Upper panels: g-band surface brightness profiles for the bulge (red dashes) and disc (blue dots) components. Main panels: observed profiles for the velocity dispersion (σ), age, metallicity [Z/H] and α-element abundance [α/Fe]. Orange shaded indicate 1 σ uncertainties.

the iron lines, is visible and coincides with the extent of the bulge dominated region.

The radial trends of the other galaxies are shown in Figures 5.21 – 5.25. The metallicity gradients are generally negative, and for the majority of galaxies, the age increases with radius, indicating that the disc is older than the bluge. All of the galaxies show a similar pattern to GMP1504, whereby the extent of the bulge component is imprinted on the radial trend in metallicity (and sometimes age, e.g. GMP1853). The strongest example of this is in GMP5160 (Figure 5.25), which shows a steep gradient within the central 2 arcsec in age and [α/Fe] (positive gradients) and [Z/H] (negative). All three parameters then abruptly return to the central value, where age and α-enhancement remain. The metallicity resumes a generally negative gradient in the outer regions. The surface brightness profile actually shows a small increase at r = 3 – 7 arcsec, which is mirrored in age, [Z/H], α-abundance and the velocity dispersion. This suggests that there may be a third component (such as a bar or a halo) dominating at some radii. Further investigation is beyond the scope of this study.

The radial trends in absorption line strengths and stellar populations have a large variation in properties. Drawing more general conclusions is not feasible with this small and unrepresentative sample. However, we have demonstrated a clear connection between the radial trends of the stellar populations and the underlying structural components.

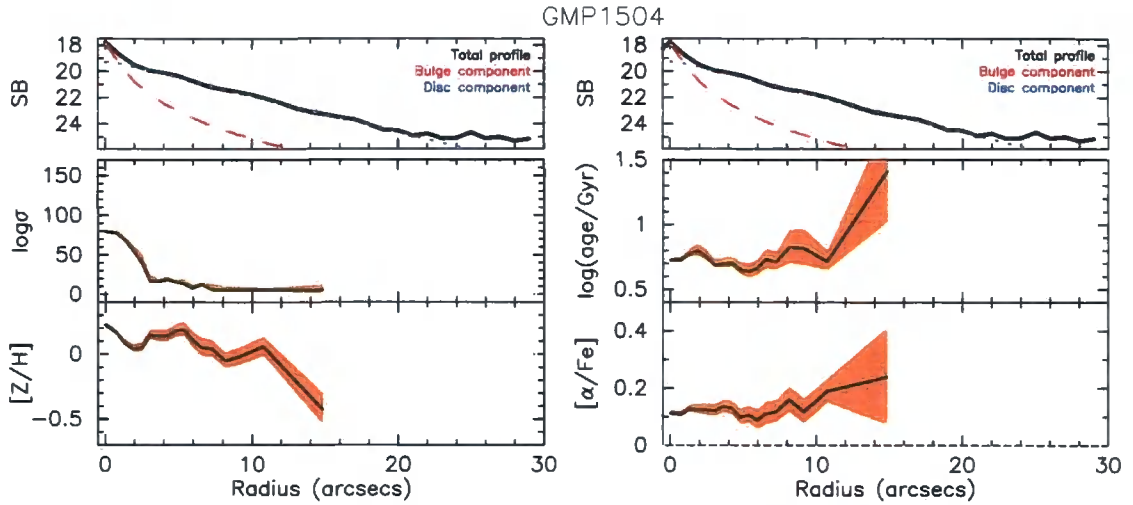

Figure 5.20: Stellar population profiles for GMP1504. Layout as in Figure 5.19.

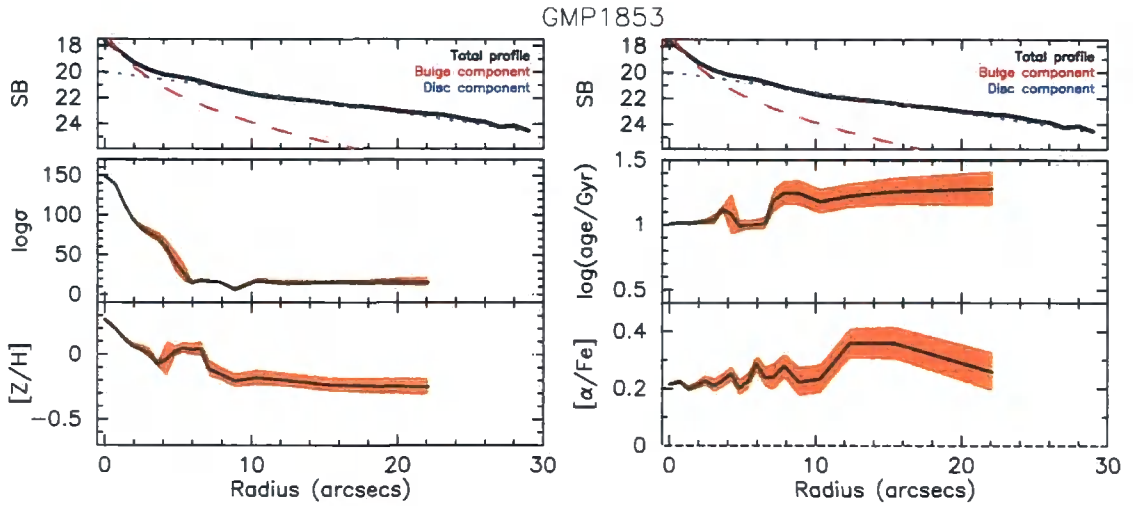

Figure 5.21: Stellar population profiles for GMP1853. Layout as in Figure 5.19.

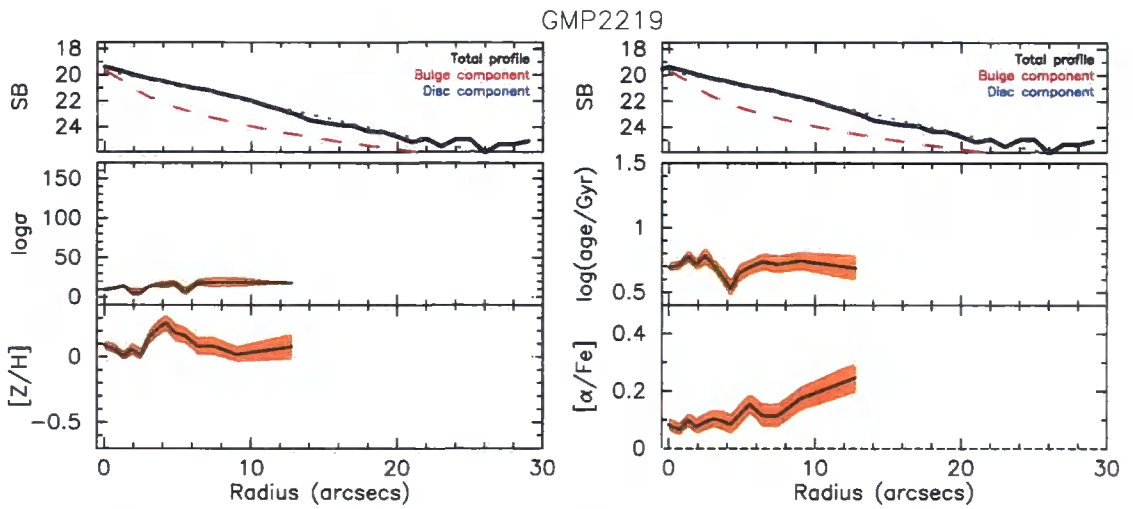

Figure 5.22: Stellar population profiles for GMP2219. Layout as in Figure 5.19.

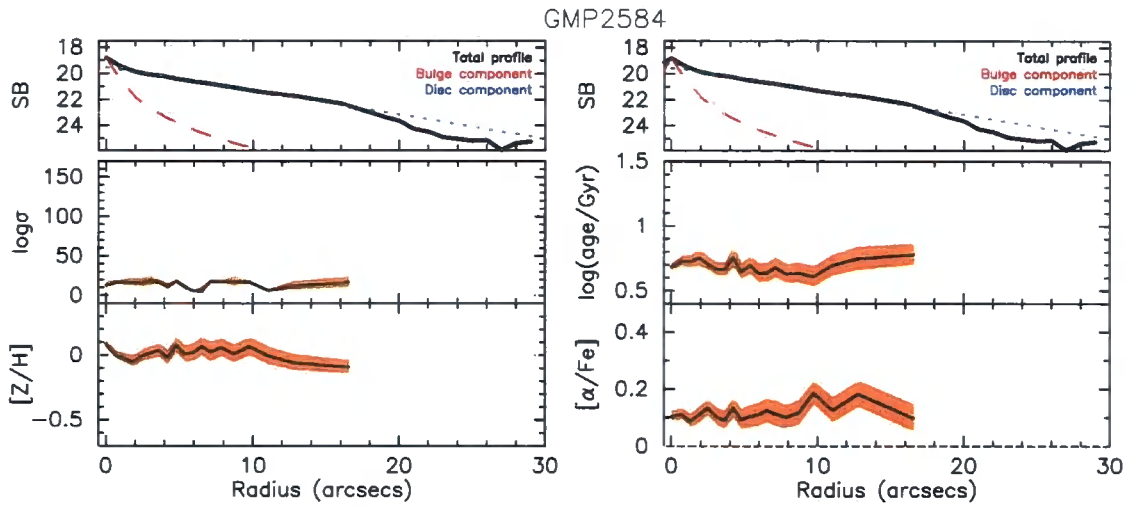

Figure 5.23: Stellar population profiles for GMP2584. Layout as in Figure 5.19.

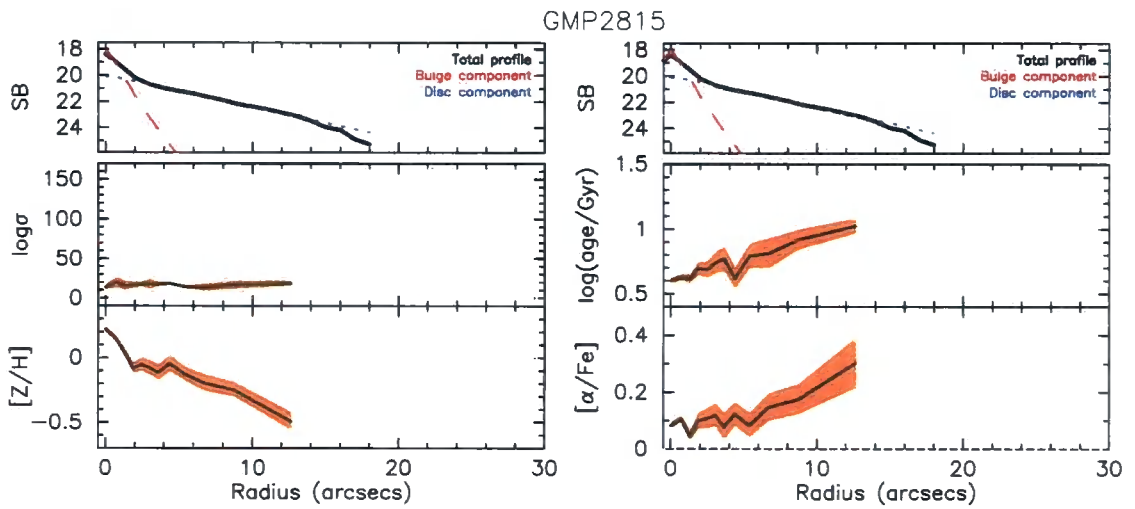

Figure 5.24: Stellar population profiles for GMP2815. Layout as in Figure 5.19.

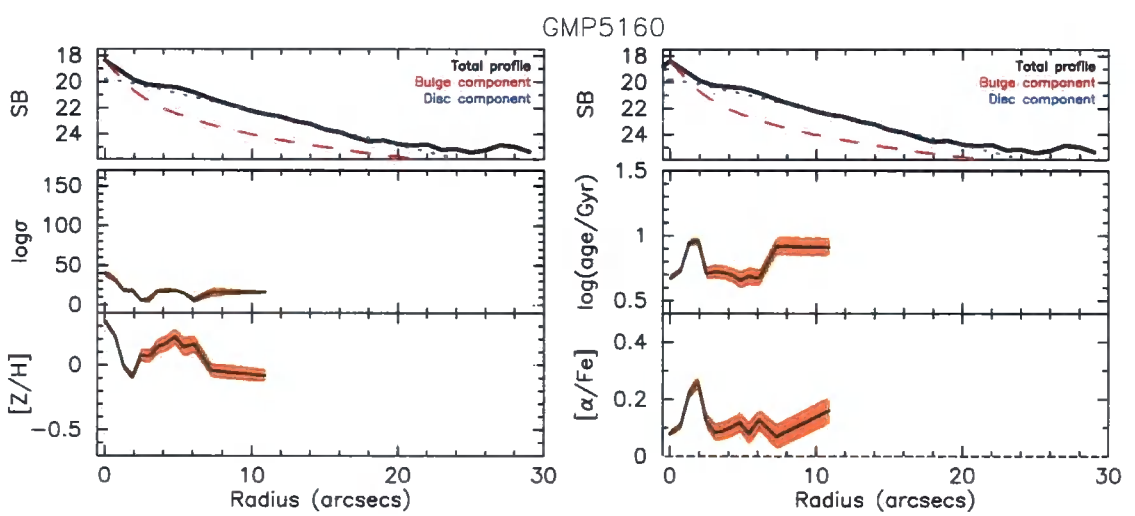

Figure 5.25: Stellar population profiles for GMP5160. Layout as in Figure 5.19.

5.4.4 Central and disc ages

In this section, we compute the single stellar populations of the galaxy centre and of the disc. We compare the age of the two components, investigate the difference in their optical and near-infrared colours, and then examine the disc age in terms of the TFR offset calculated in Section 5.4.1.

The central stellar population was derived from the innermost bin (radius $\sim$ 0.5 arcsec). Examining the surface brightness profiles of the bulge and disc components (Figure 5.6), these central values are bulge dominated for approximately two-thirds of the sample, whereas the others have a significant contribution from the disc component. Decomposition of these components in the central stellar population has not been investigated in this study. However, the average stellar population of the disc can be obtained, as each galaxy (with the exception of GMP1176) is significantly disc dominated at large radii. We extracted the disc spectrum between an inner radius $r = r_{\rm exp}$, which isolates this outer component from the bulge, and the outer radius at which the g-band surface brightness μ_r = 23 mag arcsec $^{-2}$. GMP1176 is excluded from this analysis, as the disc is not dominant at large radii.

Figure 5.26 compares the disc and central stellar populations. We combine the six Coma galaxies from GMOS with seven Fornax S0s from Bedregal et al. (2006a) and 18 local field S0s from Norris (2008). Both of these studies extracted disc and central spectra, deriving stellar populations in a similar manner to that described here. On average, the discs are older by Δlog(age/Gyr) = 0.12 $\pm$ 0.04 dex, although this is mostly due to galaxies in the Bedregal et al. sample (Δlog(age/Gyr) = 0.34 $\pm$ 0.13 dex), as the difference is not significant in either the Coma or Norris samples alone (Δlog(age/Gyr) = 0.09 $\pm$ 0.05 dex and 0.06 $\pm$ 0.04 dex respectively). The discs are more metal poor compared to the centre by Δ[Z/H] = –0.29 $\pm$ 0.05 dex (marginal in our sample: 0.22 $\pm$ 0.08, but significant in both others), which may result from generally negative gradients as much as the difference between bulge and disc populations. As the central value may incorporate a contribution from the disc as well as the bulge, the intrinsic difference between the stellar populations in the two components may be larger than shown here.

In a photometric study of disc dominated galaxies, MacArthur et al. (2004) investigated the optical and near-infrared colour gradients of 12 S0s. They found that in B–R, the bulge and disc were approximately the same colour, whereas in R–K, the disc was 0.2–0.3 mag bluer, and interpreted this as a gradient in both age and metallicity. Using

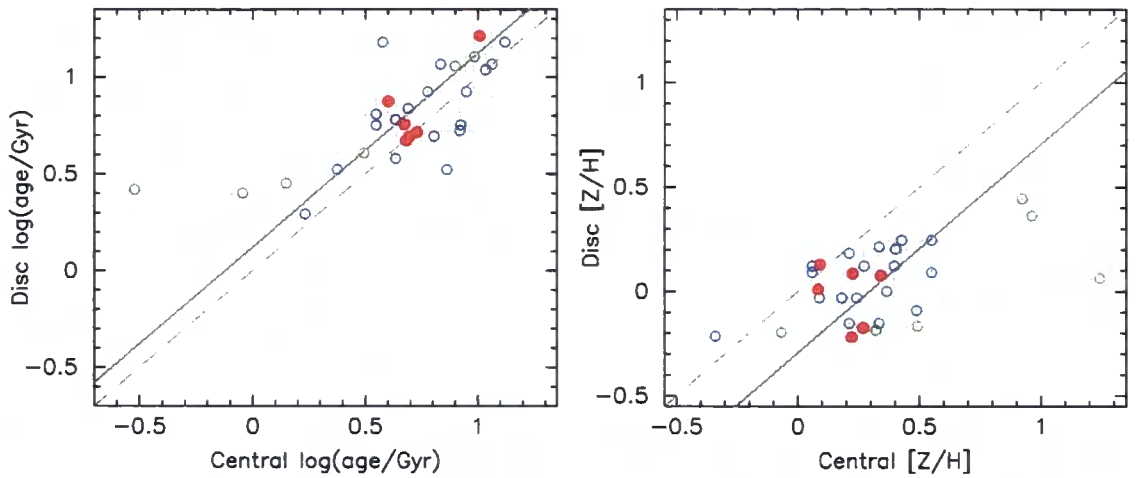

Figure 5.26: Disc versus central age (left panel) and [Z/H] (right panel). The galaxies in the Coma sample are highlighted in red. Also shown are the galaxies from Bedregal et al. (2006a, green open circles) and Norris (2008, blue open circles). The solid line shows the mean offset; the dashed line indicates equality. For reference, the Bedregal et al. S0 in Fornax with an extremely young centre (0.3 Gyr) is NGC1375.

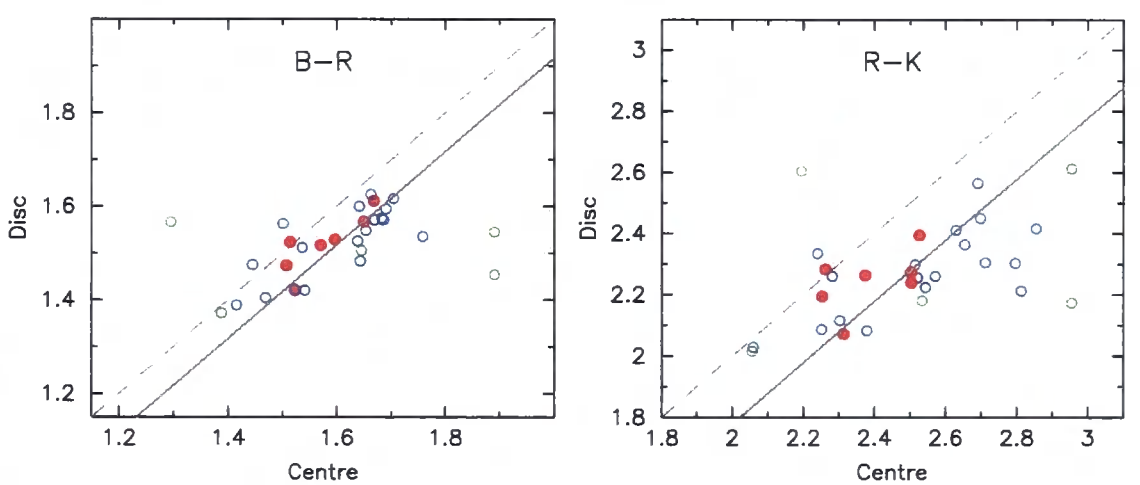

Figure 5.27: Predicted B–R (left panel) and R–K (right panel) colours for S0 galaxies (layout as in Figure 5.26). The colours are predicted from the spectroscopic age and metallicity, via the models of Maraston (2005).

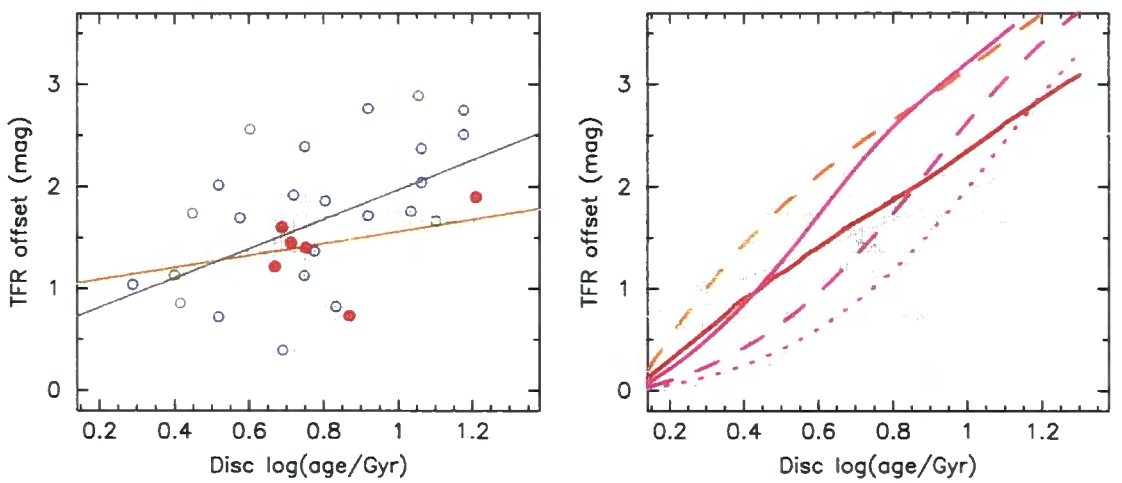

Figure 5.28: Left panel: Offset from the spiral Tully-Fisher relation versus the simple stellar population age [log(age/Gyr)] of the disc component. The galaxies in the Coma sample are highlighted in red. Open symbols show galaxies from Bedregal et al. (2006a, green) and Norris (2008, blue). The orange line is the best fit to the 7 Coma S0s, the grey line to all data.

Right panel: Simple disc fading, calculated from the models of Bruzual & Charlot (2003). Red line shows disc fading after a single instantaneous burst; orange line for abrupt truncation after prolonged (1 Gyr) star formation. Magenta lines display exponentially decreasing star formation with three e-folding times. Although the model zeropoint depends on the epoch of spiral observation, the models indicate how intrinsic scatter can be introduced by varied star formation histories.

the evolutionary stellar population synthesis models of Maraston (2005), and a method similar to Section 4.6.2, we can predict the central and disc colours for the S0 galaxies shown in Figure 5.26. Figure 5.27 present the predicted B–R and R–K colours from the disc versus the central regions. We predict a small offset in the B–R colour (–0.08 $\pm$ 0.02 mag). This is not dissimilar to the ~0.03–0.05 mag offset found in the S0 subsample of MacArthur et al. (2004). Also in agreement with MacArthur et al., we find an offset of –0.22 $\pm$ 0.04 mag in R–K, such that the disc is bluer than the central regions. We have already shown that the age tends to increase with radius (a reddening effect), so this colour offset is due to metallicity.

In the spiral-to-S0 transformation model, the disc age derived in this section should provide, to first order, a reasonable approximation of the time since star formation was quenched. The left panel of Figure 5.28 shows the offset from the spiral TFR (as in Figures 5.11 and 5.12) against the simple stellar population age of the disc component. We once again combine this data with the seven S0s from Bedregal et al. (2006a) and 18 S0s from Norris (2008). The agreement between these samples, from different global environments, is encouraging since the age-to-fade relation is not explicitly dependent on the quenching mechanism. The overall correlation is significant (4.6 σ), although there is 0.56 mag scatter (~0.4 mag intrinsic scatter). The right panel of Figure 5.28 shows several simple star formation scenarios for the S0 progenitor, calculated from the stellar population models of Bruzual & Charlot (2003). The scatter could be due to the different star formation histories of the spiral population, as well as due to variation in the truncation parameters (i.e. abrupt or slower decay).

5.5. Conclusions

We present an analysis of new, deep GMOS long-slit observations of seven S0 galaxies in the Coma cluster. Binning the data along the slit to achieve a signal-to-noise > 30 Å, we measure radial profiles in kinematics and absorption line features, and derive trends in the stellar population parameters (age, metallicity and α-abundance). We use GALFIT to decompose the surface brightness distribution of each galaxy into a bulge and disc, allowing comparison between structural components and the stellar properties. Our principal results are summarised below.

- The sample strongly supports previous evidence that in the B-band, S0s are offset

from the spiral galaxy Tully-Fisher relation. The offset corresponds to a decrease in luminosity of ~1.5 mag, and is not dependent on global environment (i.e. cluster, group, field).

- Combining this data with the Coma sample of Hinz et al. (2003), we demonstrate that the TFR offset for cluster S0s is correlated with the projected local galaxy density (>10σ significance).

- Generally, metal line indices have negative gradients, while the Balmer lines tend to have flatter radial trends. Radial profiles in the inner regions are continued at large radii (2–3 r_e).

- We qualitatively show that significant deviations from the general radial trends in age and metallicity coincide with structural and kinematic boundaries.

- We show that S0 discs are older than central regions (Δlog(age/Gyr) = 0.12 $\pm$ 0.04 dex), and are also more metal poor (Δ[Z/H] = –0.28 $\pm$ 0.05 dex). This evidence supports bulge growth in S0 progenitors.

- Optical–infrared colours predicted from the spectroscopic age and metallicity indicate that S0 discs are on average bluer than the central regions (in agreement with photometry from MacArthur et al. 2004). This is a metallicity effect.

- The age of the disc component is correlated with the TFR offset, confirming the spiral disc fade hypothesis. The trend agrees well with simple models of abrupt star formation truncation in a spiral disc.

These results suggest that the obvious dynamic structures within S0 galaxies have different stellar populations. The dominant formation process for S0s is the quenching of star formation in spiral discs, although this must be coupled with an increase of stellar mass in the bulge. Correlation with local density suggests that the responsible mechanism depends on the cluster environment. However, the similarity of various trends (i.e. TFR offset, central age versus disc age) for S0 galaxies in different global environments, indicates that cluster-specific mechanisms are not dominant.

Chapter 6

Conclusions

In this thesis we have investigated early-type galaxies in local clusters. Employing both optical-band spectroscopy and multi-wavelength imaging, we have attempted to address questions pertaining to the evolution and chemical composition of these galaxies: Do apparently quiescent red-sequence galaxies harbour low-level recent or ongoing star formation? How can internal gradients constrain the merger and formation histories of cluster early-type galaxies? Are S0 galaxies formed directly from quenched spiral galaxies?

6.1. Summary of main results

6.1.1 Near-ultraviolet colours of optically red-sequence galaxies

We use new *GALEX* ultraviolet and 2MASS J-band photometry to measure the near-ultraviolet–infrared colours of quiescent red-sequence galaxies in local clusters. The galaxies were selected using a strict emission criteria to avoid including galaxies with very recent star formation. We found that the NUV–J colour–magnitude relation has an intrinsic scatter of $\sim$0.3 mag, which is similar to previously reported values (Yi et al., 2005; Kaviraj et al., 2007b), but is an order of magnitude larger than the analogous optical red-sequence ($\sim$0.05 mag). As hot young stars dominate the UV flux for $\sim$100 Myr after a starburst, this scatter is interpreted as varying quantities of low-level recent star formation. However, hot intermediate-age stars, old metal-poor blue horizontal branch stars and low-mass, helium burning stars (UV upturn) could also contribute significantly

to the NUV.

To distinguish between these sources, we compare the NUV–IR colours to spectroscopic stellar population parameters. We find a strong correlation between the colour and metallicity (5.5σ significance) with an intrinsic scatter of 0.29 mag, and only a weak trend with age, once the metallicity effect has been removed. There is a large intrinsic scatter ($\sim$0.25 mag) in the NUV–J colour at fixed age and metallicity which cannot be easily accounted for with simple stellar populations. The unexpectedly blue colours of at least some galaxies, including an influential outlier, cannot be attributed to large radius contamination from other sources, and the UV upturn is not a significant contributor in this sample.

We conclude that the large NUV–J intrinsic scatter could be attributed to galaxy 'frosting' by a small ($<$ 5 per cent) subpopulation of young stars *or* a low metallicity blue horizontal branch.

6.1.2 Stellar population gradient in early-type cluster galaxies

The observable properties of early-type galaxies are known to vary systematically with radius, so the internal gradients offer a valuable insight into their star formation histories and chemical evolution. We present a thorough study into the internal stellar population gradients of 25 galaxies in two local cluster environments: Abell 3389 and the Shapley Supercluster core. Exploiting the excellent wavelength coverage and spatial information of the VLT VIMOS integral field unit, we measure radial trends in the absorption line indices. From these indices, we derive gradients in age, metallicity and α-element abundance.

We find an average metallicity gradient of –0.13 $\pm$ 0.04, and no galaxy was observed to have a significant positive metallicity gradient. Mean negative gradients in age and α-element abundance were insignificant or marginal (–0.02 $\pm$ 0.06 and –0.10 $\pm$ 0.04 respectively). However, 40 per cent of galaxies do have an age gradient that is not consistent with zero ($> 2\sigma$). Above a velocity dispersion of $\sigma \sim 140$ km s^{-1}, galaxies exhibit an increased intrinsic scatter in metallicity gradient, suggesting that mergers with widely varying characteristics dominate their formation histories. Below this transition point, the prevailing formation mechanism is rapid dissipative collapse, which may establish the tight relation between velocity dispersion and metallicity gradient (Kobayashi, 2004; Spolaor et al., 2009).

The stellar population gradients are primarily related to the central metallicity: early-type galaxies with super-solar centres have steep negative metallicity gradients and a preference for positive age gradients; those with solar metallicity centres have negligible [Z/H] gradients and negative age gradients. Gas-rich merging may prompt a central starburst, resulting in an increased central metallicity and a more negative metallicity gradient, reinforcing the ∇[Z/H]–central [Z/H] relation. A starburst also creates a positive age gradient, which may be the origin of the ∇log(age)–central [Z/H] relation. However, these relations could be diluted by late-epoch, gas-poor mergers and (in the case of logarithmic age gradients) the passage of time, producing the marginal trends observed.

B–R colours predicted from the spectroscopic age and metallicity are generally consistent with those measured directly from imaging. Comparison between the spectroscopically and photometrically derived B–R gradients has a reduced $\chi^2 \sim 3.4$ and an rms scatter of 0.08 mag. There is a strong observed anti-correlation between the gradients in age and metallicity, with a slope of –0.69 $\pm$ 0.19. While part of this observed trend is attributed to correlated measurement errors, we demonstrate that there is an underlying intrinsic relation.

6.1.3 The formation of S0 galaxies

Using new, deep GMOS long-slit observations, we examine seven lenticular galaxies in the Coma cluster core. Each selected target is an edge-on S0, with six having prominent bulge and disc components. The observations enabled g-band surface brightnesses as faint as $\sim$ 23 mag arcsec^{-2} to be probed, i.e. well into the disc-dominated regime. The sample strongly supports previous evidence (e.g. Neistein et al., 1999; Bedregal et al., 2006a) that S0s are offset from the spiral galaxy Tully-Fisher relation, corresponding to a decrease in luminosity of $\sim$1.5 mag (in the B-band). Combining our data with additional Coma cluster galaxies (from Hinz et al., 2003), we demonstrate that the TFR offset is strongly correlated with local density. However, comparing the mean TFR offset to previous studies of S0s in poorer clusters and local groups, we find no correlation with global environment.

For this GMOS S0 sample, the metal line indices predominantly have negative gradients, while the Balmer lines tend to have flatter radial trends. The radial profiles are generally regular and the gradient of the inner regions ($< r_e$) is continued to 2–3 r_e, confirming recent large radii studies (Proctor et al., 2009; Weijmans et al., 2009). Significant

deviations from the general radial trends in age and metallicity appear to coincide with structural and kinematic boundaries, such as the bulge–disc transition region.

Lenticular galaxy discs are older (Δlog(age/Gyr) = 0.12 $\pm$ 0.04 dex) and more metal poor (Δ[Z/H] = –0.28 $\pm$ 0.05 dex) than the central regions. This result advocates the theory of bulge growth during spiral-to-S0 transition, thereby supporting the observation that typical S0 bulge-to-disc ratios are large than in spirals (e.g. Dressler, 1980b). Imaging studies have observed bluer optical–IR colours in the disc than the centre (MacArthur et al., 2004), which we demonstrate must be a metallicity effect. Finally, we find that the disc component age is correlated with the TFR offset, and agrees well with simple models of abrupt star formation truncation in a spiral disc.

The dominant formation process for S0s is the quenching of star formation in spiral discs, although this is accompanied by an increase of stellar mass in the bulge. For cluster lenticulars, correlation between disc-fade and the local density suggests that the responsible truncation mechanism is related to cluster in-fall (intracluster medium interaction, ram-pressure stripping or tidally-induced starbursts). However, the similarity of various trends in different global environments (i.e. TFR offset, central age versus disc age), indicates that non-cluster-specific processes (minor mergers, harassment) may dominate.

6.2. Future work

Multi-wavelength imaging and aperture spectroscopy of galaxies in the Shapley Supercluster core is on-going. To expand the current spectroscopic coverage (~250 galaxies; Smith et al., 2007), we observed an additional ~100 confirmed cluster members using AAΩ. The extended study probes to larger cluster radii, enabling us to explore the effect of local density within the supercluster environment. The *GALEX* near-ultraviolet imaging presented in this thesis has also been augmented. The new observations cover an area coincident with the latest AAΩ fields, and include the far-ultraviolet band, which is important as it can help break the age–metallicity degeneracy by isolating the effect of the UV upturn phenomenon (old UV sources). Together, the larger spectroscopic sample and UV coverage in both NUV and FUV will allow further constraints on the young and metal poor populations of cluster galaxies.

The Coma cluster has also been subject to many wide-field observational campaigns in recent years (e.g. Eisenhardt et al., 2007; Carter et al., 2008). This thesis has made

use of CFHT Megacam optical imaging, but extensive infrared and spectroscopic data is also available. Until recently, one deficiency was modern UV observations of the cluster core, due to a total flux constraint on *GALEX* (the eighth magnitude foreground star HD112887 lies near to the field centre). However, with a relaxation of these safety limits, deep UV imaging in both *NUV* and *FUV* has been undertaken. Together with faint red galaxy spectroscopy from MMT Hectospec (Smith et al., 2009b), the early-type study can be extended to probe low mass galaxies in the densest low-redshift environment. Deep *GALEX* observations of the outer regions of Coma will facilitate investigation into the influence of the rich cluster environment on UV properties of this supposedly quiescent galaxy population.

Our results have successfully demonstrated the power of using an integral field unit for gradient analysis. The major limitation of the work in this thesis is sample size. For spatially resolved spectroscopy, the signal-to-noise requirement of precise stellar population analysis leads to long exposure times for each source. Further exploration of the relationship between stellar population gradients and central properties requires a larger sample of IFU observations, particularly probing lower galaxy mass.

At the confluence of these projects, it would be worthwhile to supplement the *GALEX* photometry with spatially resolved UV spectroscopy. The latest generation of spectrographs, such as the Ultraviolet and Visual Echelle Spectrograph (UVES) and X-Shooter (which can provide simultaneous UV/optical/NIR coverage at intermediate resolution), enables us to explore the internal structure of the young and metal poor components in the galaxies. In particular, these observations, together with targeted, high-resolution UV imaging from *HST* WFC3-UVIS, can help differentiate between young, nuclear components and more extended metal-poor stellar populations, addressing the age–metallicity degeneracy.

Finally, the S0 study presented here has given a fresh insight into the formation of lenticular galaxies. The current sample is again too small, with a better sampling of luminosity and local environment desirable. Parallel to expanding the Coma S0 sample, it would be interesting to study the current population of spiral galaxies in the outer regions of the cluster. Visual inspection of UV and optical imaging has identified several ($\sim$10) of these objects with ongoing gaseous stripping, which indicates that they may be in the early stages of transformation to lenticular galaxies.

Bibliography

Abadi, M. G., Moore, B., & Bower, R. G. 1999, MNRAS, 308, 947

Abazajian, K. N., Adelman-McCarthy, J. K., Agüeros, M. A., Allam, S. S., Allende Prieto, C., An, D., Anderson, K. S. J., & et al. 2009, ApJS, 182, 543

Allanson, S. P., Hudson, M. J., Smith, R. J., & Lucey, J. R. 2009, ApJ, 702, 1275

Arimoto, N. & Yoshii, Y. 1987, A&A, 173, 23

Arnett, W. D. 1973, ARA&A, 11, 73

Bacon, R., Adam, G., Baranne, A., Courtes, G., Dubet, D., Dubois, J. P., Emsellem, E., Ferruit, P., Georgelin, Y., Monnet, G., Pecontal, E., Rousset, A., & Say, F. 1995, A&AS, 113, 347

Bacon, R., Copin, Y., Monnet, G., Miller, B. W., Allington-Smith, J. R., Bureau, M., Carollo, C. M., Davies, R. L., Emsellem, E., Kuntschner, H., Peletier, R. F., Verolme, E. K., & de Zeeuw, P. T. 2001, MNRAS, 326, 23

Baldry, I. K. 2008, Astronomy and Geophysics, 49, 050000

Bamford, S. P., Nichol, R. C., Baldry, I. K., Land, K., Lintott, C. J., Schawinski, K., Slosar, A., Szalay, A. S., Thomas, D., Torki, M., Andreescu, D., Edmondson, E. M., Miller, C. J., Murray, P., Raddick, M. J., & Vandenberg, J. 2009, MNRAS, 393, 1324

Barnes, J. E. & Hernquist, L. E. 1991, ApJ, 370, L65

Baugh, C. M. 2006, Reports on Progress in Physics, 69, 3101

Baugh, C. M., Lacey, C. G., Frenk, C. S., Granato, G. L., Silva, L., Bressan, A., Benson, A. J., & Cole, S. 2005, MNRAS, 356, 1191

Bedregal, A. G., Aragón-Salamanca, A., & Merrifield, M. R. 2006a, MNRAS, 373, 1125

Bedregal, A. G., Aragón-Salamanca, A., Merrifield, M. R., & Milvang-Jensen, B. 2006b, MNRAS, 371, 1912

Bell, E. F. & de Jong, R. S. 2000, MNRAS, 312, 497

Bell, E. F., McIntosh, D. H., Katz, N., & Weinberg, M. D. 2003, ApJS, 149, 289

Bell, E. F., Wolf, C., Meisenheimer, K., Rix, H.-W., Borch, A., Dye, S., Kleinheinrich, M., Wisotzki, L., & McIntosh, D. H. 2004, ApJ, 608, 752

Bernardi, M., Nichol, R. C., Sheth, R. K., Miller, C. J., & Brinkmann, J. 2006, AJ, 131, 1288

Bernardi, M., Sheth, R. K., Nichol, R. C., Schneider, D. P., & Brinkmann, J. 2005, AJ, 129, 61

Bertin, E. & Arnouts, S. 1996, A&A, 117, 393

Blakeslee, J. P., Holden, B. P., Franx, M., Rosati, P., Bouwens, R. J., Demarco, R., Ford, H. C., Homeier, N. L., Illingworth, G. D., Jee, M. J., Mei, S., Menanteau, F., Meurer, G. R., Postman, M., & Tran, K.-V. H. 2006, ApJ, 644, 30

Blanton, M. R. 2006, ApJ, 648, 268

Blanton, M. R., Schlegel, D. J., Strauss, M. A., Brinkmann, J., Finkbeiner, D., Fukugita, M., Gunn, J. E., Hogg, D. W., Ivezić, Ž., Knapp, G. R., Lupton, R. H., Munn, J. A., Schneider, D. P., Tegmark, M., & Zehavi, I. 2005, AJ, 129, 2562

Bolton, A. S., Burles, S., Treu, T., Koopmans, L. V. E., & Moustakas, L. A. 2007, ApJL, 665, L105

Boselli, A., Cortese, L., Deharveng, J. M., Gavazzi, G., Yi, K. S., Gil de Paz, A., Seibert, M., Boissier, S., Donas, J., Lee, Y.-W., Madore, B. F., Martin, D. C., Rich, R. M., & Sohn, Y.-J. 2005, ApJ, 629, L29

Bower, R. G., Benson, A. J., Malbon, R., Helly, J. C., Frenk, C. S., Baugh, C. M., Cole, S., & Lacey, C. G. 2006, MNRAS, 370, 645

Bower, R. G., Lucey, J. R., & Ellis, R. S. 1992, MNRAS, 254, 601

Brown, M. J. I., Dey, A., Jannuzi, B. T., Brand, K., Benson, A. J., Brodwin, M., Croton, D. J., & Eisenhardt, P. R. 2007, ApJ, 654, 858

Bruzual, G. & Charlot, S. 2003, MNRAS, 344, 1000

Burstein, D. 1979, ApJ, 232, 74

Burstein, D., Bertola, F., Buson, L. M., Faber, S. M., & Lauer, T. R. 1988, ApJ, 328, 440

Burstein, D., Ho, L. C., Huchra, J. P., & Macri, L. M. 2005, ApJ, 621, 246

Butcher, H. & Oemler, Jr., A. 1978, ApJ, 219, 18

Caldwell, N., Rose, J. A., & Concannon, K. D. 2003, AJ, 125, 2891

Cappellari, M. & Copin, Y. 2003, MNRAS, 342, 345

Cappellari, M. & Emsellem, E. 2004, PASP, 116, 138

Cardelli, J. A., Clayton, G. C., & Mathis, J. S. 1989, ApJ, 345, 245

Cardiel, N., Gorgas, J., Cenarro, J., & Gonzalez, J. J. 1998, A&AS, 127, 597

Carlberg, R. G. 1984, ApJ, 286, 403

Carollo, C. M., Danziger, I. J., & Buson, L. 1993, MNRAS, 265, 553

Carter, D., Bridges, T. J., & Hau, G. K. T. 1999, MNRAS, 307, 131

Carter, D., Goudfrooij, P., Mobasher, B., Ferguson, H. C., Puzia, T. H., Aguerri, A. L., Balcells, M., Batcheldor, D., Bridges, T. J., Davies, J. I., Erwin, P., Graham, A. W., Guzmán, R., Hammer, D., Hornschemeier, A., Hoyos, C., Hudson, M. J., Huxor, A., Jogee, S., Komiyama, Y., Lotz, J., Lucey, J. R., Marzke, R. O., Merritt, D., Miller, B. W., Miller, N. A., Mouhcine, M., Okamura, S., Peletier, R. F., Phillipps, S., Poggianti, B. M., Sharples, R. M., Smith, R. J., Trentham, N., Tully, R. B., Valentijn, E., & Verdoes Kleijn, G. 2008, ApJS, 176, 424

Carter, D., Mobasher, B., Bridges, T. J., Poggianti, B. M., Komiyama, Y., Kashikawa, N., Doi, M., Iye, M., Okamura, S., Sekiguchi, M., Shimasaku, K., Yagi, M., & Yasuda, N. 2002, ApJ, 567, 772

Carter, D., Smith, D. J. B., Percival, S. M., Baldry, I. K., Collins, C. A., James, P. A., Salaris, M., Simpson, C., Stott, J. P., & Mobasher, B. 2009, MNRAS, 397, 695

Christlein, D. & Zabludoff, A. I. 2004, ApJ, 616, 192

Clemens, M. S., Bressan, A., Nikolic, B., Alexander, P., Annibali, F., & Rampazzo, R. 2006, MNRAS, 370, 702

Code, A. D. 1969, PASP, 81, 475

Cole, S., Lacey, C. G., Baugh, C. M., & Frenk, C. S. 2000, MNRAS, 319, 168

Cole, S., Percival, W. J., Peacock, J. A., Norberg, P., Baugh, C. M., Frenk, C. S., Baldry, I., Bland-Hawthorn, J., Bridges, T., Cannon, R., Colless, M., Collins, C., Couch, W., Cross, N. J. G., Dalton, G., Eke, V. R., De Propris, R., Driver, S. P., Efstathiou, G., Ellis, R. S., Glazebrook, K., Jackson, C., Jenkins, A., Lahav, O., Lewis, I., Lumsden, S., Maddox, S., Madgwick, D., Peterson, B. A., Sutherland, W., & Taylor, K. 2005, MNRAS, 362, 505

Colless, M., Dalton, G., Maddox, S., Sutherland, W., Norberg, P., Cole, S., Bland-Hawthorn, J., Bridges, T., Cannon, R., Collins, C., Couch, W., Cross, N., Deeley, K., De Propris, R., Driver, S. P., Efstathiou, G., Ellis, R. S., Frenk, C. S., Glazebrook, K., Jackson, C., Lahav, O., Lewis, I., Lumsden, S., Madgwick, D., Peacock, J. A., Peterson, B. A., Price, I., Seaborne, M., & Taylor, K. 2001, MNRAS, 328, 1039

Couch, W. J., Ellis, R. S., Sharples, R. M., & Smail, I. 1994, ApJ, 430, 121

Courteau, S., Dutton, A. A., van den Bosch, F. C., MacArthur, L. A., Dekel, A., McIntosh, D. H., & Dale, D. A. 2007, ApJ, 671, 203

Davies, R. L., Sadler, E. M., & Peletier, R. F. 1993, MNRAS, 262, 650

De Lucia, G., Springel, V., White, S. D. M., Croton, D., & Kauffmann, G. 2006, MNRAS, 366, 499

de Souza, R. E., Gadotti, D. A., & dos Anjos, S. 2004, ApJS, 153, 411

de Vaucouleurs, G. 1948, Annales d'Astrophysique, 11, 247

—. 1959, Handbuch der Physik, 53, 275

—. 1961, ApJS, 5, 233

de Vaucouleurs, G., de Vaucouleurs, A., Corwin, Jr., H. G., Buta, R. J., Paturel, G., & Fouque, P. 1991, Third Reference Catalogue of Bright Galaxies, ed. N. G. Roman, G. de Vaucouleurs, A. de Vaucouleurs, H. G. Corwin, Jr., R. J. Buta, G. Paturel, & P. Fouqué

de Zeeuw, P. T., Bureau, M., Emsellem, E., Bacon, R., Carollo, C. M., Copin, Y., Davies, R. L., Kuntschner, H., Miller, B. W., Monnet, G., Peletier, R. F., & Verolme, E. K. 2002, MNRAS, 329, 513

di Matteo, P., Pipino, A., Lehnert, M. D., Combes, F., & Semelin, B. 2009, A&A, 499, 427

Djorgovski, S. & Davis, M. 1987, ApJ, 313, 59

Donas, J., Deharveng, J.-M., Rich, R. M., Yi, S. K., Lee, Y.-W., Boselli, A., Gil de Paz, A., Boissier, S., Charlot, S., Salim, S., Bianchi, L., Barlow, T. A., Forster, K., Friedman, P. G., Heckman, T. M., Madore, B. F., Martin, D. C., Milliard, B., Morrissey, P., Neff, S. G., Schiminovich, D., Seibert, M., Small, T., Szalay, A. S., Welsh, B. Y., & Wyder, T. K. 2007, ApJS, 173, 597

Dorman, B. 1997, in Astronomical Society of the Pacific Conference Series, Vol. 116, The Nature of Elliptical Galaxies; 2nd Stromlo Symposium, ed. M. Arnaboldi, G. S. Da Costa, & P. Saha, 195–+

Dorman, B., O'Connell, R. W., & Rood, R. T. 2003, ApJ, 591, 878

Dotter, A., Chaboyer, B., Ferguson, J. W., Lee, H.-c., Worthey, G., Jevremović, D., & Baron, E. 2007, ApJ, 666, 403

Dressler, A. 1980a, ApJS, 42, 565

—. 1980b, ApJ, 236, 351

—. 1984, ApJ, 281, 512

Dressler, A., Lynden-Bell, D., Burstein, D., Davies, R. L., Faber, S. M., Terlevich, R., & Wegner, G. 1987, ApJ, 313, 42

Dressler, A., Oemler, A. J., Couch, W. J., Smail, I., Ellis, R. S., Barger, A., Butcher, H., Poggianti, B. M., & Sharples, R. M. 1997, ApJ, 490, 577

Dressler, A. & Sandage, A. 1983, ApJ, 265, 664

Drory, N., Salvato, M., Gabasch, A., Bender, R., Hopp, U., Feulner, G., & Pannella, M. 2005, ApJL, 619, L131

Efstathiou, G., Frenk, C. S., White, S. D. M., & Davis, M. 1988, MNRAS, 235, 715

Eggen, O. J., Lynden-Bell, D., & Sandage, A. R. 1962, ApJ, 136, 748

Eisenhardt, P. R., De Propris, R., Gonzalez, A. H., Stanford, S. A., Wang, M., & Dickinson, M. 2007, ApJ, 169, 225

Eisenstein, D. J., Hogg, D. W., Fukugita, M., Nakamura, O., Bernardi, M., Finkbeiner, D. P., Schlegel, D. J., Brinkmann, J., Connolly, A. J., Csabai, I., Gunn, J. E., Ivezić, Ž., Lamb, D. Q., Loveday, J., Munn, J. A., Nichol, R. C., Schneider, D. P., Strauss, M. A., Szalay, A., & York, D. G. 2003, ApJ, 585, 694

Ellingson, E., Lin, H., Yee, H. K. C., & Carlberg, R. G. 2001, ApJ, 547, 609

Emsellem, E., Cappellari, M., Krajnović, D., van de Ven, G., Bacon, R., Bureau, M., Davies, R. L., de Zeeuw, P. T., Falcón-Barroso, J., Kuntschner, H., McDermid, R., Peletier, R. F., & Sarzi, M. 2007, MNRAS, 379, 401

Emsellem, E., Cappellari, M., Peletier, R. F., McDermid, R. M., Bacon, R., Bureau, M., Copin, Y., Davies, R. L., Krajnović, D., Kuntschner, H., Miller, B. W., & de Zeeuw, P. T. 2004, MNRAS, 352, 721

Faber, S. M. & Jackson, R. E. 1976, ApJ, 204, 668

Faber, S. M., Willmer, C. N. A., Wolf, C., Koo, D. C., Weiner, B. J., Newman, J. A., Im, M., Coil, A. L., Conroy, C., Cooper, M. C., Davis, M., & Finkbeiner, D. P. 2007, ApJ, 665, 265

Ferreras, I. & Silk, J. 2000, ApJL, 541, L37

Fisher, D., Franx, M., & Illingworth, G. 1996, ApJ, 459, 110

Forbes, D. A., Sánchez-Blázquez, P., & Proctor, R. 2005, MNRAS, 361, L6

Franx, M., Illingworth, G., & Heckman, T. 1989, ApJ, 344, 613

Freeman, K. C. 1970, ApJ, 160, 811

Geach, J. E., Smail, I., Moran, S. M., Treu, T., & Ellis, R. S. 2009, ApJ, 691, 783

Girardi, L., Bressan, A., Bertelli, G., & Chiosi, C. 2000, A&AS, 141, 371

Godwin, J. G., Metcalfe, N., & Peach, J. V. 1983, MNRAS, 202, 113

Gorgas, J., Efstathiou, G., & Aragon Salamanca, A. 1990, MNRAS, 245, 217

Graves, G. J., Faber, S. M., Schiavon, R. P., & Yan, R. 2007, ApJ, 671, 243

Guzman, R., Lucey, J. R., Carter, D., & Terlevich, R. J. 1992, MNRAS, 257, 187

Haines, C. P., Gargiulo, A., & Merluzzi, P. 2008, MNRAS, 385, 1201

Heavens, A. F., Jimenez, R., & Lahav, O. 2000, MNRAS, 317, 965

Hinz, J. L., Rieke, G. H., & Caldwell, N. 2003, AJ, 126, 2622

Hogg, D. W., Blanton, M. R., Brinchmann, J., Eisenstein, D. J., Schlegel, D. J., Gunn, J. E., McKay, T. A., Rix, H.-W., Bahcall, N. A., Brinkmann, J., & Meiksin, A. 2004, ApJL, 601, L29

Holland, W. S., Robson, E. I., Gear, W. K., Cunningham, C. R., Lightfoot, J. F., Jenness, T., Ivison, R. J., Stevens, J. A., Ade, P. A. R., Griffin, M. J., Duncan, W. D., Murphy, J. A., & Naylor, D. A. 1999, MNRAS, 303, 659

Hook, I. M., Jørgensen, I., Allington-Smith, J. R., Davies, R. L., Metcalfe, N., Murowinski, R. G., & Crampton, D. 2004, PASP, 116, 425

Hopkins, P. F., Cox, T. J., Dutta, S. N., Hernquist, L., Kormendy, J., & Lauer, T. R. 2009, ApJS, 181, 135

Hubble, E. P. 1927, The Observatory, 50, 276

Jarrett, T. H., Chester, T., Cutri, R., Schneider, S., Skrutskie, M., & Huchra, J. P. 2000, AJ, 119, 2498

Jenkins, A., Frenk, C. S., White, S. D. M., Colberg, J. M., Cole, S., Evrard, A. E., Couchman, H. M. P., & Yoshida, N. 2001, MNRAS, 321, 372

Jones, D. H., Saunders, W., Colless, M., Read, M. A., Parker, Q. A., Watson, F. G., Campbell, L. A., Burkey, D., Mauch, T., Moore, L., Hartley, M., Cass, P., James, D., Russell, K., Fiegert, K., Dawe, J., Huchra, J., Jarrett, T., Lahav, O., Lucey, J., Mamon, G. A., Proust, D., Sadler, E. M., & Wakamatsu, K.-i. 2004, MNRAS, 355, 747

Jones, L. A. & Worthey, G. 1995, ApJL, 446, L31+

Jordi, K., Grebel, E. K., & Ammon, K. 2006, A&A, 460, 339

Jørgensen, I. 1999, MNRAS, 306, 607

Kauffmann, G., White, S. D. M., Heckman, T. M., Ménard, B., Brinchmann, J., Charlot, S., Tremonti, C., & Brinkmann, J. 2004, MNRAS, 353, 713

Kaviraj, S., Rey, S.-C., Rich, R. M., Yoon, S.-J., & Yi, S. K. 2007a, MNRAS, 381, L74

Kaviraj, S., Schawinski, K., Devriendt, J. E. G., Ferreras, I., Khochfar, S., Yoon, S.-J., Yi, S. K., Deharveng, J.-M., Boselli, A., Barlow, T., Conrow, T., Forster, K., Friedman, P. G., Martin, D. C., Morrissey, P., Neff, S., Schiminovich, D., Seibert, M., Small, T., Wyder, T., Bianchi, L., Donas, J., Heckman, T., Lee, Y.-W., Madore, B., Milliard, B., Rich, R. M., & Szalay, A. 2007b, ApJS, 173, 619

Kawata, D. & Gibson, B. K. 2003, MNRAS, 340, 908

Klypin, A., Kravtsov, A. V., Valenzuela, O., & Prada, F. 1999, ApJ, 522, 82

Kobayashi, C. 2004, MNRAS, 347, 740

Kobayashi, C. & Arimoto, N. 1999, ApJ, 527, 573

Kodama, T. & Arimoto, N. 1997, A&A, 320, 41

Kron, R. G. 1980, ApJS, 43, 305

Kuntschner, H. 2000, MNRAS, 315, 184

Kuntschner, H. & Davies, R. L. 1998, MNRAS, 295, L29+

Kuntschner, H., Emsellem, E., Bacon, R., Bureau, M., Cappellari, M., Davies, R. L., de Zeeuw, P. T., Falcón-Barroso, J., Krajnović, D., McDermid, R. M., Peletier, R. F., & Sarzi, M. 2006, MNRAS, 369, 497

Kuntschner, H., Lucey, J. R., Smith, R. J., Hudson, M. J., & Davies, R. L. 2001, MNRAS, 323, 615

La Barbera, F., de Carvalho, R. R., Gal, R. R., Busarello, G., Merluzzi, P., Capaccioli, M., & Djorgovski, S. G. 2005, ApJL, 626, L19

Larson, R. B. 1974a, MNRAS, 166, 585

—. 1974b, MNRAS, 169, 229

Larson, R. B., Tinsley, B. M., & Caldwell, C. N. 1980, ApJ, 237, 692

Lee, H.-c., Lee, Y.-W., & Gibson, B. K. 2002, AJ, 124, 2664

LeFevre, O., Saisse, M., Mancini, D., Brau-Nogue, S., Caputi, O., Castinel, L., D'Odorico, S., Garilli, B., Kissler-Patig, M., Lucuix, C., Mancini, G., Pauget, A., Sciarretta, G., Scodeggio, M., Tresse, L., & Vettolani, G. 2003, in Presented at the Society of Photo-Optical Instrumentation Engineers (SPIE) Conference, Vol. 4841, Instrument Design and Performance for Optical/Infrared Ground-based Telescopes. Edited by Iye, Masanori; Moorwood, Alan F. M. Proceedings of the SPIE, Volume 4841, pp. 1670-1681 (2003)., ed. M. Iye & A. F. M. Moorwood, 1670–1681

Lehmer, B. D., Alexander, D. M., Geach, J. E., Smail, I., Basu-Zych, A., Bauer, F. E., Chapman, S. C., Matsuda, Y., Scharf, C. A., Volonteri, M., & Yamada, T. 2009, ApJ, 691, 687

Leitherer, C., Schaerer, D., Goldader, J. D., Delgado, R. M. G., Robert, C., Kune, D. F., de Mello, D. F., Devost, D., & Heckman, T. M. 1999, ApJS, 123, 3

Lintott, C. J., Schawinski, K., Slosar, A., Land, K., Bamford, S., Thomas, D., Raddick, M. J., Nichol, R. C., Szalay, A., Andreescu, D., Murray, P., & Vandenberg, J. 2008, MNRAS, 389, 1179

Lucey, J. R., Guzman, R., Carter, D., & Terlevich, R. J. 1991, MNRAS, 253, 584

MacArthur, L. A., Courteau, S., Bell, E., & Holtzman, J. A. 2004, ApJS, 152, 175

Mandelbaum, R., Seljak, U., Cool, R. J., Blanton, M., Hirata, C. M., & Brinkmann, J. 2006, MNRAS, 372, 758

Maraston, C. 2005, MNRAS, 362, 799

Maraston, C. & Thomas, D. 2000, ApJ, 541, 126

Martin, D. C., Fanson, J., Schiminovich, D., Morrissey, P., Friedman, P. G., Barlow, T. A., Conrow, T., Grange, R., Jelinsky, P. N., Milliard, B., Siegmund, O. H. W., Bianchi, L., Byun, Y.-I., Donas, J., Forster, K., Heckman, T. M., Lee, Y.-W., Madore, B. F., Malina, R. F., Neff, S. G., Rich, R. M., Small, T., Surber, F., Szalay, A. S., Welsh, B., & Wyder, T. K. 2005, ApJL, 619, L1

Mathews, W. G. & Baker, J. C. 1971, ApJ, 170, 241

Mathewson, D. S., Ford, V. L., & Buchhorn, M. 1992, ApJS, 81, 413

Matković, A. & Guzmán, R. 2005, MNRAS, 362, 289

Matteucci, F. 1994, A&A, 288, 57

McCarthy, I. G., Frenk, C. S., Font, A. S., Lacey, C. G., Bower, R. G., Mitchell, N. L., Balogh, M. L., & Theuns, T. 2008, MNRAS, 383, 593

McGaugh, S. S. & de Blok, W. J. G. 1998, ApJ, 499, 41

Mehlert, D., Saglia, R. P., Bender, R., & Wegner, G. 2000, A&A, 141, 449

Mehlert, D., Thomas, D., Saglia, R. P., Bender, R., & Wegner, G. 2003, A&A, 407, 423

Mercurio, A., Merluzzi, P., Haines, C. P., Gargiulo, A., Krusanova, N., Busarello, G., Barbera, F. L., Capaccioli, M., & Covone, G. 2006, MNRAS, 368, 109

Metcalfe, N., Godwin, J. G., & Peach, J. V. 1994, MNRAS, 267, 431

Meyer, M. J., Zwaan, M. A., Webster, R. L., Schneider, S., & Staveley-Smith, L. 2008, MNRAS, 391, 1712

Michard, R. 2005, A&A, 441, 451

Mihos, J. C. & Hernquist, L. 1994, ApJ, 437, L47

Moorthy, B. K. & Holtzman, J. A. 2006, MNRAS, 371, 583

Morelli, L., Pompei, E., Pizzella, A., Méndez-Abreu, J., Corsini, E. M., Coccato, L., Saglia, R. P., Sarzi, M., & Bertola, F. 2008, MNRAS, 389, 341

Morrissey, P., Conrow, T., Barlow, T. A., Small, T., Seibert, M., Wyder, T. K., Budavári, T., Arnouts, S., Friedman, P. G., Forster, K., Martin, D. C., Neff, S. G., Schiminovich, D., Bianchi, L., Donas, J., Heckman, T. M., Lee, Y.-W., Madore, B. F., Milliard, B., Rich, R. M., Szalay, A. S., Welsh, B. Y., & Yi, S. K. 2007, ApJS, 173, 682

Navarro, J. F., Frenk, C. S., & White, S. D. M. 1996, ApJ, 462, 563

Neistein, E., Maoz, D., Rix, H.-W., & Tonry, J. L. 1999, AJ, 117, 2666

Nelan, J. E., Smith, R. J., Hudson, M. J., Wegner, G. A., Lucey, J. R., Moore, S. A. W., Quinney, S. J., & Suntzeff, N. B. 2005, ApJ, 632, 137

Norris, M. A. 2008, PhD thesis, University of Durham

Norris, M. A., Sharples, R. M., & Kuntschner, H. 2006, MNRAS, 367, 815

O'Connell, R. W. 1976, ApJ, 206, 370

—. 1999, ARA&A, 37, 603

O'Connell, R. W., Bohlin, R. C., Collins, N. R., Cornett, R. H., Hill, J. K., Hill, R. S., Landsman, W. B., Roberts, M. S., Smith, A. M., & Stecher, T. P. 1992, ApJ, 395, L45

Peletier, R. F., Davies, R. L., Illingworth, G. D., Davis, L. E., & Cawson, M. 1990, AJ, 100, 1091

Peng, C. Y., Ho, L. C., Impey, C. D., & Rix, H.-W. 2002, AJ, 124, 266

Peterson, R. C. 1976, ApJL, 210, L123

Pipino, A., D'Ercole, A., & Matteucci, F. 2008, A&A, 484, 679

Pizagno, J., Prada, F., Weinberg, D. H., Rix, H.-W., Pogge, R. W., Grebel, E. K., Harbeck, D., Blanton, M., Brinkmann, J., & Gunn, J. E. 2007, AJ, 134, 945

Poggianti, B. M., Bridges, T. J., Carter, D., Mobasher, B., Doi, M., Iye, M., Kashikawa, N., Komiyama, Y., Okamura, S., Sekiguchi, M., Shimasaku, K., Yagi, M., & Yasuda, N. 2001, ApJ, 563, 118

Poggianti, B. M., Fasano, G., Bettoni, D., Cava, A., Dressler, A., Vanzella, E., Varela, J., Couch, W. J., D'Onofrio, M., Fritz, J., Kjaergaard, P., Moles, M., & Valentinuzzi, T. 2009, ApJL, 697, L137

Proctor, R. N., Forbes, D. A., & Beasley, M. A. 2004, MNRAS, 355, 1327

Proctor, R. N., Forbes, D. A., Romanowsky, A. J., Brodie, J. P., Strader, J., Spolaor, M., Mendel, J. T., & Spitler, L. 2009, MNRAS, 398, 91

Proctor, R. N. & Sansom, A. E. 2002, MNRAS, 333, 517

Rampazzo, R., Marino, A., Tantalo, R., Bettoni, D., Buson, L. M., Chiosi, C., Galletta, G., Grützbauch, R., & Rich, R. M. 2007, MNRAS, 381, 245

Rawle, T. D., Smith, R. J., Lucey, J. R., Hudson, M. J., & Wegner, G. A. 2008a, MNRAS, 385, 2097

Rawle, T. D., Smith, R. J., Lucey, J. R., & Swinbank, A. M. 2008b, MNRAS, 389, 1891

Raychaudhury, S. 1989, Nature, 342, 251

Reda, F. M., Proctor, R. N., Forbes, D. A., Hau, G. K. T., & Larsen, S. S. 2007, MNRAS, 377, 1772

Rhoads, J. E., Malhotra, S., Dey, A., Stern, D., Spinrad, H., & Jannuzi, B. T. 2000, ApJL, 545, L85

Rich, R. M., Salim, S., Brinchmann, J., Charlot, S., Seibert, M., Kauffmann, G., Lee, Y.-W., Yi, S. K., Barlow, T. A., Bianchi, L., Byun, Y.-I., Donas, J., Forster, K., Friedman, P. G., Heckman, T. M., Jelinsky, P. N., Madore, B. F., Malina, R. F., Martin, D. C., Milliard, B., Morrissey, P., Neff, S. G., Schiminovich, D., Siegmund, O. H. W., Small, T., Szalay, A. S., Welsh, B. Y., & Wyder, T. K. 2005, ApJ, 619, L107

Rose, J. A. 1985, AJ, 90, 1927

—. 1994, AJ, 107, 206

Sakai, S., Mould, J. R., Hughes, S. M. G., Huchra, J. P., Macri, L. M., Kennicutt, Jr., R. C., Gibson, B. K., Ferrarese, L., Freedman, W. L., Han, M., Ford, H. C., Graham, J. A., Illingworth, G. D., Kelson, D. D., Madore, B. F., Sebo, K., Silbermann, N. A., & Stetson, P. B. 2000, ApJ, 529, 698

Salasnich, B., Girardi, L., Weiss, A., & Chiosi, C. 2000, A&A, 361, 1023

Salim, S., Rich, R. M., Charlot, S., Brinchmann, J., Johnson, B. D., Schiminovich, D., Seibert, M., Mallery, R., Heckman, T. M., Forster, K., Friedman, P. G., Martin, D. C., Morrissey, P., Neff, S. G., Small, T., Wyder, T. K., Bianchi, L., Donas, J., Lee, Y.-W., Madore, B. F., Milliard, B., Szalay, A. S., Welsh, B. Y., & Yi, S. K. 2007, ApJS, 173, 267

Sánchez-Blázquez, P., Forbes, D. A., Strader, J., Brodie, J., & Proctor, R. 2007, MNRAS, 377, 759

Sánchez-Blázquez, P., Gorgas, J., & Cardiel, N. 2006, A&A, 457, 823

Sandage, A. 1972, ApJ, 176, 21

—. 2005, ARA&A, 43, 581

Sarzi, M., Falcón-Barroso, J., Davies, R. L., Bacon, R., Bureau, M., Cappellari, M., de Zeeuw, P. T., Emsellem, E., Fathi, K., Krajnović, D., Kuntschner, H., McDermid, R. M., & Peletier, R. F. 2006, MNRAS, 366, 1151

Schawinski, K., Khochfar, S., Kaviraj, S., Yi, S. K., Boselli, A., Barlow, T., Conrow, T., Forster, K., Friedman, P. G., Martin, D. C., Morrissey, P., Neff, S., Schiminovich, D., Seibert, M., Small, T., Wyder, T. K., Bianchi, L., Donas, J., Heckman, T., Lee, Y.-W., Madore, B., Milliard, B., Rich, R. M., & Szalay, A. 2006, Nature, 442, 888

Schiavon, R. P. 2007, ApJS, 171, 146

Schlegel, D. J., Finkbeiner, D. P., & Davis, M. 1998, ApJ, 500, 525

Serra, P. & Trager, S. C. 2007, MNRAS, 374, 769

Skrutskie, M. F., Cutri, R. M., Stiening, R., Weinberg, M. D., Schneider, S., Carpenter, J. M., Beichman, C., Capps, R., Chester, T., Elias, J., Huchra, J., Liebert, J., Lonsdale, C., Monet, D. G., Price, S., Seitzer, P., Jarrett, T., Kirkpatrick, J. D., Gizis, J. E., Howard, E., Evans, T., Fowler, J., Fullmer, L., Hurt, R., Light, R., Kopan, E. L., Marsh, K. A., McCallon, H. L., Tam, R., Van Dyk, S., & Wheelock, S. 2006, AJ, 131, 1163

Smith, G. P., Treu, T., Ellis, R. S., Moran, S. M., & Dressler, A. 2005, ApJ, 620, 78

Smith, R. J., Hudson, M. J., Nelan, J. E., Moore, S. A. W., Quinney, S. J., Wegner, G. A., Lucey, J. R., Davies, R. L., Malecki, J. J., Schade, D., & Suntzeff, N. B. 2004, AJ, 128, 1558

Smith, R. J., Lucey, J. R., & Hudson, M. J. 2007, MNRAS, 381, 1035

—. 2009a

Smith, R. J., Lucey, J. R., Hudson, M. J., Allanson, S. P., Bridges, T. J., Hornschemeier, A. E., Marzke, R. O., & Miller, N. A. 2009b, MNRAS, 392, 1265

Spergel, D. N., Bean, R., Doré, O., Nolta, M. R., Bennett, C. L., Dunkley, J., Hinshaw, G., Jarosik, N., Komatsu, E., Page, L., Peiris, H. V., Verde, L., Halpern, M., Hill, R. S., Kogut, A., Limon, M., Meyer, S. S., Odegard, N., Tucker, G. S., Weiland, J. L., Wollack, E., & Wright, E. L. 2007, ApJS, 170, 377

Spinrad, H., Smith, H. E., & Taylor, D. J. 1972, ApJ, 175, 649

Spolaor, M., Proctor, R. N., Forbes, D. A., & Couch, W. J. 2009, ApJ, 691, L138

Springel, V. & Hernquist, L. 2003, MNRAS, 339, 289

Stott, J. P., Pimbblet, K. A., Edge, A. C., Smith, G. P., & Wardlow, J. L. 2009, MNRAS, 394, 2098

Swinbank, A. M., Bower, R. G., Smith, G. P., Smail, I., Kneib, J.-P., Ellis, R. S., Stark, D. P., & Bunker, A. J. 2006, MNRAS, 368, 1631

Tamura, N., Kobayashi, C., Arimoto, N., Kodama, T., & Ohta, K. 2000, AJ, 119, 2134

Tamura, N. & Ohta, K. 2003, AJ, 126, 596

—. 2004, MNRAS, 355, 617

Thomas, D. & Davies, R. L. 2006, MNRAS, 366, 510

Thomas, D., Maraston, C., & Bender, R. 2003, MNRAS, 339, 897

Thomas, D., Maraston, C., Bender, R., & Mendes de Oliveira, C. 2005, ApJ, 621, 673

Thomas, D., Maraston, C., & Korn, A. 2004, MNRAS, 351, L19

Trager, S. C., Faber, S. M., & Dressler, A. 2008, MNRAS, 386, 715

Trager, S. C., Faber, S. M., Worthey, G., & González, J. J. 2000a, AJ, 120, 165

—. 2000b, AJ, 119, 1645

Tran, K.-V. H., van Dokkum, P., Illingworth, G. D., Kelson, D., Gonzalez, A., & Franx, M. 2005, ApJ, 619, 134

Tripicco, M. J. & Bell, R. A. 1995, AJ, 110, 3035

Tully, R. B. & Fisher, J. R. 1977, A&A, 54, 661

Tully, R. B. & Pierce, M. J. 2000, ApJ, 533, 744

van Dokkum, P. G. 2001, PASP, 113, 1420

Vazdekis, A. 1999, ApJ, 513, 224

Verheijen, M. A. W. 2001, ApJ, 563, 694

Visvanathan, N. & Sandage, A. 1977, ApJ, 216, 214

Vogt, N. P., Phillips, A. C., Faber, S. M., Gallego, J., Gronwall, C., Guzman, R., Illingworth, G. D., Koo, D. C., & Lowenthal, J. D. 1997, ApJL, 479, L121+

Weijmans, A., Cappellari, M., Bacon, R., de Zeeuw, P. T., Emsellem, E., Falcon-Barroso, J., Kuntschner, H., McDermid, R. M., van den Bosch, R. C. E., & van de Ven, G. 2009, ArXiv e-prints

White, S. D. M. 1980, MNRAS, 191, 1P

White, S. D. M. & Frenk, C. S. 1991, ApJ, 379, 52

White, S. D. M. & Rees, M. J. 1978, MNRAS, 183, 341

Williams, M. J., Bureau, M., & Cappellari, M. 2009, ArXiv e-prints

Wilman, D. J., Oemler, A., Mulchaey, J. S., McGee, S. L., Balogh, M. L., & Bower, R. G. 2009, ApJ, 692, 298

Worthey, G. 1994, ApJS, 95, 107

Worthey, G., Dorman, B., & Jones, L. A. 1996, AJ, 112, 948

Worthey, G., Faber, S. M., Gonzalez, J. J., & Burstein, D. 1994, ApJS, 94, 687

Wu, H., Shao, Z., Mo, H. J., Xia, X., & Deng, Z. 2005, ApJ, 622, 244

Yi, S., Demarque, P., & Oemler, A. J. 1997, ApJ, 486, 201

Yi, S. K., Yoon, S.-J., Kaviraj, S., Deharveng, J.-M., Rich, R. M., Salim, S., & Boselli, A. 2005, ApJ, 619, L111

Appendix A

VIMOS central parameters

Tables A.1 and A.2 present the central stellar population parameters derived from VIMOS. All central values are from an $r_e/3$ circular aperture, as described in Chapter 3.

Table A.1: Central velocity dispersion and stellar populations for the 12 galaxies in the A3389 sample.

ID	$\log\sigma$	log(age/Gyr)	[Z/H]	[α/Fe]
D40	2.273 ± 0.012	1.006 ± 0.038	0.230 ± 0.042	0.369 ± 0.039
D41	2.315 ± 0.005	1.018 ± 0.021	0.347 ± 0.018	0.137 ± 0.013
D42	2.455 ± 0.005	1.008 ± 0.019	0.339 ± 0.017	0.324 ± 0.012
D43	2.194 ± 0.009	1.044 ± 0.037	0.233 ± 0.037	0.073 ± 0.030
D44	2.406 ± 0.009	0.928 ± 0.047	0.380 ± 0.025	0.239 ± 0.024
D48	2.216 ± 0.009	1.077 ± 0.030	0.241 ± 0.030	0.083 ± 0.025
D49	2.306 ± 0.011	1.331 ± 0.042	0.101 ± 0.035	0.391 ± 0.026
D52	2.446 ± 0.005	1.310 ± 0.019	0.128 ± 0.016	0.292 ± 0.012
D53	2.077 ± 0.012	0.642 ± 0.072	0.354 ± 0.048	0.182 ± 0.042
D60	2.317 ± 0.003	0.805 ± 0.030	0.308 ± 0.015	0.159 ± 0.013
D61	2.168 ± 0.011	0.652 ± 0.064	0.340 ± 0.045	0.076 ± 0.037
D89	2.416 ± 0.006	1.033 ± 0.022	0.304 ± 0.020	0.217 ± 0.015

Table A.2: Central velocity dispersion and derived stellar populations for the 19 galaxies in the Shapley sample.

ID	$\log\sigma$	log(age/Gyr)	[Z/H]	[α/Fe]
MGP0129	2.015 ± 0.026	0.867 ± 0.115	–0.024 ± 0.061	0.090 ± 0.089
MGP1189	2.461 ± 0.007	0.945 ± 0.039	0.249 ± 0.030	0.240 ± 0.028
MGP1195	2.063 ± 0.012	0.869 ± 0.068	0.204 ± 0.042	0.144 ± 0.038
MGP1211	1.949 ± 0.050	1.013 ± 0.079	0.007 ± 0.101	–0.016 ± 0.129
MGP1230	1.759 ± 0.029	0.734 ± 0.076	–0.171 ± 0.052	0.133 ± 0.076
MGP1440	2.273 ± 0.013	1.213 ± 0.049	–0.012 ± 0.038	0.334 ± 0.037
MGP1490	1.885 ± 0.028	0.639 ± 0.082	0.119 ± 0.082	0.186 ± 0.078
MGP1600	2.473 ± 0.007	1.148 ± 0.026	0.274 ± 0.022	0.362 ± 0.018
MGP1626	2.414 ± 0.012	0.491 ± 0.111	0.660 ± 0.130	0.260 ± 0.042
MGP1835	2.306 ± 0.009	0.874 ± 0.048	0.475 ± 0.028	0.177 ± 0.020
MGP1988	2.245 ± 0.014	0.778 ± 0.054	0.299 ± 0.036	0.303 ± 0.036
MGP2083	2.387 ± 0.006	1.014 ± 0.027	0.160 ± 0.028	0.222 ± 0.021
MGP2146	2.084 ± 0.015	0.836 ± 0.080	0.109 ± 0.044	0.225 ± 0.045
MGP2399	1.906 ± 0.042	0.662 ± 0.098	0.073 ± 0.106	0.051 ± 0.088
MGP2437	2.271 ± 0.014	1.412 ± 0.053	0.100 ± 0.043	0.382 ± 0.035
MGP2440	2.356 ± 0.007	1.043 ± 0.019	0.096 ± 0.022	0.206 ± 0.020
MGP3971	2.261 ± 0.022	1.144 ± 0.051	0.117 ± 0.051	0.349 ± 0.044
MGP3976	2.402 ± 0.009	1.118 ± 0.031	0.194 ± 0.030	0.358 ± 0.025
MGP4358	1.832 ± 0.070	0.659 ± 0.153	0.237 ± 0.148	–0.188 ± 0.120

Appendix B

VIMOS radial bins and gradients

Figures B.1 – B.31 in this appendix presents the adopted radial bins, absorption line measurements and stellar population gradients for each galaxy observed with VIMOS (as described in Chapter 3).

The broadband, wavelength-collapsed image of the galaxy from VIMOS, displayed in the top-left, is overlaid by the bin boundaries (green; see Section 3.3.2) and the elliptical effective radius (r_e; red) for reference. Immediately below this panel, a histogram presents the S/N Å^{-1} (averaged over the region 4700 – 5000 Å) within each annulus out to 10 arcsec; again r_e is indicated in red.

The upper set of panels in the right column display the measured line strengths for each index in the relevant 'master' set. For galaxies in Abell 3389 (Dnn), these indices are HγF, Hβ, Fe4383, Fe4531, Fe4668, Fe5270, Fe5335, Mgb5177. For Shapley Supercluster galaxies (MGPnnnn), the indices are HδF, HγF, Hβ, Fe4383, Fe4531, Fe4668, Fe5015, Fe5406, Mgb5177. (See Section 3.4.3 for further details). Black points show the measurements, while the black line is the unweighted fit to points within r_e, with the gradient recorded in red text at the top of each panel. The red points show the estimated index values at 0.1 $\times$ r_e and r_e, connected by a red line (see Section 3.5.2). Galaxies with only two bins within the effective radius have not been fit for gradients. Grey dotted lines show the bin boundaries, while the orange and blue dashed lines indicate r_e and the approximate PSF radius (= $\mathrm{PSF_{FWHM}}/2.355$) respectively.

The three lowest panels on the right-hand side present the stellar population gradients. The red points show the derived stellar population for the inner and outer points, and the resulting gradient is recorded at the top of each panel (in red). For comparison, the black points show the alternate method – stellar populations derived for each radial

bin, and the black line is an unweighted linear fit within r_e. This gradient is also shown at the top of each panel (in black). Vertical lines have the same meaning as above.

Tables B.1 and B.2 list the index gradient values for all galaxies. Finally, Tables B.3 and B.4 display the stellar population gradients.

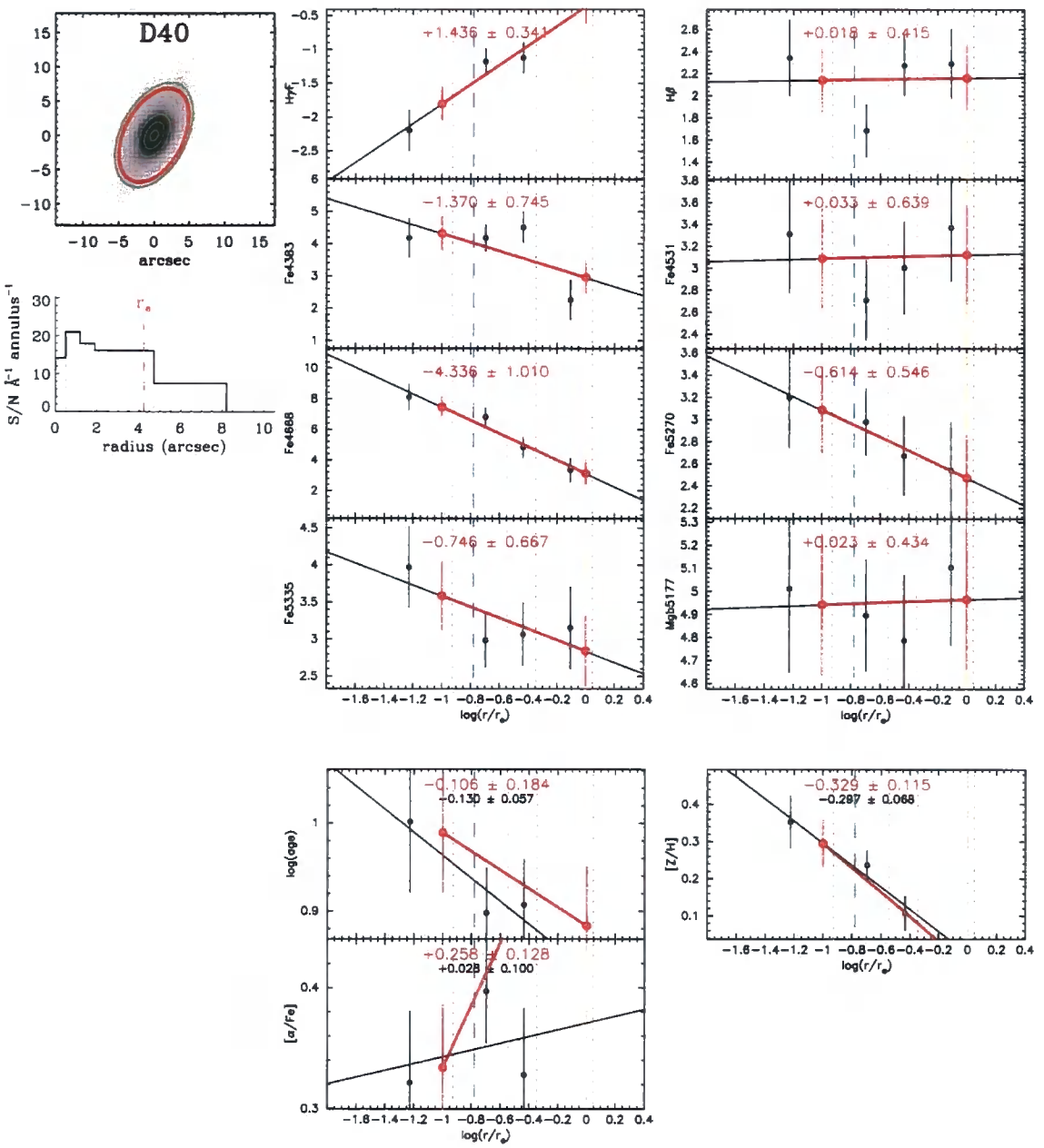

Figure B.1: D40. Adopted bins and gradients. Layout described above.

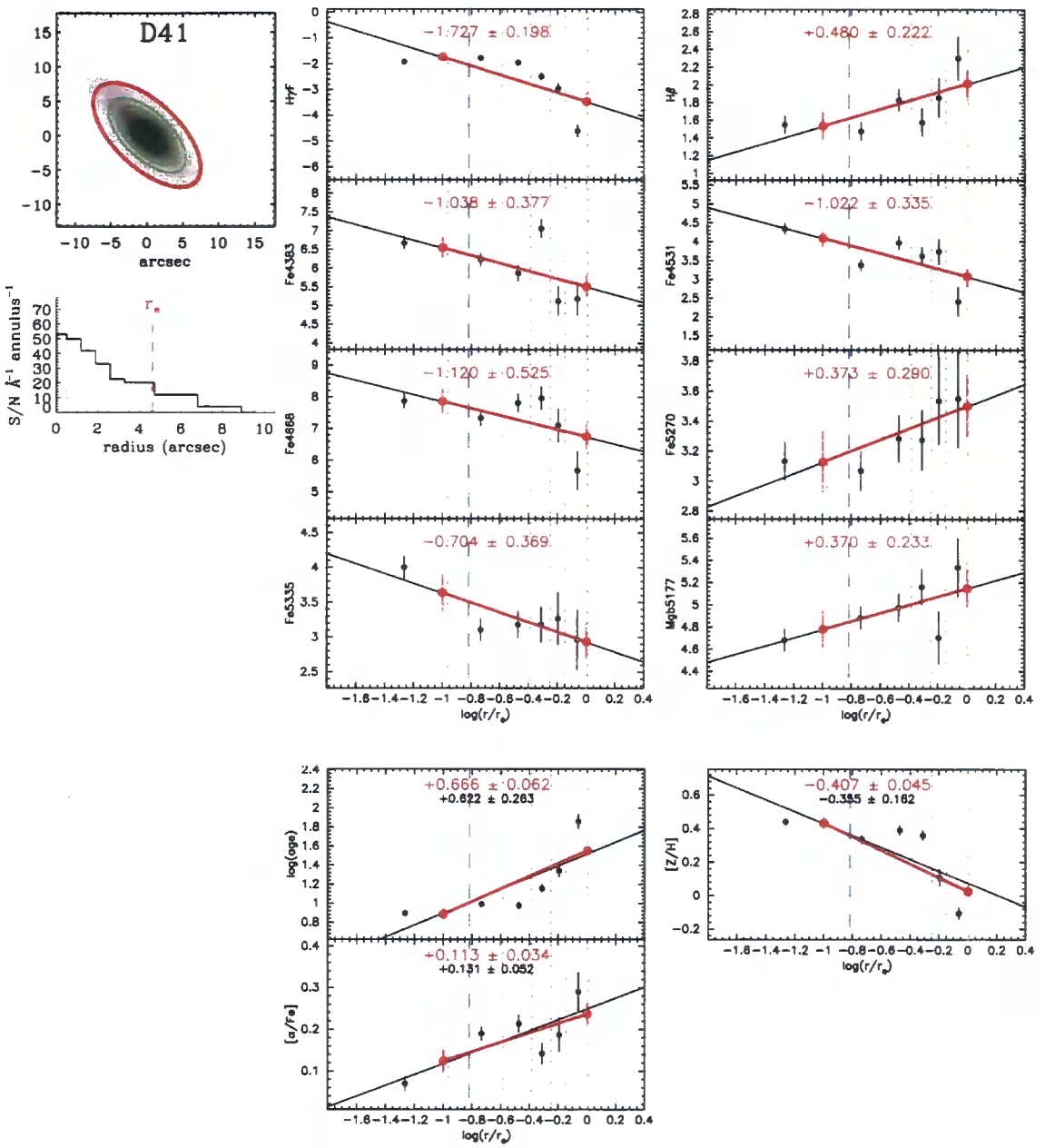

Figure B.2: D41. Adopted bins and gradients. Layout described above.

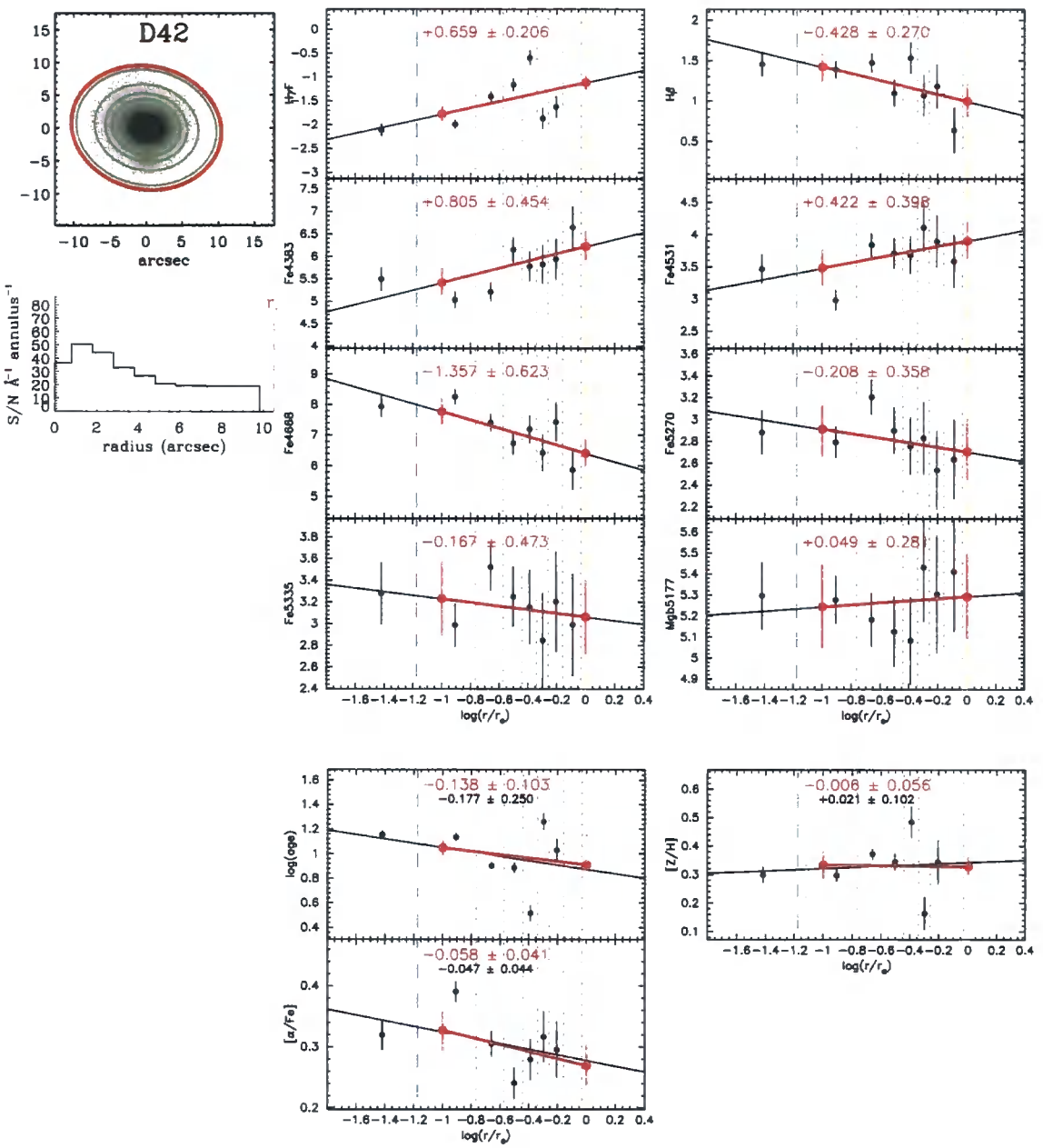

Figure B.3: D42. Adopted bins and gradients. Layout described above.

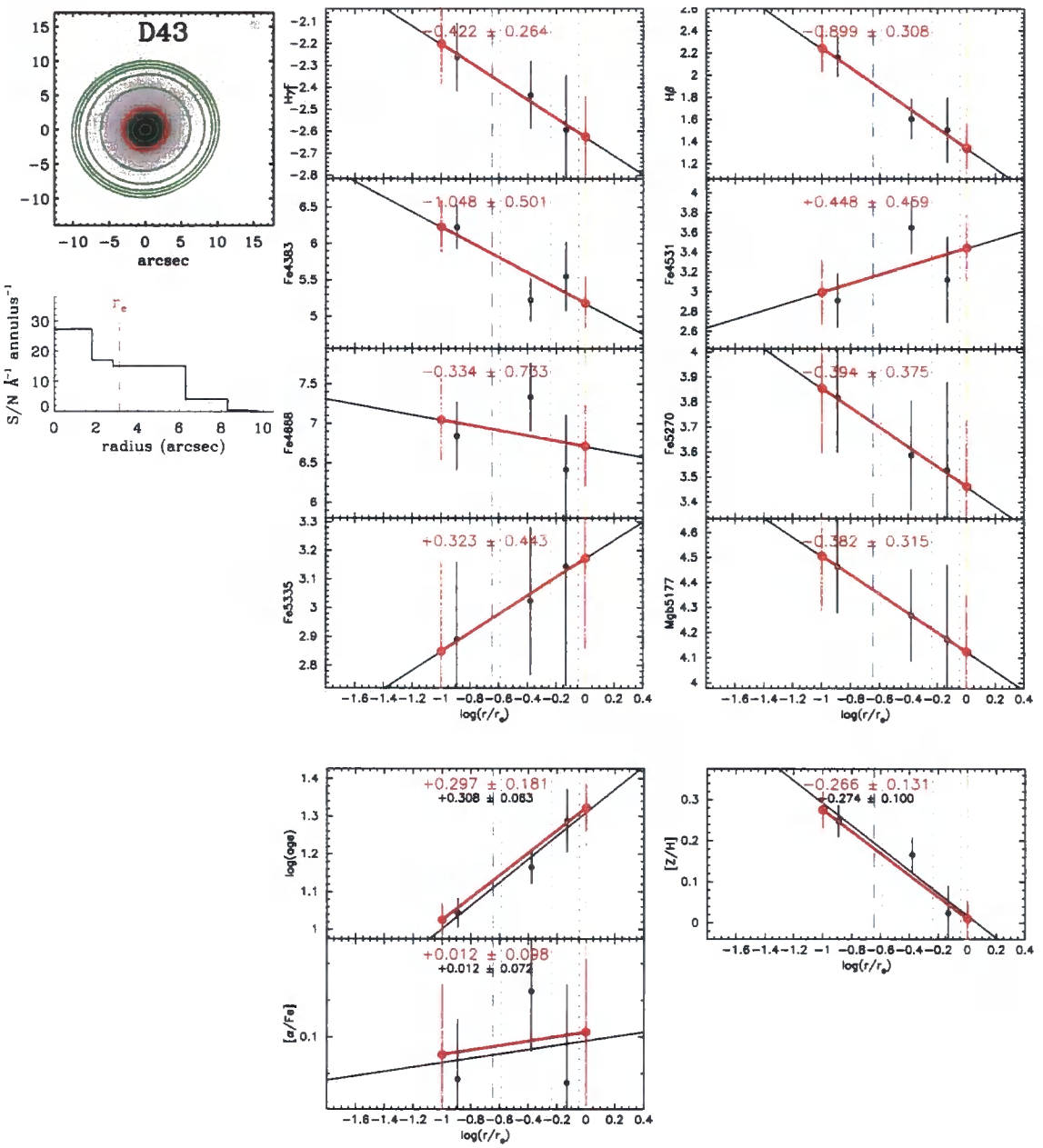

Figure B.4: D43. Adopted bins and gradients. Layout described above.

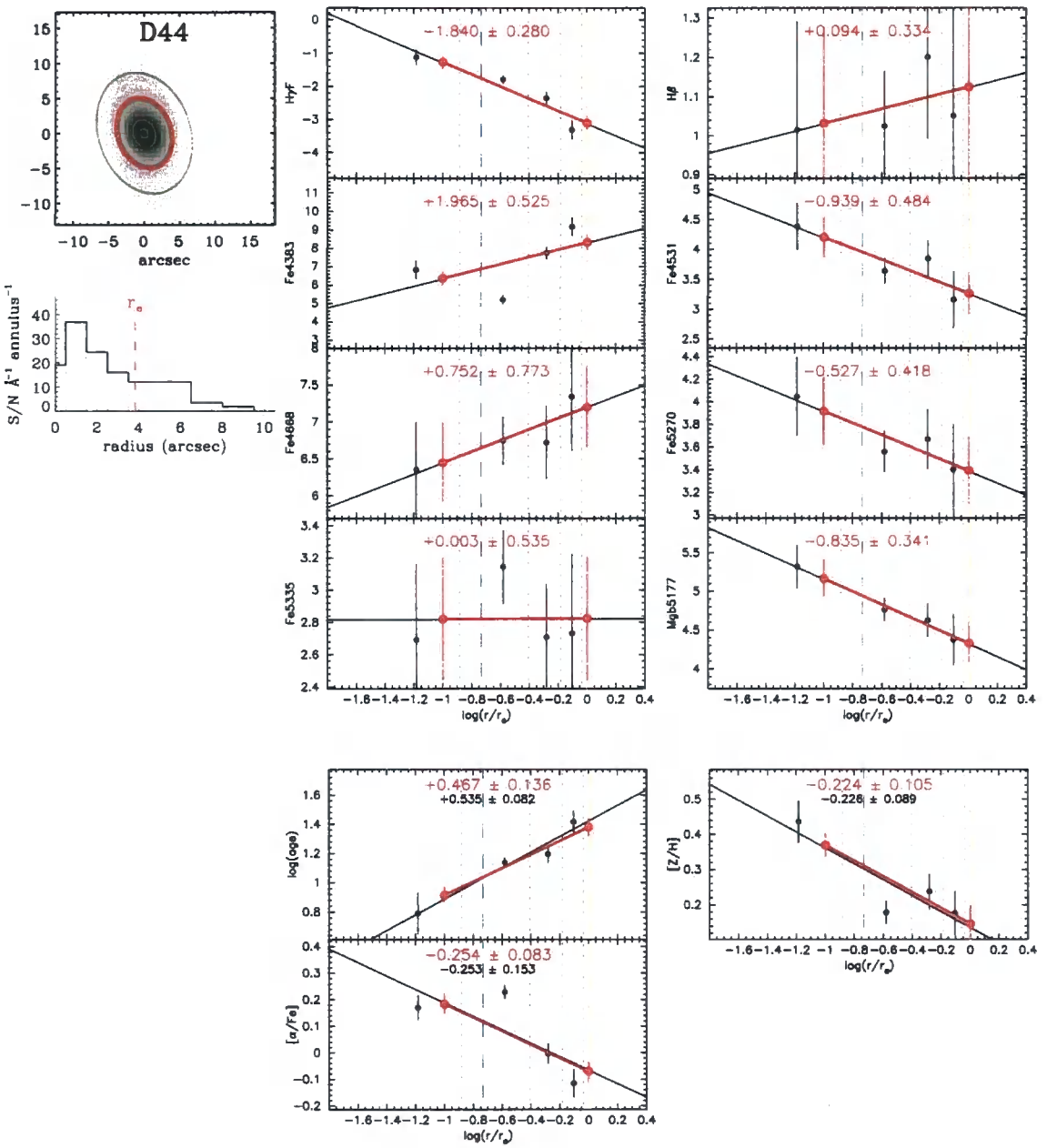

Figure B.5: D44. Adopted bins and gradients. Layout described above.

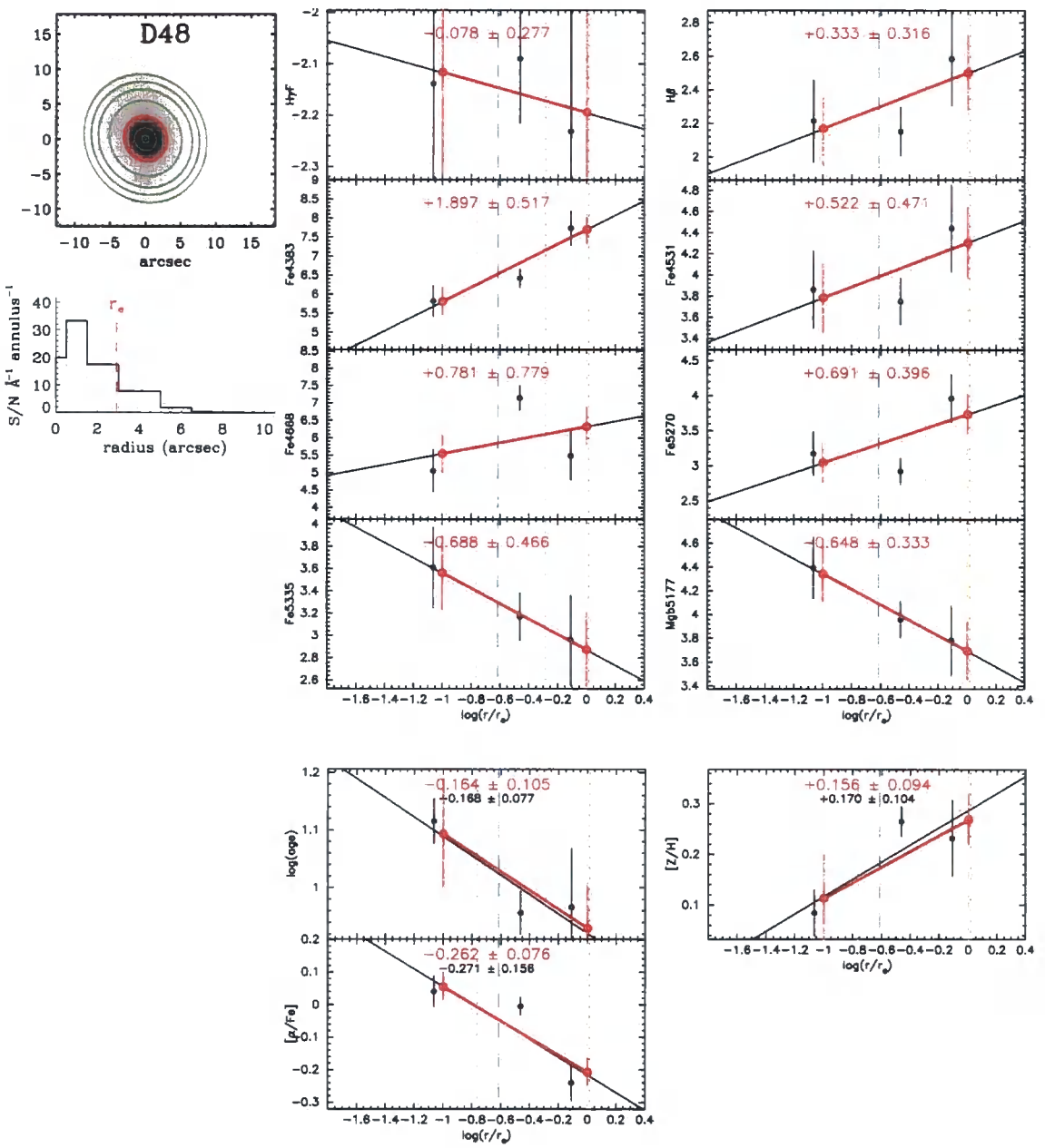

Figure B.6: D48. Adopted bins and gradients. Layout described above.

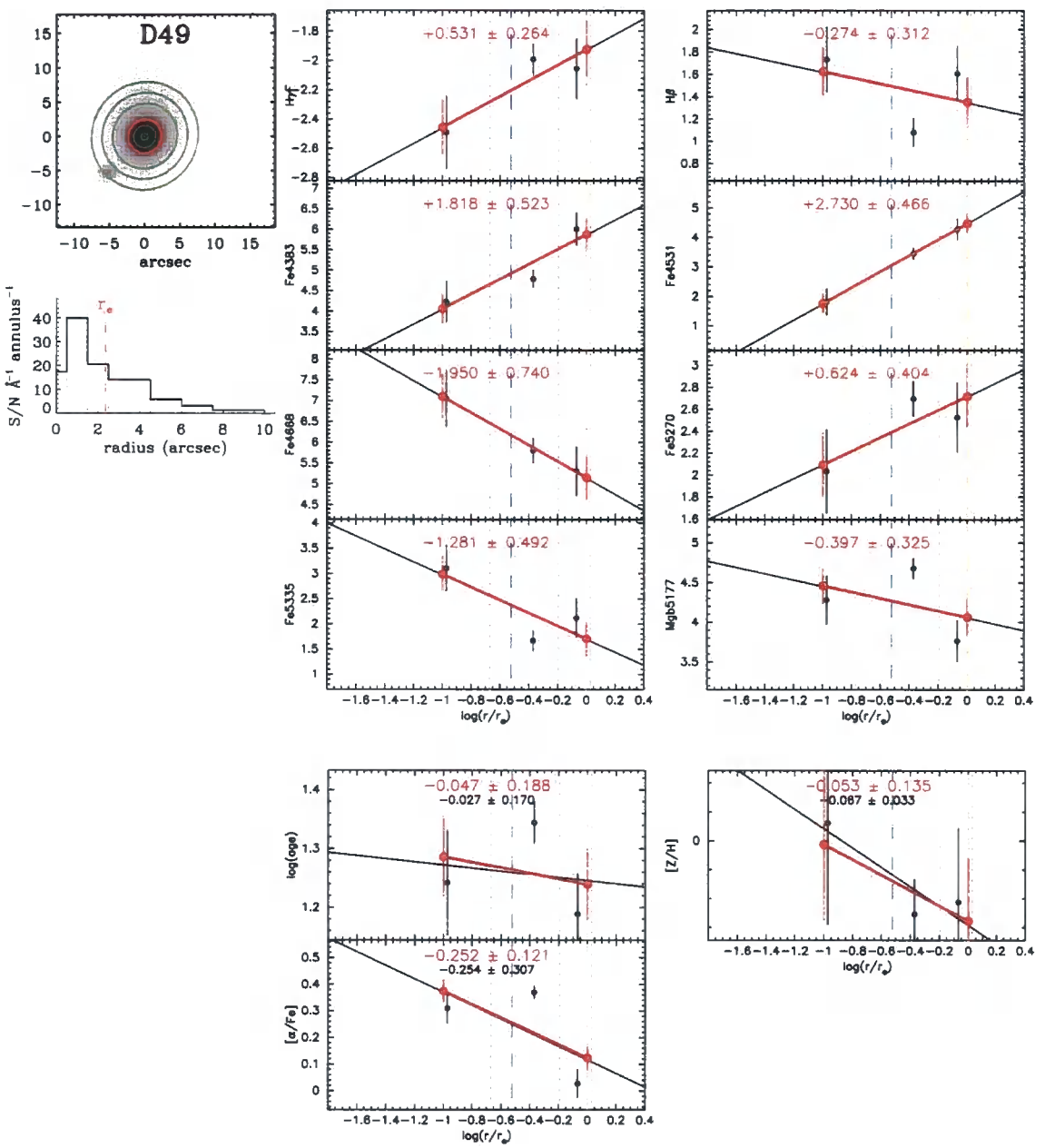

Figure B.7: D49. Adopted bins and gradients. Layout described above.

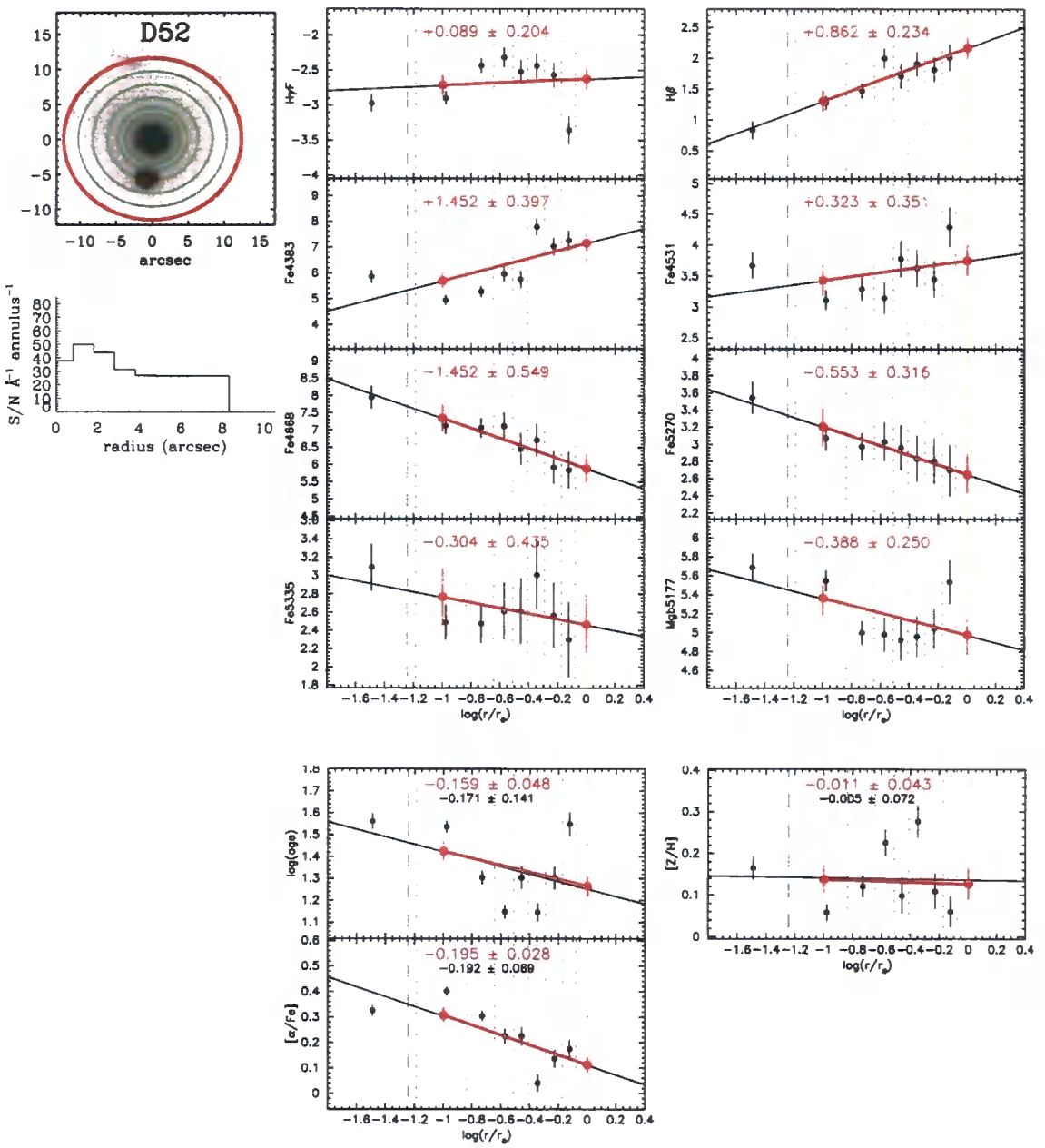

Figure B.8: D52. Adopted bins and gradients. Layout described above.

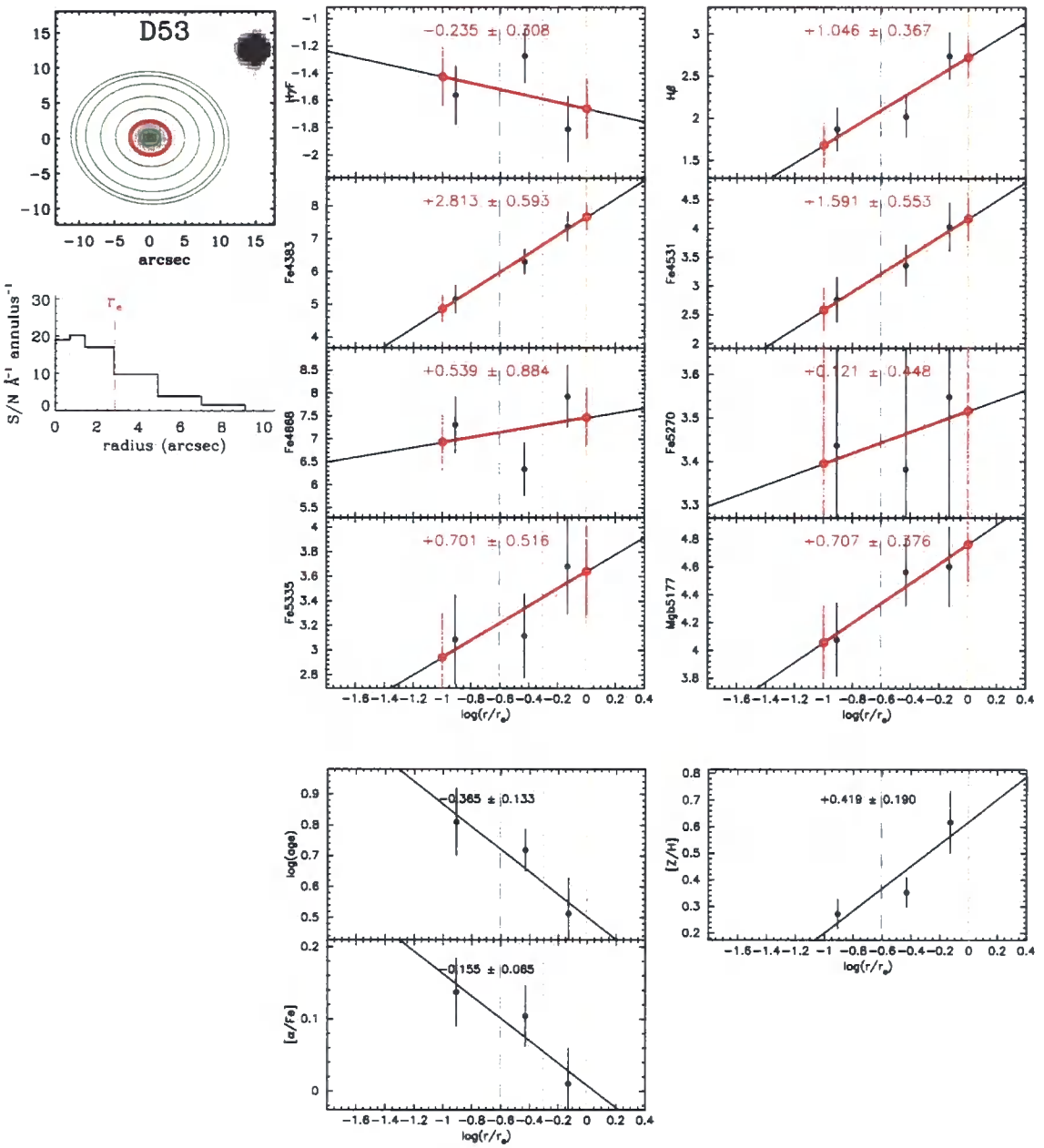

Figure B.9: D53. Adopted bins and gradients. Layout described above.

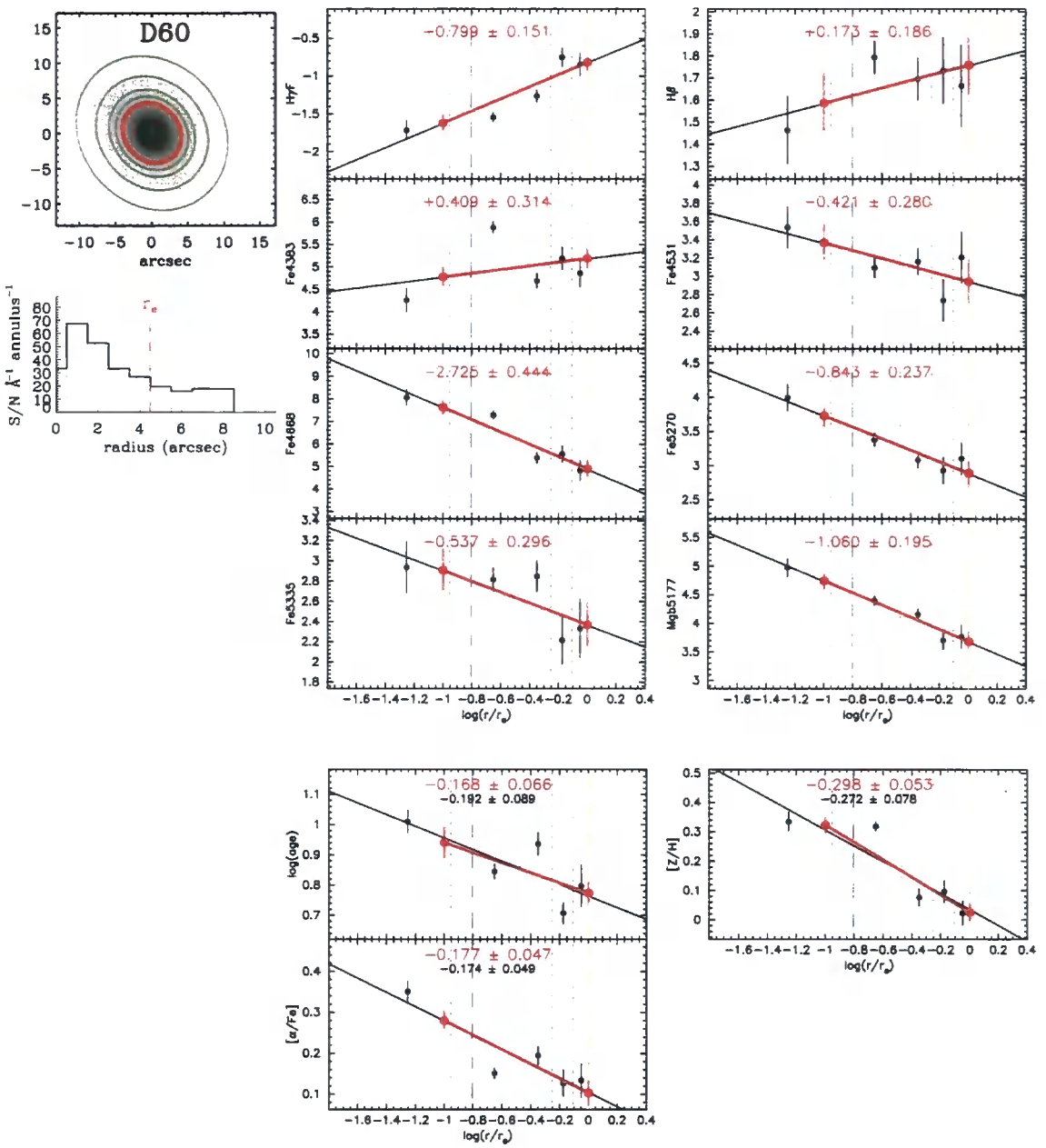

Figure B.10: D60. Adopted bins and gradients. Layout described above.

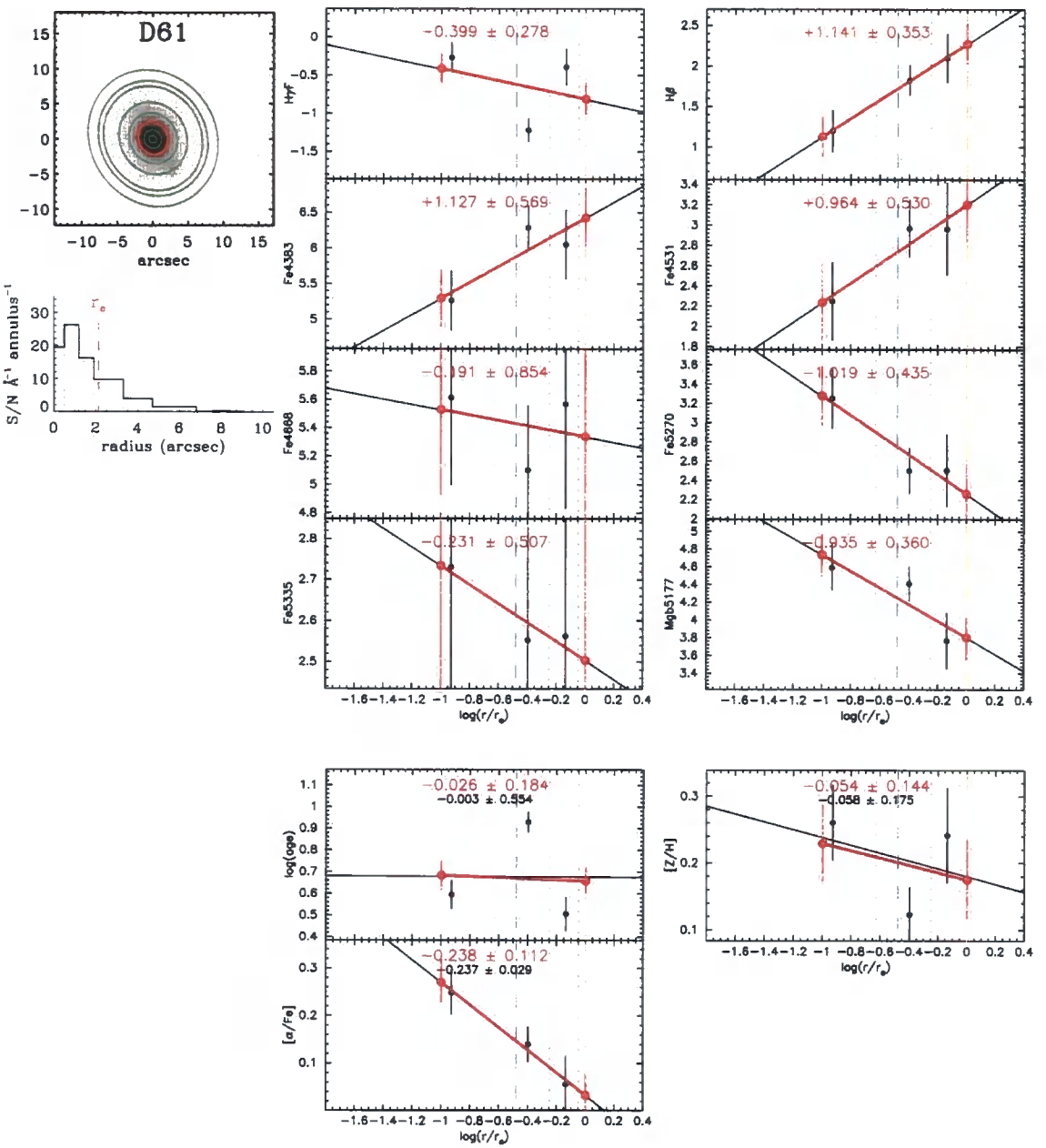

Figure B.11: D61. Adopted bins and gradients. Layout described above.

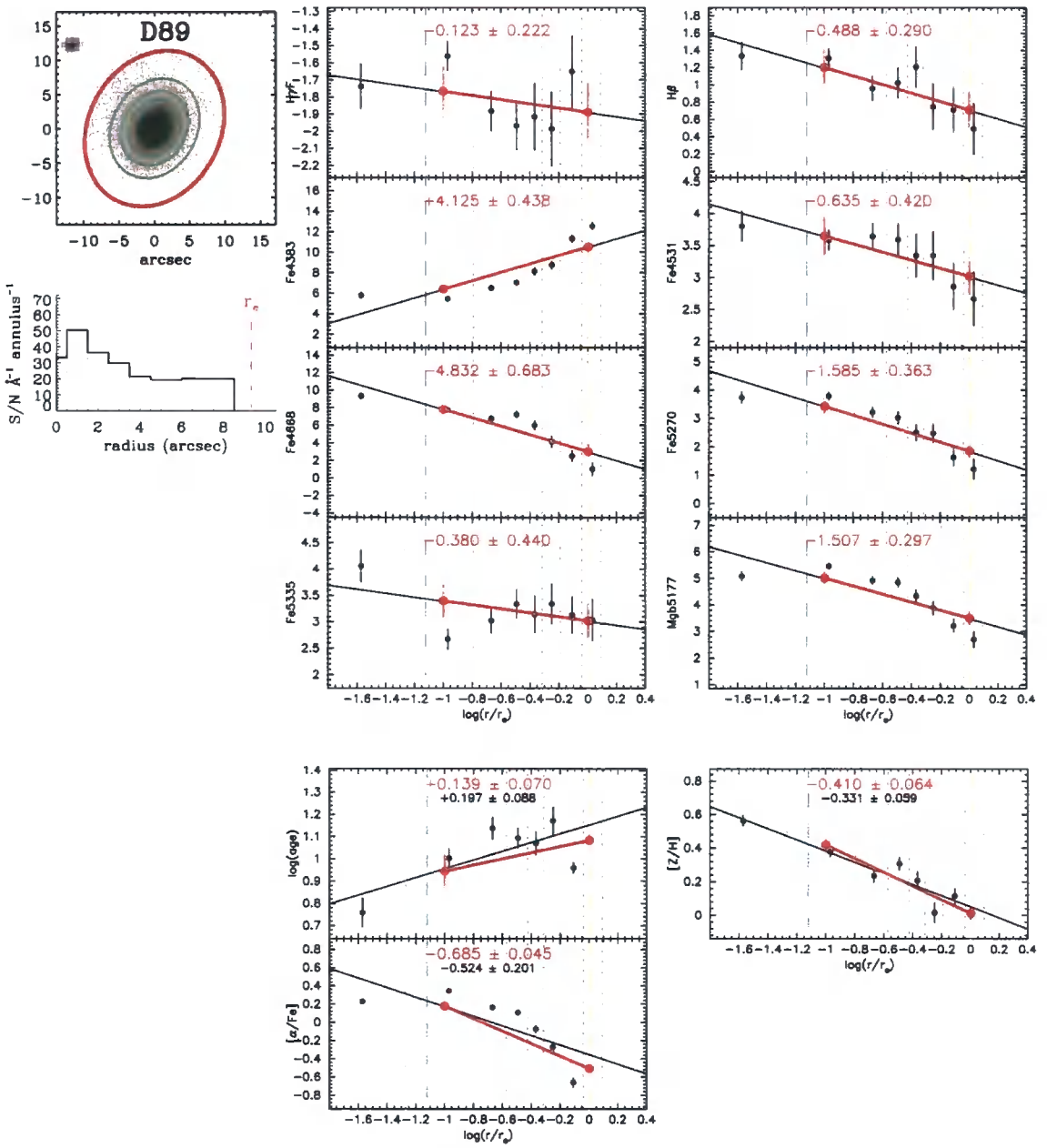

Figure B.12: D89. Adopted bins and gradients. Layout described above.

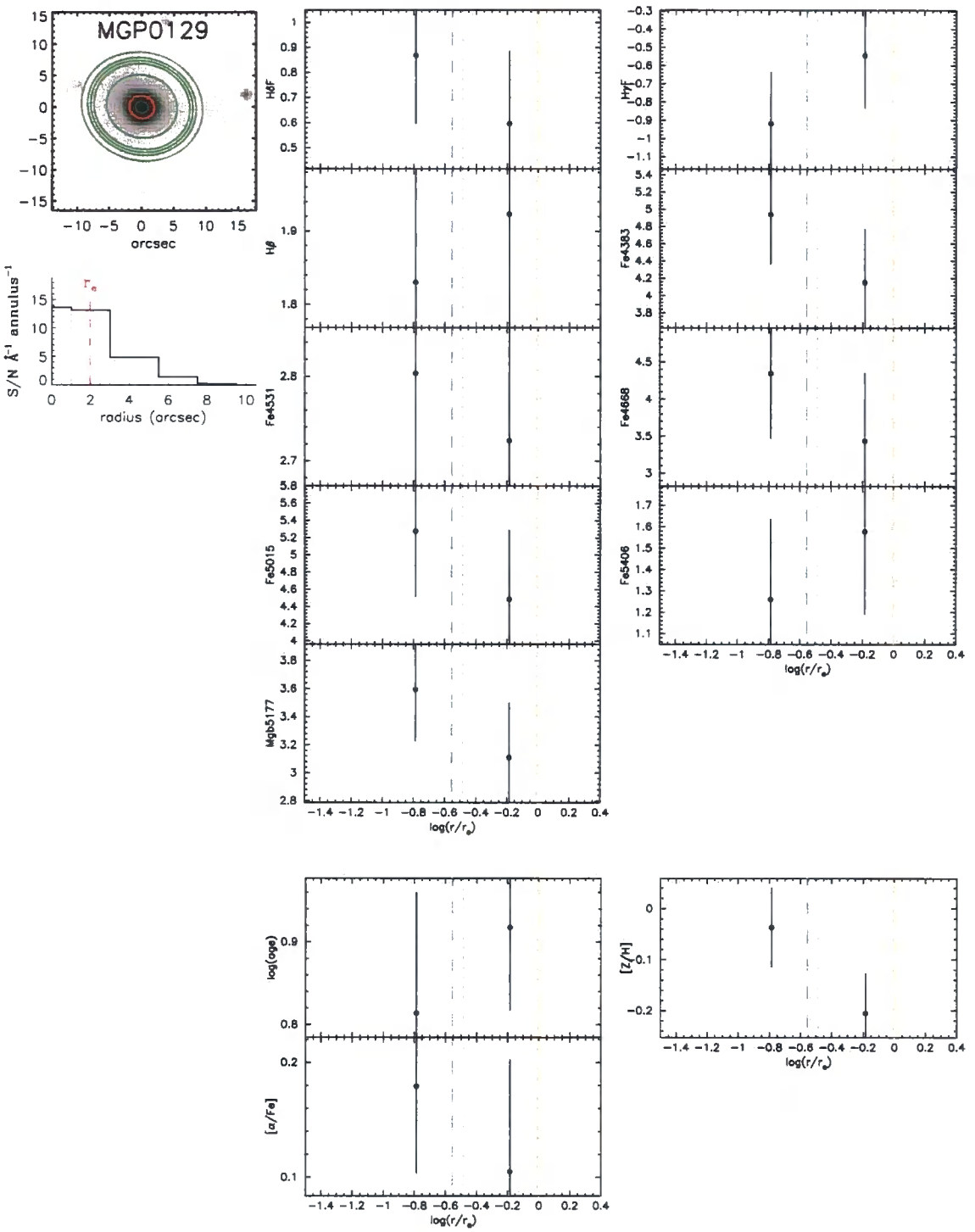

Figure B.13: MGP0129. Adopted bins and gradients. Layout described above.

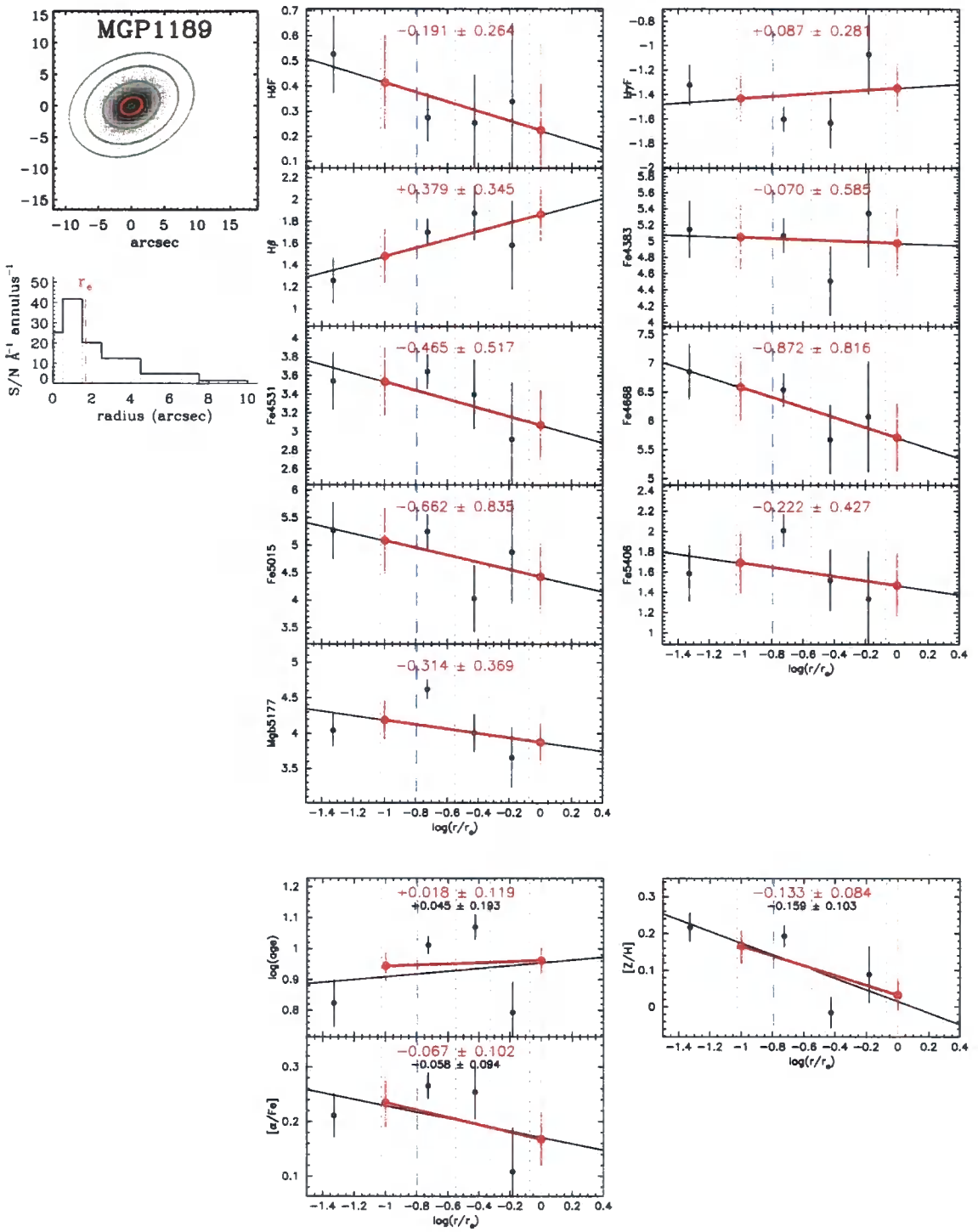

Figure B.14: MGP1189. Adopted bins and gradients. Layout described above.

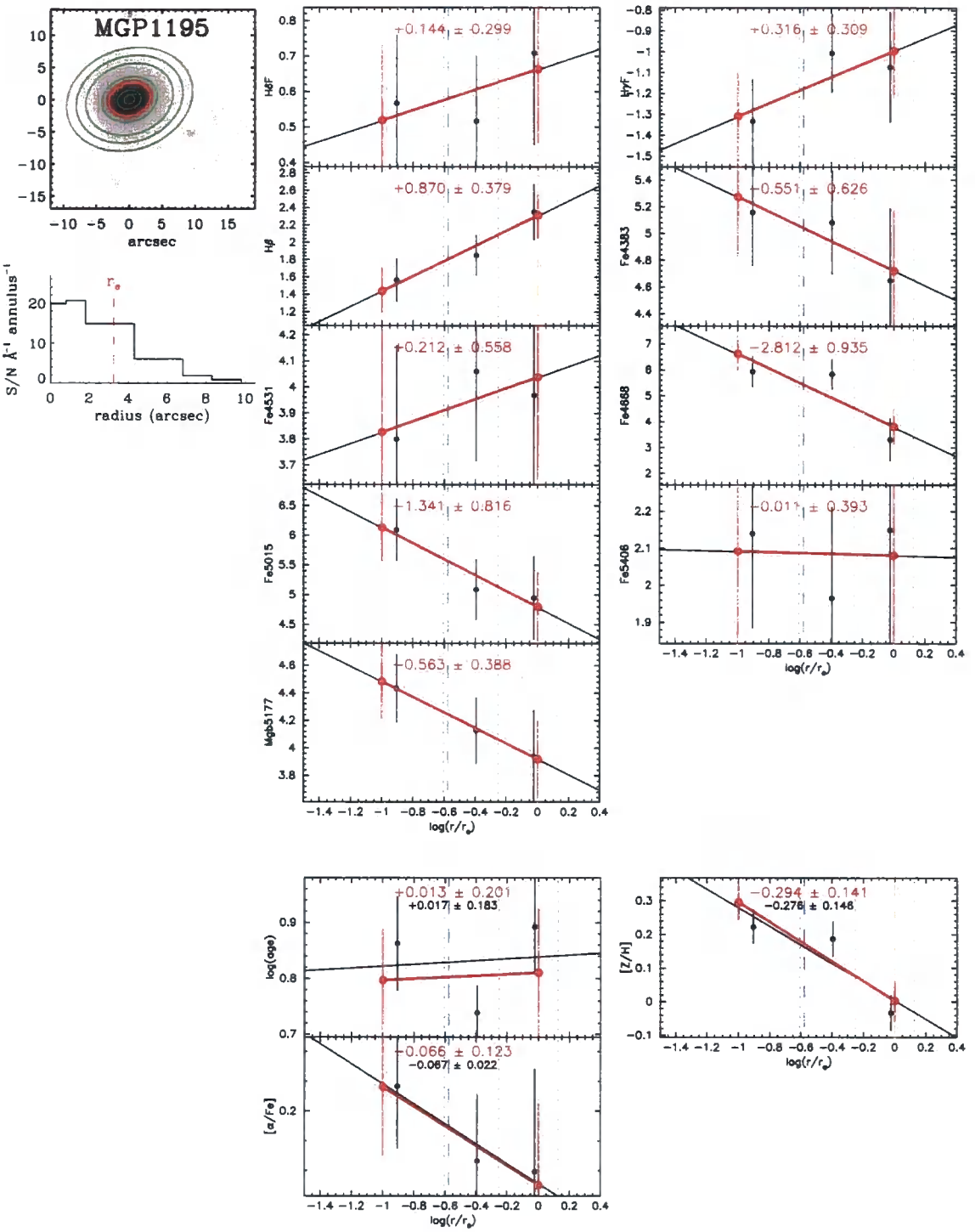

Figure B.15: MGP1195. Adopted bins and gradients. Layout described above.

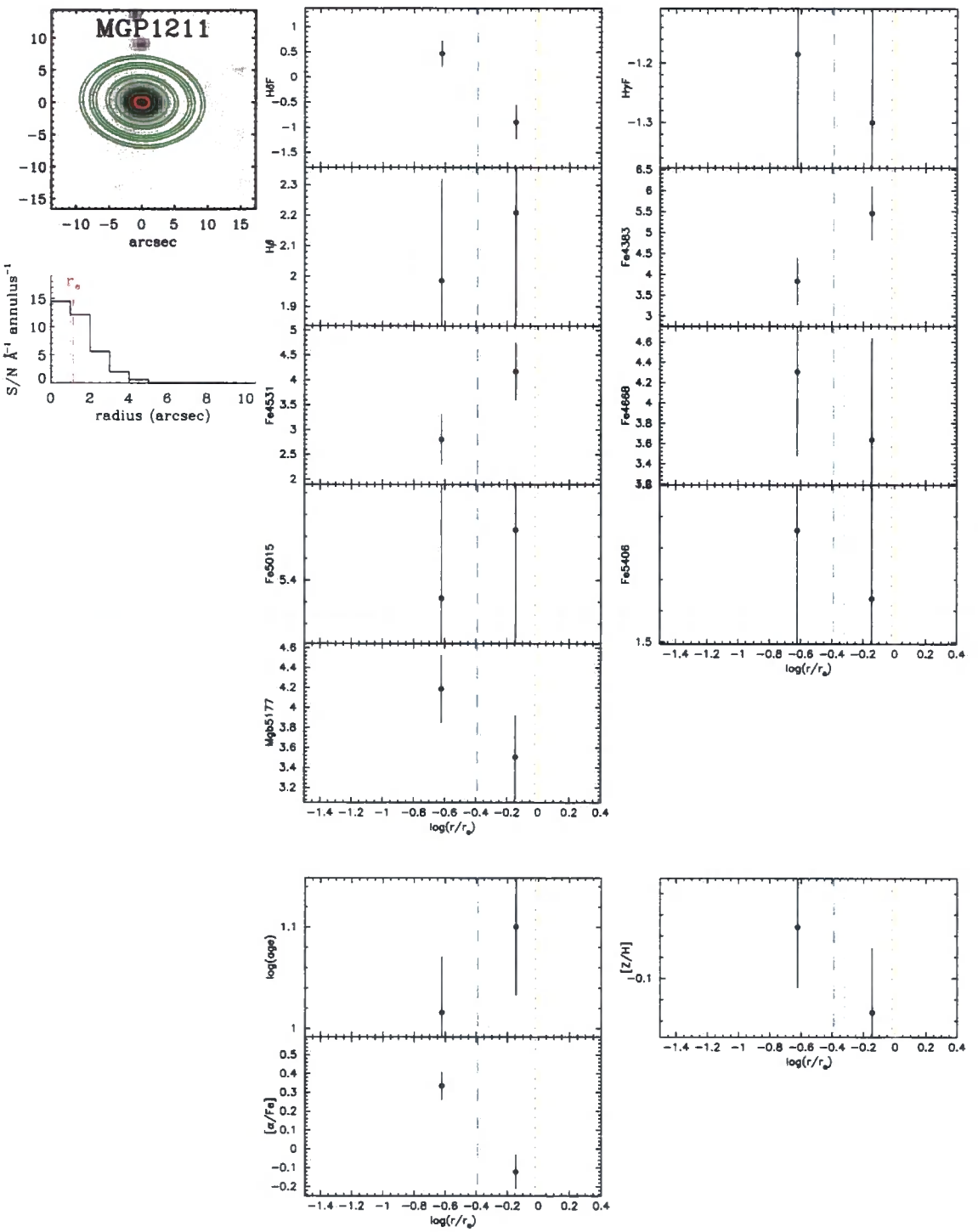

Figure B.16: MGP1211. Adopted bins and gradients. Layout described above.

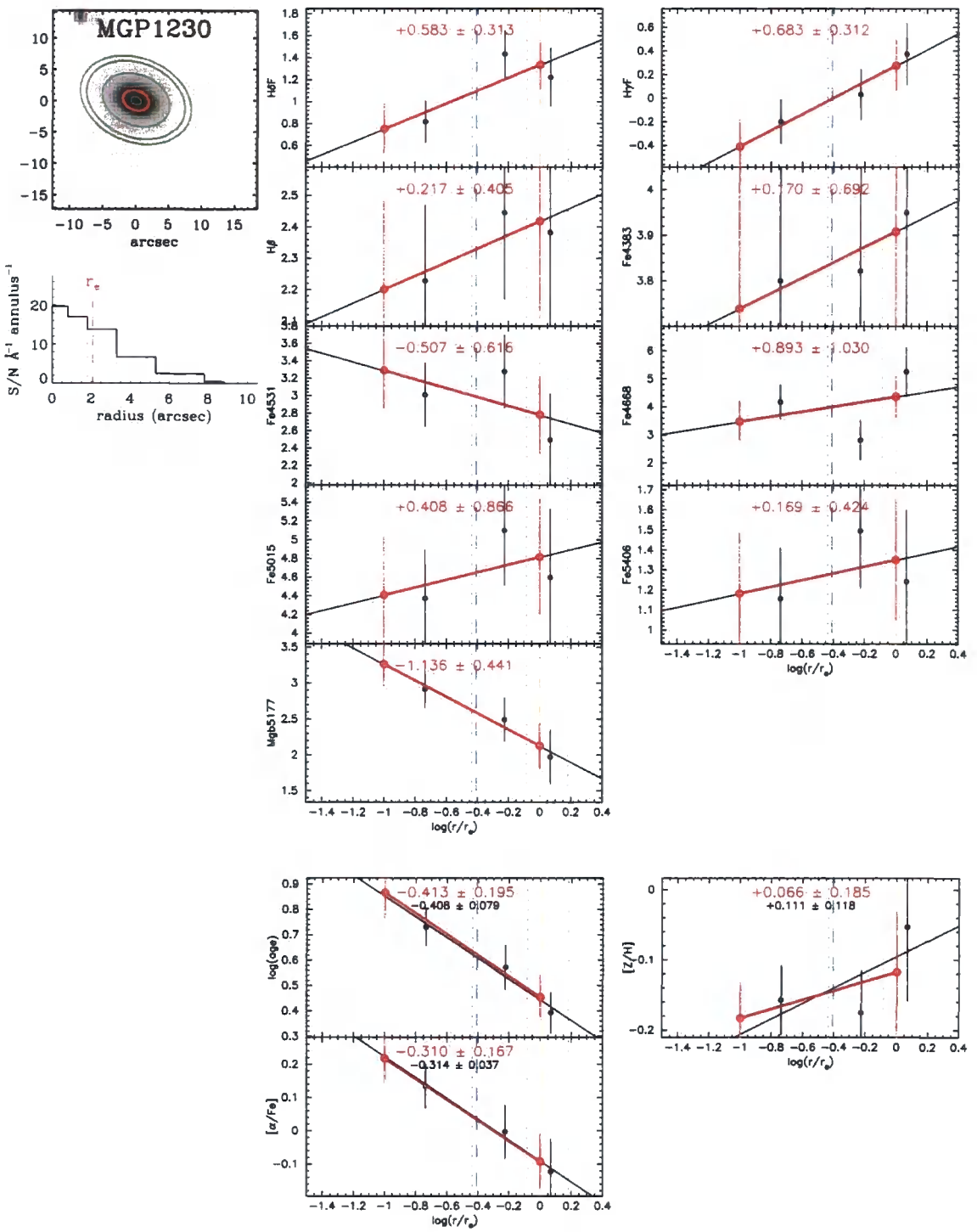

Figure B.17: MGP1230. Adopted bins and gradients. Layout described above.

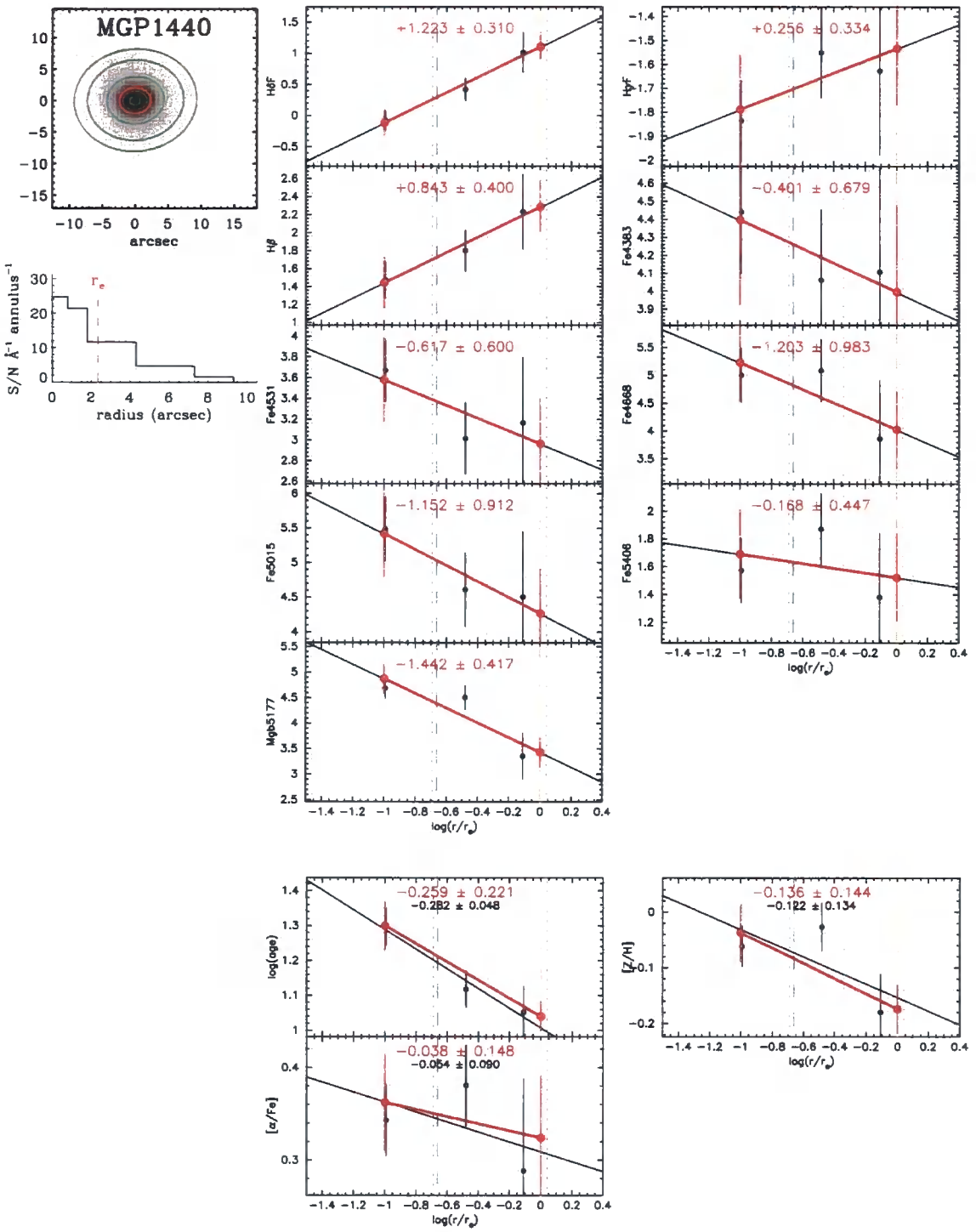

Figure B.18: MGP1440. Adopted bins and gradients. Layout described above.

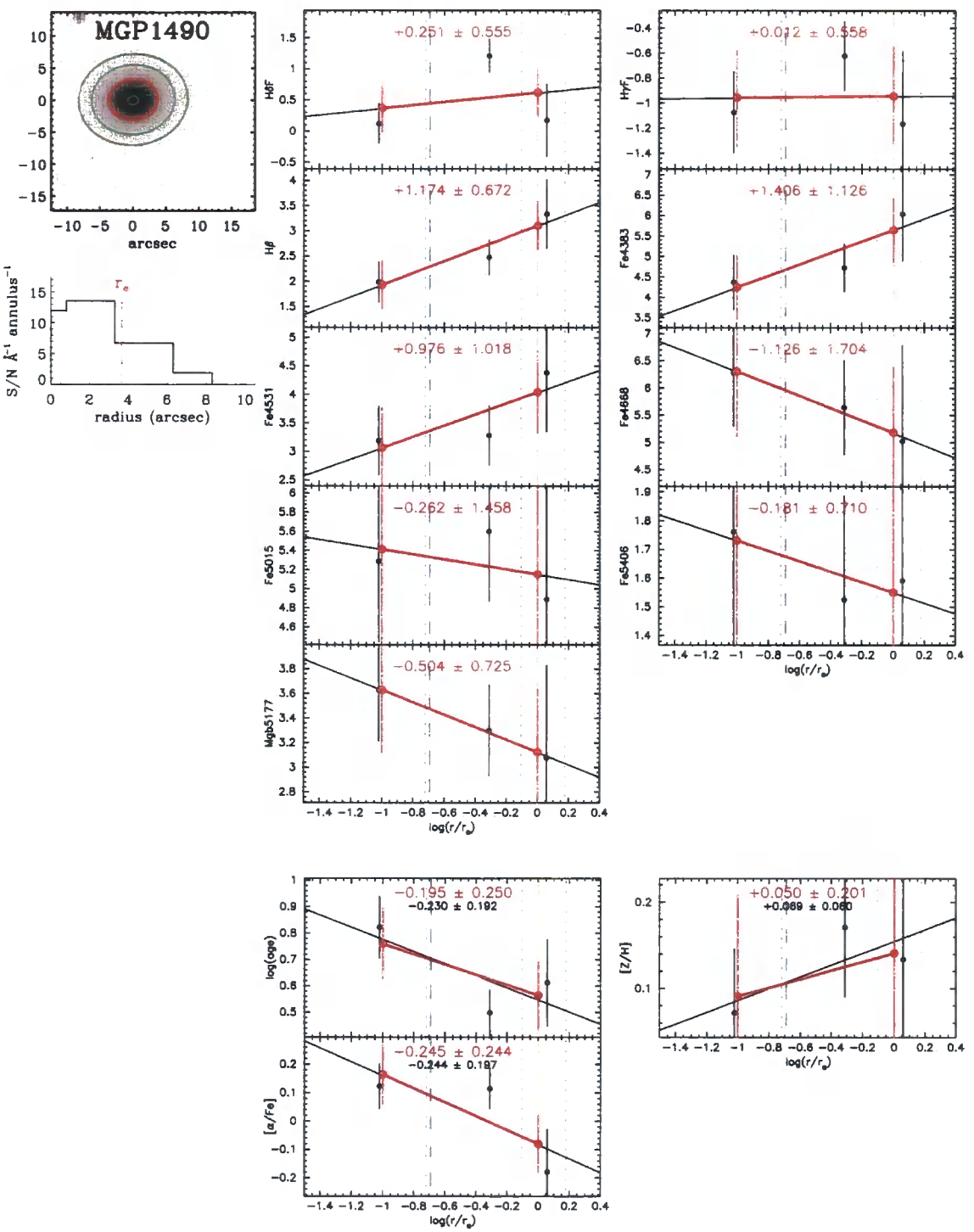

Figure B.19: MGP1490. Adopted bins and gradients. Layout described above.

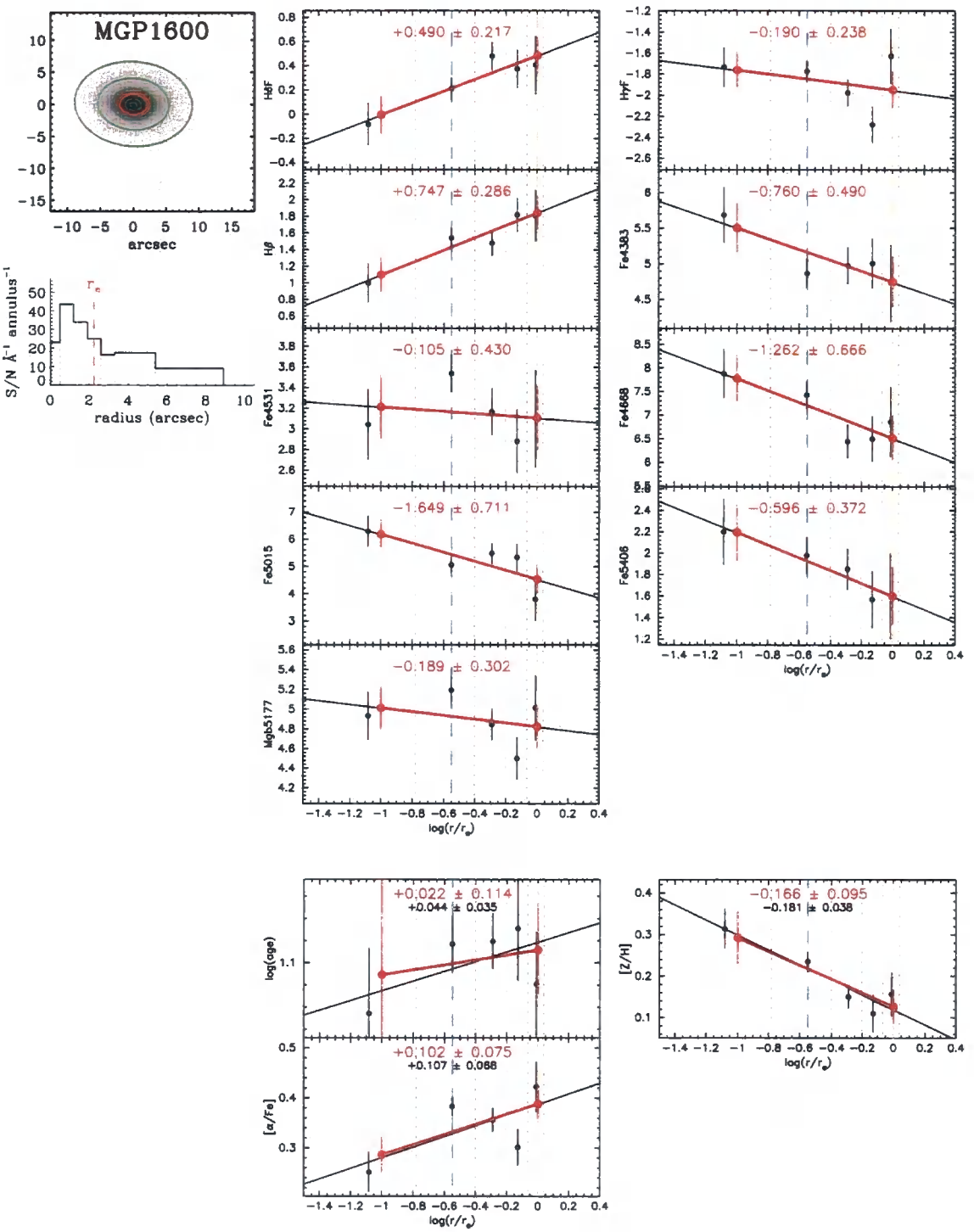

Figure B.20: MGP1600. Adopted bins and gradients. Layout described above.

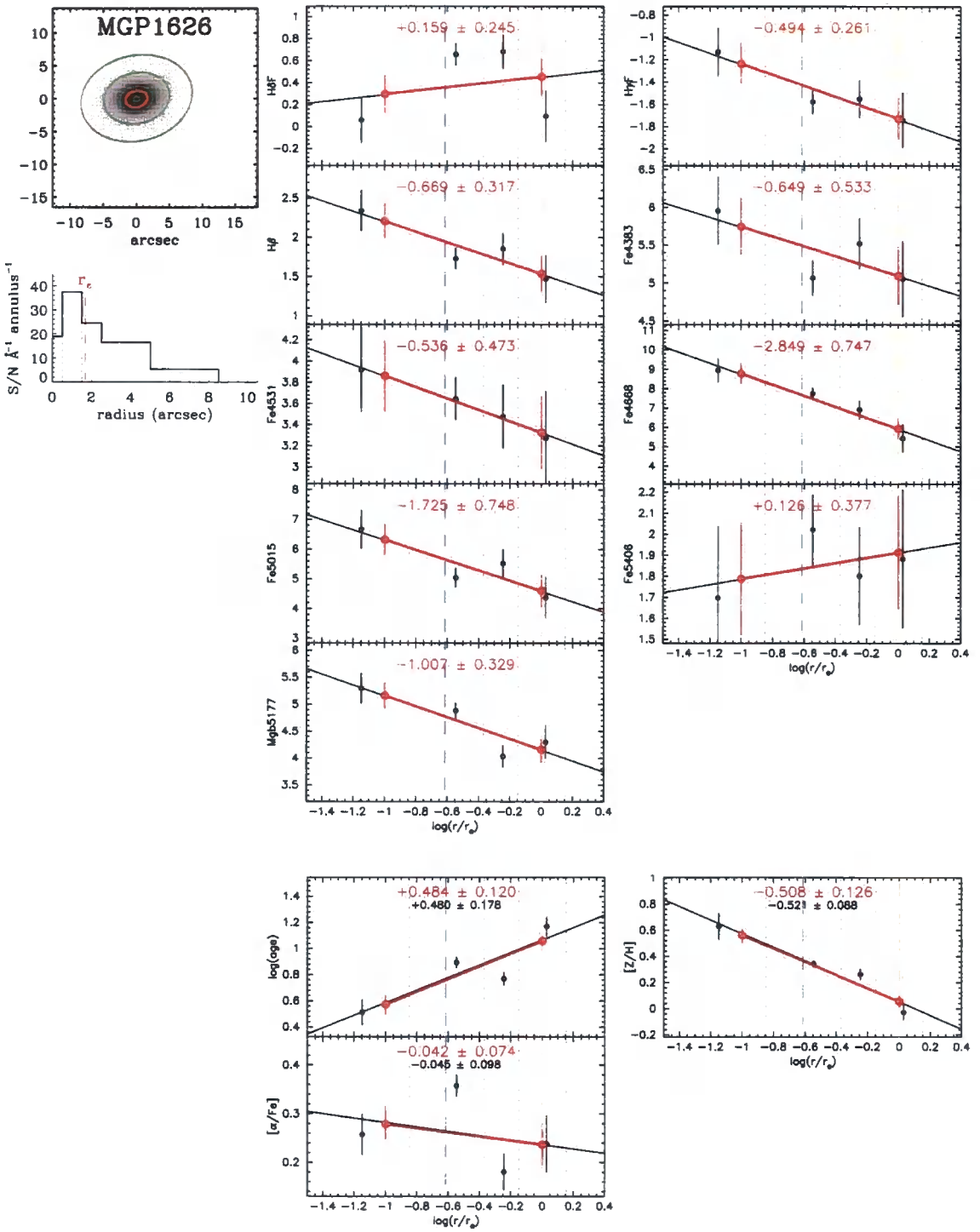

Figure B.21: MGP1626. Adopted bins and gradients. Layout described above.

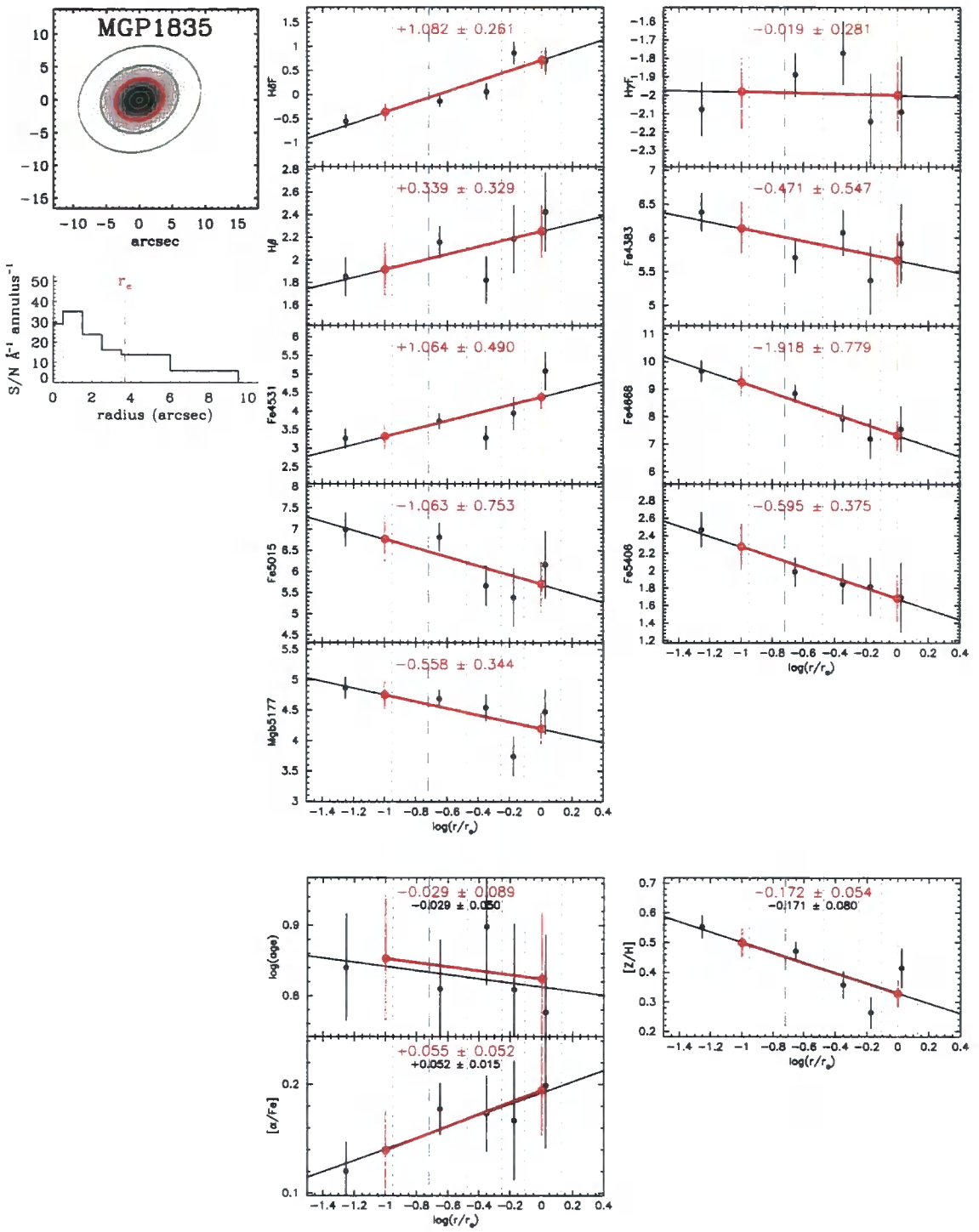

Figure B.22: MGP1835. Adopted bins and gradients. Layout described above.

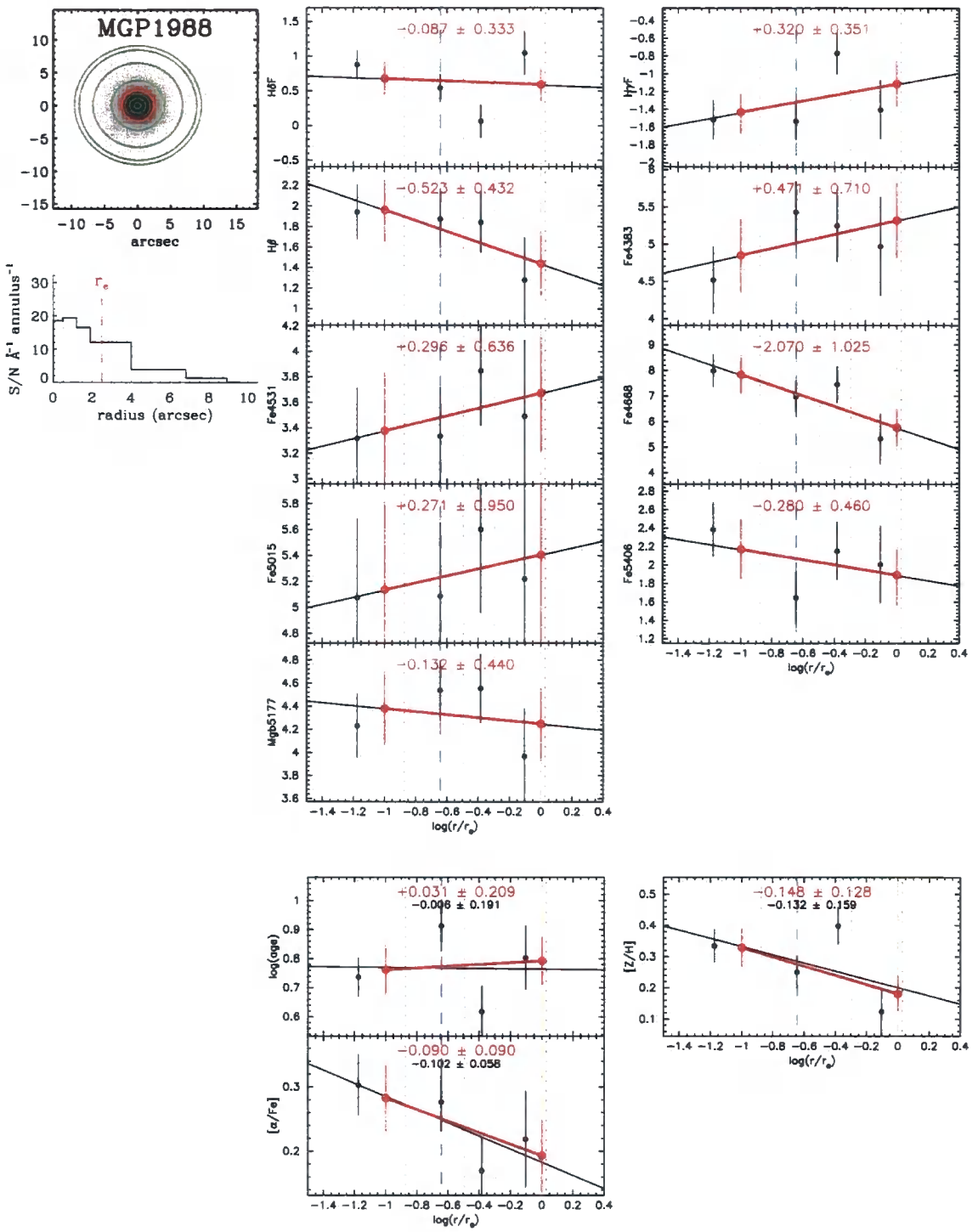

Figure B.23: MGP1988. Adopted bins and gradients. Layout described above.

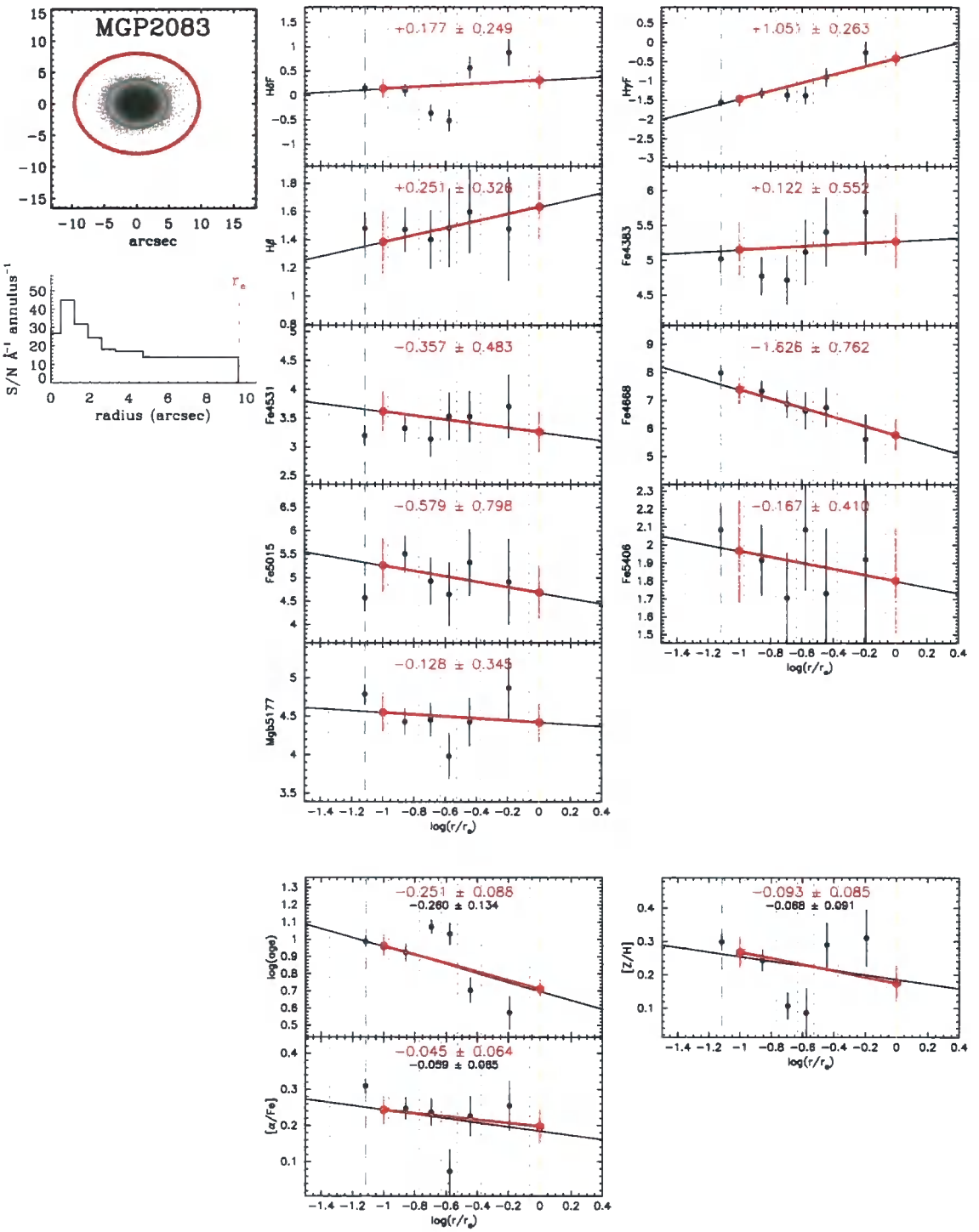

Figure B.24: MGP2083. Adopted bins and gradients. Layout described above.

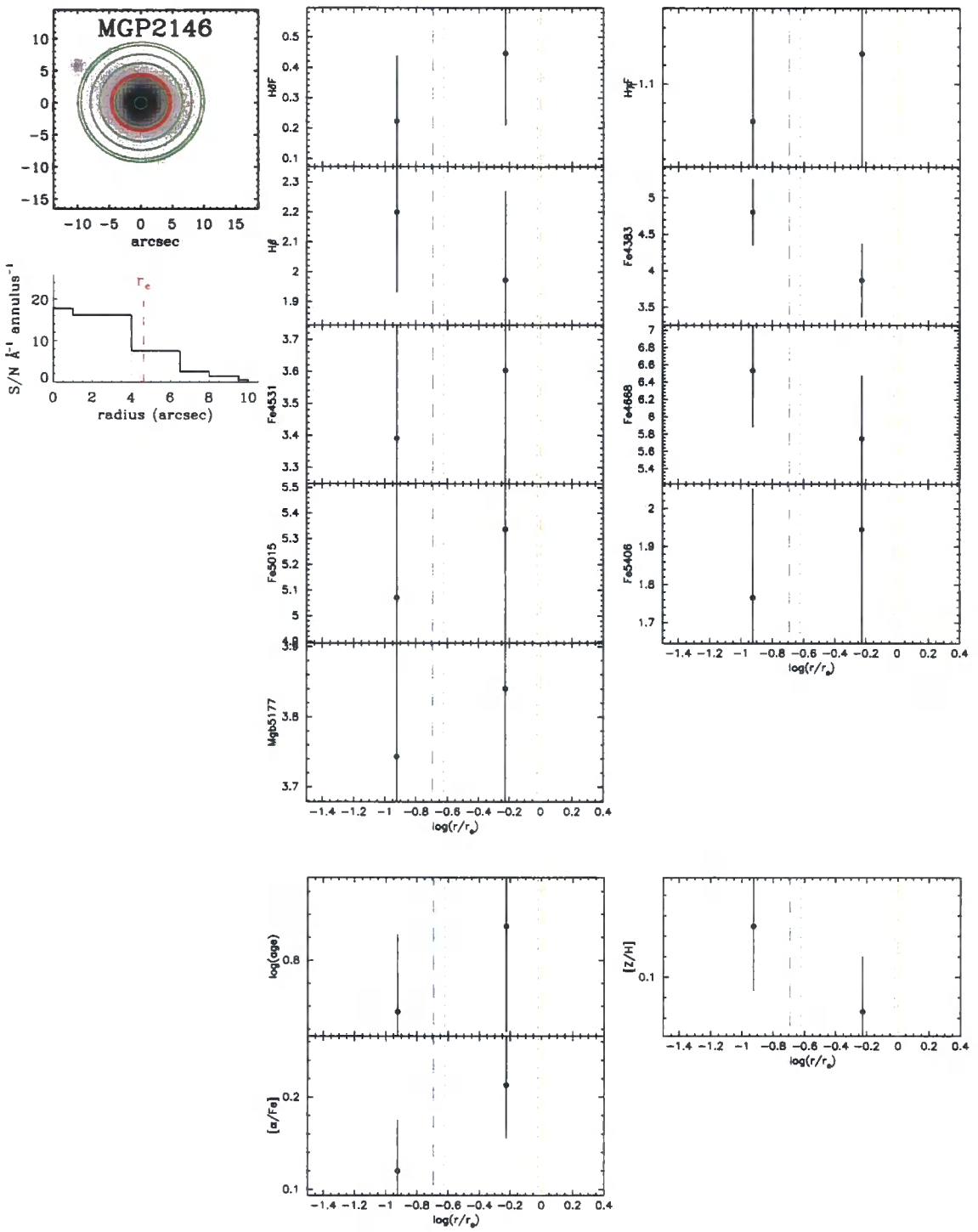

Figure B.25: MGP2146. Adopted bins and gradients. Layout described above.

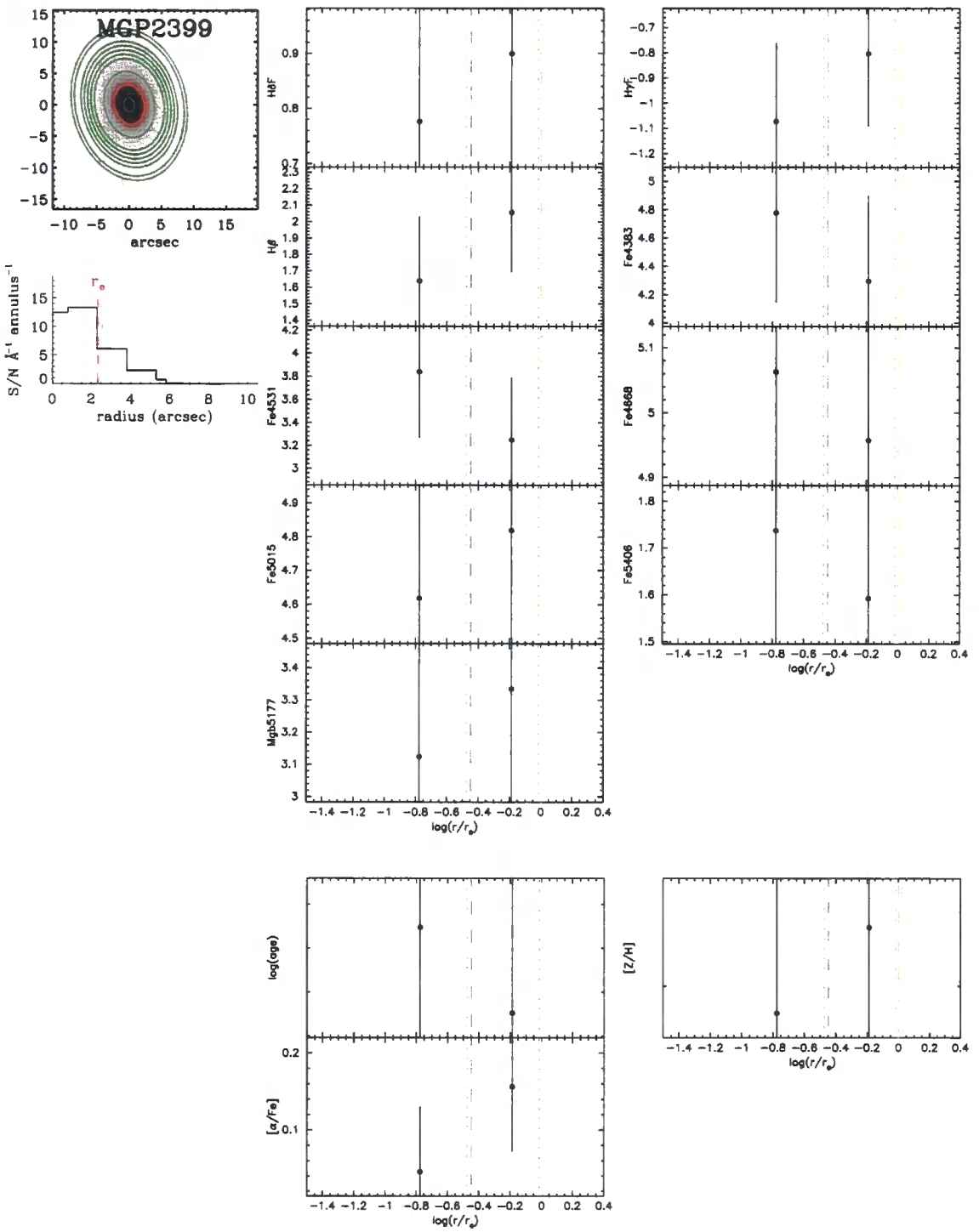

Figure B.26: MGP2399. Adopted bins and gradients. Layout described above.

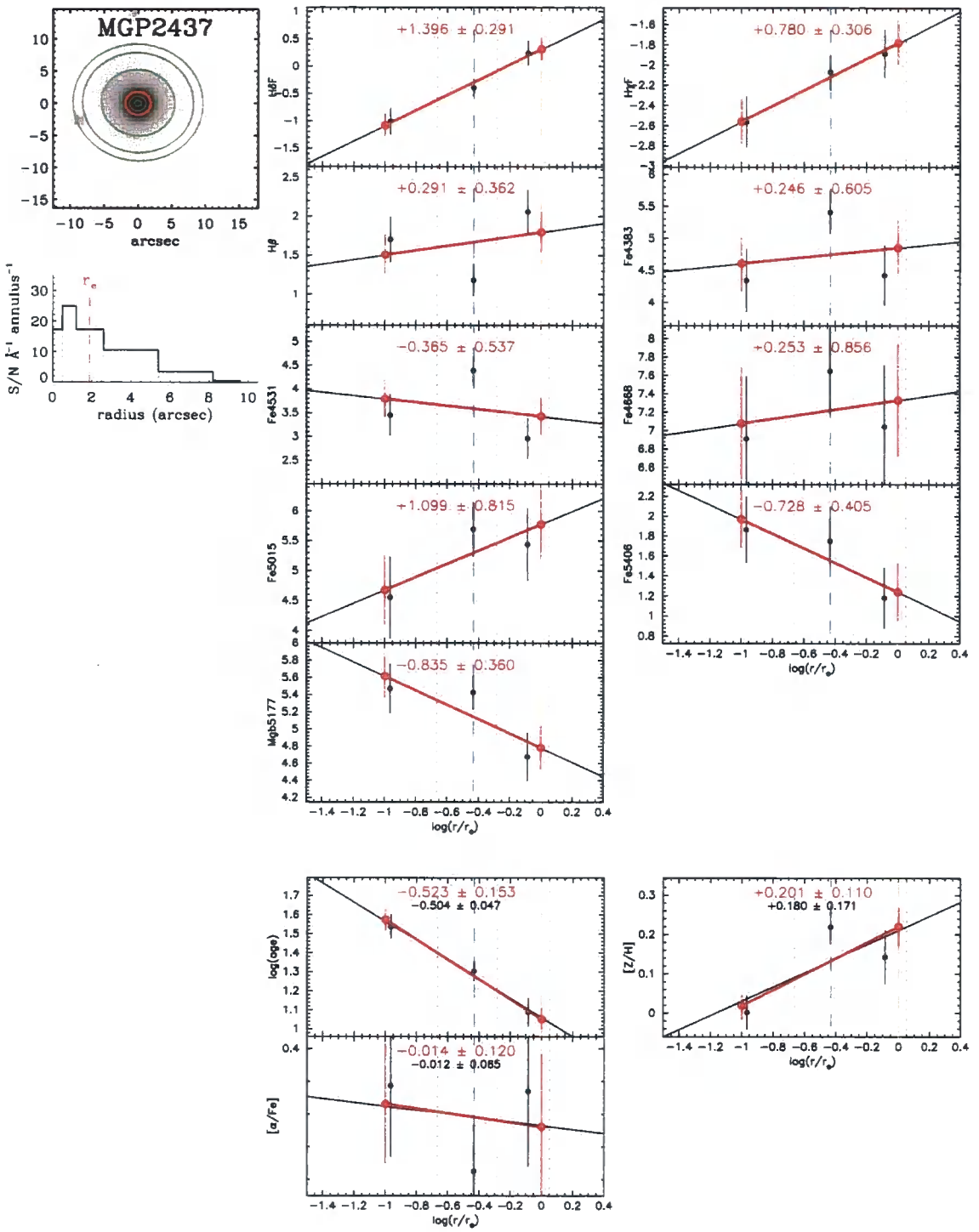

Figure B.27: MGP2437. Adopted bins and gradients. Layout described above.

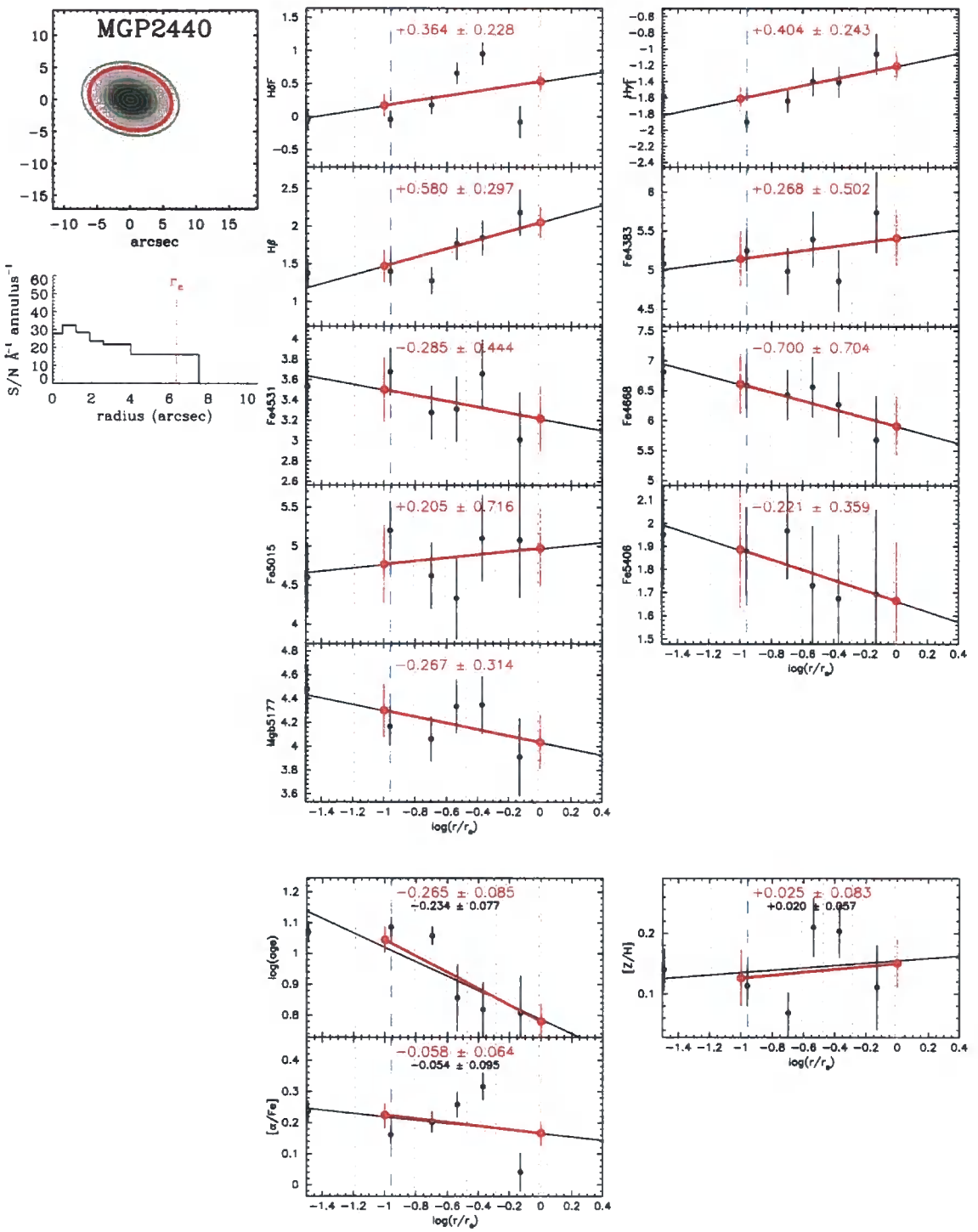

Figure B.28: MGP2440. Adopted bins and gradients. Layout described above.

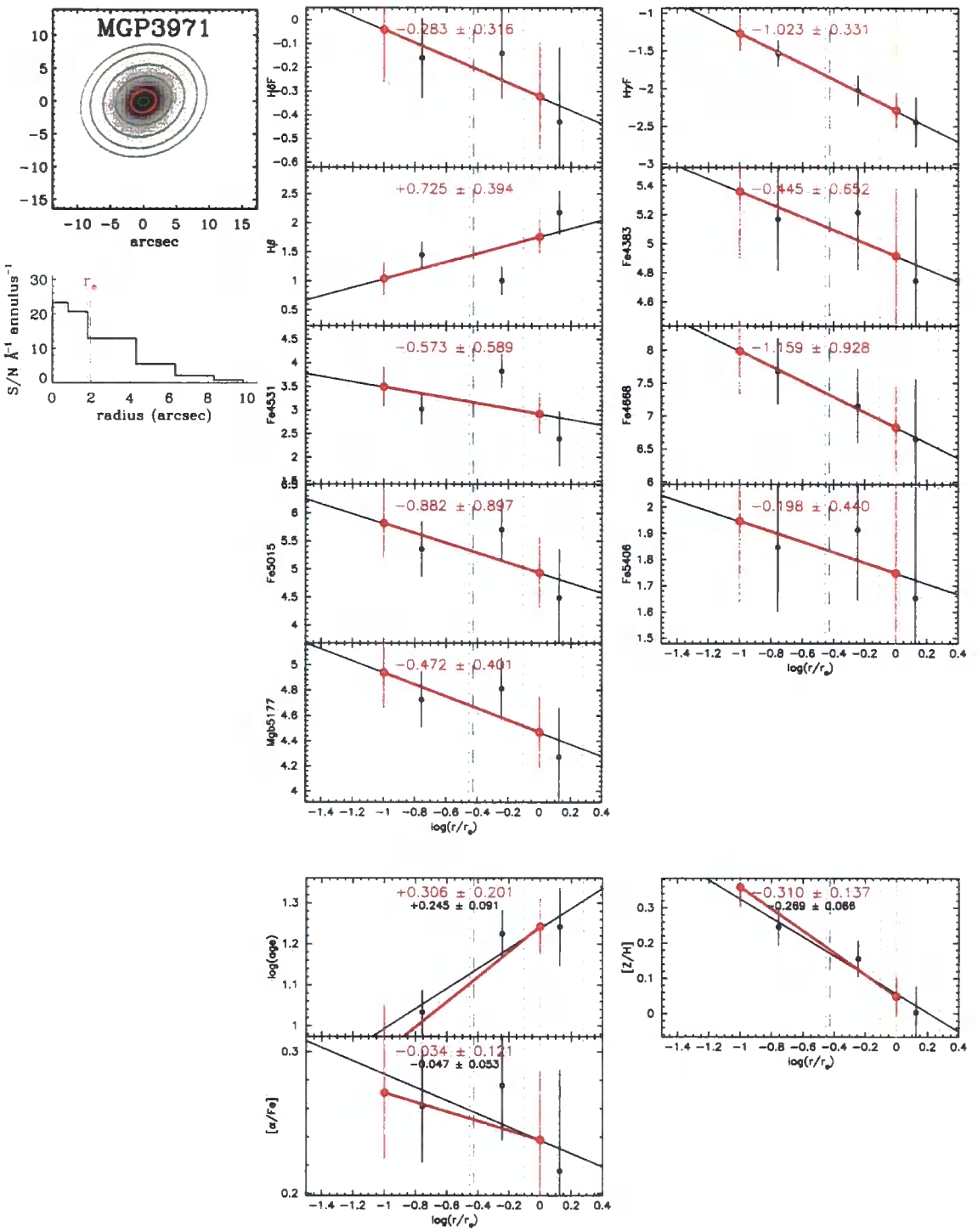

Figure B.29: MGP3971. Adopted bins and gradients. Layout described above.

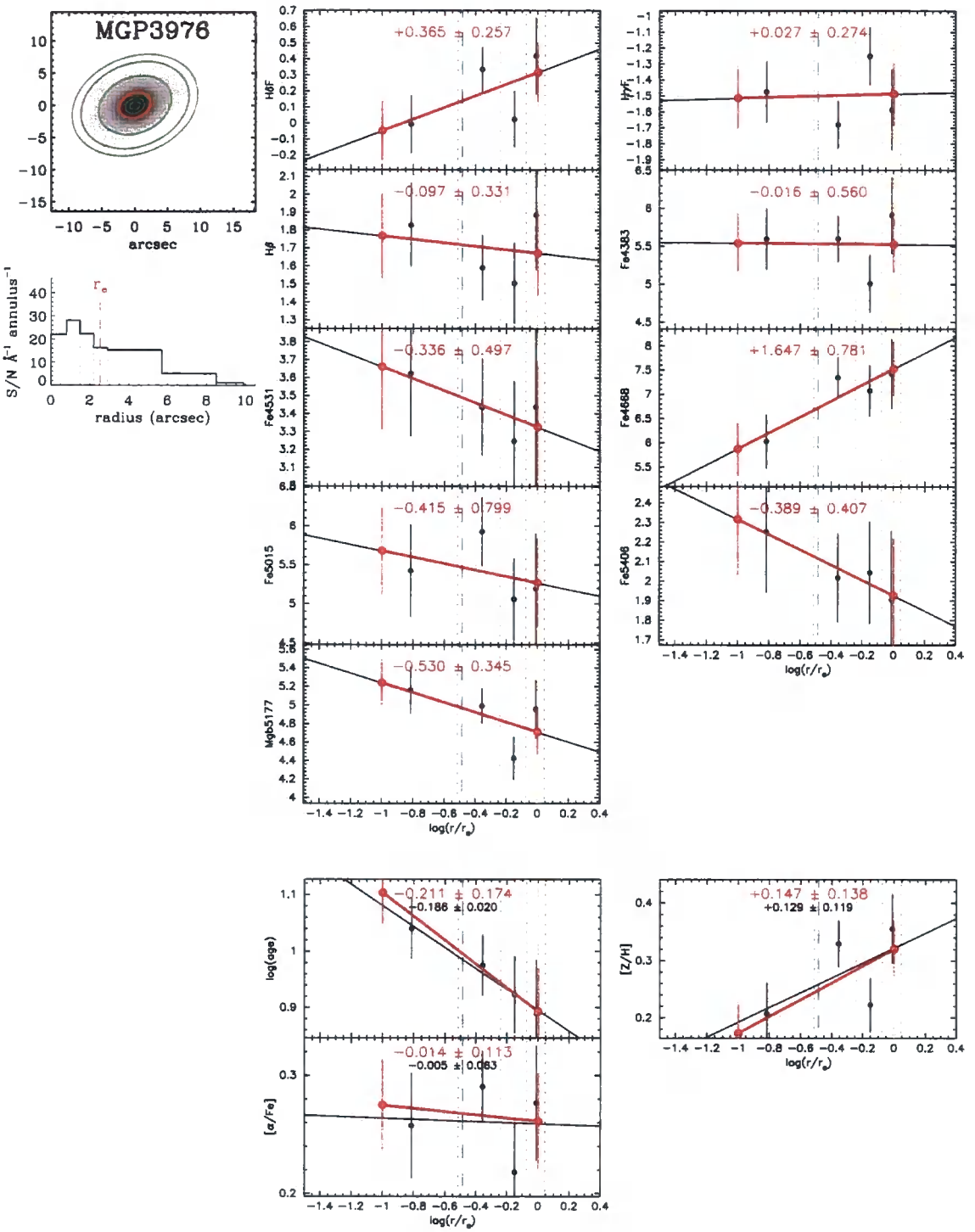

Figure B.30: MGP3976. Adopted bins and gradients. Layout described above.

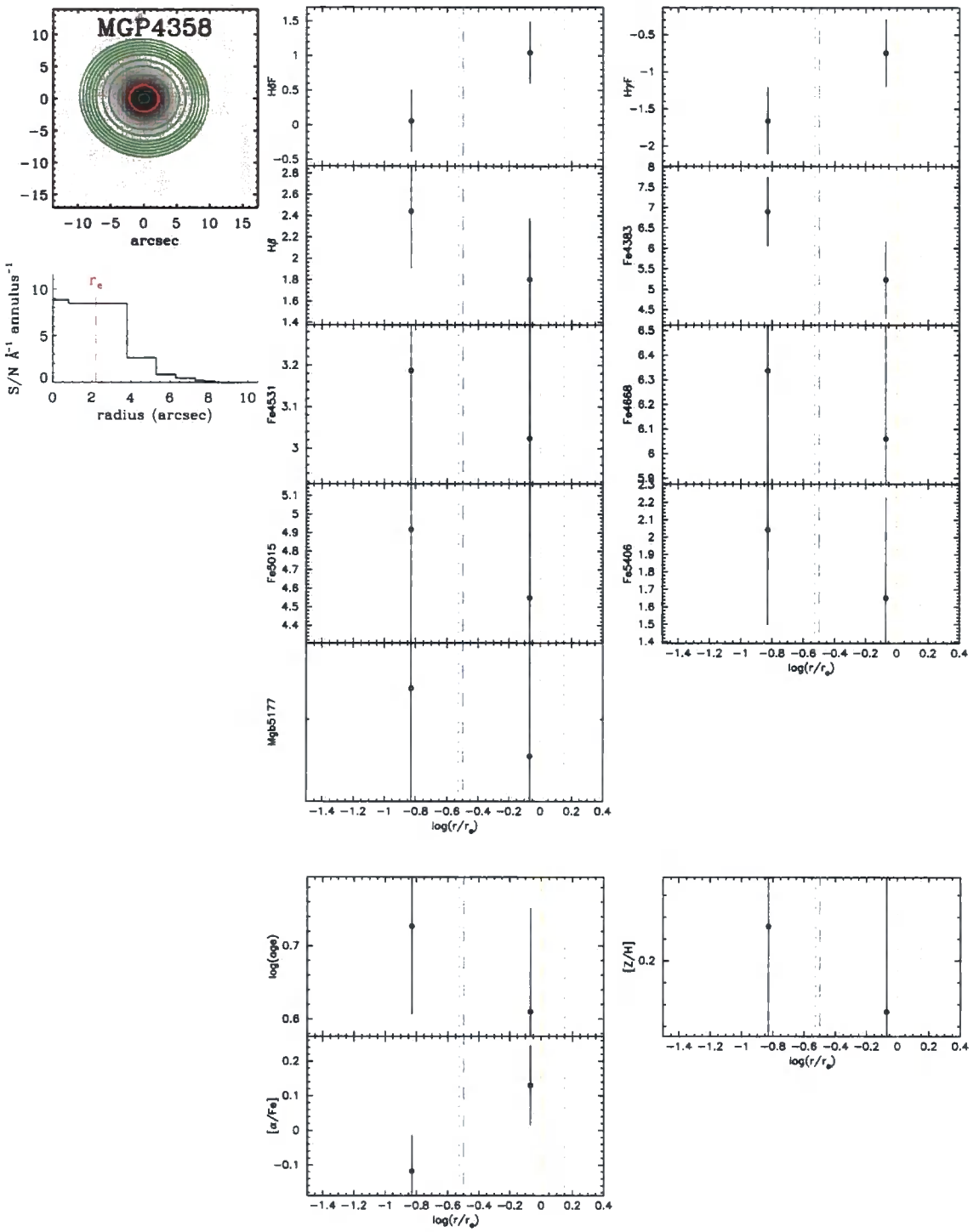

Figure B.31: MGP4358. Adopted bins and gradients. Layout described above.

Table B.1: Absorption line gradients for the Abell 3389 galaxies.

ID	HγF	Hβ	Fe4383	Fe4531
	Fe4668	Fe5270	Fe5335	Mgb5177
D40	+1.436 ± 0.341	+0.018 ± 0.415	−1.370 ± 0.745	+0.033 ± 0.639
	−4.336 ± 1.010	−0.614 ± 0.546	−0.746 ± 0.667	+0.023 ± 0.434
D41	−1.727 ± 0.198	+0.480 ± 0.222	−1.038 ± 0.377	−1.022 ± 0.335
	−1.120 ± 0.525	+0.373 ± 0.290	−0.704 ± 0.369	+0.370 ± 0.233
D42	+0.659 ± 0.206	−0.428 ± 0.270	+0.805 ± 0.454	+0.422 ± 0.398
	−1.357 ± 0.623	−0.208 ± 0.358	−0.167 ± 0.473	+0.049 ± 0.281
D43	−0.422 ± 0.264	−0.899 ± 0.308	−1.048 ± 0.501	+0.448 ± 0.459
	−0.334 ± 0.733	−0.394 ± 0.375	+0.323 ± 0.443	−0.382 ± 0.315
D44	−1.840 ± 0.280	+0.094 ± 0.334	+1.965 ± 0.525	−0.939 ± 0.484
	+0.752 ± 0.773	−0.527 ± 0.418	+0.003 ± 0.535	−0.835 ± 0.341
D48	−0.078 ± 0.277	+0.333 ± 0.316	+1.897 ± 0.517	+0.522 ± 0.471
	+0.781 ± 0.779	+0.691 ± 0.396	−0.688 ± 0.466	−0.648 ± 0.333
D49	+0.531 ± 0.264	−0.274 ± 0.312	+1.818 ± 0.523	+2.730 ± 0.466
	−1.950 ± 0.740	+0.624 ± 0.404	−1.281 ± 0.492	−0.397 ± 0.325
D52	+0.089 ± 0.204	+0.862 ± 0.234	+1.452 ± 0.397	+0.323 ± 0.351
	−1.452 ± 0.549	−0.553 ± 0.316	−0.304 ± 0.435	−0.388 ± 0.250
D53	−0.235 ± 0.308	+1.046 ± 0.367	+2.813 ± 0.593	+1.591 ± 0.553
	+0.539 ± 0.884	+0.121 ± 0.448	+0.701 ± 0.516	+0.707 ± 0.376
D60	+0.799 ± 0.151	+0.173 ± 0.186	+0.409 ± 0.314	−0.421 ± 0.280
	−2.725 ± 0.444	−0.843 ± 0.237	−0.537 ± 0.296	−1.060 ± 0.195
D61	−0.399 ± 0.278	+1.141 ± 0.353	+1.127 ± 0.569	+0.964 ± 0.530
	−0.191 ± 0.854	−1.019 ± 0.435	−0.231 ± 0.507	−0.935 ± 0.360
D89	−0.123 ± 0.222	−0.488 ± 0.290	+4.125 ± 0.438	−0.635 ± 0.420
	−4.832 ± 0.683	−1.585 ± 0.363	−0.380 ± 0.440	−1.507 ± 0.297

Table B.2: Absorption line gradients for the Shapley Supercluster galaxies.

ID	HδF	HγF	Hβ
	Fe4383	Fe4531	Fe4668
	Fe5015	Fe5406	Mgb5177
MGP1189	−0.191 ± 0.264	+0.087 ± 0.281	+0.379 ± 0.345
	−0.070 ± 0.585	−0.465 ± 0.517	−0.872 ± 0.816
	−0.662 ± 0.835	−0.222 ± 0.427	−0.314 ± 0.369
MGP1195	+0.144 ± 0.299	+0.316 ± 0.309	+0.870 ± 0.379
	−0.551 ± 0.626	+0.212 ± 0.558	−2.812 ± 0.935
	−1.341 ± 0.816	−0.011 ± 0.393	−0.563 ± 0.388
MGP1230	+0.583 ± 0.313	+0.683 ± 0.312	+0.217 ± 0.405
	+0.170 ± 0.692	−0.507 ± 0.616	+0.893 ± 1.030
	+0.408 ± 0.866	+0.169 ± 0.424	−1.136 ± 0.441
MGP1440	+1.223 ± 0.310	+0.256 ± 0.334	+0.843 ± 0.400
	−0.401 ± 0.679	−0.617 ± 0.600	−1.203 ± 0.983
	−1.152 ± 0.912	−0.168 ± 0.447	−1.442 ± 0.417
MGP1490	+0.251 ± 0.555	+0.012 ± 0.558	+1.174 ± 0.672
	+1.406 ± 1.126	+0.976 ± 1.018	−1.126 ± 1.704
	−0.262 ± 1.458	−0.181 ± 0.710	−0.504 ± 0.725
MGP1600	+0.490 ± 0.217	−0.190 ± 0.238	+0.747 ± 0.286
	−0.760 ± 0.490	−0.105 ± 0.430	−1.262 ± 0.666
	−1.649 ± 0.711	−0.596 ± 0.372	−0.189 ± 0.302
MGP1626	+0.159 ± 0.245	−0.494 ± 0.261	−0.669 ± 0.317
	−0.649 ± 0.533	−0.536 ± 0.473	−2.849 ± 0.747
	−1.725 ± 0.748	+0.126 ± 0.377	−1.007 ± 0.329

Table B.2 continued...

ID	HδF	HγF	Hβ
	Fe4383	Fe4531	Fe4668
	Fe5015	Fe5406	Mgb5177
MGP1835	+1.082 ± 0.261	–0.019 ± 0.281	+0.339 ± 0.329
	–0.471 ± 0.547	+1.064 ± 0.490	–1.918 ± 0.779
	–1.063 ± 0.753	–0.595 ± 0.375	–0.558 ± 0.344
MGP1988	–0.087 ± 0.333	+0.320 ± 0.351	–0.523 ± 0.432
	+0.471 ± 0.710	+0.296 ± 0.636	–2.070 ± 1.025
	+0.271 ± 0.950	–0.280 ± 0.460	–0.132 ± 0.440
MGP2083	+0.177 ± 0.249	+1.051 ± 0.263	+0.251 ± 0.326
	+0.122 ± 0.552	–0.357 ± 0.483	–1.626 ± 0.762
	–0.579 ± 0.798	–0.167 ± 0.410	–0.128 ± 0.345
MGP2437	+1.396 ± 0.291	+0.780 ± 0.306	+0.291 ± 0.362
	+0.246 ± 0.605	–0.365 ± 0.537	+0.253 ± 0.856
	+1.099 ± 0.815	–0.728 ± 0.405	–0.835 ± 0.360
MGP2440	+0.364 ± 0.228	+0.404 ± 0.243	+0.580 ± 0.297
	+0.268 ± 0.502	–0.285 ± 0.444	–0.700 ± 0.704
	+0.205 ± 0.716	–0.221 ± 0.359	–0.267 ± 0.314
MGP3971	–0.283 ± 0.316	–1.023 ± 0.331	+0.725 ± 0.394
	–0.445 ± 0.652	–0.573 ± 0.589	–1.159 ± 0.928
	–0.882 ± 0.897	–0.198 ± 0.440	–0.472 ± 0.401
MGP3976	+0.365 ± 0.257	+0.027 ± 0.274	–0.097 ± 0.331
	–0.016 ± 0.560	–0.336 ± 0.497	+1.647 ± 0.781
	–0.415 ± 0.799	–0.389 ± 0.407	–0.530 ± 0.345

Table B.3: Velocity dispersion and stellar population gradients for 11 galaxies in the A3389 sample (D53 is excluded).

ID	$\nabla \log \sigma$	∇log(age/Gyr)	∇[Z/H]	$\nabla[\alpha/\mathrm{Fe}]$
D40	0.075 ± 0.085	-0.106 ± 0.184	-0.329 ± 0.115	0.258 ± 0.128
D41	0.037 ± 0.035	0.666 ± 0.062	-0.407 ± 0.045	0.113 ± 0.034
D42	-0.076 ± 0.008	-0.138 ± 0.103	-0.006 ± 0.056	-0.058 ± 0.041
D43	-0.072 ± 0.023	0.297 ± 0.181	-0.266 ± 0.131	0.012 ± 0.098
D44	-0.097 ± 0.018	0.467 ± 0.136	-0.224 ± 0.105	-0.254 ± 0.083
D48	-0.090 ± 0.049	-0.164 ± 0.105	0.156 ± 0.094	-0.262 ± 0.076
D49	-0.036 ± 0.006	-0.047 ± 0.188	-0.053 ± 0.135	-0.252 ± 0.121
D52	0.002 ± 0.012	-0.159 ± 0.048	-0.011 ± 0.043	-0.195 ± 0.028
D60	-0.069 ± 0.011	-0.168 ± 0.066	-0.298 ± 0.053	-0.177 ± 0.047
D61	-0.046 ± 0.064	-0.026 ± 0.184	-0.054 ± 0.144	-0.238 ± 0.112
D89	-0.268 ± 0.042	0.139 ± 0.070	-0.410 ± 0.064	-0.685 ± 0.045

Table B.4: Velocity dispersion and stellar population gradients for 14 galaxies in the Shapley sample (MGP0129, MGP1211, MGP2146, MGP2399, MGP4258 are excluded).

ID	$\nabla \log \sigma$	$\nabla \log(\mathrm{age/Gyr})$	$\nabla[\mathrm{Z/H}]$	$\nabla[\alpha/\mathrm{Fe}]$
MGP1189	-0.137 ± 0.040	0.018 ± 0.119	-0.133 ± 0.084	-0.067 ± 0.102
MGP1195	-0.094 ± 0.057	0.013 ± 0.201	-0.294 ± 0.141	-0.066 ± 0.123
MGP1230	-0.073 ± 0.130	-0.413 ± 0.195	0.066 ± 0.185	-0.310 ± 0.167
MGP1440	-0.152 ± 0.058	-0.259 ± 0.221	-0.136 ± 0.144	-0.038 ± 0.148
MGP1490	-0.038 ± 0.031	-0.195 ± 0.250	0.050 ± 0.201	-0.245 ± 0.244
MGP1600	-0.071 ± 0.028	0.022 ± 0.114	-0.166 ± 0.095	0.102 ± 0.075
MGP1626	-0.145 ± 0.046	0.484 ± 0.120	-0.508 ± 0.126	-0.042 ± 0.074
MGP1835	-0.088 ± 0.026	-0.029 ± 0.089	-0.172 ± 0.054	0.055 ± 0.052
MGP1988	-0.179 ± 0.039	0.031 ± 0.209	-0.148 ± 0.128	-0.090 ± 0.090
MGP2083	-0.046 ± 0.029	-0.251 ± 0.088	-0.093 ± 0.085	-0.045 ± 0.064
MGP2437	-0.232 ± 0.112	-0.523 ± 0.153	0.201 ± 0.110	-0.014 ± 0.120
MGP2440	-0.036 ± 0.011	-0.265 ± 0.085	0.025 ± 0.083	-0.058 ± 0.064
MGP3971	-0.088 ± 0.010	0.306 ± 0.201	-0.310 ± 0.137	-0.034 ± 0.121
MGP3976	-0.198 ± 0.038	-0.211 ± 0.174	0.147 ± 0.138	-0.014 ± 0.113

Appendix C

Shapley Supercluster B–R colour gradients

This appendix presents the measured colour gradients described in Section 4.6, for the 14 Shapley galaxies with derived index gradients. Colours are predicted from VIMOS spectroscopic age and metallicity via the evolutionary stellar population models of Maraston (2005).

The layout of Figures C.1 – C.14 is as follows. Upper panels: display the B- (left) and R-band (right) imaging overlaid by the adopted bin boundaries (thin cyan/orange ellipses) and r_e (thicker blue/red ellipse). Central panel: the B- and R-band photometry from each radial bin (B = blue/cyan; R = red/orange). Open points are not included in the best fits. Lower panel: circles and solid line show the B–R gradient as measured from the imaging. The gradient is given to the top-right of the panel. Green stars/dashed line show the gradient predicted from VIMOS when converting the age and metallicity in each bin to a colour, and then fitting to all bins with r_e. The green squares/dotted line show the predicted gradient derived from VIMOS using the inner/outer points. Generally, these two methods give near-identical results (given in the top-right of the panel). Grey vertical dashed line indicate are the adopted bin boundaries and the orange dashed line is at r_e.

Table C.1 lists two sets of B–R central colours ($r_e/3$ aperture) and colour gradients. 'Photometric' are measured from SOS imaging as described in Section 4.6.1. 'VIMOS predicted' are from the first method described in Section 4.6.2, whereby a colour is predicted from the age and metallicity of each radial bin, and the gradient is calculated from a linear fit to all points within r_e.

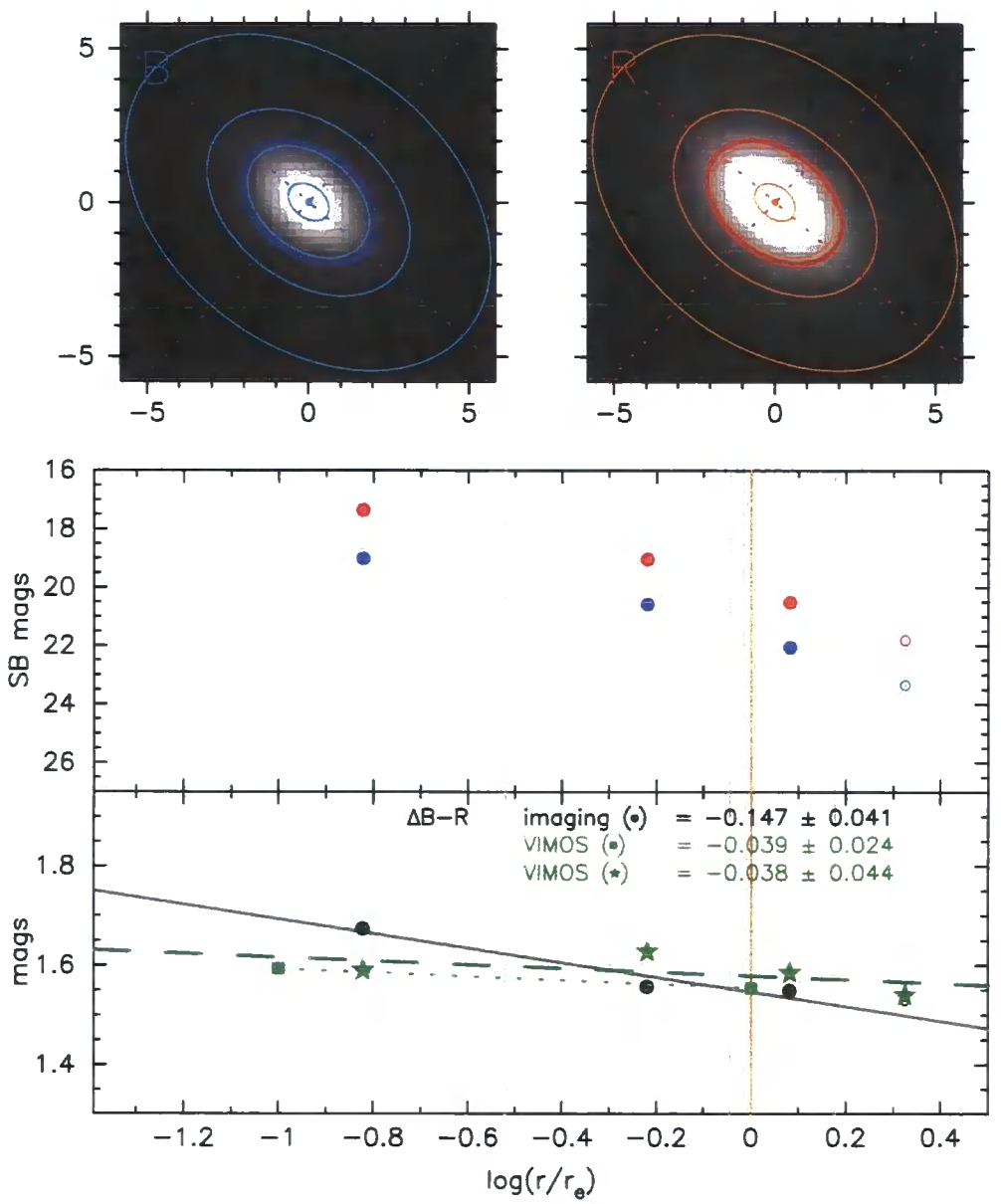

Figure C.1: B–R colour gradients for MGP1189.

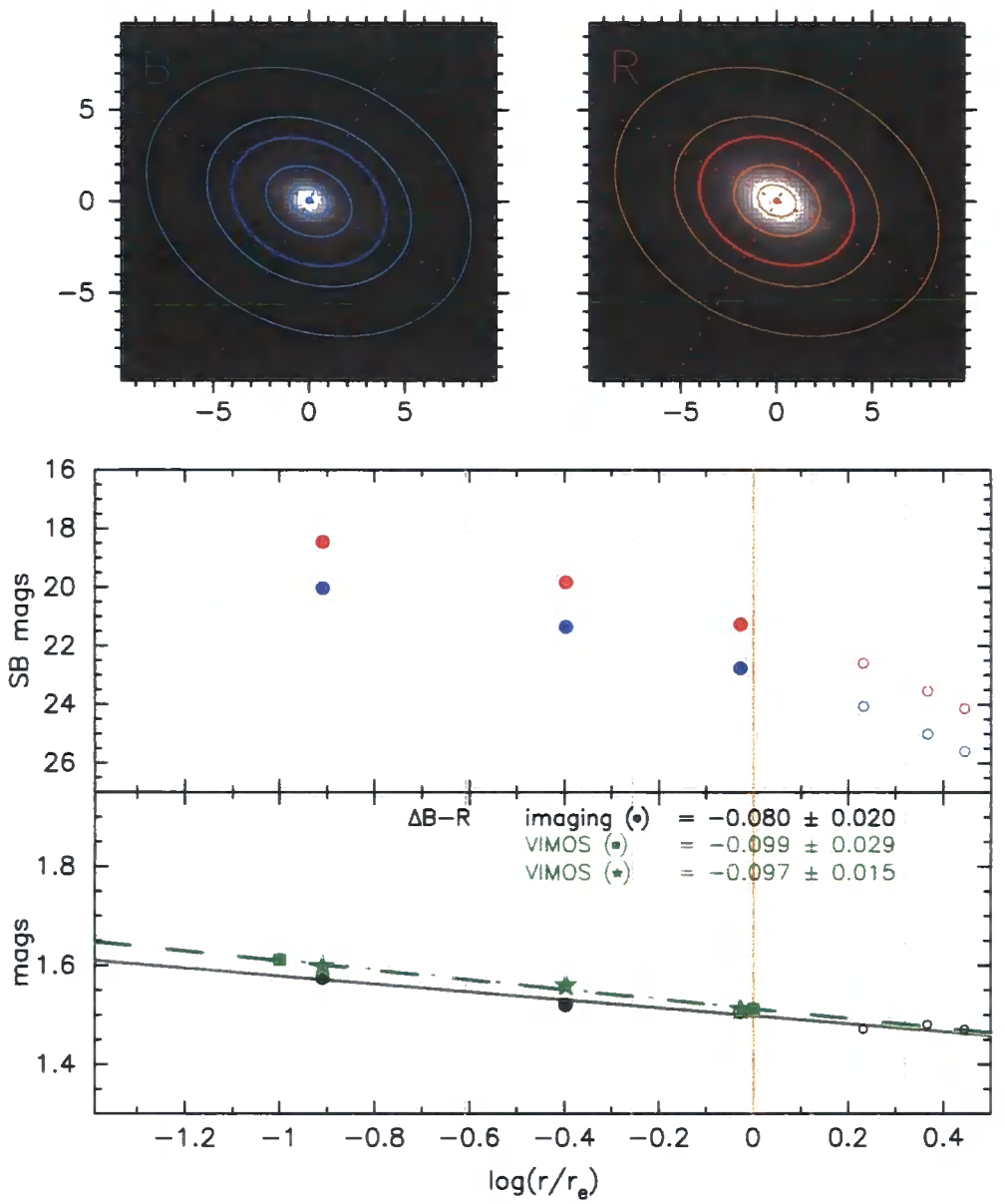

Figure C.2: B–R colour gradients for MGP1195.

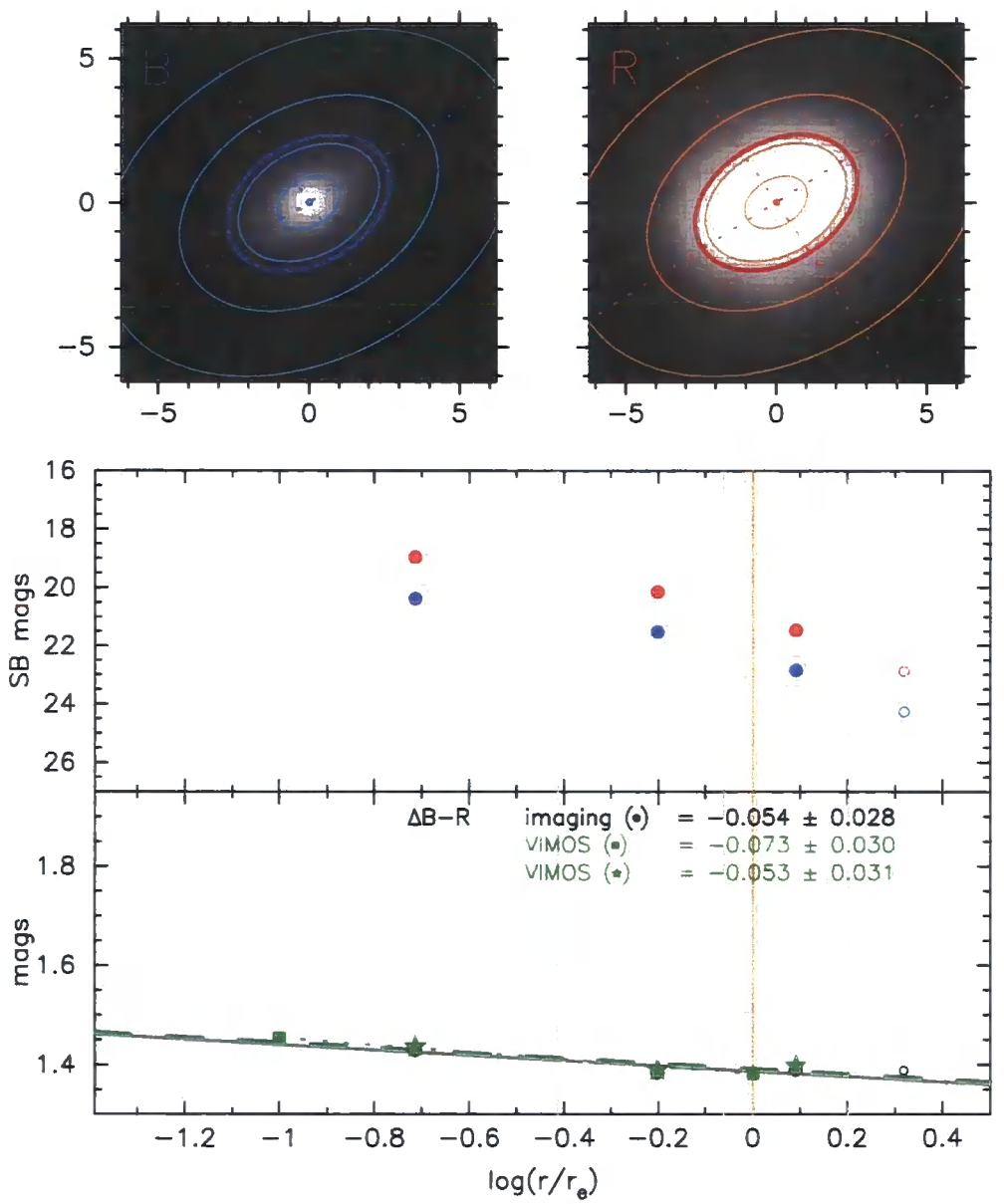

Figure C.3: B–R colour gradients for MGP1230.

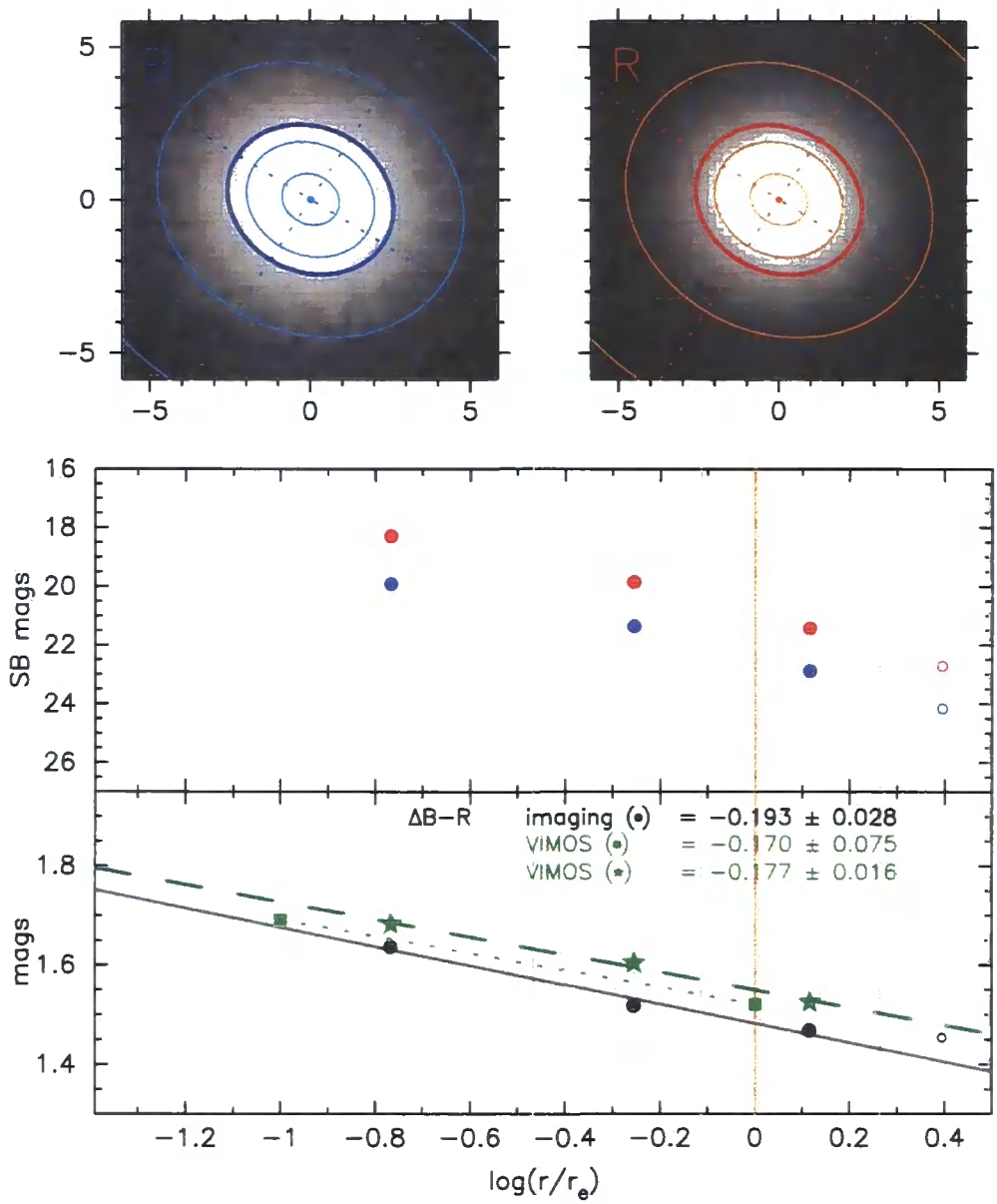

Figure C.4: B–R colour gradients for MGP1440.

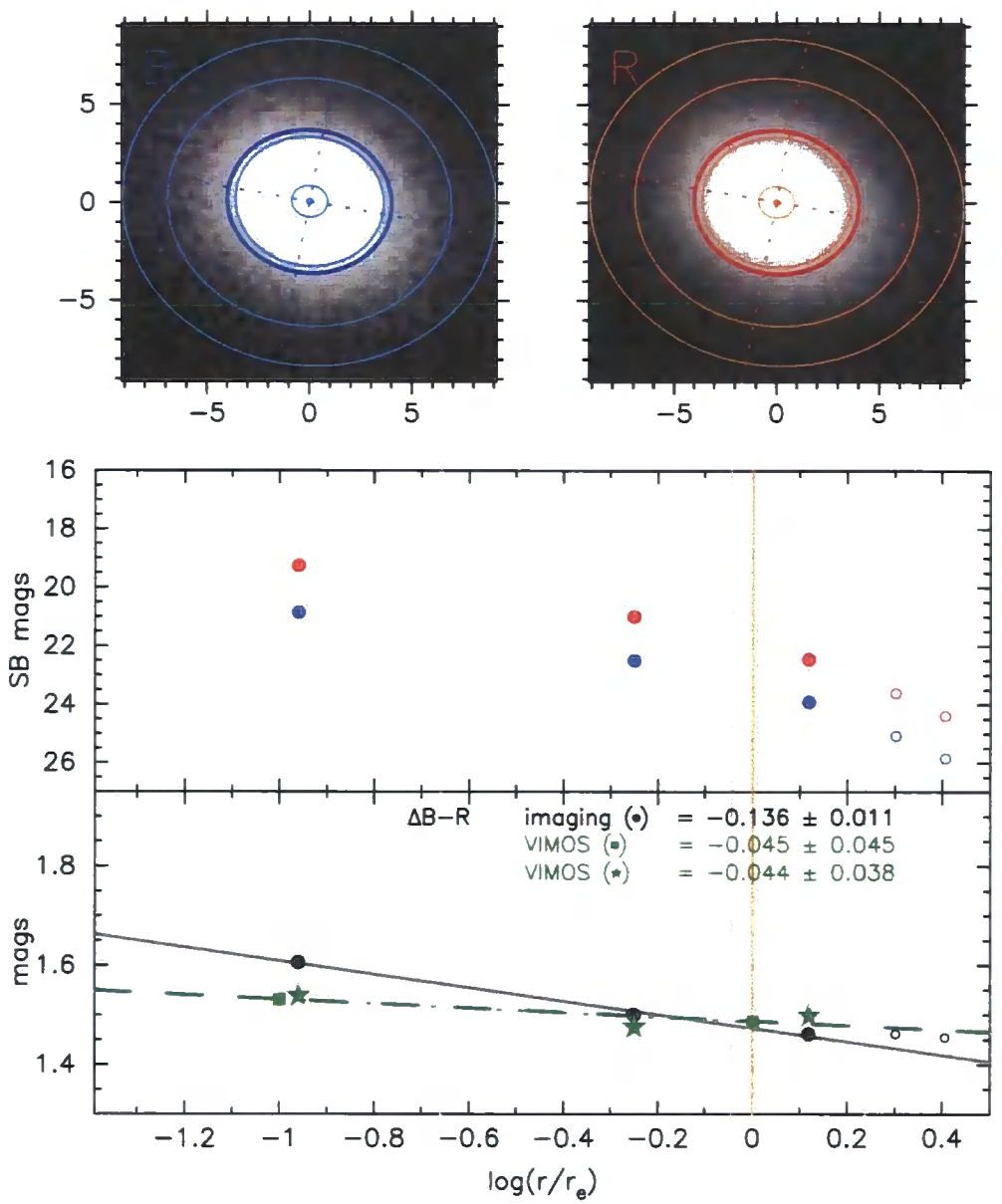

Figure C.5: B–R colour gradients for MGP1490.

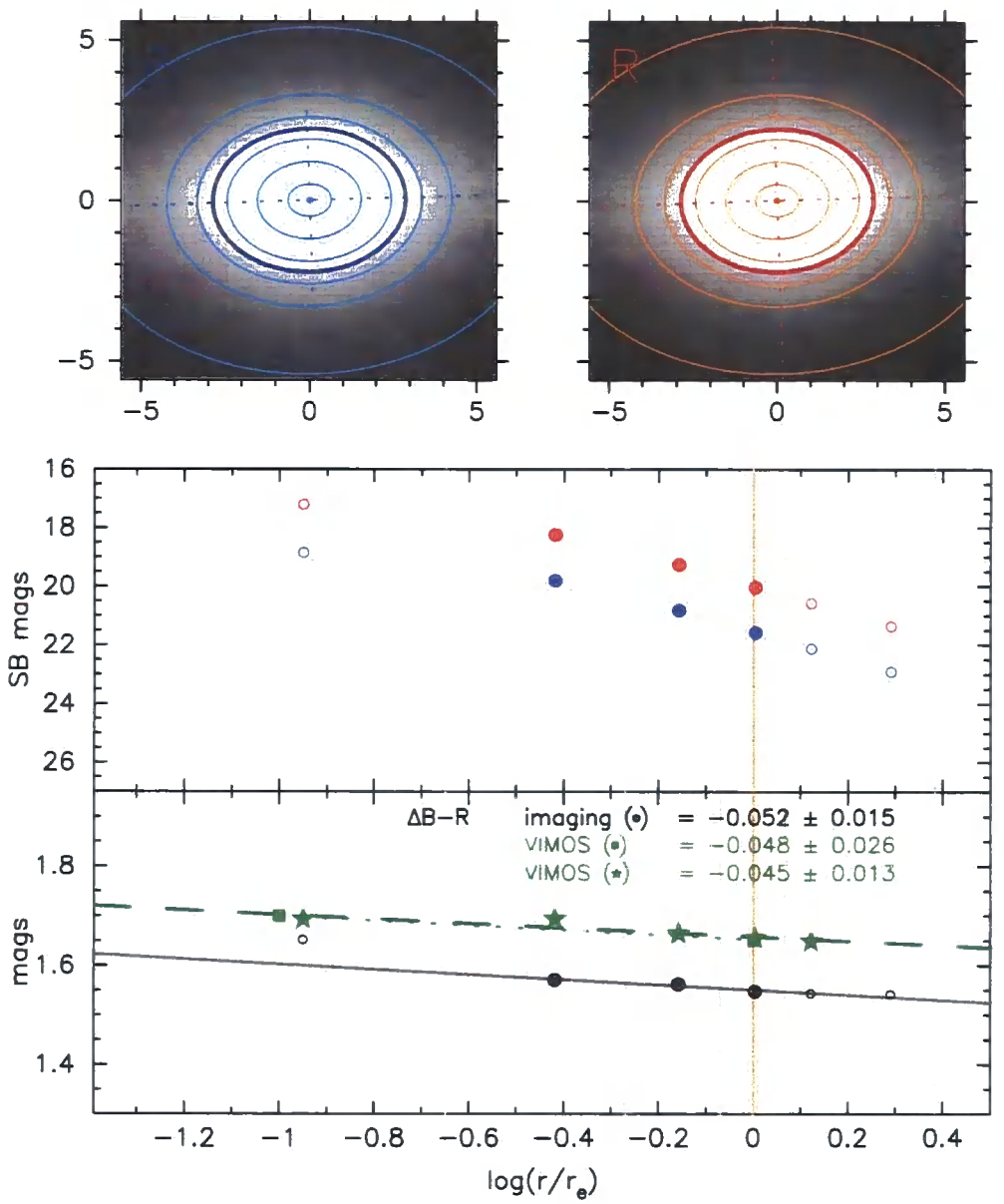

Figure C.6: B–R colour gradients for MGP1600.

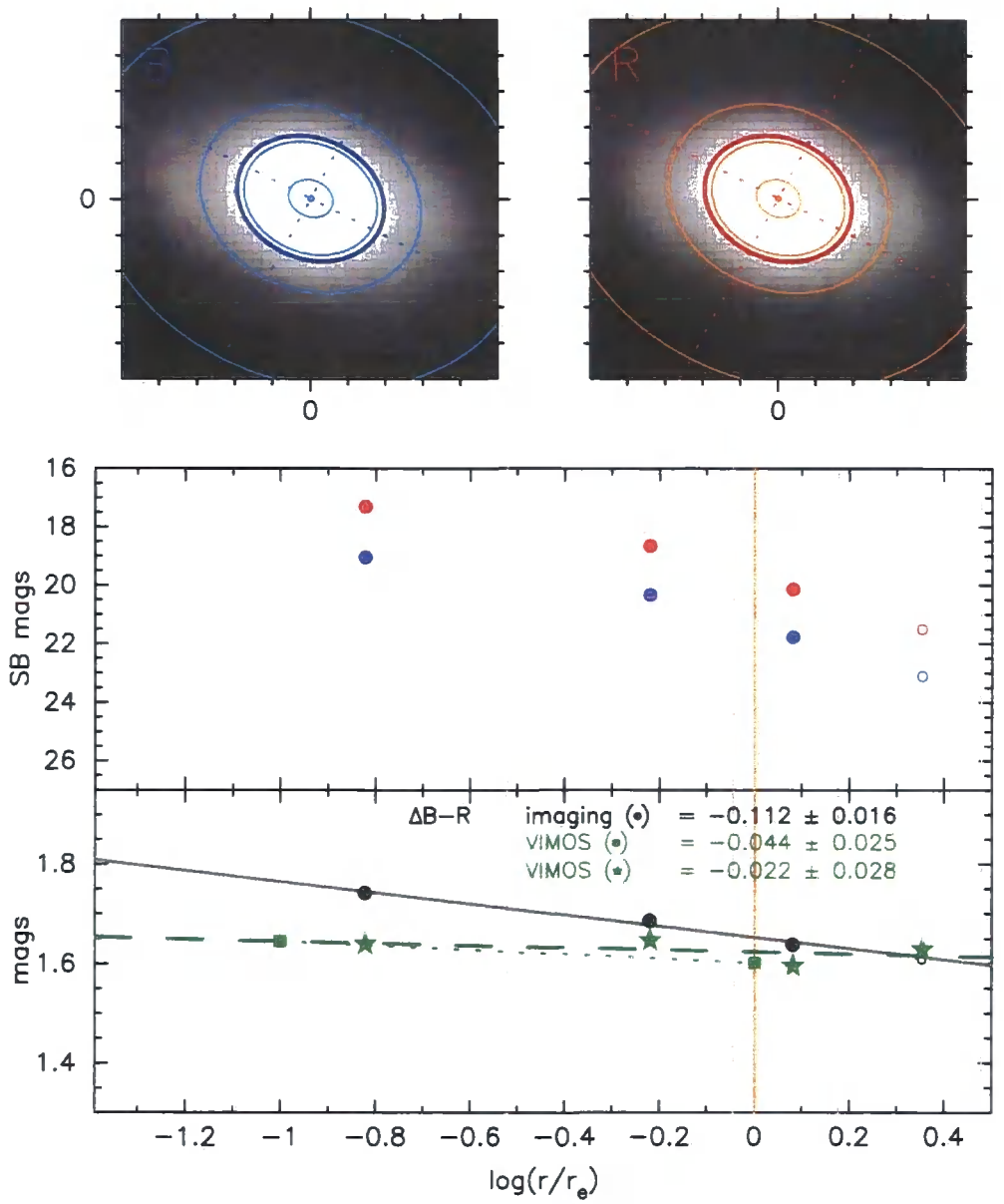

Figure C.7: B–R colour gradients for MGP1626.

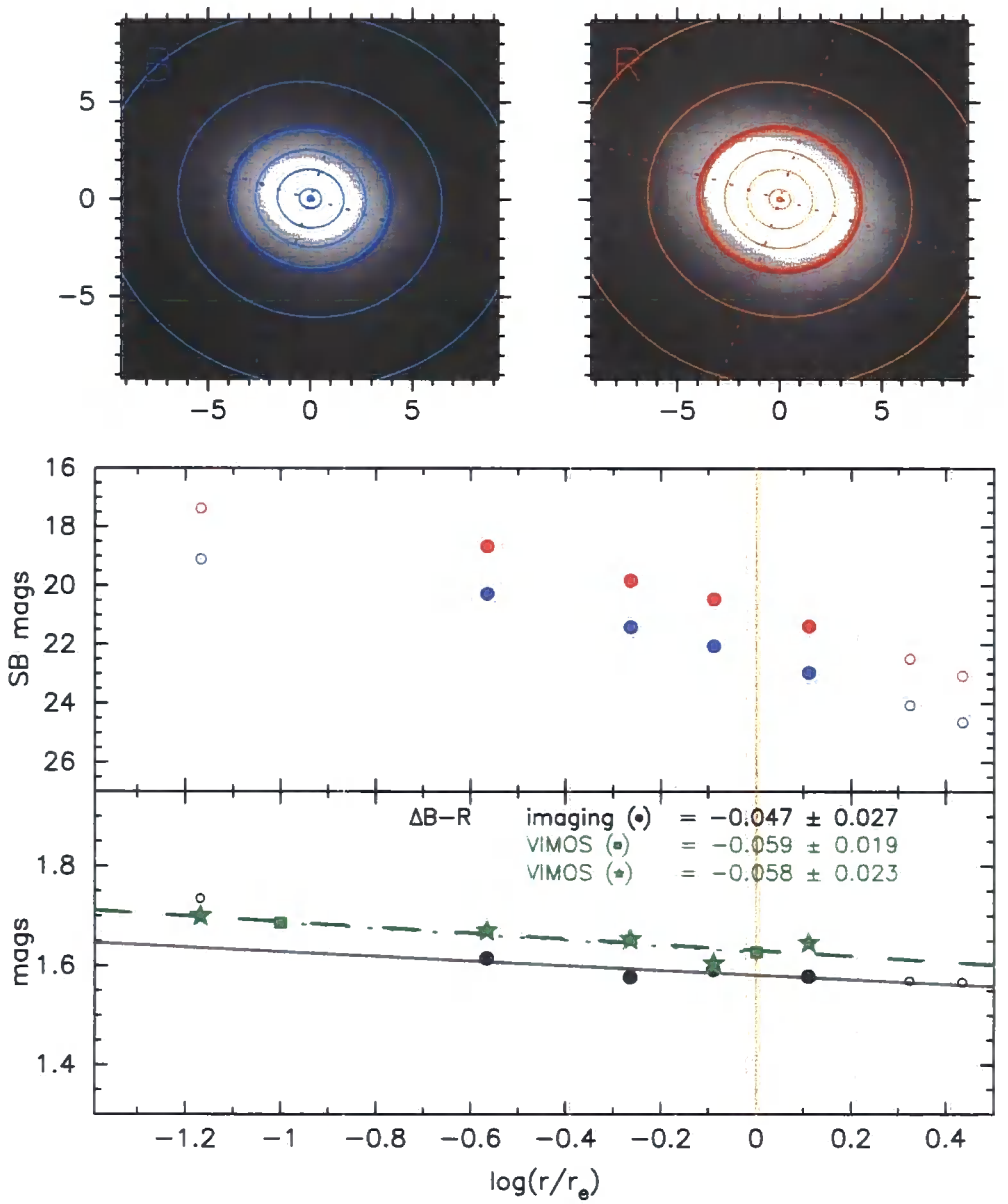

Figure C.8: B–R colour gradients for MGP1835.

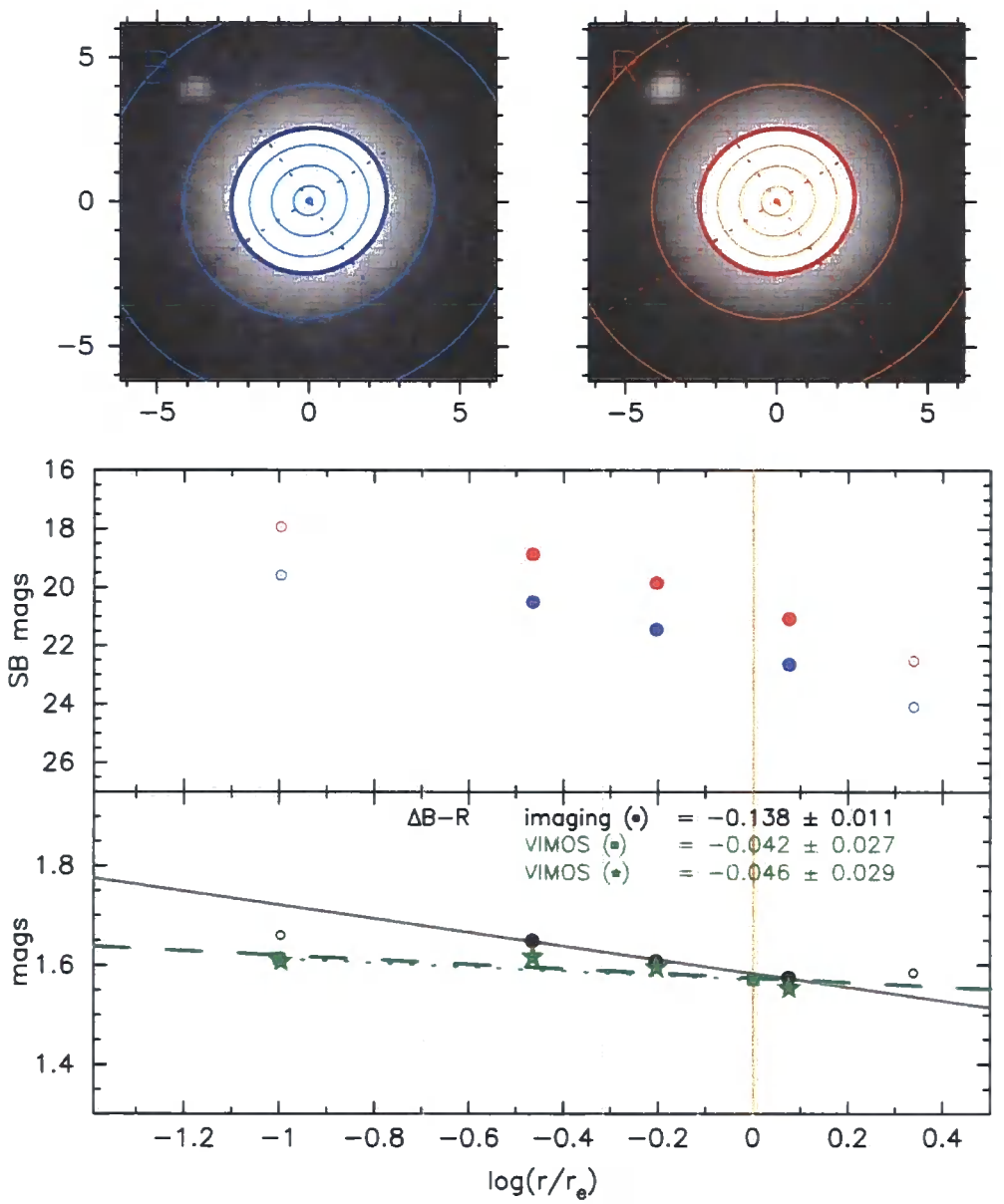

Figure C.9: B–R colour gradients for MGP1988.

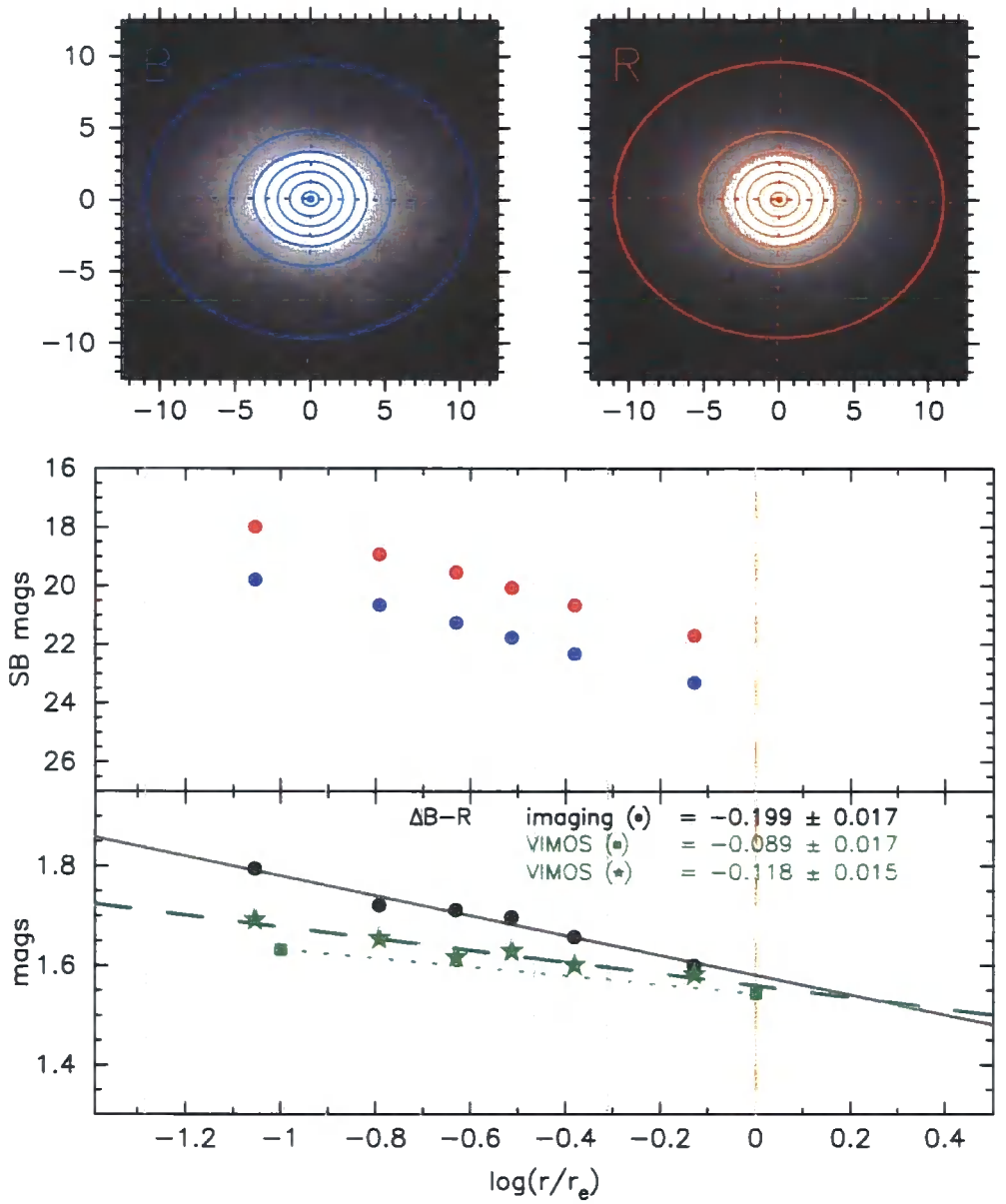

Figure C.10: B–R colour gradients for MGP2083.

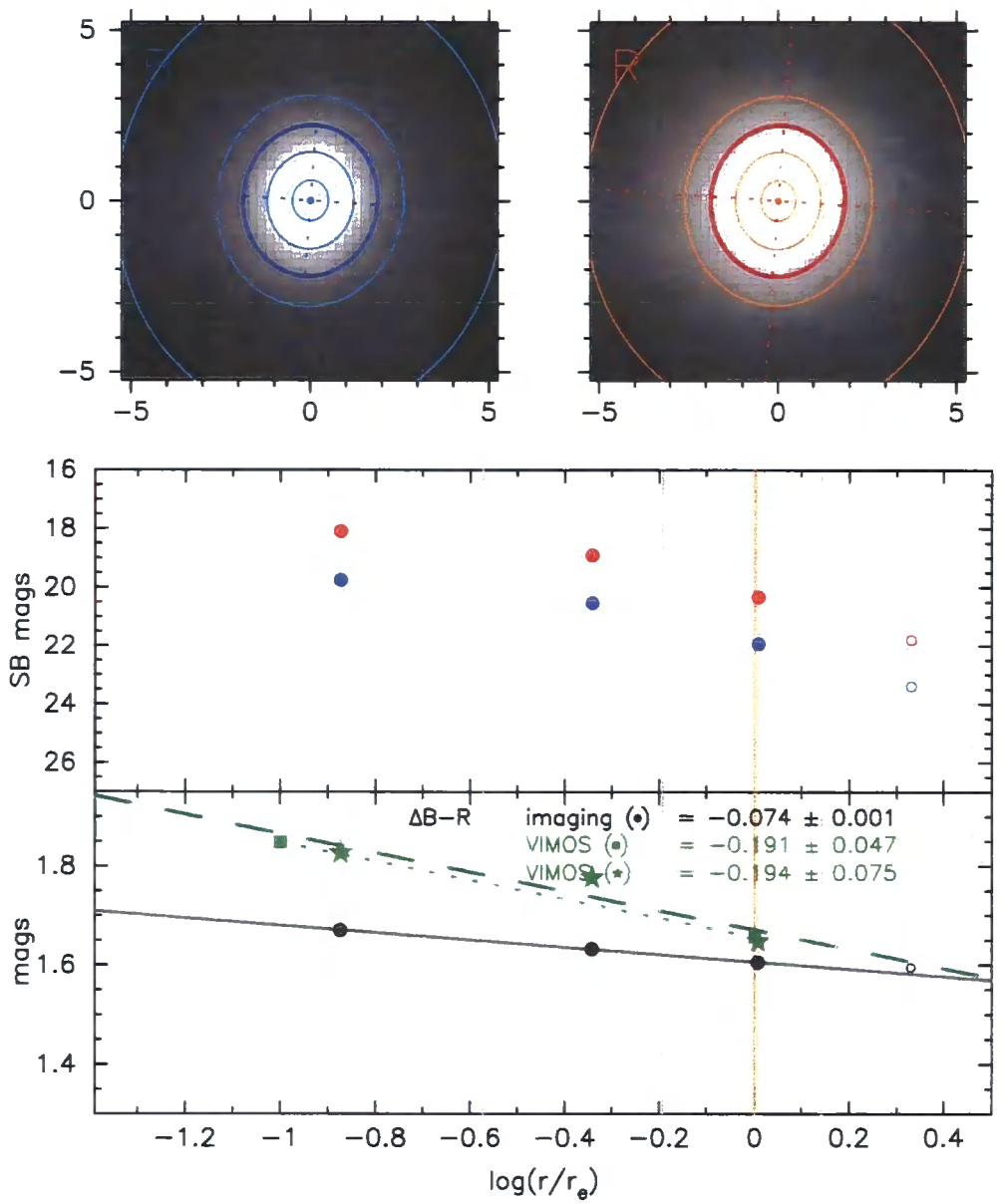

Figure C.11: B–R colour gradients for MGP2437.

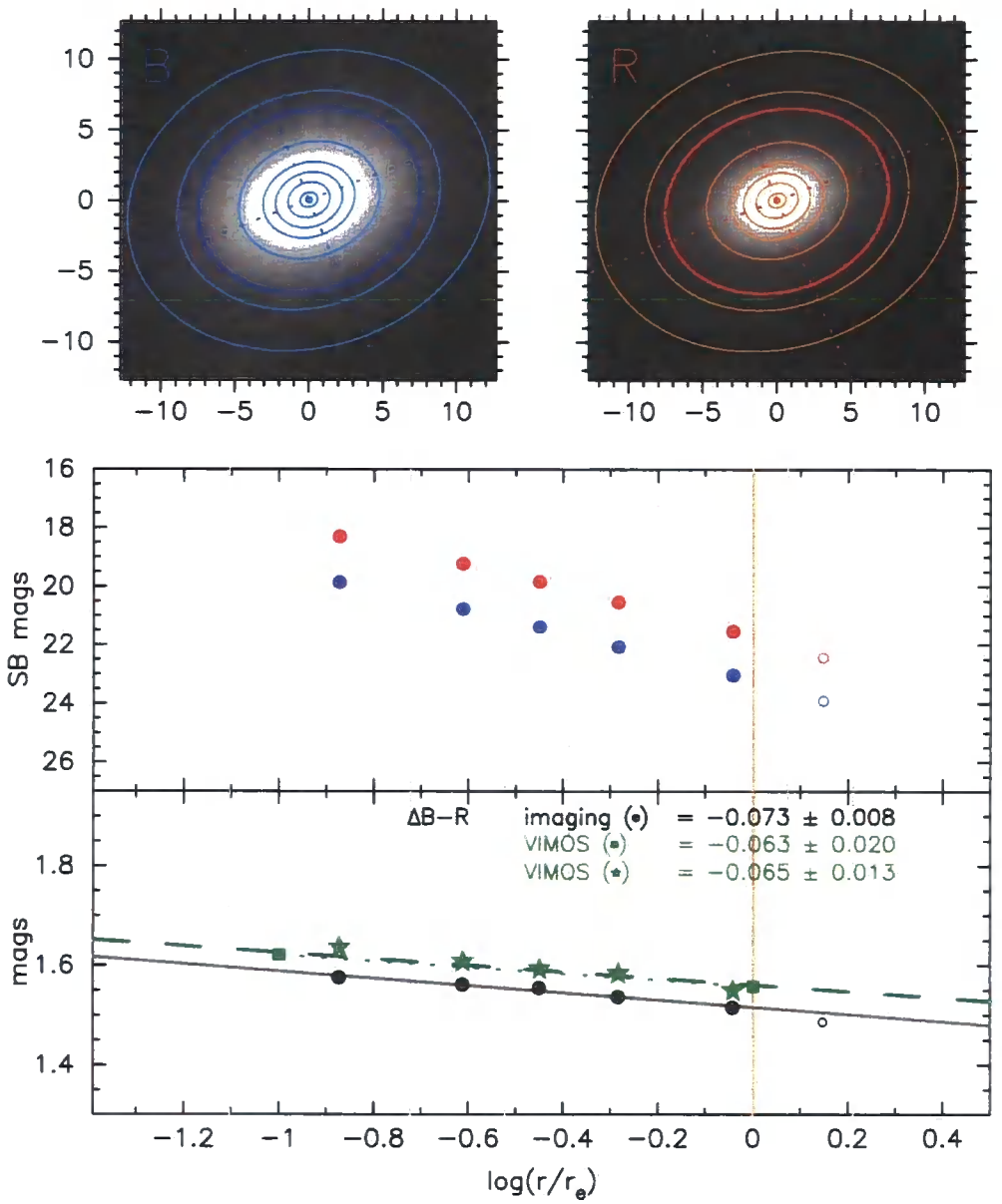

Figure C.12: B–R colour gradients for MGP2440.

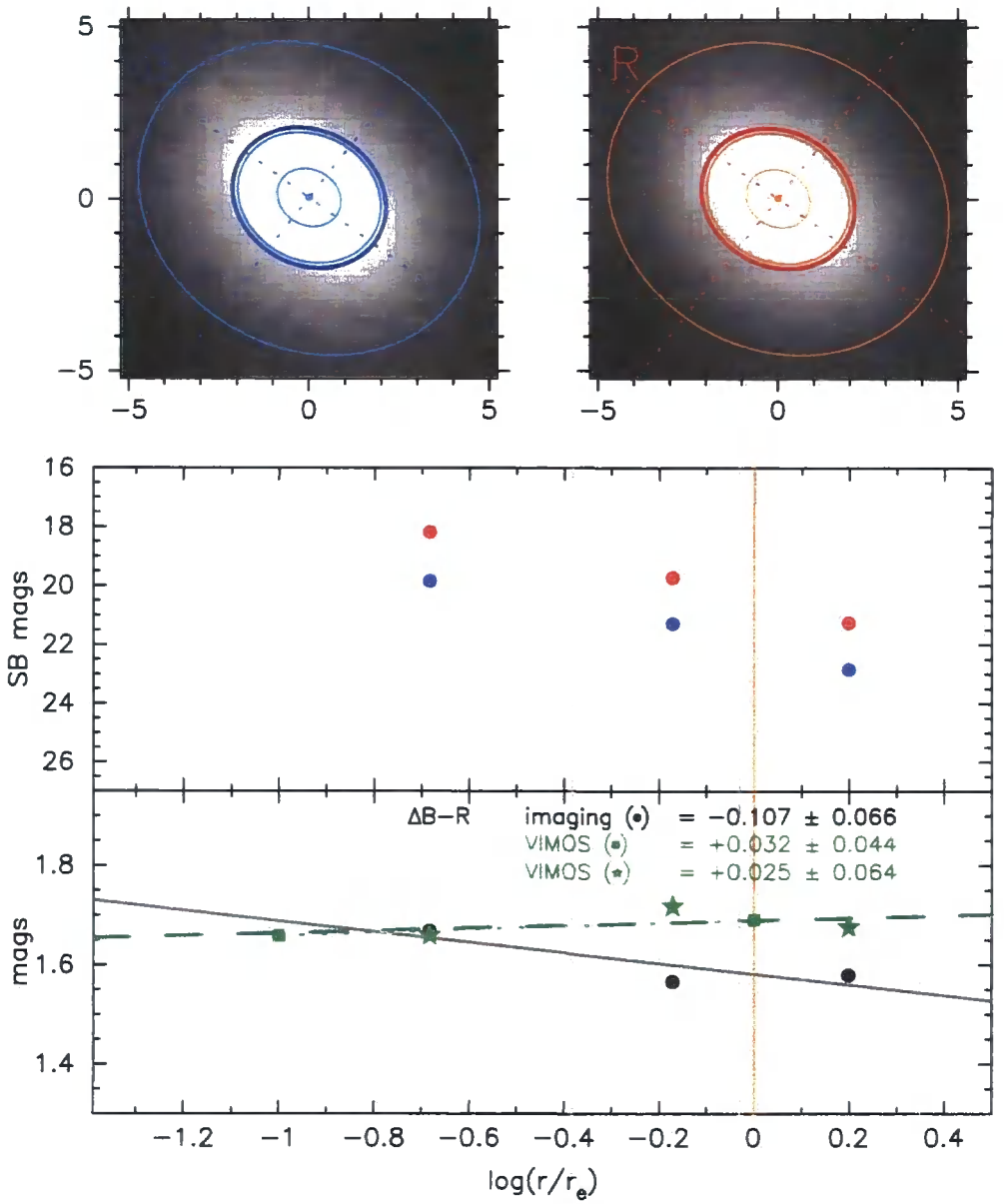

Figure C.13: B–R colour gradients for MGP3971.

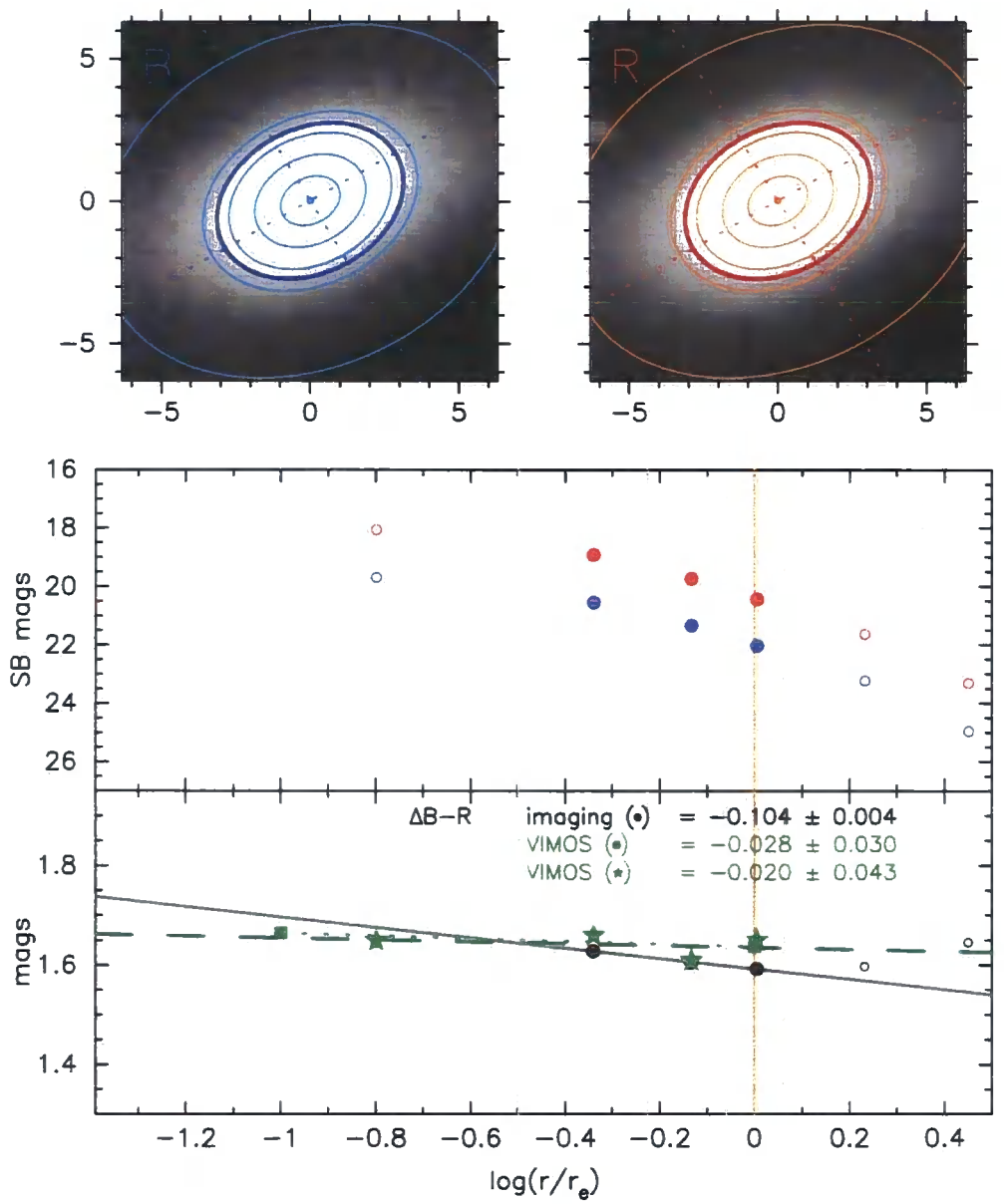

Figure C.14: B–R colour gradients for MGP3976.

Table C.1: Central B–R colour ($r_e/3$ aperture) and colour gradient for each galaxy in the Shapley sample (in Vega magnitudes and corrected for galactic extinction).

ID	Photometric		VIMOS predicted	
	central B–R	∇B–R	central B–R	∇B–R
MGP0129	1.62	–	1.51	–
MGP1189	1.63	–0.15 ± 0.04	1.62	–0.04 ± 0.04
MGP1195	1.57	–0.08 ± 0.02	1.59	–0.10 ± 0.01
MGP1211	1.61	–	1.56	–
MGP1230	1.55	–0.05 ± 0.03	1.43	–0.05 ± 0.03
MGP1440	1.64	–0.19 ± 0.03	1.65	–0.18 ± 0.02
MGP1490	1.54	–0.14 ± 0.01	1.50	–0.04 ± 0.04
MGP1600	1.69	–0.05 ± 0.02	1.72	–0.04 ± 0.01
MGP1626	1.70	–0.11 ± 0.02	1.64	–0.02 ± 0.03
MGP1835	1.65	–0.05 ± 0.03	1.68	–0.06 ± 0.02
MGP1988	1.71	–0.14 ± 0.01	1.61	–0.05 ± 0.03
MGP2083	1.75	–0.20 ± 0.02	1.62	–0.12 ± 0.01
MGP2146	1.52	–	1.55	–
MGP2399	1.52	–	1.49	–
MGP2437	1.55	–0.07 ± 0.01	1.79	–0.19 ± 0.07
MGP2440	1.58	–0.07 ± 0.02	1.61	–0.07 ± 0.01
MGP3971	1.74	–0.11 ± 0.07	1.66	+0.03 ± 0.06
MGP3976	1.63	–0.10 ± 0.02	1.68	–0.02 ± 0.04
MGP4358	1.59	–	1.55	–

Appendix D

GMOS S0 radial profiles

Figure D.1 presents the seven Coma cluster lenticular galaxies observed with the GMOS long-slit spectrograph (Chapter 5). The 2 arcsec wide slit, truncated to 60 arcsec in length, is indicated for reference.

The remainder of the appendix presents the kinematic and absorption line profiles for the seven S0 galaxies. Stellar population profiles are shown in Figures 5.19 – 5.25. The layout of Figures D.2 – D.8 is as follows. $1\,\sigma$ errors are indicated by orange shading throughout.

The first set of panels show the kinematic profiles along the slit. The two sides of the galaxy are shown independently to highlight the differential rotation. Upper panel: The observed g-band surface brightness profile for each galaxy (black line). The profiles for the model bulge (red dashes) and disc (blue dots) components, as derived using GALFIT, are superimposed. The dashed horizontal line indicates the approximate limit of the GMOS observations (23 mag arcsec^{-2}). The galaxy name is indicated at the top of each panel, and the structural types are described in Table 5.3. Central panels: observed rotational velocity ($V_{\rm obs}$) and velocity dispersion ($\sigma_{\rm obs}$). Lowest panel: open circles repeat the observed velocities, and filled circles show the circular rotation velocity (V_c, see Section 5.3.3 for details). The maximum values of $V_{\rm obs}$ and V_c are given in the top right.

The second set of panels present the absorption line strength profiles, combining the data from either side of the galaxy centre. Upper panels: Repeat the g-band surface brightness profile for each column, to facilitate radial comparison between structural and spectral features. Main panels: observed line strength profiles for the eight chosen Lick indices: HδF, HγF, Fe4383, Fe4531, Hβ, Mgb5177, Fe5270, Fe5335.

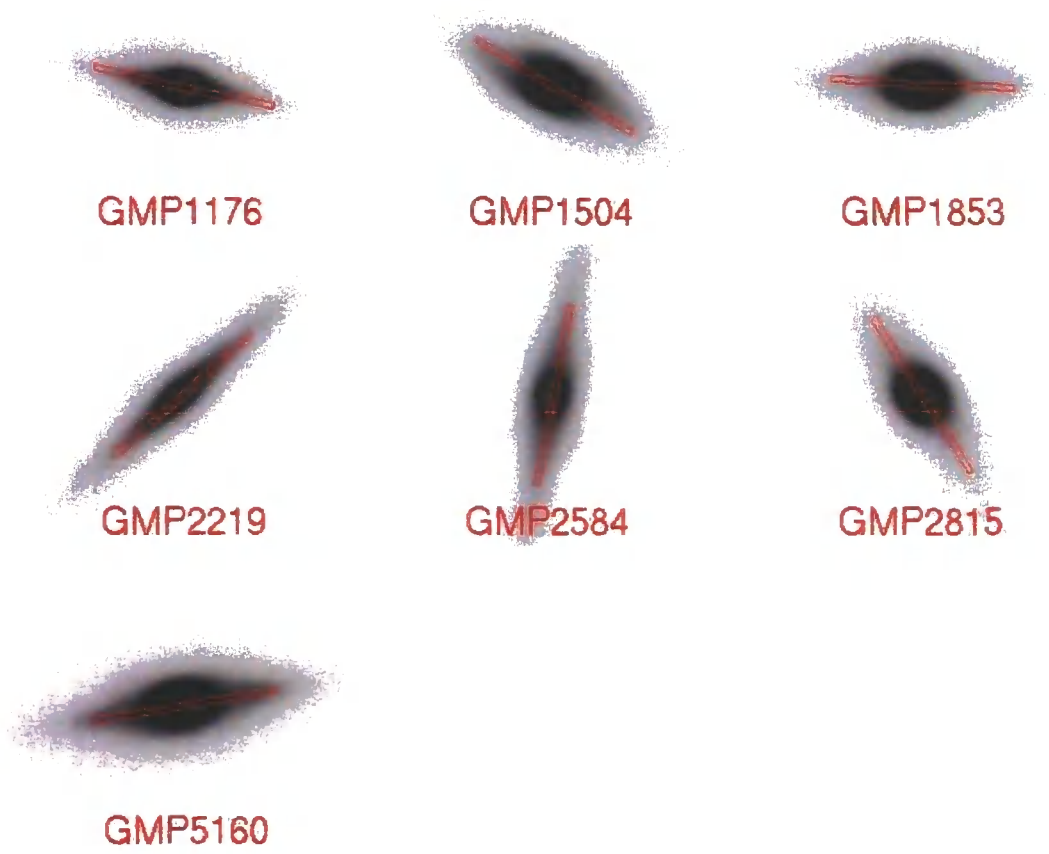

Figure D.1: The GMOS S0 sample, showing the 2 arcsec wide slit at the observed position angle. The slit length has been truncated to 60 arcsec, to indicate scale.

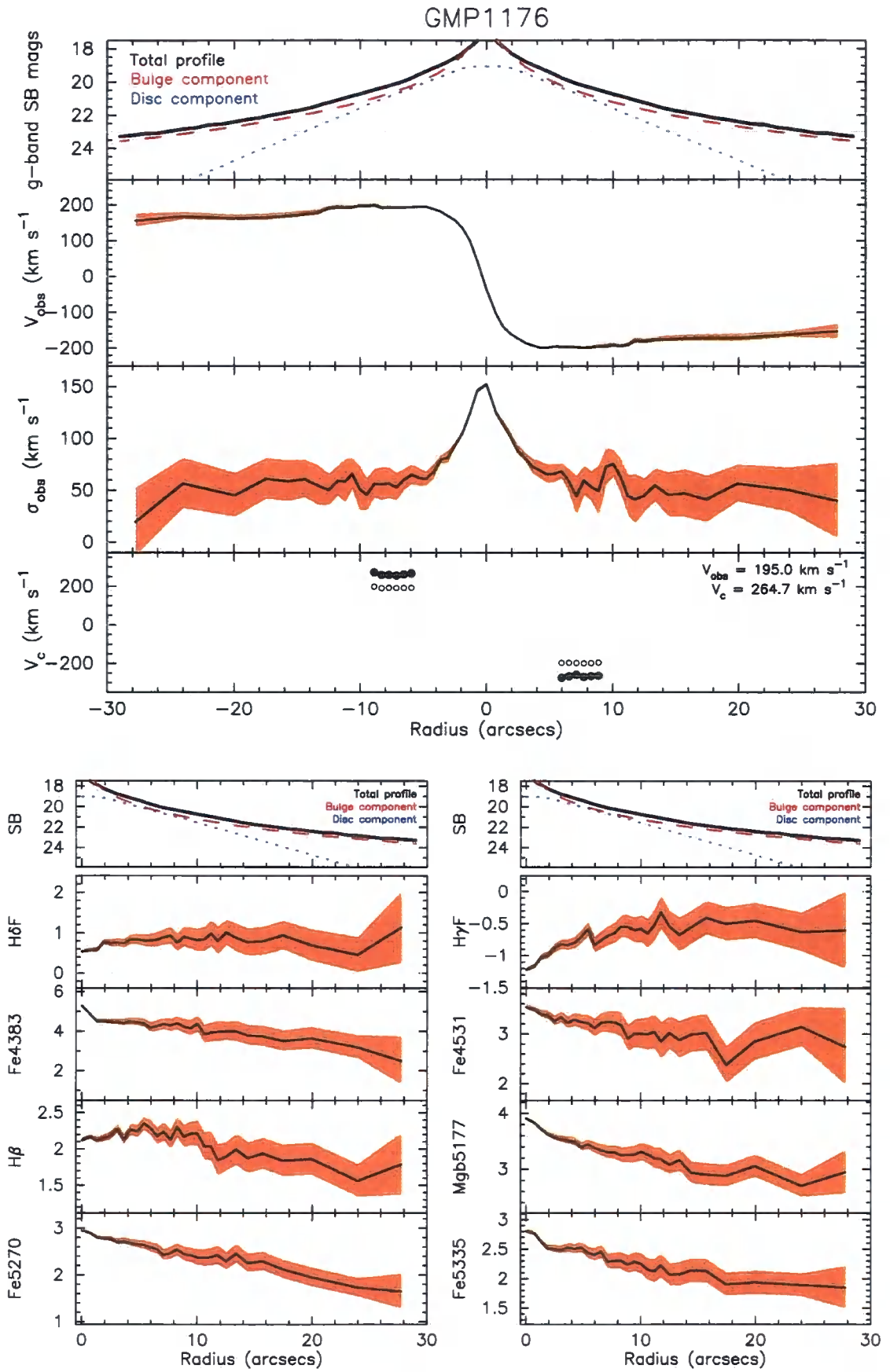

Figure D.2: Kinematic and absorption line profiles for GMP1176.

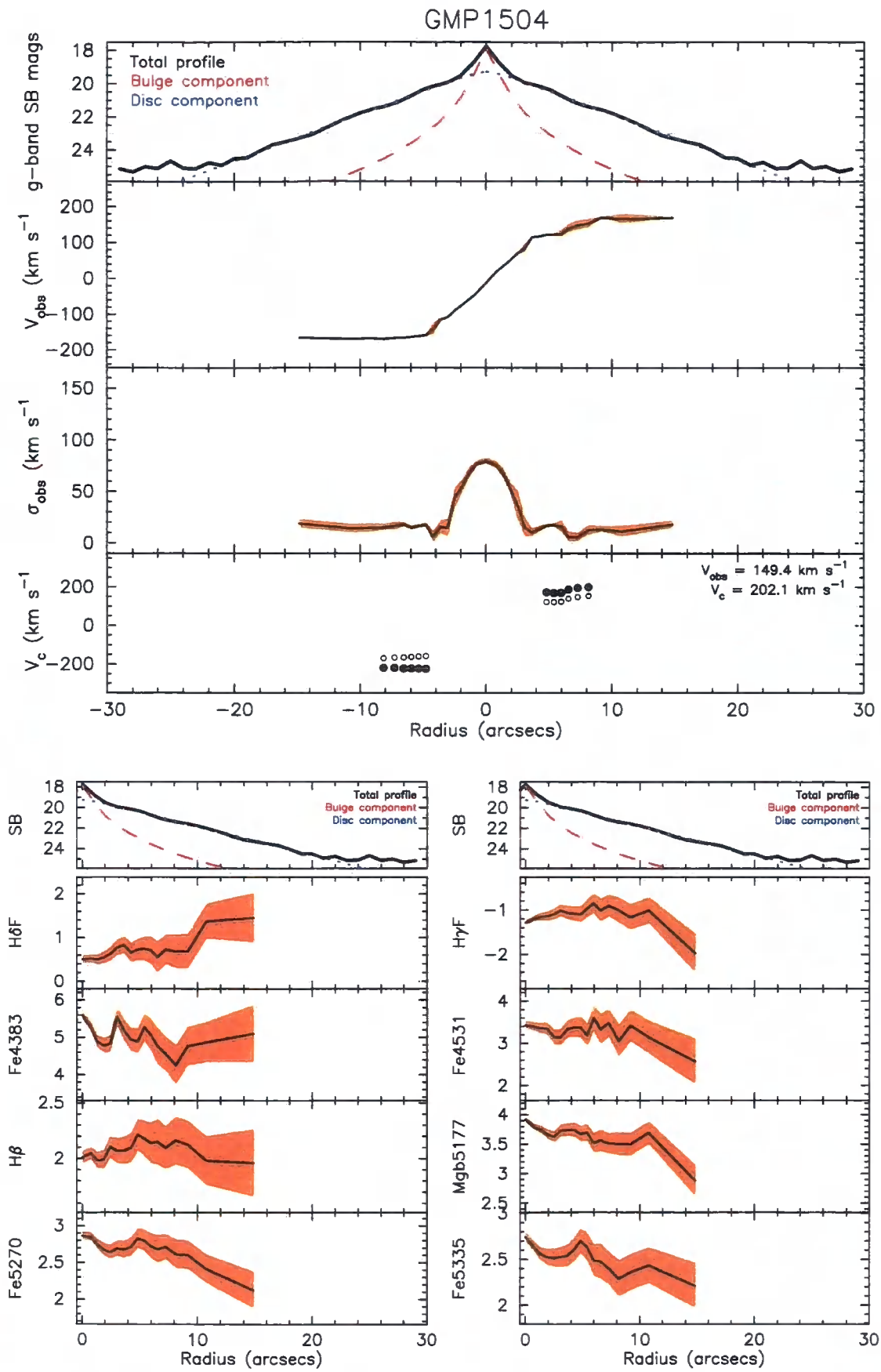

Figure D.3: Kinematic and absorption line profiles for GMP1504.

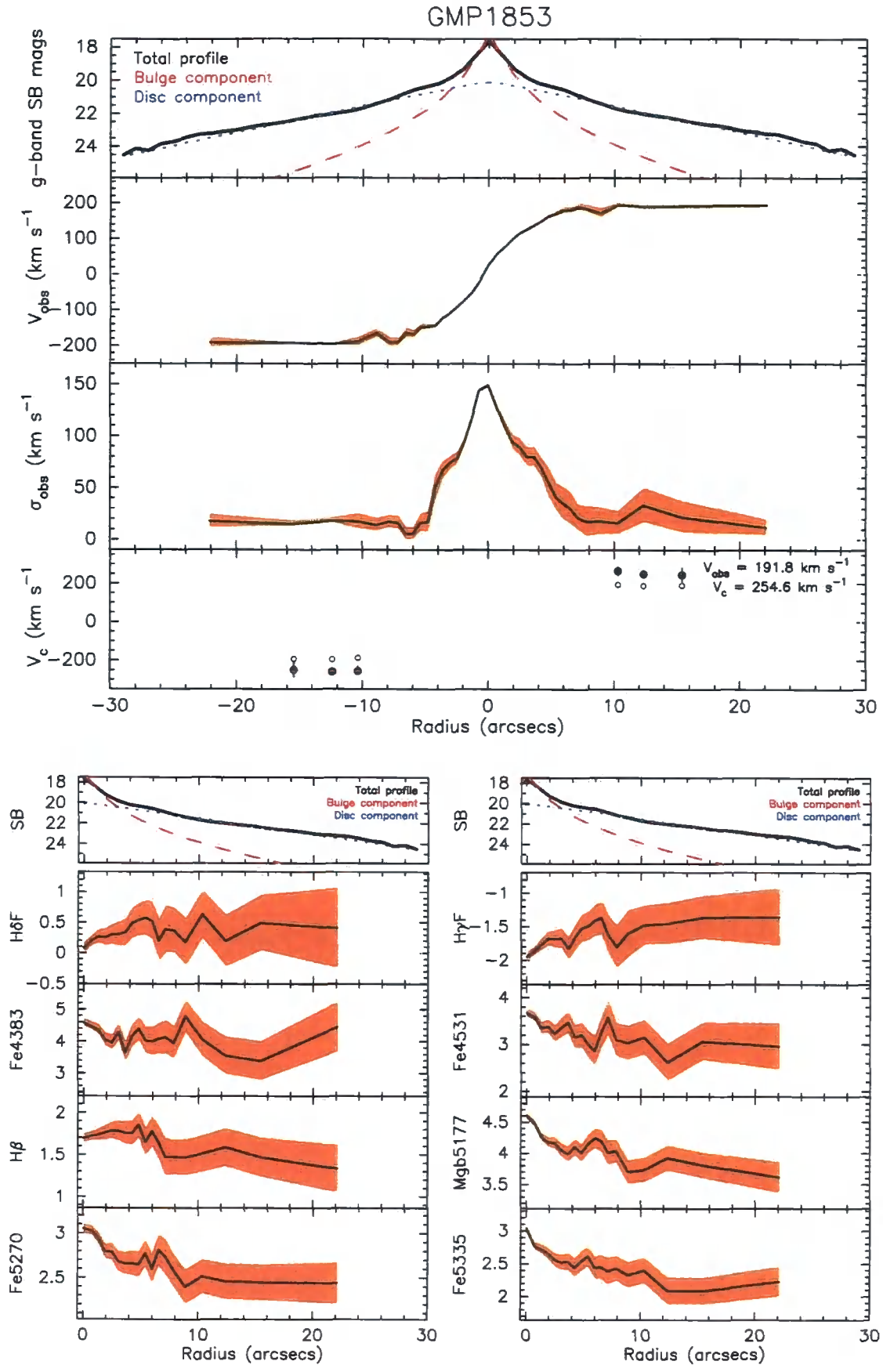

Figure D.4: Kinematic and absorption line profiles for GMP1853.

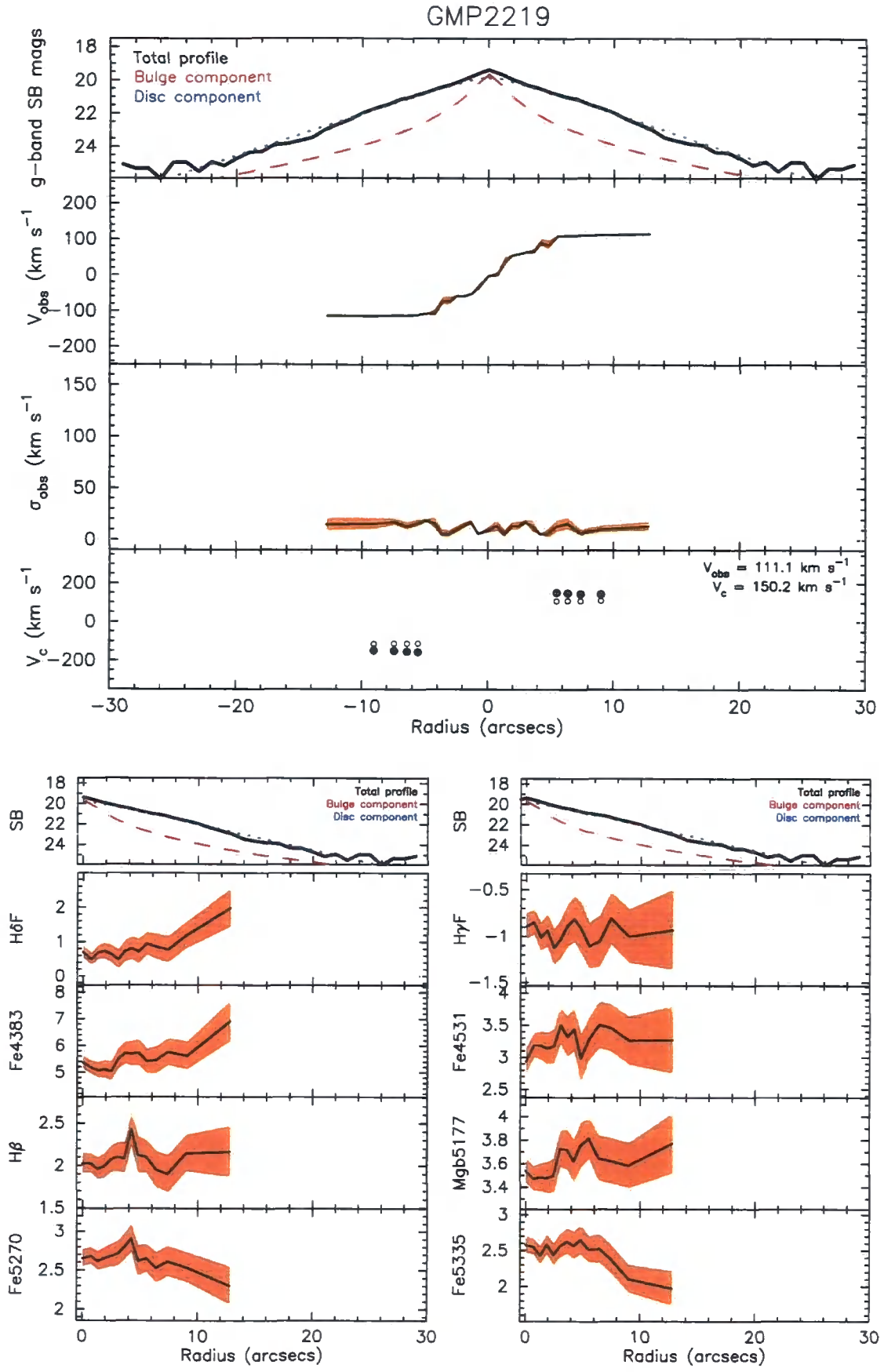

Figure D.5: Kinematic and absorption line profiles for GMP2219.

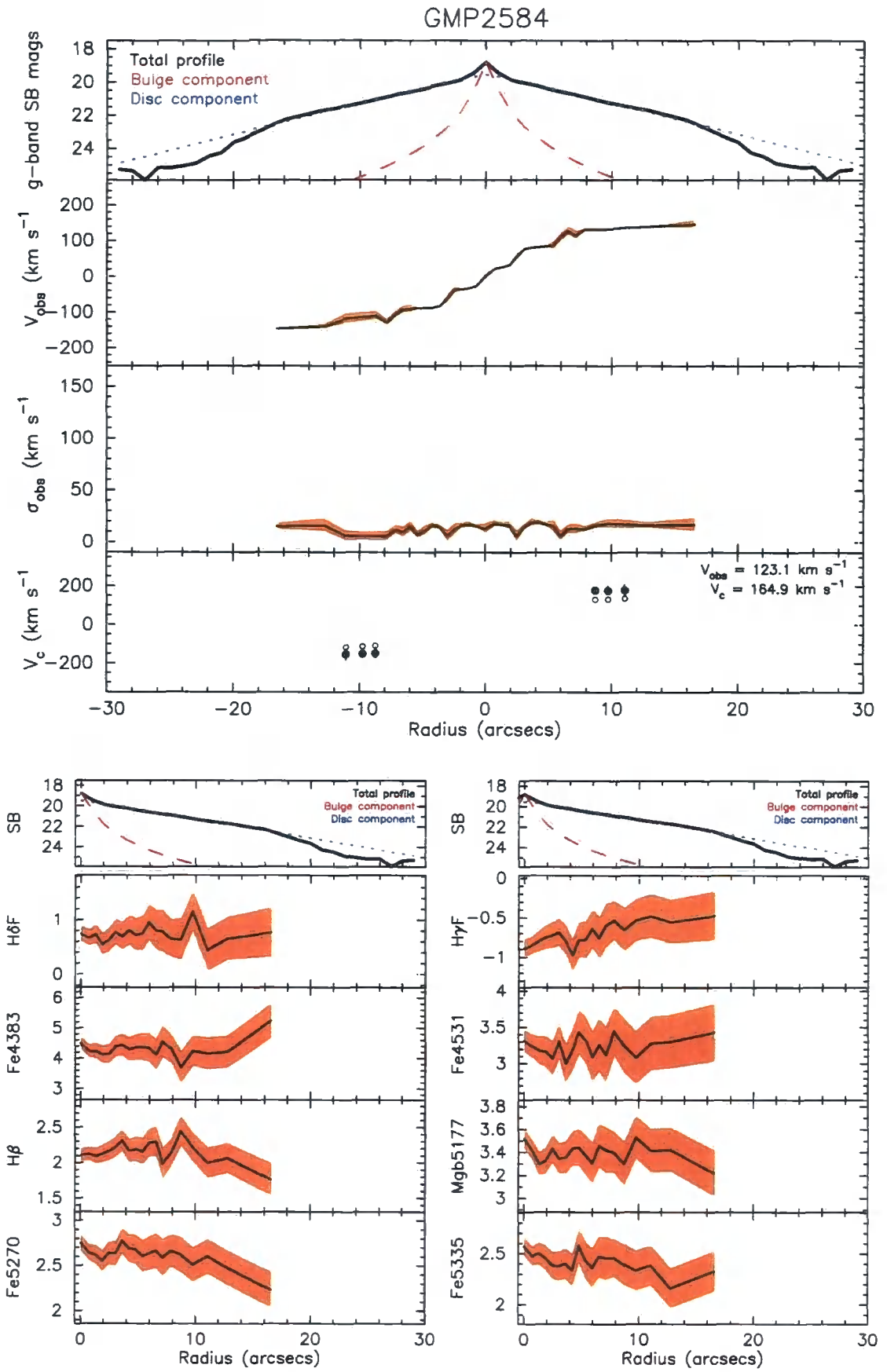

Figure D.6: Kinematic and absorption line profiles for GMP2584.

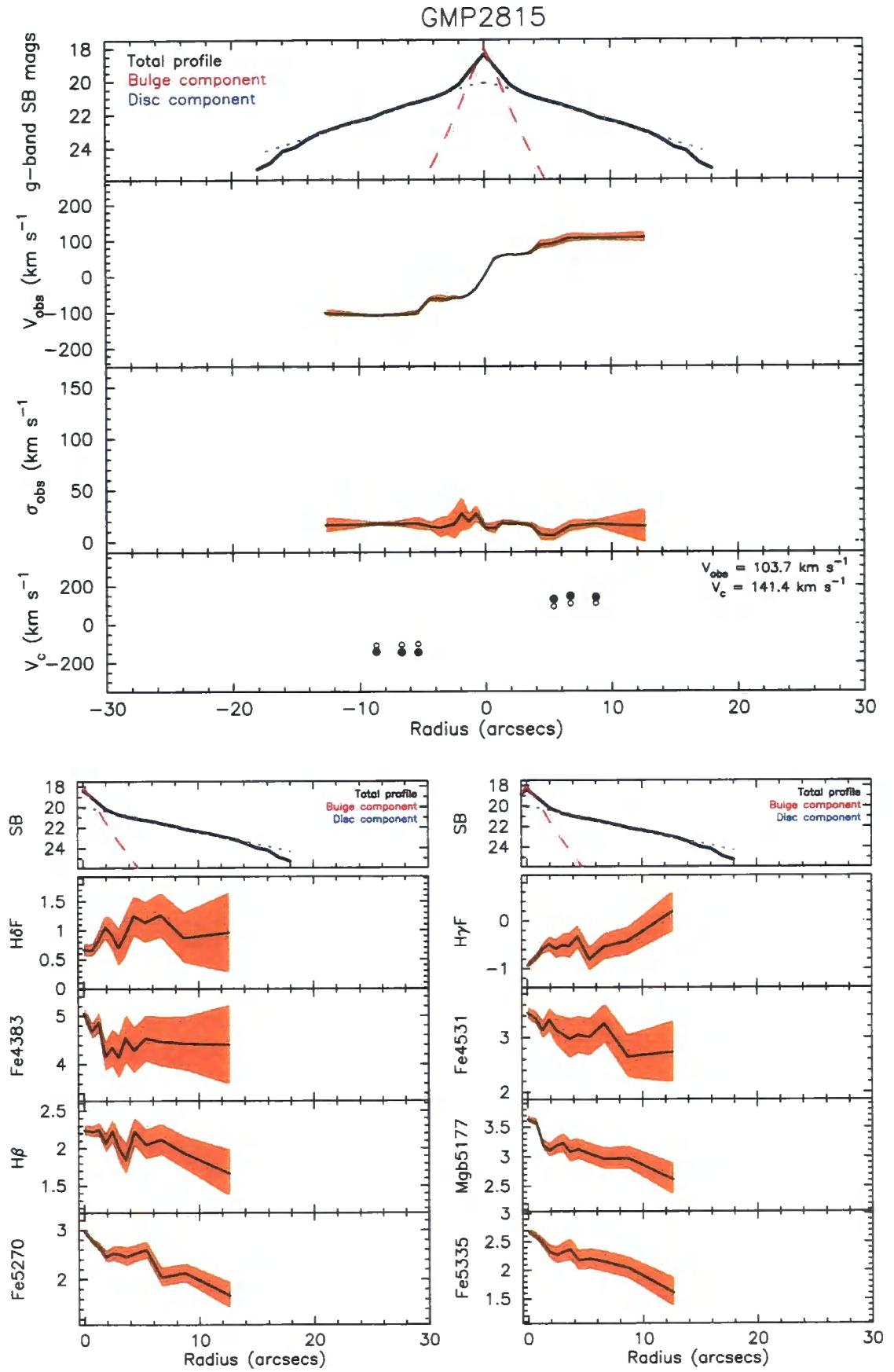

Figure D.7: Kinematic and absorption line profiles for GMP2815.

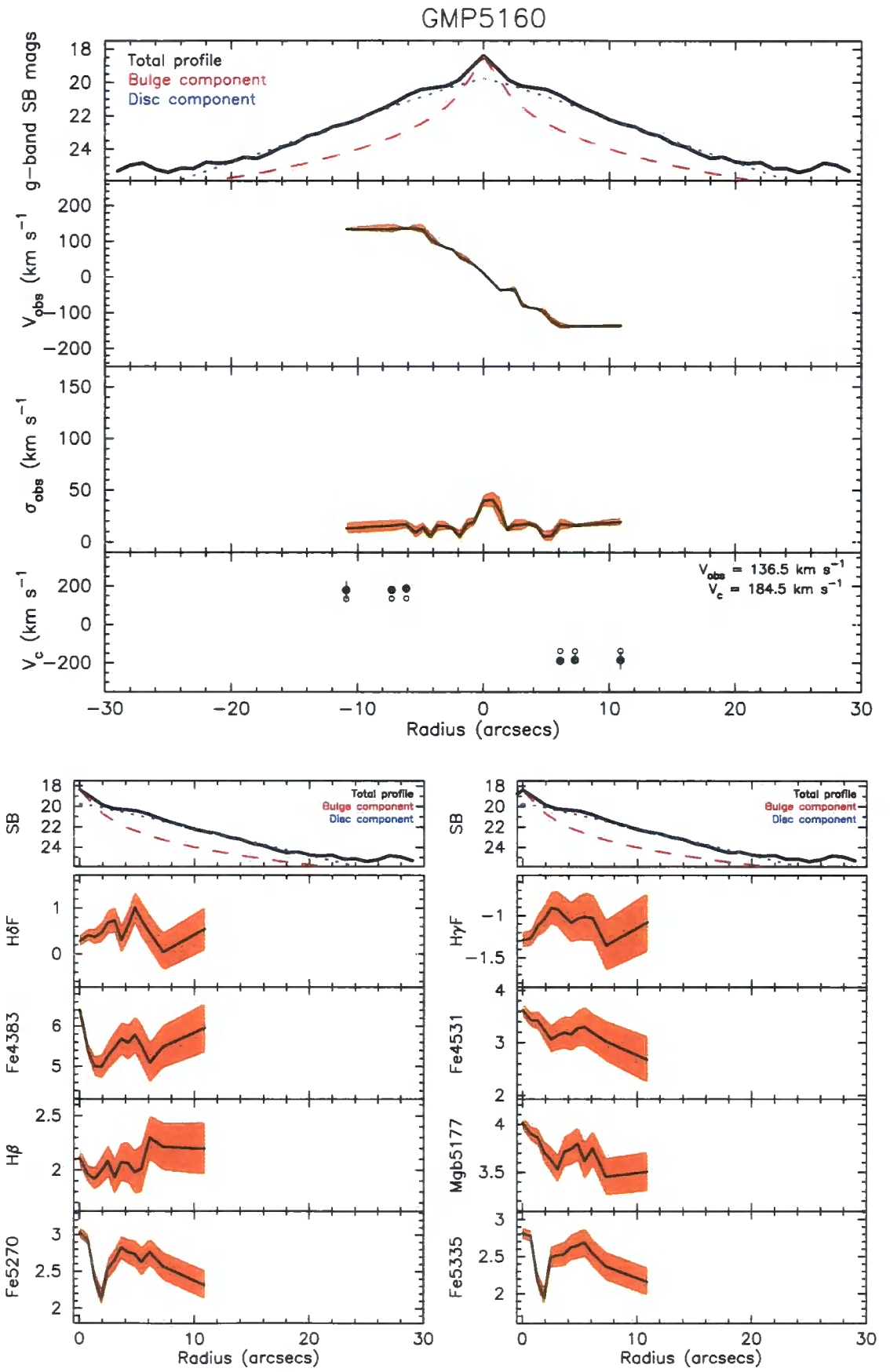

Figure D.8: Kinematic and absorption line profiles for GMP5160.